Sensitivity of simulated clouds to aerosols in the Benguela Region

N Kwatala

orcid.org/0000-0003-2962-9905

Dissertation accepted in fulfilment of the requirements for the degree *Master of Science in Environmental Sciences with Atmospheric Chemistry* at the North-West University

Supervisor:	Prof RM Garland
Co-supervisor:	Prof SJ Piketh

Graduation May 2023

25785125

ABSTRACT

Aerosol-cloud interactions have been studied since the 1970s. The interactions of the processes, such as aerosols' direct, semi-direct, and indirect effects on clouds in the atmosphere, are complex. There are large uncertainties in resolving the impact of aerosols on clouds in global circulation models. One area that has been identified with some of the largest uncertainties is the ubiquitous stratocumulus over the Benguela Region. Understanding how aerosols influence the lifetime and characteristics of the stratocumulus has not been fully explored in the Benguela Region. This study seeks to evaluate the representation of simulated aerosols and their effect on stratocumulus clouds in the Benguela Region in the Conformal Cubic Atmospheric Model (CCAM). The first aspect evaluated how CCAM simulates the magnitude, spatial pattern and seasonal cycles of total aerosol optical depth (AOD), as well as compositional AOD (i.e. black carbon, organic carbon, sulphate, small dust and sea salt) against satellite observations from a Moderate Resolution Imaging Spectroradiometer (MODIS) and a reanalysis product (i.e. Modern-Era Retrospective analysis for Research and Applications (MERRA)). The second aspect evaluated how CCAM simulates the magnitude, spatial pattern, and seasonal cycle of cloud fraction and liquid water path against satellite observations. The third aspect examined the seasonal spatial correlation between simulated aerosol optical depth, and cloud fraction and liquid water path using the CCAM model. To carry out the analysis for all three aspects, numerous tests were used, including eyeball verification as well as bias, spatial root mean square error and spatial correlation (r). The time period that the study considered was 2002 to 2017.

In general, the simulated total AOD in CCAM was lower compared to MODIS total AOD across all seasons. The aerosol optical depth attributable to black carbon and organic carbon, which peak during biomass burning, was underestimated by CCAM when compared to MODIS or MERRA. During biomass burning season, there is a positive linear correlation between aerosol optical depth attributable to black carbon and organic carbon, indicating that there is a linear association with how CCAM simulates aerosol optical depth compared to MODIS and MERRA. Aerosol optical depth attributable to sulphate

was overestimated by CCAM when compared to MERRA. Dust aerosols (i.e. small dust) and marine aerosols (i.e. sea salt) were underestimated by CCAM when compared to MERRA. This study also found that aerosol optical depth attributable to black carbon and organic carbon had interannual seasonal peaks in the spring in CCAM, MODIS and MERRA. Dust aerosols (i.e. small dust) and marine aerosols (i.e. sea salt) had different interannual seasonal peaks in different seasons within CCAM and within MERRA. Furthermore, dust aerosols and marine aerosols had different interannual seasonal peaks when comparing the CCAM simulation to MERRA.

Secondly, this study found that CCAM underestimates low cloud fractions at the northern region and the coast for all seasons, and that CCAM overestimates cloud fractions in the southern region of the domain when compared to satellite observations. Furthermore, CCAM has a magnitude of error ranging between 40 and 60% at the northern region and 0 and 30% in the southern region of the domain compared to satellite observations. It was also found that when aerosol optical depth was >0.22 in CCAM, there was no correlation ($r = -0.19 – 0.19$) between aerosol optical depth and cloud fraction. When aerosol optical depth was <0.22, aerosol optical depth and cloud fraction were weakly positively correlated in the northern region of the domain ($r = 0.20 – 0.39$). This study found that CCAM underestimated the liquid water path over the ocean when compared to satellite observations. Also, CCAM produced a magnitude of error ranging between 10 and 60 kg/m^2 when compared to satellite observations. Cloud fractions or liquid water path correlations between CCAM and satellite observations were more often weak positive ($r = 0.20 – 0.39$) than negative, although not strong. It was also found that when any correlation between cloud fraction or liquid water path and aerosol optical depth was found between CCAM and satellite observations, it was more often positive in the northern regions and negative in the southern domain.

Thirdly, this study found that aerosol optical depth attributable to black carbon and organic carbon had moderate or strong negative correlations ($r = -0.79 - -0.40$) with cloud fraction or liquid water path in winter within CCAM. Within CCAM, aerosol optical depth attributable to sulphate had strong positive correlation ($r = 0.60 – 0.79$) with cloud fraction in summer. Dust aerosols and marine aerosols had no strong correlations ($r = -0.19 – 0.19$) with cloud fraction within CCAM. Interannual seasonal plots for total aerosol optical

depth and compositional AOD and cloud fraction are similar, though not always within CCAM. Within CCAM, aerosol optical depth attributable to sulphate had no strong correlation (r = -0.19 – 0.19) with liquid water path. Dust aerosols had no correlation (r = -0.19 – 0.19) with liquid water path within CCAM. Marine aerosols had strong positive correlations (r = 0.60 – 0.79) in autumn and winter, and strong negative correlations (r = -0.79 - -0.60) in spring with liquid water path within CCAM.

The main findings of this study relative to the objectives were: (i) CCAM simulates the spatial distribution and peaks of aerosols, cloud fraction and liquid water path well, (ii) aerosols do influence cloud fraction and liquid water path, either directly proportionally or indirectly proportionally, and (iii) the influence of cloud fraction and liquid water path is not due to aerosols only, but also other parameters.

Keywords: Aerosols, AOD, aerosol-cloud interactions, AOD-cloud fraction, AOD-LWP, Benguela Region, Southeast Atlantic Ocean, CCAM model

PREFACE

This dissertation followed the North-West University's (NWU) Faculty of Natural and Agricultural Sciences General Rules. This dissertation entails the abstract, introduction and background (Chapter 1), literature review (Chapter 2), data and methods (Chapter 3), results and discussion (Chapters 4 and 5), as well as summary and conclusions (Chapter 6).

Acknowledgements

I would like to express my gratitude to those who made the completion of this dissertation possible:

- My supervisor and co-supervisor, Prof Garland and Prof Piketh, respectively, for their research guidance, motivation and also for providing me with the platform to learn from you.
- The Council for Scientific and Industrial Research (CSIR) for the graduate-in-training position and the skills and resources I was provided with.
- National Research Foundation (NRF) for funding this MSc study.
- ACCESS for the initiation of the project that my research topic stemmed from.
- Prof Engelbrecht for CCAM runs.
- Mr Sovara and Mr Koos for their guidance on data retrieval and technical support.
- Mr Mateyisi for guidance on the study methodology.
- Ms Mulovhedzi and Ms Kobo for their assistance with programming languages.

Scientific outputs

The results of this research study were presented at the South African Society for Atmospheric Sciences (SASAS) 2021 online virtual conference.

Table of contents

ABSTRACT i

PREFACE iv

LIST OF TABLES x

LIST OF FIGURES x

CHAPTER 1: INTRODUCTION AND BACKGROUND 1

1.1 Introduction 1

1.2 Aerosol-cloud interactions 2

1.3 Benguela Region 5

1.4 Justification 6

1.5 Aims and objectives 6

1.6 Outline of the dissertation 8

CHAPTER 2: LITERATURE REVIEW 10

2.1 Geographic location of study: Benguela Region 10

2.2 Aerosols 15

2.3 Aerosol variability 15

2.3.1 Introduction 15

2.3.2 Sources of aerosols 16

2.3.3 Transport of aerosols in southern Africa 20

2.4 Stratiform clouds 24

2.5 Aerosol-cloud interactions 24

2.6 Relationship between stratocumulus cloud fraction and aerosols 26

2.7 Relationship between stratocumulus cloud liquid water path and aerosols 27

2.8 Summary 29

CHAPTER 3: DATA AND METHODS 30
3.1 Study domain 30
3.2 Data and model output 31
3.2.1 Introduction 31
3.2.2 The CCAM model 31
3.2.3 MODIS satellite 36
3.2.4 AIRS instrument 37
3.2.5 MERRA-2 reanalysis 38
3.2.6 Data manipulation 40
3.3 Analysis methods 40
3.3.1 Introduction 40
3.3.2 Eyeball verification 41
3.3.3 Bias 42
3.3.4 Root mean square error 43
3.3.5 Pearson's correlation 43
3.3.6 Seasonal cycles 44
CHAPTER 4: VERIFICATION OF CCAM MODEL AGAINST MODIS OR MERRA OBSERVATIONS IN SIMULATING AEROSOLS 46
4.1 Magnitude between CCAM and MODIS or MERRA 46
4.1.1 Total aerosol optical depth 47
4.1.2 Compositional AOD: Black carbon 49
4.1.3 Compositional AOD: Organic carbon 51
4.1.4 Compositional AOD: Small dust 53
4.1.5 Compositional AOD: Sulphate 55
4.1.6 Compositional AOD: Sea salt 57

4.1.7 Summary 59
4.2 Quantitative verification between the CCAM and MODIS or MERRA 59
4.2.1 Total aerosol optical depth 60
4.2.2 Compositional AOD: Black carbon 64
4.2.3 Compositional AOD: Organic carbon 68
4.2.4 Compositional AOD: Small dust 72
4.2.5 Compositional AOD: Sulphate 76
4.2.6 Compositional AOD: Sea salt 80
4.2.7 Summary 83
4.3 Seasonal cycles between the CCAM and MODIS or MERRA 84
4.3.1 Total aerosol optical depth 85
4.3.2 Compositional AOD: Black carbon 85
4.3.3 Compositional AOD: Organic carbon 87
4.3.4 Compositional AOD: Small dust 88
4.3.5 Compositional AOD: Sulphate 89
4.3.6 Compositional AOD: Sea salt 90
4.3.7 Summary 91
CHAPTER 5: INTERACTIONS BETWEEN AEROSOLS AND CLOUD PROPERTIES SIMULATED BY CCAM 92
5.1 Magnitude of cloud fraction between CCAM and AIRS 92
5.1.1 CCAM vs AIRS (ascending vs descending) 93
5.2 Quantitative verification between CCAM and AIRS 95
5.2.1 CCAM vs AIRS (ascending vs descending) 96
5.3 Relationship between aerosols and cloud fraction 102
5.3.1 Total aerosol optical depth and cloud fraction 103

5.3.2 Compositional AOD of black carbon and cloud fraction 106
5.3.3 Compositional AOD of organic carbon and cloud fraction 109
5.3.4 Compositional AOD of small dust and cloud fraction 111
5.3.5 Compositional AOD of sulphate and cloud fraction 114
5.3.6 Compositional AOD of sea-salt and cloud fraction 116
5.3.7 Summary 118
5.4 Magnitude of liquid water path between CCAM and MODIS 119
5.4.1 CCAM vs MODIS (Aqua vs Terra) 120
5.5 Quantitative verification between CCAM and MODIS 122
5.5.1 CCAM vs MODIS (Aqua vs Terra) 123
5.6 Relationship between aerosols and liquid water path 129
5.6.1 Total aerosol optical depth and liquid water path 130
5.6.2 Compositional AOD of black carbon and liquid water path 132
5.6.3 Compositional AOD of organic carbon and liquid water path 134
5.6.4 Compositional AOD of small dust and liquid water path 136
5.6.5 Compositional AOD of sulphate and liquid water path 138
5.6.6 Compositional AOD of sea-salt and liquid water path 140
5.6.7 Summary 142
CHAPTER 6: CONCLUSIONS 144
6.1 Evaluation of aerosols in the CCAM model 144
6.2 Effects of aerosols on cloud fraction 146
6.3 Effects of aerosols on liquid water path 147
6.4 Synthesised results 148
6.5 Limitations and future research 148
Annexure A 150

Annexure B 166

Annexure C 172

Bibliography 178

LIST OF TABLES

Table 3. 1: Size distributions of dry tropospheric aerosol (taken from Rotstayn et al., 2007). 35

Table 5. 1: Correlation between cloud fraction total AOD and compositional AOD (i.e. black carbon, organic carbon, small dust, sulphate and sea salt).: Correlation between cloud fraction total AOD and compositional AOD (i.e. black carbon, organic carbon, small dust, sulphate and sea salt) 118

Table 5. 2: Correlation between liquid water path, total AOD and compositional AOD (i.e. black carbon, organic carbon, small dust, sulphate and sea salt).Table 5.2: Correlation between liquid water path, total AOD and compositional AOD (i.e. black carbon, organic carbon, small dust, sulphate and sea salt). 142

LIST OF FIGURES

Figure 1.1: Schematic diagram showing effects of aerosols in the atmosphere and clouds. On the diagram, small black dots represent aerosol particles; open circles represent cloud droplets; straight lines represent the incident and reflected solar radiation (taken from IPCC, 2007..... 3

Figure 2.1: The map of the Benguela Region bordering Namibia and South Africa, showing the approximate locations of the Angola Current, the Angola/Benguela (AB) Front, the Lüderitz upwelling cell (which separates the northern and southern Benguela subsystems), and the Agulhas Current (taken from Roux *et al.*, 2013) 10

Figure 2.2: Major features that affect the atmosphere and ocean of the Benguela Region (taken from Hutchings *et al.*, 2009) 13

Figure 2.3: Weather systems that affect the Benguela Region in austral winter (taken from Hutchings *et al.*, 2009) 14

Figure 2.4: Depicted locations of active fire detections by month (large image) and the biomes (small image) over Africa (taken from Gareth *et al.*, 2009) 19

Figure 2.5: Schematic diagram of seasonal fire occurrences in Africa (taken from Haywood *et al.*, (2008) 20

Figure 2.6: The average percentage transport and recirculation of air masses of major circulation types in southern Africa for the individual general circulation patterns proposed by Tyson *et al.* (1996)..... 21

Figure 2.7: The major pathways transporting and recirculating aerosols over southern Africa (taken from Piketh *et al.*, 1999) 22

Figure 2.8: Schematic representation of the four major near-surface trajectory modes that are likely to occur because of the eastwards or westward aerosol exit, or an anticyclonic circulation exit in southern Africa (Garstang *et al.*, 1996; Sinha *et al.*, 2004) 23

Figure 2.9: The processes by which aerosols influence the incoming solar radiation, including the ways in which they perturb cloud properties (taken from Jerez *et al.*, 2019) 25

Figure 3.1: The study area of interest (Benguela Region, denoted by the orange square on the left). The right shows the domain with subdomain 1, subdomain 2, subdomain 3 and subdomain 4 (EUMETSAT Southern Africa images (taken from EUMETSAT Image Gallery Animation - Meteosat 0 degree Natural Colour Enhncd. Southern Africa) 30

Figure 4.1: The multi-year (2002-2017) averaged total AOD simulated by CCAM (top) and observed MODIS AOD from Aqua (bottom) over the Benguela Region 47

Figure 4.2: The multi-year (2002-2017) averaged compositional AOD of black carbon simulated by CCAM (top) and MERRA (bottom) over the Benguela Region 49

Figure 4.3: The multi-year (2002-2017) averaged compositional AOD of organic carbon simulated by CCAM (top) and MERRA (bottom) over the Benguela Region 51

Figure 4.4: The multi-year (2002-2017) averaged compositional AOD of small dust simulated by CCAM (top) and MERRA (bottom) over the Benguela Region 53

Figure 4.5: The multi-year (2002-2017) averaged compositional AOD of sulphate simulated by CCAM (top) and MERRA (bottom) over the Benguela Region 55

Figure 4.6: The multi-year (2002-2017) averaged compositional AOD of sea-salt simulated by CCAM (top) and MERRA (bottom) over the Benguela Region 57

Figure 4.7: The multi-year (2002-2017) averaged bias (top), RMSE (middle) and correlation (bottom) of total AOD between CCAM and MODIS 61

Figure 4.8: The multi-year (2002-2017) averaged bias (top), RMSE (middle) and correlation (bottom) of compositional AOD of black carbon between CCAM and MERRA 65

Figure 4.9: The multi-year (2002-2017) averaged bias (top), RMSE (middle) and correlation (bottom) of compositional AOD of organic carbon between CCAM and MERRA 70

Figure 4.10: The multi-year (2002-2017) averaged bias (top), RMSE (middle) and correlation (bottom) of compositional AOD of small dust between CCAM and MERRA 74

Figure 4.11: The multi-year (2002-2017) averaged bias (top), RMSE (middle) and correlation (bottom) of compositional AOD of sulphate between CCAM and MERRA .. 78

Figure 4.12: The multi-year (2002-2017) averaged bias (top), RMSE (middle) and correlation (bottom) of compositional AOD of sea-salt between CCAM and MERRA ... 82

Figure 4.13: Area-averaged interannual seasonality of total AOD between CCAM simulations and MODIS observations for subdomain 1 85

Figure 4.14: Area-averaged interannual seasonality of compositional AOD of black carbon between CCAM simulations and MERRA for subdomain 1 86

Figure 4.15: Area-averaged interannual seasonality of compositional AOD of organic carbon between CCAM simulations and MERRA for subdomain 1 87

Figure 4.16: Area-averaged interannual seasonality of compositional AOD of small dust between CCAM simulations and MERRA for subdomain 1 88

Figure 4.17: Area-averaged interannual seasonality of compositional AOD of sulphate between CCAM simulations and MERRA for subdomain 1 89

Figure 4.18: Area-averaged interannual seasonality of compositional AOD of sea salt between CCAM simulations and MERRA for subdomain 1 90

Figure 5.1: The multi-year (2002-2017) averaged magnitude of simulated CCAM (top) and measured AIRS (ascending) (bottom) cloud fraction over the Benguela Region ... 93

Figure 5.2: The multi-year (2002-2017) averaged magnitude of simulated CCAM (top) and measured AIRS (descending) (bottom) cloud fraction over the Benguela Region . 95

Figure 5.3: The multi-year (2002-2017) averaged bias (top), RMSE (middle) and correlation (bottom) of cloud fraction between the CCAM and AIRS (ascending) 98

Figure 5.4: The multi-year (2002-2017) averaged bias (top), RMSE (middle) and correlation (bottom) of cloud fraction between the CCAM and AIRS (descending) 101

Figure 5.5: The multi-year (2002-2017) averaged spatial correlation between total AOD and cloud fraction 103

Figure 5.6: Area-averaged interannual seasonality between total AOD and cloud fraction for subdomain 1 105

Figure 5.7: The multi-year (2002-2017) averaged spatial correlation between compositional AOD of black carbon and cloud fraction 106

Figure 5.8: Area-averaged interannual seasonality between compositional AOD of black carbon and cloud fraction for subdomain 1 108

Figure 5.9: The multi-year (2002-2017) averaged spatial correlation between compositional AOD of organic carbon and cloud fraction 109

Figure 5.10: Area-averaged interannual seasonality between compositional AOD of organic carbon and cloud fraction for subdomain 1 111

Figure 5.11: The multi-year (2002-2017) averaged spatial correlation between compositional AOD of small dust and cloud fraction 111

Figure 5.12: Area-averaged interannual seasonality between compositional AOD of small dust and cloud fraction for subdomain 1 113

Figure 5.13: The multi-year (2002-2017) averaged spatial correlation between compositional AOD of sulphate and cloud fraction 114

Figure 5.14: Area-averaged interannual seasonality between compositional AOD of sulphate and cloud fraction for subdomain 1 116

Figure 5.15: The multi-year (2002-2017) averaged spatial correlation between compositional AOD of sea-salt and cloud fraction 116

Figure 5.16: Area-averaged interannual seasonality between compositional AOD of sea-salt and cloud fraction for subdomain 1 117

Figure 5.17: The multi-year (2002-2017) averaged magnitude of simulated CCAM (top) and measured Aqua (bottom) liquid water path in kg/m^2 over the Benguela Region... 121

Figure 5.18: The multi-year (2002-2017) averaged magnitude of simulated CCAM (top) and measured Terra (bottom) liquid water path in kg/m^2 over the Benguela region.... 121

Figure 5.19: The multi-year (2002-2017) averaged bias (top), RMSE (middle) and correlation (bottom) of liquid water path between the CCAM and MODIS Aqua 125

Figure 5.20: The multi-year (2002-2017) averaged bias (top), RMSE (middle) and correlation (bottom) of liquid water path between the CCAM and MODIS Terra 128

Figure 5.21: The multi-year (2002-2017) averaged spatial correlation between total AOD and liquid water path 130

Figure 5.22: Area-averaged interannual seasonality between total AOD and liquid water path for subdomain 1..... 132

Figure 5.23: The multi-year (2002-2017) averaged spatial correlation between compositional AOD of black carbon and liquid water path 132

Figure 5.24: Area-averaged interannual seasonality between compositional AOD of black carbon and liquid water path for subdomain 1..... 133

Figure 5.25: The multi-year (2002-2017) averaged spatial correlation between compositional AOD of organic carbon and liquid water path 134

Figure 5.26: Area-averaged interannual seasonality between compositional AOD of organic carbon and liquid water path for subdomain 1 135

Figure 5.27: The multi-year (2002-2017) averaged spatial correlation between compositional AOD of small dust and liquid water path..... 136

Figure 5.28: Area-averaged interannual seasonality between compositional AOD of small dust and liquid water path for subdomain 1 137

Figure 5.29: The multi-year (2002-2017) averaged spatial correlation between compositional AOD of sulphate and liquid water path 138

Figure 5.30: Area-averaged interannual seasonality between compositional AOD of sulphate and liquid water path for subdomain 1 139

Figure 5.31: The multi-year (2002-2017) averaged spatial correlation between compositional AOD of sea-salt and liquid water path 140

Figure 5.32: Area-averaged interannual seasonality between compositional AOD of sea-salt and liquid water path for subdomain 1 141

CHAPTER 1: INTRODUCTION AND BACKGROUND

1.1 Introduction

Aerosols are defined as small particles suspended in the air as either liquid or solid particles (Hendricks *et al.*, 2012). Aerosol particles are produced by natural and anthropogenic sources. Natural sources that produce aerosol particles include sea-salt spray, dust or volcanic ashes (Hendricks *et al.*, 2012). Anthropogenic sources that produce aerosol particles include domestic burning, vehicle emissions or industrial emissions (Hendricks *et al.*, 2012). Primary aerosols are particles emitted directly into the atmosphere, and secondary aerosols are particles that are the products of chemical reactions occurring in the atmosphere (France *et al.*, 2013). Secondary aerosols, such as secondary organic aerosols, are produced when gas-phase species react and then condense in the atmosphere. Aerosol particles are an air pollutant that has negative impacts on human health (Hendricks *et al.*, 2012). The existence of aerosols in the atmosphere influences climate through their impact on the radiation budget (Bott, 1999).

The output of this research can contribute to improving the understanding of the relationship between aerosols and stratocumulus clouds in the Benguela Region, which will contribute to the knowledge of aerosol-cloud interactions. Clouds and aerosols' interactions and the processes they undergo are well studied and explained in detail in theory. Theoretical studies have found that the interactions between clouds and aerosols and the processes that affect the interactions are highly complex (Chauvigné *et al.*, 2020; Kuik *et al.*, 2015). Some of the highly complex processes are hard to parameterise in models, leading to processes being overly simplified or completely unaccounted for, which leads to uncertainties regarding climate modelling studies (Chauvigné *et al.*, 2020; Kuik *et al.*, 2015). Aerosols are one of the components that attribute to climate change either by altering cloud formation and growth, or altering the amount of solar radiation in the atmosphere. Although climate change affects all countries on the planet, developing

countries, where my study domain is located, are more vulnerable to the impacts of climate change such as changes in rainfall patterns and wildfires (IPCC, 2014).

It is of significance that parameters such as aerosols and clouds be researched over the Benguela Region to determine how they contribute to the climate change of the entire planet. The outcome of this work will demonstrate how well the Conformal Cubic Atmospheric Model (CCAM) simulates aerosols and clouds, as compared to satellite observations and an aerosol reanalysis product. This research focused on total aerosol optical depth (AOD) as well as compositional contribution to total aerosol optical depth by black carbon, organic carbon, sulphate, small dust and sea salt. The cloud parameters that were investigated were cloud fraction and liquid water path. Aerosol optical depth is defined as a measure of attenuation of solar radiation by a column of aerosols. This research will demonstrate the relationship between the simulated aerosol optical depth and cloud parameters. The results are presented spatially and seasonally.

1.2 Aerosol-cloud interactions

Aerosol-cloud interactions have been studied since the 1970s, but the interactions pertaining to all processes, such as direct, semi-direct, and indirect effects of aerosols on clouds, still have uncertainties. Aerosols affect the climate by scattering and/or absorbing radiation, and this is defined as the direct effect (Liu *et al.*, 2020). Fig. 1.1 shows the interactions between aerosols and clouds. The direct effects address how shortwave and longwave radiation is scattered or absorbed by aerosols in the atmosphere. Aerosols that scatter radiation let the Earth lose energy (i.e. the Earth becomes cooler), leading to negative radiative forcing occurring at the top of the atmosphere. Aerosols that absorb radiation let the Earth gain energy (i.e. the Earth becomes warmer), leading to positive radiative forcing occurring at the top of the atmosphere. These forcings affect global mean surface temperature (Gao *et al.*, 2020).

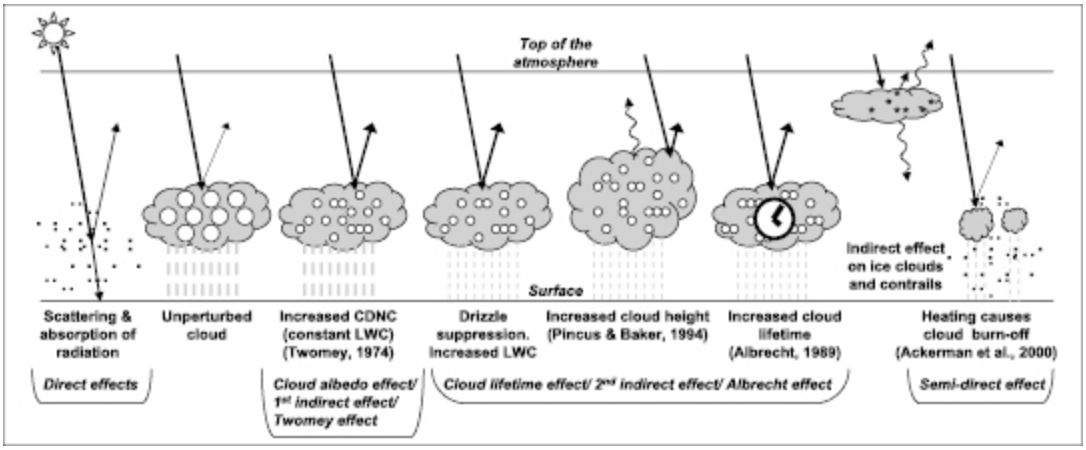

Figure 1.1: Schematic diagram showing effects of aerosols in the atmosphere and clouds. On the diagram, small black dots represent aerosol particles; open circles represent cloud droplets; straight lines represent the incident and reflected solar radiation (taken from IPCC, 2007.

Twomey (1977) was first to describe the first indirect effect, and proposed that aerosols and clouds interact. Twomey (1977) stated that an increase of aerosols leads to an increase of cloud condensation nuclei (CCN), which, in turn, leads to more cloud droplets, but with smaller cloud droplet size. This will increase cloud albedo. In general, an increase in CCN leads to a decrease in the cloud droplet size, and an increase in cloud optical thickness (Fig. 1.1) (Sporre *et al.*, 2012). The indirect effects address how clouds' microphysics are changed by aerosols in the atmosphere. The cloud formation, growth, precipitation and lifetime trends change with the presence of aerosols. Albrecht (1989) first described the second indirect effect, and hypothesised that the increased smaller water droplets do not precipitate, because the water content in the atmosphere was heavily reduced; and because there is no precipitation, the cloud lifetime increases (Fig. 1.1).

The semi-direct effects address how the air parcel is affected by aerosols in the atmosphere. Aerosols that absorb radiation change the air temperature, relative humidity, atmospheric stability, and evaporation of clouds. The warming generated from radiation affects the climate through dissipating low clouds that scatter shortwave radiation into space, but do not significantly reduce outgoing longwave radiation. Semi-direct effects had positive radiative forcing when studied through low-level clouds (Mallet *et al.*, 2020;

Muhlbauer *et al.*, 2014). The physical and chemical processes of aerosols are well understood in theory; however, the representation of this is not well represented in global circulation models (Li *et al.*, 2022).

Global circulation models (GCMs) are tools used to simulate the atmosphere for the projection of the future climate. These models use the laws of physics and mathematical equations that are solved by means of complex numerical methods (Engelbrecht *et al.*, 2011). Global circulation models were introduced several decades ago, and they have been improving ever since (i.e. finer resolutions, better understanding of physics and chemistry processes and laws, and complex parameterisations). However, there are still uncertainties that affect the climate model performance. One uncertainty in aerosol-cloud interactions is some simplified parameterisations that fail to capture cloud microphysical properties such as the phase or amplitude of the diurnal cycle of cloud fraction (Burleyson & Yuter, 2015). Furthermore, some GCMs struggle to simulate meteorological processes and systems that influence aerosols and aerosol properties (i.e. driving mechanisms of aerosol emissions) (Zhao *et al.*, 2022). However, over the years, regional models had been developed and are more sophisticated for specific areas using the specific area's meteorology, synoptic scale forcing, orography, and diurnal cycle. It is important to understand/evaluate how well models today simulate cloud, aerosol, and their properties. Are they skilful in determining the relationships between multiple variables (i.e. correlation between an increase in aerosols and cloud cover)?

Satellite-based remote sensing had been the primary tool used to observe aerosol-cloud interactions in the research community, though it limited the research community in studying the processes involved (Cecchini *et al.*, 2017; Rosenfeld *et al.*, 2019). Satellite-based remote sensing is advantageous over *in-situ* measurements, which are sparsely distributed and are prone to vandalism and loss of data. Satellite-based remote sensing is advantageous because of larger spatial coverage of the earth, meaning that their observations are studied at across multiple environments of different attributes (Nakajima *et al.*, 2001; Sekiguchi *et al.*, 2003; Wagner *et al.*, 2010). Satellite-based remote sensing in the research community is used to measure and monitor the atmosphere's ozone layer, solar radiation, aerosols, greenhouse gases, temperature, humidity, winds, cloud cover, and volcanic ash plumes (Yu *et al.*, 2013).

1.3 Benguela Region

The Benguela Region is located on the west coast of southern Africa. This region hosts the Benguela upwelling system, which is a complex and vast ecosystem. The Benguela Region has persisting stratocumulus clouds (Kaufman *et al.*, 2005). These clouds affect the sea surface temperatures, thereby changing the Earth's energy distribution (Formenti *et al.*, 2019). Multiple measurement campaigns (SAFARI-1992, SAFARI-2000, CLARITY, AEROCLO-sA and ORACLES) have been conducted in and near this region that have focused on aerosols and their interactions with the stratocumulus clouds. The Southern African Fire-Atmosphere Research Initiative (SAFARI-1992) was a campaign that took place in the dry season of 1992 (Lindesay *et al.*, 1996). The major objective of SAFARI-92 was to study the impact of vegetation fires in atmospheric chemistry, climate and the ecology of Southern Africa (Lindesay *et al.*, 1996). The Southern African Regional Science Initiative (SAFARI-2000) was a campaign that took place from 2000 to 2001, and its major objective was to study the land-atmospheric interactions and biogeochemical processes in Southern Africa (Swap *et al.*, 2003). The methodology used both satellite-based remote sensing with airborne and *in-situ* instruments to study multiple components of land-atmospheric interactions and biogeochemical processes The methodology used both satellite-based remote sensing with airborne and *in-situ* instruments to study multiple components of land-atmospheric interactions and biogeochemical processes (Swap *et al.*, 2003). The AEROCLO-sA campaign studied the effect of natural and anthropogenic aerosols on stratocumulus clouds along the coast of Namibia (Formenti *et al.*, 2019). ObseRvations of Aerosols above CLouds and their intEractionS (ORACLES) investigated biomass burning and how it affects the climate and alters atmospheric processes (Redemann *et al.*, 2021). Generally, the campaigns were investigating the aerosols and components related to aerosols, as well as their effect on the atmosphere and the components related to the atmosphere such as clouds.

1.4 Justification

There are large uncertainties due to oversimplified parameterisations or unaccounted theoretical processes of aerosols in GCMs. There are persistent stratocumulus cloud decks throughout the year in the Benguela Region. Understanding how aerosols influence cloud parameters of the stratocumulus in the Conformal Cubic Atmospheric Model (CCAM) has not been fully explored in the Benguela Region. This study seeks to evaluate the representation of simulated aerosols and their effect on stratocumulus clouds in the Benguela Region with the CCAM model. This study will focus on simulated aerosol optical depth and compare, on a seasonal basis, simulated stratocumulus cloud fractions and liquid water path in the CCAM. These two cloud parameters were selected because they have been found to have a direct relationship with total aerosol optical depth and compositional AOD (i.e. black carbon and sea salt) when using satellite-based remote sensing (Balakrishnaiah *et al.*, 2012; Nyasulu *et al.*, 2020). Black carbon aerosols, organic carbon aerosols, sulphate aerosols, small dust and sea salt affect the magnitude of cloud droplets, which, in turn, affect cloud fraction; and they also affect the lifetime of clouds by altering the liquid water path (Hendricks *et al.*, 2012). This study will assess the performance of CCAM, and it will initiate an understanding of the linkages between aerosol optical depth and cloud fraction, and aerosol optical depth and liquid water path in the CCAM. This is important, as the CCAM is used in this area mostly for climate projections, however, the association of cloud variables against aerosols has not been explored. The research questions of this study are (i) how well CCAM simulates aerosols and cloud properties compared to observations, and (ii) what effects aerosols has of cloud fraction and liquid water path. The output of this research can contribute to improving the understanding of the relationship between aerosols and stratocumulus clouds in the Benguela Region, which will contribute to the knowledge of aerosol-cloud interactions.

1.5 Aims and objectives

This study evaluated the representation of simulated aerosols and their effect on stratocumulus cloud parameters in the Benguela Region in the Conformal Cubic Atmospheric Model (CCAM).

Objective 1

To investigate the seasonal, temporal and spatial variations of total aerosol optical depth (AOD) and compositional AOD (i.e. black carbon, organic carbon, sulphate, small dust and sea salt) using the CCAM and satellite observations over the Benguela Region.

Magnitude of AOD: The magnitude of the simulated total aerosol optical depth from the CCAM and measured aerosol optical depth from the satellite instrument, Moderate Resolution Imaging Spectroradiometer (MODIS) Terra, was compared over the domain of interest (shown in Fig. 3.1).

Magnitude of compositional AOD: The magnitude of the simulated compositional AOD (black carbon, organic carbon, sulphate, small dust and sea salt) from the CCAM and output from the Modern-Era Retrospective analysis for Research and Applications (MERRA) reanalysis product was compared over the domain of interest.

Quantitative verification of AOD: The bias, root mean square error and correlation of the CCAM and MODIS total aerosol optical depth were performed.

Quantitative verification of compositional AOD: The bias, root mean square error and correlation of the CCAM and MERRA compositional AOD (black carbon, organic carbon, sulphate, small dust and sea salt) were performed.

Seasonal cycles of AOD: The area-averaged seasonal cycle of the domain of total aerosol optical depth simulated in the CCAM was compared with measurements from MODIS.

Seasonal cycles of AOD: The area-averaged seasonal cycle of the domain of compositional AOD (black carbon, organic carbon, sulphate, small dust and sea salt) simulated in the CCAM was compared with reanalysis from MERRA.

Objective 2

To examine the effects of simulated aerosol optical depth (total and compositional) on stratocumulus cloud fraction.

Magnitude of cloud fraction: The magnitude of the simulated cloud fraction from the CCAM and measured cloud fraction from the Atmospheric Infrared Sounder (AIRS) were compared over the domain of interest.

Quantitative verification of cloud fraction: The bias, root mean square error and correlation of the CCAM and AIRS cloud fraction were performed.

Relationship between AOD and cloud fraction: The relationship between the simulated aerosol optical depth (total and compositional) and simulated cloud fraction from the CCAM was assessed using correlation analysis.

Seasonal cycle of AOD and cloud fraction: The area-averaged seasonal cycle of simulated aerosol optical depth (total and compositional) and simulated cloud fraction from the CCAM was performed over the domain of interest.

Objective 3

To determine the effects of simulated aerosol optical depth (total and compositional) on liquid water path stratocumulus clouds.

Magnitude of liquid water path: The magnitude of the simulated liquid water path from CCAM and measured liquid water path from the satellite MODIS was compared over the domain of interest.

Quantitative verification of liquid water path: The bias, root mean square error and correlation of the CCAM and MODIS liquid water path were performed.

Relationship between AOD and liquid water path: The relationship between the simulated aerosol optical depth (total and compositional) and simulated liquid water path from CCAM was developed using correlation analysis.

Seasonal cycle of AOD and liquid water path: The area-averaged seasonal cycle of simulated aerosol optical depth (total and compositional) and simulated liquid water path from CCAM was performed.

1.6 Outline of the dissertation

Chapter 1: Introduction and background

Introduction to aerosols, their effect on the atmosphere, aerosol composition, and their origin in southern Africa. Introduction to aerosol-cloud interactions and how GCMs

simulate aerosol composition and stratocumulus clouds. The justification of the study's aims and objectives and the outline of the dissertation are presented in this chapter.

Chapter 2: Literature review

Information about the study area is presented in this chapter. The details of types of aerosols, sources of aerosols in southern Africa, and aerosol-cloud interactions are provided. The relationship between stratocumulus clouds' cloud fraction and aerosols, and the relationship between stratocumulus clouds' liquid water path and aerosols are presented in this chapter.

Chapter 3: Data and methods

A description of data sources, where data was sourced, how data was measured/simulated, and how data was manipulated for this study are presented in this chapter. Qualitative and quantitative methodologies are explained in detail, and why they were selected for this study and how they were applied.

Chapter 4: Verification of CCMA against MODIS or MERRA observations in simulating aerosols

The findings for objective 1 of the study and a discussion of the results relative to previous research are presented in this chapter.

Chapter 5: Interactions between aerosols and cloud properties simulated by CCAM

The findings for objectives 2 and 3 and the discussion of the results relative to previous research are presented in this chapter.

Chapter 6: Conclusions

The findings of this study are summarised and synthesised in this chapter. Limitations of the current study as well as recommendations for future research are included.

CHAPTER 2: LITERATURE REVIEW

2.1 Geographic location of study: Benguela Region

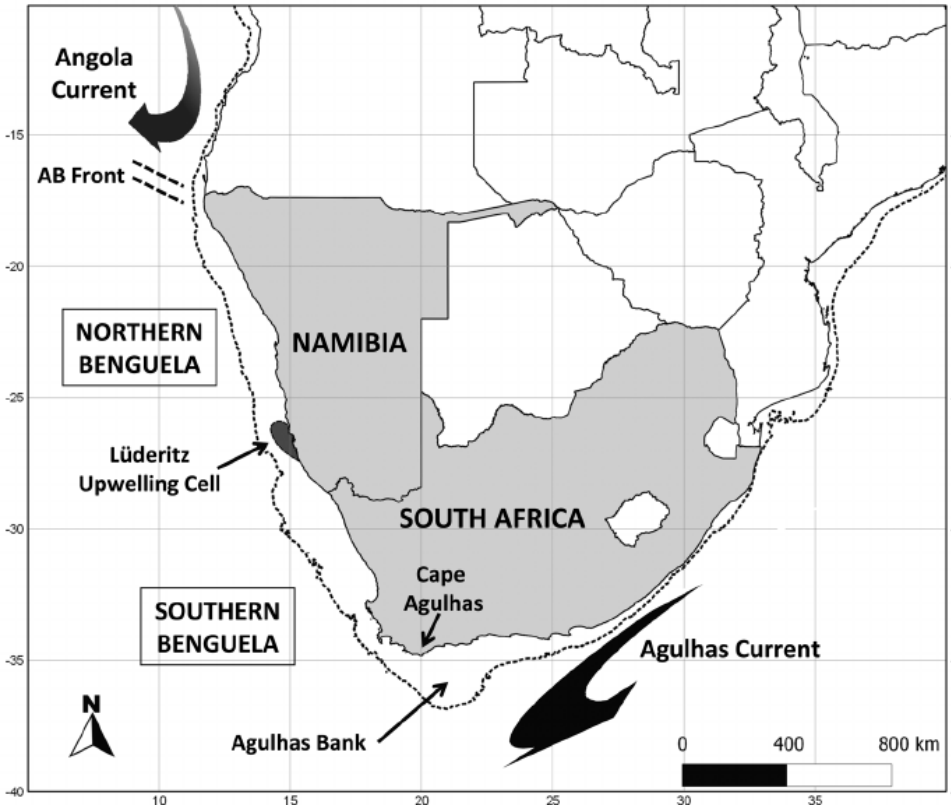

Figure 2.1: The map of the Benguela Region bordering Namibia and South Africa, showing the approximate locations of the Angola Current, the Angola/Benguela (AB) Front, the Lüderitz upwelling cell (which separates the northern and southern Benguela subsystems), and the Agulhas Current (taken from Roux *et al.*, 2013)

The Benguela Region is located along the coast of southwestern Africa, extending from Cabinda (approximately 5°S) in Angola on the north, and southwards to Cape of Good Hope (approximately 35°S) in South Africa (see Fig. 2.1) (James, 2011; Shannon, 1985). The Benguela Region houses one of the four main upwelling systems in the world that lie at the eastern boundaries of the oceans, i.e. the Benguela upwelling system (O'Toole *et*

al., 2001; Skogen, 1999). Upwelling systems are areas where cooler water with nutrients from the deep ocean rises to the surface of the ocean near the coast. This cooler water replaces warmer water that has been blown by the wind into the inner ocean. The Benguela Region is divided into the northern subtropical region and southern subtropical region by the Luderitz upwelling cell located between 26°S and 34°S (Hutchings *et al.*, 2009; Wedepohl *et al.*, 2000). The northern subtropical region is a cool temperate upwelling region, while the southern subtropical region is a warm temperate region (Hutchings *et al.*, 2009).

The dynamic processes of the Benguela Region from the north to the south are shown in Fig. 2.2. In summary, the northern boundary located next to Cabinda (approximately 5°S) separates the tropical Gulf of Guinea from Angola's subtropical system (Hutchings *et al.*, 2009). The Angola Current is bound by the northern boundary and the Angola-Benguela front at approximately 17°S. The Angola Current is a segment of the south equatorial counter-current that flows from north to south along the coast of Angola towards the very dynamic but shallow Angola-Benguela front (Hutchings *et al.*, 2009). Significant embayment exist at Lobito (12°S), Walvis Bay (23°S) and St Helena Bay (32°S) (Hutchings *et al.*, 2009). Between Cape Point and Cape Agulhas, at approximately 34°S, the orientation changes from north-south to east-west (Hutchings *et al.*, 2009). A major wind-driven upwelling zone of the Benguela Region is located between Cape Frio and Cape Agulhas (Hutchings *et al.*, 2009). The wind-driven upwelling system, Luderitz, is a very strong upwelling system that contains strong winds, strong turbulent mixing and high off-shore advection (Shillington *et al.*, 2006). Minor upwelling centres are created when shelf width combines with coastal topography (Shillington *et al.*, 2006). Cool productive water surfaces (comes up to the surface from deep waters) in the Agulhas Bank where the Agulhas Current diverges and where the cool ridge manifests as shallow isotherms (Hutchings *et al.*, 2009). The Agulhas Current flows on the edge of the shelf-break of the Agulhas Bank to the west (Hutchings *et al.*, 2009; Shillington *et al.*, 2006). The majority of 60 to 80 sverdrup current flow is retroflected back to the south Indian Ocean (Shillington *et al.*, 2006). Some of the warm saline water flows towards the north as jets, filaments and Agulhas Ring into the South Atlantic (Shillington *et al.*, 2006). The estimated current flow into the South Atlantic varies by latitude and it is 18.7 sverdrup, 20 sverdrup, 21

sverdrup and 13 sverdrup on average 18°S relative to 1200 m, 32°S relative to 500 m, 32°S, 30 °S, respectively (Fu, 1981; Garzoli & Gordon, 1996; Shannon, 1985).

The atmospheric circulation in the Benguela Region is dominated by two pressure cells, namely the semipermanent South Atlantic high pressure that develops in austral winter and continental low pressure that develops in austral summer (see Fig. 2.3) (Peterson & Stramma, 1991). The South Atlantic High (SAH) pressure shifts north and south seasonally, and the interactions between continental low pressure and the inter-tropical convergence zone make upwelling-favourable winds (Shillington *et al.*, 2006). In the austral winter, SAH on the west coast of the Benguela Region shifts northwards and it intensifies the zonal pressure gradient, which, in turn, enhances the southerly wind stress of the region (Boyd & Nelson, 1998). Wind stress is the force exerted on the ocean surface by the wind, in the direction of the wind. In the austral summer, a surface heat-induced continental low pressure develops on the west coast of the Benguela Region, and it intensifies the zonal pressure gradient, which, in turn, enhances southerly wind stress in the region (Boyd & Nelson, 1998). Another rare heat-induced cut-off low pressure develops over the northern coast of Namibia, and it is associated with westerly wind stress that feeds into the convergence of the Inter-tropical convergence zone and the Congo air boundary (Boyd & Nelson, 1998). Additional seasonal changes in low-level winds are due to mesoscale, synoptic and intra-seasonal (Boyd & Nelson, 1998). Cold fronts and cut-off lows are synoptic features that tend to significantly perturb anticyclonic equatorward wind flow (Boyd & Nelson, 1998). Cold fronts are prevalent in austral winter and cut-off lows are most common in austral spring and autumn, although they can occur in any season (Boyd & Nelson, 1998). Berg winds, which are sometimes followed by coastal lows, and sea breezes are mesoscale features that tend to perturb coastal wind fields (Boyd & Nelson, 1998; Reason & Jury, 1990). West coast troughs are prevalent over the northern coast of Namibia in winter and over the southern coast of Namibia in summer, and they affect the entire coast south of approximately 10°S (Boyd & Nelson, 1998).

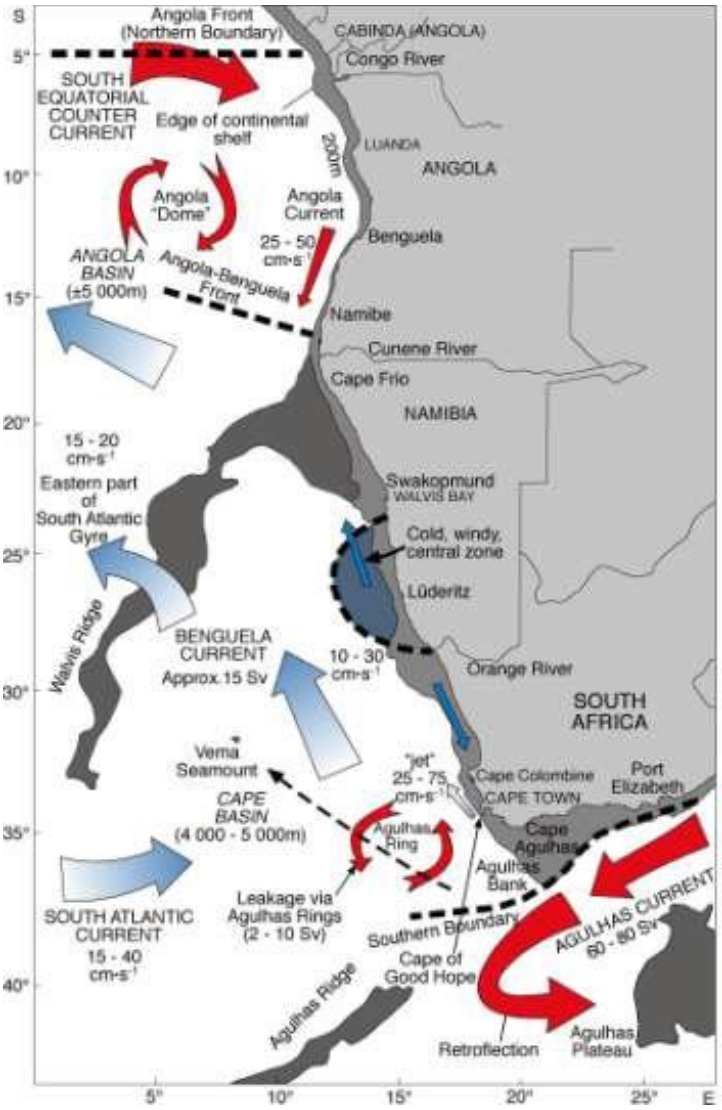

Figure 2.2: Major features that affect the atmosphere and ocean of the Benguela Region (taken from Hutchings *et al.*, 2009)

Large-scale modes of variability that affect the atmospheric circulation over the Benguela Region are detailed in Reason *et al.* (2006). There are four major modes (Hutchings *et al.*, 2009). The first mode is derived from the equatorial Atlantic north and south Atlantic, and it connects the occurrence of Benguela Niños and the strength of trade winds (Florenchie *et al.*, 2004). The second mode is derived from the South Atlantic anticyclone, and it is connected to El Niño Southern Oscillation (ENSO) events (Martín *et al.*, 2007; Mo & Paegle, 2001; Shillington *et al.*, 2006). The third mode is derived from the

midlatitudes, and it is connected to strong interdecadal patterns (Reason & Jury, 1990). The fourth mode is the Southern Annual Mode, and it affects the intensity and pathways of westerly winds (Reason *et al.,* 2006; Kidson, 1988). Strong dipole-like sea-surface temperature variability that is prevalent in austral summer affects the Benguela Region by impacting the atmospheric forcings of the region (Fauchereau *et al.*, 2003; Hermes & Reason, 2005).

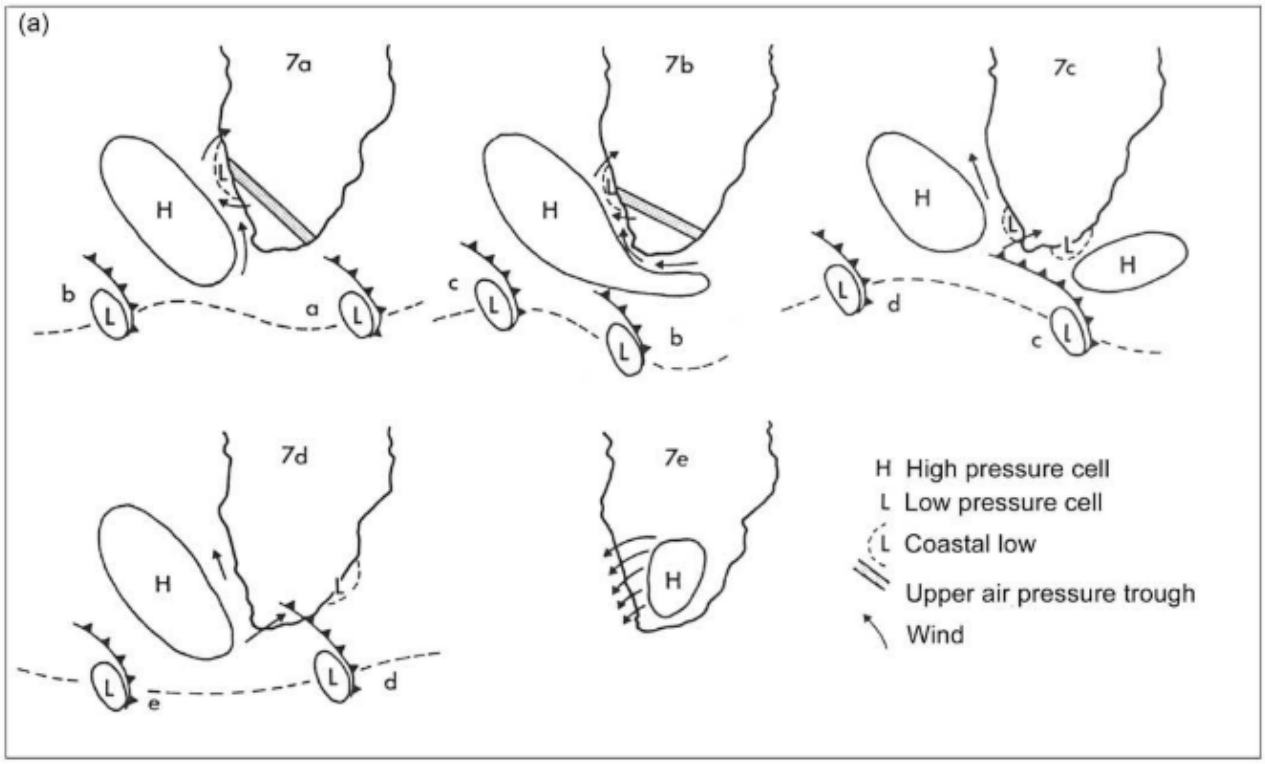

Figure 2.3: Weather systems that affect the Benguela Region in austral winter (taken from Hutchings *et al.*, 2009)

The Benguela Region's prevailing winds are from the south and southeast (Peterson & Stramma, 1991). Average seasonal surface wind speeds are estimated to be 10 m/s (Lima *et al.*, 2019). The Benguela Region has unique bathymetry, hydrography, chemistry and trophodynamics, placing the ocean among the most productive oceans globally, having an annual average of primary productivity of 1 to 2 g C m^{-2} y^{-1} (Brown *et al.*, 1991). The Benguela Region encompasses important biodiversity and biomass of

phytoplankton, zooplankton, fish, seabirds, kelp, marine mammals, rich deposits of minerals found off-shore and on-shore, and oil and gas reserves (O'Toole *et al.*, 2001). The rapid degradation of the coast due to pollution from industries, poorly planned coastal developments, and near-shore are a threat to the vulnerable ecosystem of this region (O'Toole *et al.*, 2001).

2.2 Aerosols

Aerosols are defined as small particles suspended in the air as either liquid or solid particles (Hendricks *et al.*, 2012). Aerosol particles are produced by natural and anthropogenic sources. Aerosols from natural sources include sea-salt spray, dust or volcanic ashes (Hendricks *et al.*, 2012). Aerosols from anthropogenic sources include domestic burning, vehicle emissions or industrial emissions (Hendricks *et al.*, 2012). Aerosols can either be emitted into the atmosphere directly or are formed in the atmosphere. Aerosols that are emitted directly into the atmosphere are called primary aerosols, and aerosols that form from chemical reactions occurring in the atmosphere are called secondary aerosols (France *et al.*, 2013). The sizes of aerosols differ based on the composition and source. In general, they range from a few nanometres to over ten micrometres (Hendricks *et al.*, 2012). Aerosol particles are an air pollutant that has negative impacts on human health (Hendricks *et al.*, 2012). The existence of aerosols in the atmosphere influences climate through their impact on the radiation budget (Bott, 1999).

2.3 Aerosol variability

2.3.1 Introduction

This section outlines the sources of aerosols, how aerosols are transported, and which atmospheric circulations influence the transport of aerosols in southern Africa. The are several sources of aerosols; however, selecting the sources for study purposes depends on what the study is about (i.e. the combustion of fossil fuels will be important for indoor air quality compared to dust). The focus of this research is on the influence of aerosols

on clouds, and sources such as biomass burning, dust, and marine aerosols are high contributors that could be transported to far away distances.

2.3.2 Sources of aerosols

(a) Dust

Dust aerosols are small soil particles that are found naturally on land from soil or rock debris. The size of dust aerosols ranges between nanometres and micrometres, depending on the region, soil type and exposure of soil layers. Dust originates from arid and dry regions where rainfall is low, or dry-lake beds or in areas where land has been disturbed by grazing and cultivation, deforestation and erosion (Ginoux *et al.*, 2001; Tesfaye *et al.*, 2013). Dust of smaller sizes is able to enter humans' lungs through inhalation and this causes respiratory health problems (Mahowald *et al.*, 2014). Dust aerosols are ejected into the atmosphere by strong winds that force particles with diameters between 100 and 200 μm to move (Alfaro *et al*., 1998). Large dust (>50 μm in diameter) is merely shifted, but does not reach the boundary layer (Betzer *et al.*, 1988). Small dust (<50 μm in diameter) is lifted to the boundary layer and higher, and it is transported for kilometres (Grousset *et al.*, 2003; Prospero, 1996). The lifetime of the dust aerosols depends on the size. Small dust falls much slower to the surface compared to large dust. The estimated dust emissions per year range between 10^3 and 5×10^3 teragram globally (Andreae, 2009; Kanakidou *et al.*, 2005). Dust aerosols affect the biogeochemical cycle by transporting and depositing nutrients (Mahowald *et al.*, 2014; Tlhalerwa *et al.*, 2005).

Dust that affects the Benguela Region originates from the lake basins of Etosha Pan and the Namib Desert (Gkikas *et al.*, 2022; Vickery *et al.*, 2013). Dust is transported to the ocean by strong wind speeds and weather systems. Large dust is transported to the ocean by north easterly or south easterly winds. Coastal lows, south westerly winds, cold front, easterly winds, and semi-permanent subcontinental high are other forms of systems that transport dust (Formenti *et al.*, 2019; Gkikas *et al.*, 2022). Small dust is transported to the ocean by winds from all directions (Zuidema *et al.*, 2016). The emissions from

Etosha Pan occur between April and November, while from the Namib Desert they occur between April and September (Vickery *et al.*, 2013; Zhao *et al.*, 2022). Summer followed by spring has the maximum seasonal emissions; however, the difference between maximum and minimum seasonal cycles is small, meaning that dust activity is similar during the year (Gkikas *et al.*, 2022).

(b) Marine aerosols

Marine aerosols are the largest natural aerosol source (Liu *et al.*, 2020a). Marine aerosols are produced on the ocean's surface, which covers at least 70% of the earth's surface (Liu *et al.*, 2020a). Marine aerosols are divided into two types, namely primary sea spray aerosols (i.e. sea salt) and secondary marine aerosols (i.e. dimethyl sulphide (DMS) and biogenic volatile organic compounds (VOCs)) (Mayer *et al.*, 2020). Primary sea spray aerosols are produced by many physical processes all depending on strong wind speeds, the most common being when the entrained air bubbles burst during whitecap formation, followed by the breaking of drops from wave tops (Afeti & Resch, 1990; Monahan, 1988; Tegen *et al.*, 1997). Secondary marine aerosols are produced through gas-to-particle conversion of the oxidation products in gas phase compounds, and are emitted from the ocean into the atmosphere (Mayer *et al.*, 2020). Biogenic VOCs can form new aerosols through nucleation or condense on pre-existing aerosols (Kroll & Seinfeld, 2008). The size of marine aerosol particles for coarse mode ranges between 0.05 and 10 µm in diameter (Quinn *et al.*, 1998). The lifespan of marine aerosols ranges from days to a few weeks (Myhre, 2013; Yu *et al.*, 2013). Marine aerosols play a critical role in several aspects of the earth's systems, such as climate and aquatic ecosystems.

Marine aerosols (particularly sea salt) that affect the Benguela Region originate from the South Atlantic Ocean. Sea-salt aerosols are generated by strong wind speeds over the South Atlantic ocean's surface, and they are transported by winds. The estimated salinity intensity over the south Atlantic Ocean ranges from 35 to 39 $g.kg^{-1}$ (Gierach, 2013). The salinity is higher in the ocean and decreases towards the coast (Gierach, 2013). The emissions of sea salt occur all year round and it has maximum emissions in summer when the wind speed is high in the south of the Benguela Region, and in winter when the wind

speeds are high in the north of the Benguela Region (Shannon, 1985; Skogen, 1999; Wedepohl *et al.*, 2000).

(c) Combustion of fossil fuels

The combustion of fossil fuels, such as coal and oil, emits pollutants like carbon dioxide (CO_2), sulphur dioxide (SO_2), nitrogen oxides (NO_x), particulate matter (PM) and other substances. Trace gases formed from nucleation react further to form secondary aerosols. Fossil fuels were created millions of years ago from plant and animal decomposition and today are found as coal, oil and natural gas. Over recent years, civilisation required energy/power to run vehicles, ships, airplanes, industrial machinery and electricity, and fossil fuels were used as the source of energy/power.

The combustion of fossil fuels that affect the Benguela Region originate from Angola, Botswana and South Africa (Wood & Baldwin, 1985). Angola, Botswana and South Africa are developing countries made up of larger portions of rural areas where electricity is not the main source of power. The populations in the countries still depend on wood, coal and oil for heating and cooking.

(d) Biomass burning

Biomass burning is a major source of carbonaceous aerosols in the atmosphere (Das *et al.*, 2017). Biomass burning is an activity that takes places all over the world, depending on the types of vegetation and climate regimes (Das *et al.*, 2017). Biomass burning is used to clear the forest for agricultural practices, for regeneration of nutrients in crop lands, to manage accumulation of fuel in the forest, for the generation of charcoal for domestic use, and as a source of heat for cooking (Andreae, 1991). The current estimated biomass burning is approximately 2080 Tg Cyr^{-1} (Wees *et al.*, 2022).

An estimated 126 Mega hectares of African land is burned every year (Wees *et al.*, 2022). Africa is the single largest source of biomass burning, because approximately 30 to 50% of all global vegetation burned occurs in Africa (Andreae, 1991). Fig. 2.4 shows the types of vegetation found in Africa and the detection of active fires by month. The tropics are dominated by woodland, which encompasses the savanna vegetation. The subtropics are

dominated by grassland, followed by cropland. Active fires are seen over Angola between April and August. Biomass burning in southern Africa shifts northwards in austral summer and southward in austral winter (Fig. 2.5). The southward shift begins in June and peaks in July and August and ends in October. The maximum number of fires occur in austral winter, because it has less to no rainfall, making it a dry season and favourable for burning (Tummon *et al.*, 2010). November to April is a wet season in most (not all) of southern Africa, and the burning of the forest is less to none. Biomass burning is the source of black carbon, organic carbon and sulphate aerosol compositions.

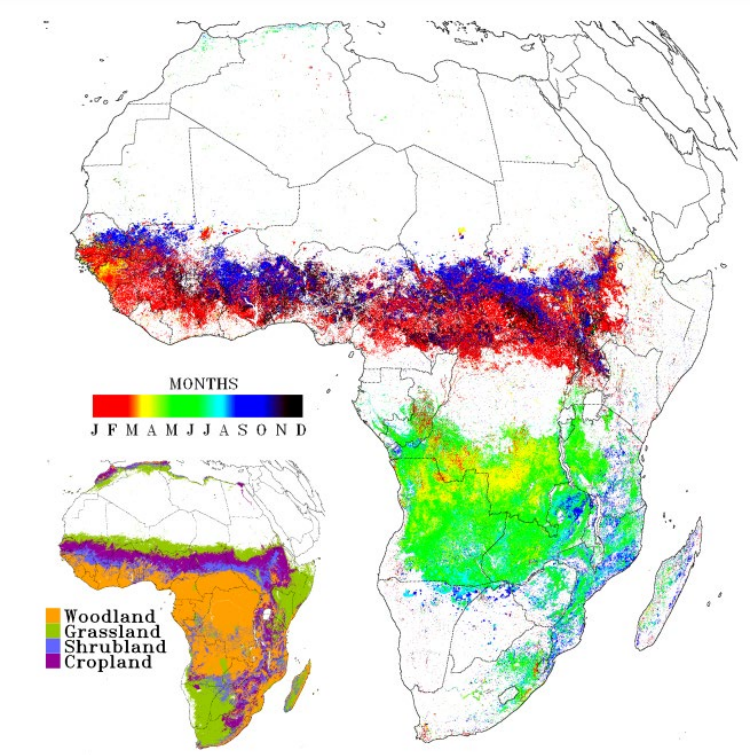

Figure 2.4: Depicted locations of active fire detections by month (large image) and the biomes (small image) over Africa (taken from Gareth *et al.*, 2009)

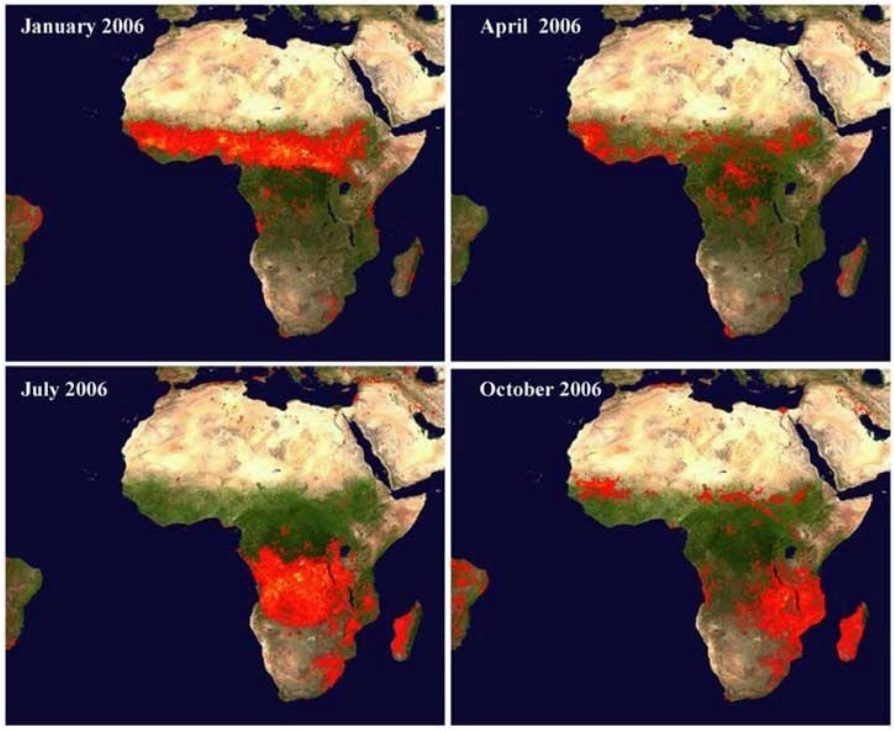

Figure 2.5: Schematic diagram of seasonal fire occurrences in Africa (taken from Haywood *et al.*, (2008)

2.3.3 Transport of aerosols in southern Africa

The transport of aerosols in southern Africa is influenced by four general circulation patterns, namely semi-permanent subtropical continental anticyclones, transient baroclinic westerly waves, quasi-stationary barotropic easterly waves and transient mid-latitude ridging anticyclones (Tyson & Preston-Whyte, 2000; Tyson *et al*., 1996). The effect of each circulation pattern depends on the season, and they are driven by meridional migration towards the south in austral summer and towards the north in austral winter (Formenti *et al.*, 2019).

The estimated percentages of aerosol transport and recirculation for semi-permanent subtropical continental anticyclones, transient baroclinic westerly waves, quasi-stationary barotropic easterly waves and transient mid-latitude ridging anticyclones patterns are shown in Fig. 2.6. In recirculating air masses, aerosols are suspended in the atmosphere for several days due to subcontinental anticyclones and mesoscale low pressures at the

coast (Garstang *et al.*, 1996; Tyson *et al.*, 1996). Approximately 4% of total aerosol loading are transported and recirculated by the continental anticyclones for seven days over the subcontinent, and then dumped into the Benguela Region. Approximately 24% of total aerosols loading are transported and recirculated by the ridging anticyclones for four days over the subcontinent, and then dumped into the Benguela Region. Approximately 60% (the largest aerosol exit) of total aerosols loading are transported by the easterly waves for five days over the subcontinent, and then dumped into the Benguela Region. Approximately 7% of total aerosols loading are transported and recirculated by the westerly waves for seven days over the subcontinent, and then dumped into the Benguela Region. Aerosols that are emitted to the east or recirculated over the subcontinent will not be discussed, as they are not within the study domain of this research.

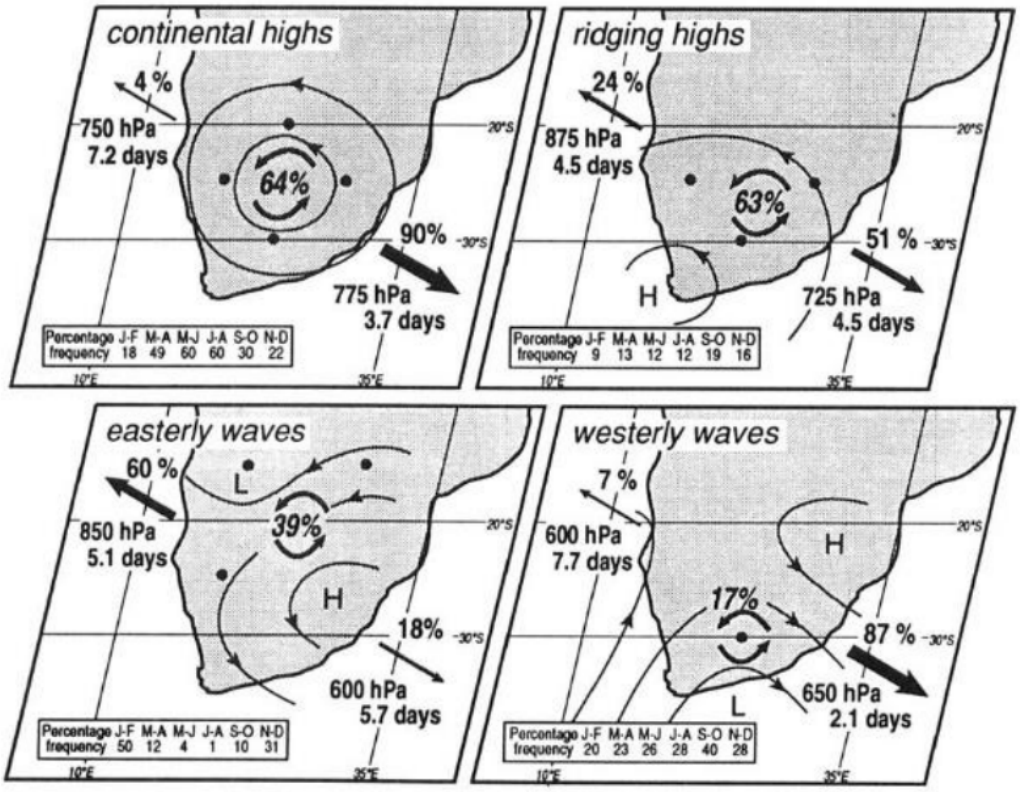

Figure 2.6: The average percentage transport and recirculation of air masses of major circulation types in southern Africa for the individual general circulation patterns proposed by Tyson *et al.* (1996)

Average atmospheric transport pathways and recirculation over southern Africa are shown in Fig. 2.7. Southern Africa is dominated by a semi-permanent subtropical continental anticyclone that separates the Hadley cell and the Ferell cell, and it varies spatially by change of season (Garstang *et al.*, 1996; Piketh *et al.*, 1999; Tyson & Von Gogh, 1976). The minor air mass transport towards the west coast of southern Africa is strengthened by easterly waves (Fig. 2.7). The minor transport then exits the subcontinent into the Benguela Region, depending on the season. Some of the aerosols originating from the subcontinent are recirculated back to the west coast of southern Africa through anticyclonic circulation (Garstang *et al.*, 1996). Approximately 5% of aerosols are transported to the Benguela Region (Fig. 2.7).

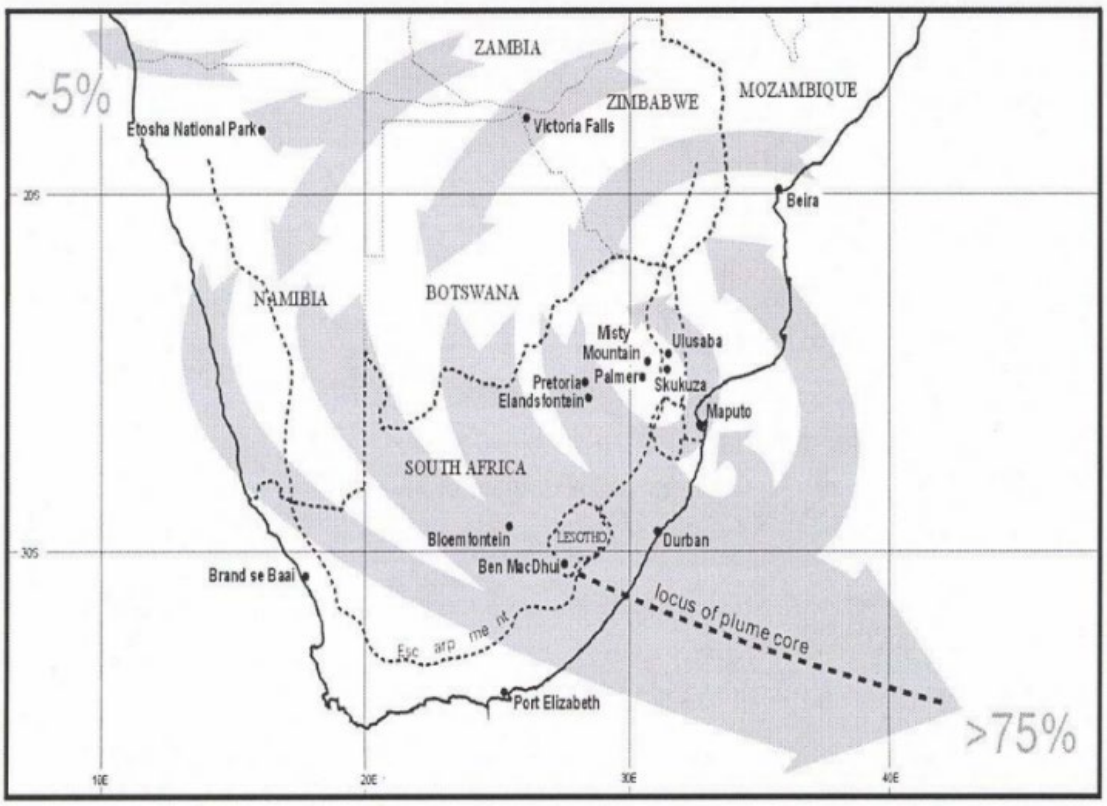

Figure 2.7: The major pathways transporting and recirculating aerosols over southern Africa (taken from Piketh *et al.*, 1999)

The major near-surface trajectory modes in southern Africa are: (a) direct eastward transport, (b) anticyclonic circulation and westward transport, and (c) anticyclonic

recirculation transport (Fig. 2.8) (Garstang *et al.*, 1996). Direct transport occurs when the initial movement from the source is parallel to both meridional and latitudinal planes (Tyson & D'Abreton, 1998). Recirculation transport occurs when the initial movement from the source is opposite to both meridional and latitudinal planes (Tyson & D'Abreton, 1998). The direct westward transport is due to continental anticyclonic circulation, which makes the subcontinental air mass exit into the Benguela Region through the west coast of Southern Africa. The air masses' exit to the Benguela Region is caused by easterly waves. The recirculation transport is due to ridging anticyclones, which transport the air mass toward the Indian Ocean, which is then re-circulated it into the subcontinent, and finally the air mass is taken out into the Benguela Region (Garstang *et al.*, 1996; Tyson *et al.*, 1996).

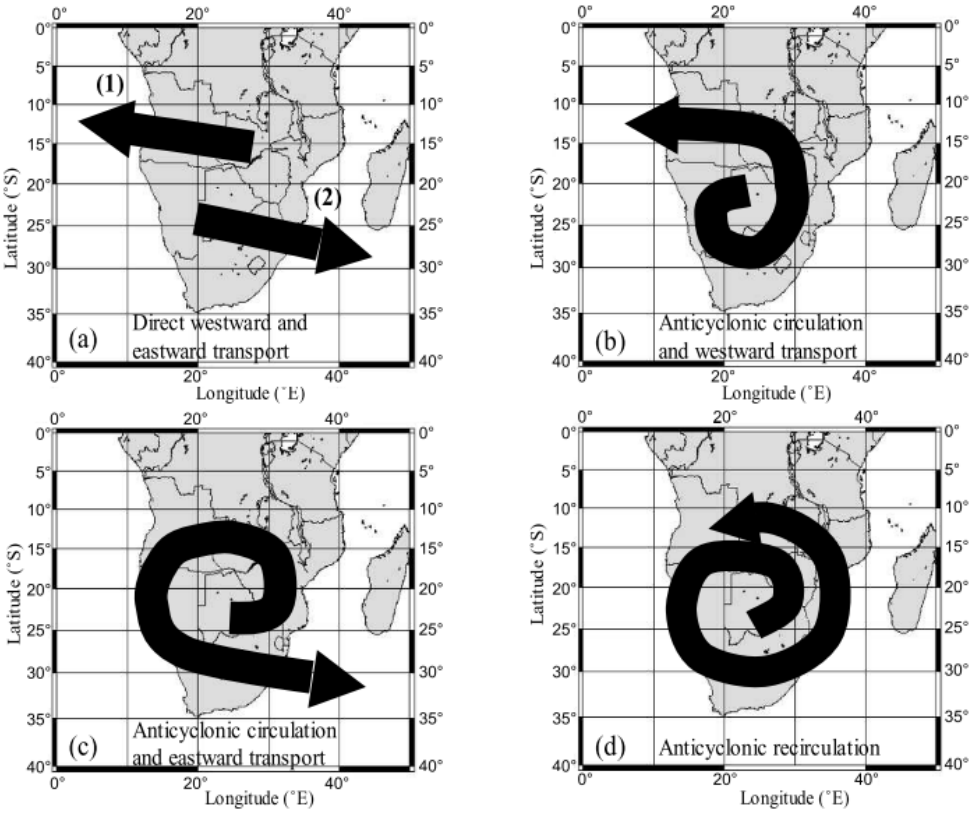

Figure 2.8: Schematic representation of the four major near-surface trajectory modes that are likely to occur because of the eastwards or westward aerosol exit, or an anticyclonic circulation exit in southern Africa (Garstang *et al.*, 1996; Sinha *et al.*, 2004)

2.4 Stratiform clouds

Stratiform clouds are layered clouds that occur closer to the earth's surface. Stratiform clouds form when there are no extreme temperatures, under high static stability, and under low wind speeds. Stratiform clouds are divided into two, namely stratus and stratocumulus. Stratocumulus clouds are 200 to 400m in thickness and they form at the top of the boundary layer (Wood, 2015). Stratocumulus clouds have cloud top heights ranging between 500 and 2000m (Wood, 2015). Stratocumulus clouds are associated with liquid water, and it is very unlikely that ice could be found inside. The cloud tops of stratocumulus clouds are flatter compared to the cloud base. Stratocumulus clouds forming in the ocean form either as open cells or closed cells. Closed cells have smaller gaps between the stratocumulus cloud, while open cells have larger horizontal gaps between a single stratocumulus cloud (Wood, 2015). Stratocumulus clouds are maintained by the balance between radiative cooling, the surface, and the entrainment. Stratocumulus clouds are precipitation clouds, as rain or drizzle, and that might have an effect on energy and moisture budgets. Stratocumulus clouds have a strong diurnal variability, but not in all areas.

2.5 Aerosol-cloud interactions

Aerosols impact the climate through a radiative effect and microphysical effect (Fig. 2.9). Radiative effect, also known as the direct effect, refers to the scattering or absorption of incoming solar radiation by aerosols, which changes the Earth's energy budget (Duan *et al.*, 2019). Aerosols that scatter solar radiation create localised cooling as less solar radiation reaches the surface. The amount of solar radiation scattered by aerosols depends on the size and composition of the aerosol. The aerosol diameter ranging between 0.2 and 1.0 μm is the most efficient size to scatter solar radiation (Quinn *et al.*, 1998). The amount of solar radiation absorbed or scattered by aerosols depend onhygroscopicity (Quinn *et al.*, 1998). Sulphate and sea salt scatter solar radiation, while black carbon, organic carbon and dust absorb solar radiation (Li *et al.*, 2022). Aerosols are denser compared to air, but turbulence keeps aerosols suspended in the atmosphere unless the gravitational settling is greater than turbulence. Aerosols of several

micrometres or more have a shorter lifespan in the atmosphere than smaller aerosols do. Aerosols that absorb solar radiation create localised warming as more solar radiation is trapped in the aerosols that redistribute thermal energy.

The microphysical effect, also known as the indirect effect, refers to how aerosols change the microphysical properties of clouds (Fig. 2.4) (Duan *et al.*, 2019; Da Silva *et al.*, 2020). The first indirect effect on climate was proposed by Twomey (1977), and states that an increase in aerosols results in an increase in cloud condensation nuclei (CCN), which results in more cloud droplets, but smaller droplet size, which will increase cloud albedo. The second indirect effect on climate was proposed by Albrecht (1989), hypothesising that smaller droplet sizes associated with lower collection of cloud droplets may influence coalescence efficiencies in clouds. This will lead to slower drop growth, in turn leading to suppressed precipitation and prolonged cloud lifetimes. Most aerosols are capable of acting as CCN (Fig. 2.9) (Gryspeerdt *et al.*, 2016; Storelvmo *et al.*, 2006).

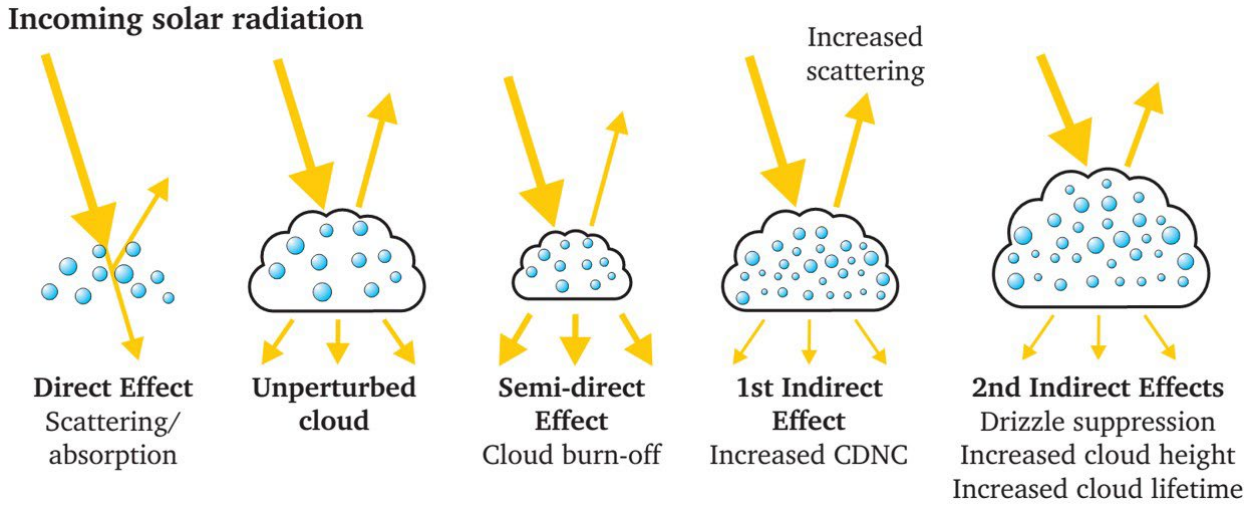

Figure 2.9: The processes by which aerosols influence the incoming solar radiation, including the ways in which they perturb cloud properties (taken from Jerez *et al.*, 2019)

The AOD AOD has been used as a proxy for CCN. The reason AOD is used as a proxy is because there is a great deal of AOD data available, as it is routinely measured remotely (AERONET and satellites), while CCN is not. In an instance where CCN data is not available, AOD is used as a proxy. AOD is a measure of attenuation of solar radiation

resulting from the absorption or scattering of light in an atmospheric column. Aerosols that act as CCNs are fine mode particles ranging between 0.01 and 0.2 um in diameter (Bates *et al.*, 2012; O'Dowd, 1993).

Aerosols that scatter or absorb solar radiation change the radiative balance in the atmosphere, which, in turn, impacts clouds (Lau *et al.*, 2006). The reduction of cloudiness due to absorbing aerosols is termed the semi-direct effect. The semi-direct effect happens because of changes in cloud cover due to the heating from absorbed solar radiation (Fig. 2.9). The changes may also be driven by (1) liquid water path over land or over the ocean, (2) near-surface temperature, (3) an increase in free tropospheric temperature, and/or (4) reduced large-scale subsidence (Sakaeda *et al.*, 2011). Therefore, while aerosols impact cloud properties, they are not the only factor, but also other parameters such as meteorological variables (i.e. temperature, relative humidity, winds) and weather systems.

2.6 Relationship between stratocumulus cloud fraction and aerosols

Cloud fraction is one of the cloud parameters used to study Albrecht's (1989) hypothesis. Cloud fraction is defined as a percentage of each pixel in a satellite image covered with clouds. Aerosols are capable of acting as cloud condensation nuclei, influencing the cloud droplet number concentration (CDNC). It has been hypothesised that increasing the CDNC in the atmosphere can increase cloud fraction (Albrecht, 1989). A decrease in the CDNC can result in increased evaporation and a decrease in cloud fraction (Small *et al.*, 2009).

Strong correlations between AOD and cloud fraction have been recorded in several locations around the globe using a wide variety of instruments, but the magnitude of the influence of aerosols on clouds is highly uncertain (Sekiguchi *et al.*, 2003; Yuan *et al.*, 2008; Zhang *et al.*, 2005; Zheng *et al.*, 2020). The correlation between aerosols and cloud fraction found in these studies varies, and has been found to be positive, negative or none. Some previous studies (Adebiyi & Zuidema, 2018; Balakrishnaiah *et al.*, 2012; Costantino & Bréon, 2013; Grandey *et al.*, 2013; Gryspeerdt *et al.*, 2016; Myhre *et al.*,

2007) have found that there was a positive correlation between aerosols and cloud fraction. Adebiyi and Zuidema (2018) did a study in the South-East Atlantic Ocean (which includes the study domain of this dissertation) using satellite observations during the peak biomass burning season. In contrast, other studies (Nyasulu *et al.*, 2020), compiled over Kenya, found that there was a negative correlation between aerosols and cloud fraction. Other studies (Liu *et al.*, 2020), compiled in inland China, found that when AOD was below a certain threshold (<0.3), there was a negative correlation, and when it was above that particular threshold, there was a positive correlation.

Cloud resolving models have found that the influence that aerosols have on cloud fraction is small or slightly negative, particularly on shallow clouds (Stevens, 2008; Xue, 2006). Myhre *et al.* (2007) found that two models simulated different magnitudes of aerosols and cloud fractions. The parameterisation of hygroscopic growth and cloud processes in the cloud model influence what the simulations of the results look like. This dissertation will enquire how CCAM parameterisations compare to other models or observations as the parameterisation schemes differ across models.

2.7 Relationship between stratocumulus cloud liquid water path and aerosols

A liquid water path is defined as the total amount of liquid water present between two points in the atmosphere. A liquid water path is one of the critical control variables of longwave and shortwave radiative effects (Kim *et al.*, 2020). A liquid water path is used to determine the lifetime of clouds in the atmosphere. Smaller droplet sizes in the atmosphere are associated with lower collection that influences coalescence efficiencies in clouds. This leads to slower drop growth, which, in turn, leads to suppressed precipitation and prolonged cloud lifetimes. The link between aerosols and liquid water path is that, when there is a certain amount of water in the atmosphere, and a certain amount of aerosols are introduced in the atmosphere, the amount of water splits itself into the amount of aerosols available. As such, when there are higher concentrations of aerosol particles, the water will split into very small droplets. Small droplet sizes do not precipitate, as such prolonging the lifetime of ice-free clouds. An increase in liquid water

path when aerosols increase leads to precipitation suppression, which may be because of two components, namely moistening or drying (Costantino & Bréon, 2013; Storelvmo *et al.*, 2006). When precipitation decreases, there is higher moisture, which increases liquid water path with an increase in aerosols (Costantino & Bréon, 2013). Furthermore, when the entrainment of dry air increases, it also enables liquid water path to increase (Costantino & Bréon, 2013).

The relationship between liquid water path and aerosols is still poorly quantified (Jacob *et al.*, 2019). The correlation between aerosols and liquid water path has been found to be positive (Liu *et al.*, 2020a; Myhre *et al.*, 2007; Nakajima *et al.*, 2001) or negative, and has been found to vary by region or the type of aerosol (Nakajima *et al.*, 2001). In theory, an increase of aerosols in the atmosphere decreases cloud droplet size; as a result, precipitation is suppressed, and clouds develop further and live longer in a more developed stage, such as increasing liquid water path in the area (Savane *et al.*, 2015). In areas where it just rained, aerosols are reduced, and a reduction in aerosols is linked to a decrease of liquid water path (Savane *et al.*, 2015).

Previous studies (Liu *et al.*, 2020a; Myhre *et al.*, 2007; Nakajima *et al.*, 2001) have found that there was a positive correlation between aerosols and liquid water path. Myhre *et al.* (2007) did a study across the globe, but divided it into regions (based on continents and oceans) and found that liquid water path increase with an increase in AOD and the correlation was stronger over land than the ocean. Myhre *et al.* (2007) also found that there are some areas in the ocean where liquid water path were decreasing with an increase in AOD. Nakajima *et al.* (2001) did a study across the globe that found that liquid water path do not change based on an increase or decrease of aerosols. Lu *et al.* (2018) did a study along the study domain of this study and found that liquid water path increase with aerosols during the night and the day, though during the day the magnitude of liquid water path is reduced. As such, those studies highlight that there is no consistency in the relationship between liquid water path and aerosols. The relation perhaps depends on the location, or measurement instrument, or parameterisations used in the simulation. It is therefore of interest to determine the relationship of liquid water path and aerosols in the Benguela Region.

2.8 Summary

There have been impressive improvements in models over the years. However, there are still differences depending on the model parameterisations and schemes used. It is imperative to evaluate model performance against observations, particularly for variables in the model that have not been evaluated yet. The influence of aerosols on clouds is not consistent across locations, temporal resolution and models/observations. It is imperative to study the interactions of aerosols and clouds in models in order to understand how different sources of aerosols influence clouds, how models simulate the relations between aerosols and clouds, and whether the influence is directly from these variables or whether there are other processes that influence the interactions between aerosols and clouds.

CHAPTER 3: DATA AND METHODS

3.1 Study domain

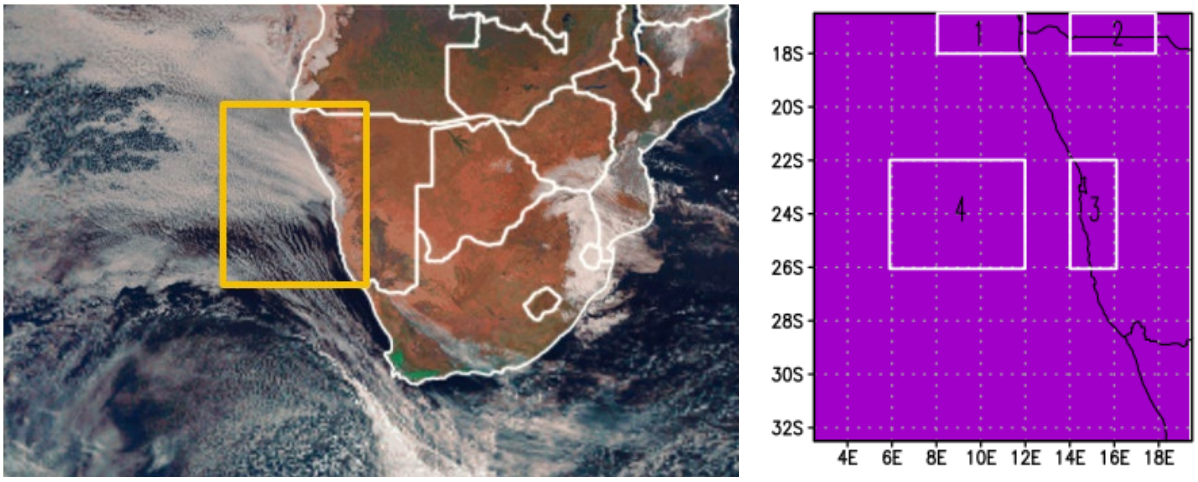

Figure 3.1: The study area of interest (Benguela Region, denoted by the orange square on the left). The right shows the domain with subdomain 1, subdomain 2, subdomain 3 and subdomain 4 (EUMETSAT Southern Africa images (taken from EUMETSAT Image Gallery Animation - Meteosat 0 degree Natural Colour Enhncd. Southern Africa)

The study domain of this research lies over Namibia, Angola and the Atlantic Ocean, which is covered between 17° and 32°S latitude, and 2° and 18°E longitude (Fig. 3.1). However, the study domain was divided into four small subdomains, because each aerosol composite has a different origin and how far it could travel, and as such, the concentration is different at each subdomain. The subdomains were chosen based on the presence of aerosols and which aerosol types are likely to be found in the region. Subdomain 1 contains aerosols that travelled further from Angola's biomass burning and industrial emissions. Subdomain 2 has aerosols that travelled a smaller distance from Angola's biomass burning and industrial emissions. Subdomain 3 had aerosols from biomass burning transported from Namibia's biomass burning and dust originating from the Namib Desert and Etosha Pan. Subdomain 4 contains aerosols that travelled further from Angola's biomass burning, Namibia's biomass burning and dust, and marine

aerosols. The main objective of this study is to understand how the CCAM simulates the sensitivity of clouds to aerosols over the Benguela Region. Subdomains 1 and 4 consist of both marine stratocumulus clouds and aerosols.

3.2 Data and model output

3.2.1 Introduction

Three types of data are used in this study, namely model, reanalysis and satellite data. Model data was used to study the aerosol-cloud interactions. The model contains aerosol parameters such as total aerosol optical depth, and the compositional AOD (black carbon, organic carbon, sulphate, small dust and sea salt). The model also contains cloud parameters such as cloud fraction and liquid water path. Satellite data and reanalysis data are used to evaluate the model data. Satellite data is used to evaluate total AOD and cloud parameters (cloud fraction and liquid water path) against model data. Reanalysis data is used to evaluate the compositional AOD (black carbon, organic carbon, sulphate, small dust and sea salt) against model data. Reanalysis data is used because there is no satellite data for the compositional AOD. The CCAM calculates AOD (total and compositional) in its radiative scheme, while reanalysis (specifically MERRA) computes compositional AOD as extinction. Extinction is the reduction from any amount to zero in the intensity of light as it passes through a medium, due to absorption or scattering by aerosols.

3.2.2 The CCAM model

The Conformal Cubic Atmospheric Model (CCAM) is a global atmospheric circulation model that was developed by the Commonwealth Scientific and Industrial Research Organisation (CSIRO) in 1997 (McGregor, 2005). The CCAM uses large-scale forcing and can be downscaled from low spatial resolutions to higher spatial resolutions (Engelbrecht *et al.*, 2011). Downscaling in the CCAM was possible because the model can be set to a parameter resolution mode to function as a regional climate model (RCM) (Engelbrecht *et al.*, 2011). The parameter resolution uses a 3D cubic grid projected into a sphere using the Schmidt transformation (Thatcher *et al.*, 2015). Large-scale

atmospheric circulation is assimilated using spectral nudging (Thatcher *et al.*, 2015). The CCAM is run in a global mode with a variable resolution for regional climate modelling. The CCAM is a dynamic climate model; that is, it is a model that replicates the earth's system that was governed by laws of physics (Engelbrecht *et al.*, 2011). The laws are defined as mathematical equations when applied into the dynamic model (Engelbrecht *et al.*, 2011). The equations are then solved numerically at each grid point. In instances where the processes cannot be resolved at a grid point, parameterisation schemes are defined to provide simulations (Engelbrecht *et al.*, 2011). The CCAM uses a semi-implicit, semi-Lagrangian method to solve hydrostatic primitive equations (Engelbrecht *et al.*, 2011).

For this study, the CCAM was run at a quasi-uniform resolution of 50km horizontal resolution and 27 sigma vertical levels (similar to the model set-up in Horowitz *et al*. (2017) and Garland *et al.* (2013)) for this study. Initial conditions for the CCAM for this study were from the European Centre for Medium Range Weather Forecasting (ECMWF) reanalysis ERA interim data. A detailed description of ERA interim was documented by Dee *et al*. (2011). The CCAM-modelled outputs for 2002 to 2017 were used in this study because this was the period in which satellite observation data of aerosols and cloud parameters were available. Six-hourly model outputs, re-gridded to 0.5° × 0.5° spatial resolution over the Benguela Region, were used in this study. The CCAM output variables used in this study are low cloud cover (cll (frac)), liquid water path (lwp_ave), total AOD VIS (aero_vis), black carbon optical depth VIS (bc_vis), organic carbon optical depth VIS (oc_vis), small dust optical depth VIS (sdust_vis), sulphate optical depth VIS (so4_vis) and sea-salt optical depth VIS (ssalt_vis). CCAM simulations were initialised in 1979 so that the prognostic variables and aerosol fields can intertwine sufficiently (Gordon, Rotstayn, McGregor, Dix, Kowalczyk, O'Farrell, Waterman, Hirst, Wilson, Collier & Watterson, 2002; Rotstayn *et al.*, 2010). A detailed description of aerosol parameterisation in the CCAM has been documented elsewhere (Huang *et al.*, 2013; Rotstayn, 1997; Rotstayn *et al.*, 2007, 2010; Rotstayn & Lohmann, 2002), and will be described briefly here.

Aerosols in the CCAM

Aerosols in the CCAM interact with the meteorology; however, there are some limits to how they interact (Rotstayn *et al.*, 2010). Transport of aerosols in the CCAM is done by advection, mixing of vertical turbulence, and vertical movements in deep convective clouds (Rotstayn *et al.*, 2007). Vertical advection is conducted by a flux-corrected transport scheme and the horizontal advection is conducted by the semi-Langrangian scheme (Van Leer, 1977). The mixing of vertical turbulence is based on the stability-dependent K-theory (Louis, 1979). Transport in convective clouds is based on vertical profiles between updraft and downdraft mass flux made by the convection scheme (Gregory & Rowntree, 1990). Aerosols are removed from the atmosphere through wet and dry deposition (Rotstayn *et al.*, 2010). Wet deposition is linked to warm rain and snow scavenged in cloud microphysics parameterisations (i.e. in-clouds and below-clouds) (Rotstayn & Lohmann, 2002). In-cloud scavenging correlates with the amount of precipitation removed over the liquid water content (Rotstayn & Lohmann, 2002). Below-cloud scavenging correlates with the area where it just precipitated, based on the negative exponential size distribution of the raindrop or snowflake (Rotstayn & Lohmann, 2002). In addition to the removal of aerosols in the atmosphere, it is the settling of aerosols due to evaporation of rain or snow (Rotstayn & Lohmann, 2002). Dust is removed from the atmosphere by means of gravitational settling (Rotstayn & Lohmann, 2002).

The aerosol scheme in CCAM is a bulk mass scheme that represents prognosed carbonaceous aerosols, dust, sulphur cycle and diagnosed sea salt (Rotstayn *et al.*, 2007). Carbonaceous aerosols' prognostic variables are represented by black carbon and organic carbon (Rotstayn *et al.*, 2007). The CCAM determines how prognostic aerosols (carbonaceous, sulphur cycle and dust) are emitted, transported and removed (Rotstayn *et al.*, 2007). The size distribution of prognostic aerosols (carbonaceous and sulphur) is represented by a mode radius with a geometric standard deviation (refer to Table 3.1). The transport of hydrophobic and hydrophilic forms of black carbon and organic carbon is separate. Hydrophobic black carbon and organic carbon are not hygroscopic, but hydrophilic black carbon and organic carbon with hygroscopic growth are based on Kohler's theory (Rotstayn *et al.*, 2007). The CCAM assumes emissions of biomass

burning are 100% hydrophilic and those of fossil fuels are 50% hydrophilic (Rotstayn *et al.*, 2007).

The sulphur cycle's prognostic variables are dimethyl sulphide (DMS), sulphur dioxide (SO_2), and sulphate (SO_4). One of the sources of sulphate is the aqueous oxidation of sulphur dioxide, but does not amount to much as compared to biomass burning, which is a component of emissions inventory (Smith & Andres, 2004). Sulphur chemistry's treatment is based on ECHAM4 (Rotstayn *et al.*, 2007).

Dust is made-up of four size bins (mode radii ranging between 0.1-1 μm, 1-2 μm, 2-3 μm, and 3-6 μm) (Rotstayn *et al.*, 2007). Dust treatment is based on dust sources identified by satellites (Rotstayn *et al.*, 2007). Sea salt above the ocean's surface is diagnosed at each time step and as a function of wind speeds at 10 m. Sea salt, as a natural aerosol, depends strongly on meteorology. The CCAM assumes that sea salt is well mixed in the marine boundary layer, which is a layer close to the ocean's surface. Sea salt is made up of two size bins (mode radii of 0.035 μm and 0.35 μm) (Rotstayn *et al.*, 2007). Because sea salt is diagnostic, it is not emitted, transported or removed in the atmosphere in the CCAM, and as such, it is not transported over land (Rotstayn *et al.*, 2007). Sea salt's hygroscopic growth is based on Kohler's theory (Rotstayn *et al.*, 2007).

Anthropogenic emissions of biomass burning annual cycle vary monthly and for non-biomass burning the annual cycle is constant (Horowitz *et al.*, 2017). Changes in AOD from WCRP Coupled Model Intercomparison Project - Phase 5 (CMIP5) emissions less than monthly temporal scales for prognostic aerosols are not a result of changes of sources, rather changes in transport, deposition and sinks from the variability of the meteorology (Horowitz *et al.*, 2017).

Table 3. 1: Size distributions of dry tropospheric aerosol (taken from Rotstayn et al., 2007).

	Mode Radius, μm	Geometric Standard Deviation	Density, g cm^{-3}
Sulfate[a]	0.05	1.9	1.77
POM + BC[b]	0.08	1.65	1.25 (mixture) 1.5 (BC)
Small dust[c]	0.01	1.4	2.4
	0.045	1.6	2.4
Large dust[c]	0.275	2.5	2.4
Small sea salt[e]	0.035	1.92	2.165
Large sea salt[e]	0.35	1.7	2.165

Stratiform clouds in CCAM

The cloud microphysics scheme in the CCAM is a bulk mass scheme that represents prognosed water vapour, liquid and frozen cloud water, snow, rain and graupel. The treatment of formation and dissipation of stratocumulus clouds is based on a statistical condensation scheme (Rotstayn, 1997). The statistical condensation scheme assumes a triangular probability density function of sub-grid distribution for moisture (Rotstayn, 1997). The output from the sub-grid for moisture is used to calculate the cloud fraction in the model (Gordon *et al.*, 2002). A detailed description of stratiform clouds is documented in Rotstayn (1997) and Lin (1983). In brief, this scheme is a development on the previous diagnosed condensation scheme that was based on specific humidities, while this scheme uses mixing ratios that are more consistent with water vapour. In addition, this scheme incorporates a simple parameterisation of cloud fraction, prognostic variables for cloud liquid water, treatments of rain from stratiform clouds, and variable cloud radiative properties. The precipitation of stratiform clouds happens through auto-conversion, and the collection of cloud liquid water through raindrops. In the CCAM, auto-conversion parameterisation is sensitive to specification of the cloud droplet number concentration, which is estimated empirically from the mass concentration of aerosols. In the CCAM, it is assumed that clouds are randomly overlapping in the vertical, and this assumption is consistent with the radiation scheme. The CCAM assumes that all clouds fill their layers completely in the vertical, which is consistent with cloud radiative properties. The total cloud fraction is calculated as the sum of ice and liquid water cloud fractions. The liquid

water path is given by the cloud scheme and has the SI units of kg/m^3 (Gordon *et al.*, 2002).

Aerosol-cloud interactions in CCAM

In the CCAM, auto-conversion parameterisation is sensitive to specification of the cloud droplet number concentration, which is estimated empirically from the mass concentration of aerosols. Cloud droplet number concentration is used to calculate droplets' effective radius in the radiation scheme. As such, aerosols act as cloud condensation nuclei, meaning that aerosols then feed back into the model.

3.2.3 MODIS satellite

A moderate resolution imaging spectroradiometer (MODIS) is a sensor onboard the Aqua and Terra satellites developed by NASA in 2002 and 1999, respectively (Masuoka *et al.*, 1998;Savtchenko *et al.*, 2004). Aqua's orbit passes south to north across the equator in the afternoon, while Terra's orbit passes north to south across the equator in the morning. Terra and Aqua cross the equator at 10:30 and 13:30 local solar time (LST), respectively (Balakrishnaiah *et al.*, 2012). Terra and Aqua pass the study area at 09:30 and 12:30, respectively. As noted above, the CCAM uses the 6-hr averages, meaning the CCAM provides simulations for the whole day and the MODIS satellite provides observations twice a day. The temporal resolutions for both CCAM and MODIS were averaged seasonally, then the seasonal averages were averaged multi-yearly, and as such the differences in times were adjusted to be comparable between modelled vs measured aerosol optical depth. MODIS Terra and Aqua use 36 spectral bands of 0.41 to 14.385 µm wavelengths and a spatial resolution of 250m, 500m or 1000m (Levy *et al.*, 2007). Of the hundreds of products derived from MODIS, Terra and Aqua's measured radiances are a set of aerosol products (Levy *et al.*, 2007) and a set of cloud products (King *et al.*, 2003; Platnick *et al.*, 2003), including AOD and liquid water path.

The dataset used in this study for AOD at 550nm wavelength is retrieved from the MODIS Aqua data level 3 collection 6 from NASA's GIOVANNI website (https://giovanni.gsfc.nasa.gov/giovanni/). A detailed description of algorithms for the retrieval of aerosols is available at https://modis-atmos.gsfc.nasa.gov/. MODIS data is available at three processing levels, namely level 1.0 (geolocated radiance and

brightness temperature), level 2.0 (retrieved geophysical data products), and level 3.0 (gridded points) (Gopal *et al.*, 2016). This study used level 3.0 data and the name of the dataset product downloaded for this study is MYD08_M3_6_1_AOD_550_Dark_Target_Deep_Blue_Combined_Mean_Mean from MODIS Aqua, at a 1° × 1° spatial resolution and monthly temporal resolution. The reason Aqua was used in this study is because it is carrying both MODIS and Atmospheric Infrared Sounder instruments, which will be used in other sections of the study. Also, my study period is from 2002 and We did not need earlier years from Terra.

AOD is used as a proxy for cloud condensation nuclei (Andreae, 2009). The reliability of AOD as proxy depends on the aerosol size, aerosol composition and the vertical distribution of aerosols, but it can be used as a first approximation for CCN concentration (Gopal *et al.*, 2016).

MODIS uses infrared bands to determine cloud physical properties such as cloud top temperature and cloud top pressure, and visible and near-infrared bands to determine the microphysical and optical properties of clouds (Levy *et al.*, 2007; Remer *et al.*, 2005). The dataset used in this study for liquid water path was retrieved from the MODIS Terra and MODIS Aqua data level 3 collection 6 from NASA's GIOVANNI website (https://giovanni.gsfc.nasa.gov/giovanni/). The names of the dataset products downloaded for this study are MYD08_M3_V6.1 from MODIS Aqua and MOD08_M3_V6.1 from MODIS Terra measured in g/m^2, at a 1° × 1° spatial resolution and monthly temporal resolution.

3.2.4 AIRS instrument

The atmospheric infrared sounder (AIRS) is an instrument on the Aqua satellite (Aumann *et al.*, 2003). AIRS is a hyperspectral infrared sounder that has two multichannel microwave instrument companions, i.e. the advanced Microwave Sounding Unit (AMSU) and the Humidity Sounder for Brazil (HSB) (Ding *et al.*, 2020). Aqua's orbit passes south to north (daytime/ascending) across the equator at approximately 13:30 local solar time, and north to south (night time/descending) across the equator at approximately 01:30

local solar time (Parkinson, 2003). Both daytime and night-time measurements of AIRS were used in this study separately.

AIRS has a high spectral resolution with 2378 IR channels between 3,74 and 4,61, 6.20-8.22, and 8.8-15.5 μm (Aumann *et al.*, 2003; Chahine *et al.*, 2006). A detailed description of AIRS is documented in Lambrigtsen (2004). This instrument collects essential atmospheric cloud parameters such as cloud fraction, cloud top pressure and water vapour data (Botes *et al.*, 2012). One of the main advantages of AIRS over ground observations is that it provides data in remote areas where radiosondes cannot be ejected.

The dataset used in this study for cloud fraction was retrieved from the AIRS Aqua data level 3 version 6 from NASA's GIOVANNI website (https://giovanni.gsfc.nasa.gov/giovanni/). The type of cloud fraction used in this study is a low-level cloud fraction. Version 6 algorithm is the most updated algorithm with greater stability, yield, and quality of data products (Susskind *et al.*, 2014). AIRS level 3 data went through quality control and it is gridded globally at 1° × 1° grid resolution (Susskind *et al.*, 2019). AIRS data is available at three processing levels, namely level 1 (radiances), level 2 (retrieved parameters), and level 3 (globally gridded averages) (Ding *et al.*, 2020). The name of the dataset product downloaded for this study is AIRS3STM v006 from AIRS Aqua, at a 1° × 1° spatial resolution and monthly temporal resolution. The datasets used in this study are for cloud fraction (daytime/ascending) and cloud fraction (night time/descending).

3.2.5 MERRA-2 reanalysis

The Modern-Era Retrospective analysis for Research and Applications, version 2 (MERRA-2) is a reanalysis product developed by NASA (Gelaro *et al.*, 2017). Reanalysis is a process where a static data assimilation system is used to give a consistent reprocessing of atmospheric, oceanic and chemistry observations from recorded historical data (Gelaro *et al.*, 2017). The process depends on the underlying forecast model in order to combine different observations in a physically consistent manner, leading to the production of gridded datasets that cover several variables regardless whether there are *in situ* measurements or not (Gelaro *et al.*, 2017). MERRA-2 reanalysis

is based on the Goddard Earth Observing System Model, version 5 (GEOS-5) (Ou *et al.*, 2022). the GEOS-5 model is coupled with the Goddard Chemistry Aerosol Radiation and Transport model (GOCART) chemistry module to simulate the chemistry, aerosol, radiation, and transport of pollutants (Ou *et al.*, 2022). GOCART represents aerosols in 15 tracers, made up of five size bins of 0.03 to 10 μm for sea salt, 0.1 to 10 μm for dust, hydrophilic and hydrophobic carbonaceous (black carbon and organic carbon), and sulphate (Rizza *et al.*, 2019; Zhang *et al.*, 2020). Aerosols can be internally and externally mixed with meteorology in the GEOS-5 (Buchard *et al.*, 2017). MERRA-2 assimilates AOD data from satellite retrievals of aerosol products from the advanced very high resolution radiometer (1980 to August 2002), multi-angle imaging spectroradiometer (February 2002 to June 2014), MODIS Terra (March 2002 to present) and MODIS Aqua (August 2002 to present), and the ground-based aerosol robotic network (1999 to October 2014) (Zhang *et al.*, 2020). Aerosol optical Depth in MERRA-2 is the total column extinction due to all aerosol species (Buchard *et al.*, 2017). Aerosol optical depth assimilated undergoes cloud screening and homogenisation of the observing system using a neural scheme that converts satellite radiances to the aerosols robotic network-calibrated AOD at 550 nm (Buchard *et al.*, 2017). A detailed description of MERRA-2 is documented in Rienecker *et al.* (2011). MERRA-2 output is available from 1 January 1980 to present, and it has a horizontal spatial resolution of 0.5° × 0.625° latitude by longitude and 72 pressure levels from the surface to 0.01 hPa (Buchard *et al.*, 2017).

The dataset used in this study for compositional AOD (black carbon, organic carbon, sulphate, small dust and sea salt) at 550nm wavelength was retrieved from MERRA-2 from NASA's GIOVANNI website (https://giovanni.gsfc.nasa.gov/giovanni/). The name of the dataset products downloaded for this study is M2TMNXAER v5.12.4 from MERRA-2, at a 0.5° × 0.625° spatial resolution and monthly temporal resolution. The names of datasets used in this study are black carbon extinction AOD 550 nm, organic carbon extinction AOD 550 nm, dust extinction AOD 550 nm, SO4 extinction AOD 550 nm, and sea-salt extinction AOD 550 nm. MERRA-2 calls the aforementioned datasets as aerosol optical depth, but We refer to them as compositional AOD of black carbon, organic carbon, dust, sulphate and sea salt. There are no measurements (both ground and

satellite based) of compositional AOD in this region, and these MERRA simulations should not be considered as measurements.

3.2.6 Data manipulation

The spatial and temporal resolutions of CCAM, MODIS, AIRS and MERRA-2 are not the same. The CCAM (0.5° × 0.5°) has a higher spatial resolution compared to MODIS (1° × 1°), AIRS (1° × 1°), and MERRA-2 (0.5° × 0.625°). In order to make the spatial resolutions the same, some fields were re-gridded. To successfully re-grid the dataset, datasets with higher spatial resolutions are re-gridded to lower spatial resolutions (i.e. MODIS has lower spatial resolution compared to the CCAM). The temporal resolution of MODIS, AIRS and MERRA downloaded or retrieved was monthly (daily averages of a single month). The temporal resolution of CCAM was six-hourly averages. This study's temporal resolution is averaged to seasonal, i.e. December-January-February (DJF), March-April-May (MAM), June-July-August (JJA), and September-October-November (SON). To convert to the desired temporal resolution, the monthly data was averaged to seasonal for this study. The wavelength for AOD and compositional AOD (i.e. black carbon, organic carbon, sulphate, small dust and sea salt) is 550 nm across all datasets.

3.3 Analysis methods

3.3.1 Introduction

This section explains how data was analysed in this study. The data instruments that are used are model outputs, reanalysis and observations. To answer my objectives, the data requires both qualitative and quantitative analyses. For the analysis to provide optimum information, the data was adjusted to have the same spatial and temporal resolution.

There were two general comparisons performed, namely the comparison between the CCAM and satellite measurements/reanalysis, and the comparison between simulated aerosols and clouds.

Comparisons between CCAM and Satellites/reanalysis

CCAM output is compared to satellite to see how the two instruments simulate or measure aerosol optical depth. Firstly, the magnitude of aerosol optical depth, cloud fraction and liquid water path between CCAM and satellites is examined using quantitative analysis. The quantitative analysis method in this study helps to determine the gradient as seen from both images. There is one image of CCAM and one image of satellite, side by side, and then by looking at the images, compare whether the spatial peaks are located on the same spot and also whether the gradient of AOD is similar.

Secondly, the average errors and magnitude of errors of aerosol optical depth, cloud fraction and liquid water path between CCAM and satellites are examined using quantitative analysis. The quantitative analysis method in this study helps to determine the direction and deviation of errors of CCAM from satellites. From a single grid point, 15 simulated and measured values from CCAM and satellites are averaged and the average errors and magnitude of errors of AOD are calculated. The comparison provides an idea as to how different simulations from measurements are.

Understand aerosol-cloud parameter relationships in CCAM output

In order to understand the aerosol-cloud parameter relationship, quantitative methods are used. The quantitative analysis method in this study helps to determine linear association between aerosols and cloud parameters. From a single grid point, 15 simulated values from aerosols and cloud parameters each, are calculated and the answer provides insight into whether one parameter has a linear association with the other. Secondly, the seasonal cycle is used as an analysis tool. The seasonal cycle analysis investigates when the seasonal increase or decrease is between aerosols and cloud parameters.

3.3.2 Eyeball verification

Eyeball verification is a subjective method where human judgement is used to determine the model output errors between observations and model outputs by visually comparing them side by side (Stanski & Wilson, 1989). It is used to qualitatively recognise spatial displacements between the observations and the models (Stanski & Wilson, 1989). This method can be applied to time series or maps. Though it is susceptible to personal bias,

it is a tool that provides a qualitative correspondence between the observations and modelled values.

In this study, the eyeball verification method was used to visually compare the spatial maps between CCAM simulations and satellite observations/reanalysis. From the maps, magnitude and spatial pattern information was used to qualitatively judge how the CCAM simulated these aspects of the parameters against satellite observations. The temporal resolution for this section is multi-year seasonal averages.

3.3.3 Bias

Bias is a quantitative measure of overall reliability between the mean observations and mean model outputs. It indicates the deviation of model output values from observed values, but it does not measure the magnitude of the errors. It provides whether the model output underestimates or overestimates the observations. This quantitative test ranges from -∞ to +∞, having a perfect score at 0. Values greater than zero indicate that the mean model output exceeds the mean observation. Values less than zero indicate that the mean model output was lower than the mean observation. Though a perfect score is at zero, it does not necessarily mean you have a good model output, it simply means there was correspondence in the values between observations and model outputs. Model outputs can have the same value as the observations at a particular point, but find that on average, the deviation of model output from observations is large. Bias is given by equation 1:

Bias = $\frac{1}{N}\sum_{i=1}^{N}(F_i - O_i)$ …… (1) (Jolliffe, 2012; Stanski & Wilson, 1989)

where F represents the model outputs, O represents observations, N represents the number of model output-observation pairs and i represents the starting point of model output-observation pairs.

In this study, bias was used to determine whether CCAM simulations underestimate or overestimate the satellite observations/reanalysis. The results of the bias are presented as spatial maps. Additionally, for selected study domains, the bias was calculated by

using the area average of the grid points in the domain. The temporal resolution for this section is multi-year seasonal averages.

3.3.4 Root mean square error

Root mean square error (RMSE) is a measure of overall accuracy between the mean observations and mean model outputs. It indicates the average magnitude of errors weighted according to the square of the error. RMSE does not give the direction of deviations of model output values from observed values. This quantitative test ranges from 0 to +∞, having a perfect score at 0. RMSE is given by equation 2:

RMSE = $\sqrt{\frac{1}{N}\sum_{i=1}^{N}(F_i - O_i)^2}$ …… (2) (Jolliffe, I.T., 2012; Stanski, H.R., L.J. Wilson, 1989)

Where RMSE represents root mean square error, F represents the model outputs, F represents observations, N represents the number of model output-observation pairs and i represents the starting point of model output-observation pairs.

In this study, the RMSE method was used to determine the average magnitude of error between CCAM simulations and satellite observations/reanalysis. It is presented as spatial maps. Additionally, for selected study domains, the RMSE value was calculated by using the area average of the grid points in the domain. RMSE provides the same units as the parameters. The temporal resolution for this section is multi-year seasonal averages.

3.3.5 Pearson's correlation

The Pearson correlation coefficient is a measure of linear association between two continuous parameters. This statistical test ranges from -1 to +1, having a perfect score at -1 or 1. The value of zero means that there was no relationship between the two parameters. Values less than zero show that there was a negative relationship between the two parameters. A negative relationship in this instance means, when one parameter increases, the other parameter decreases. The values greater than zero show that there was a positive relationship between the two parameters. A positive relationship in this

instance means, when one parameter increases, so does the other parameter, and *vice versa*. Pearson's correlation was given by equation 3:

$$r = \frac{\sum_{i=1}^{N}(F_i-\overline{F_i})(O_i-\overline{O_i})}{\sqrt{\sum_{i=1}^{N}(F_i-\overline{F_i})^2}\sqrt{\sum_{i=1}^{N}(O_i-\overline{O_i})^2}} \quad \text{..... (3) (Jolliffe, I.T., 2012; Stanski, H.R., L.J. Wilson, 1989)}$$

where r represents the correlation coefficient, F represents the model outputs' values, $\overline{F}$ represents model outputs' mean, O represents observation values and $\overline{O}$ represents observation mean, N represents the number of model output-observation pairs and i represents the starting point of model output-observation pairs.

In this study, r was used to determine the strength of the relationship between total AOD as well as compositional AOD (i.e. black carbon, organic carbon, sulphate, small dust and sea salt) CCAM simulations and satellite observations/reanalysis at each grid point. It was also used to determine the strength of the relationship between CCAM AOD and CCAM cloud parameters to assess the linear association between AOD and cloud parameters. It is presented as spatial maps. The temporal resolution for this section is multi-year seasonal averages.

Additionally, for selected study domains, the correlation value was calculated by using the area average of the grid points in the domain. The analysis was divided by nine classes of r, namely no correlation (r = -0.19-0.19), weak positive correlation (r = 0.20-0.39), moderate positive correlation (r = 0.40-0.59), strong positive correlation (r = 0.60-0.79), perfect positive correlation (r = 0.80-1), weak negative correlation (r = -0.39- -0.20), moderate negative correlation (r = -0.59- -0.40), strong negative correlation (r = -0.79- -0.60), and perfect negative correlation (r = -1-0.79) (Mandailina *et al.*, 2019; Mardesci, 2020; Selvanathan *et al.*, 2020).

3.3.6 Seasonal cycles

For the seasonal analysis, the seasons were defined as summer (December-January-February), autumn (March-April-May), winter (June-July-August) and spring (September-October-November).

In this study, the seasonal cycles between two CCAM simulations and satellite observations/reanalysis, and CCAM AOD and CCAM cloud parameters were compared. It was also used to determine which seasons CCAM simulations and satellite observations/reanalysis, and CCAM AOD and CCAM cloud parameters peak or have their minimum. The temporal resolution for this section is seasonal averages.

CHAPTER 4: VERIFICATION OF CCAM MODEL AGAINST MODIS OR MERRA OBSERVATIONS IN SIMULATING AEROSOLS

This chapter presents spatial and seasonal variations of CCAM simulations of aerosols against satellite observations/reanalysis over the Benguela Region. Firstly, the comparison of spatial variation between CCAM simulations, and MODIS Aqua measurements (for total AOD) and MERRA simulations (compositional AOD) is performed using the eyeball verification method to determine magnitude and spatial patterns. Secondly, statistical scores were calculated to quantify the comparison of spatial variation using bias, RMSE and correlation. Thirdly, a comparison of seasonal variation was compiled as a time series to determine the area-averaged seasonal cycle and peaks.

4.1 Magnitude between CCAM and MODIS or MERRA

This section presents the results of CCAM simulations and MODIS observations or MERRA. We evaluated the spatial variation from CCAM simulations against observed AOD from MODIS and MERRA. To carry out the analysis, the eyeball verification method was used to compare the magnitude, spatial pattern and spatial peaks between CCAM simulations and MODIS observations and MERRA. In this study, magnitude refers to the magnitude of AOD over the domain, spatial pattern refers to the shape or contours of AOD over the domain, and spatial peak refers to a geographical point on the study domain that has the maximum value. The first focus was magnitude, followed by spatial patterns, and lastly spatial peaks over the whole domain. In this section, subdomains were not used for analysis in qualitative analysis (Chapter 4.1), however, they were highlighted in order to note the regions used in quantitative analysis (Chapter 4.2).

4.1.1 Total aerosol optical depth

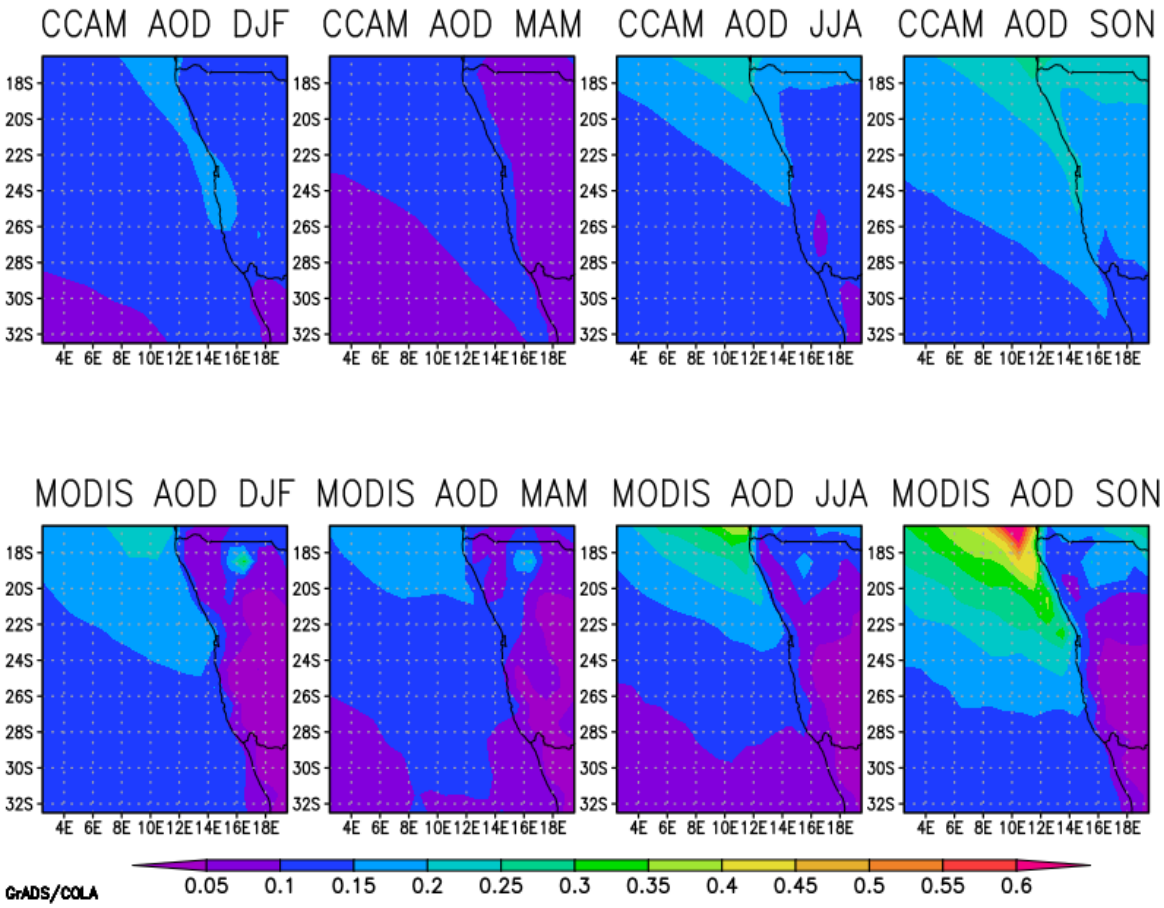

Figure 4.1: The multi-year (2002-2017) averaged total AOD simulated by CCAM (top) and observed MODIS AOD from Aqua (bottom) over the Benguela Region

The AOD simulated by CCAM is lower (0-0.3) compared to observations by MODIS Aqua (0-0.6) for all seasons over the whole domain (Fig. 4.1). There are lower AOD values at the southern region of the study domain and higher AOD values at the northern region for both CCAM and MODIS. The coast has higher AOD compared to the sea and the land in all seasons. Fig. 4.1 also shows that total AOD simulated by CCAM has a similar spatial pattern compared to total AOD measured by MODIS. The spatial pattern has a narrow region of higher values of AOD along the coast as simulated by CCAM compared to MODIS that has a wider area of higher values of AOD measured along the coast for all

seasons. Furthermore, Fig. 4.1 shows that the peaks of total AOD simulated by the CCAM are similar to those measured by MODIS, meaning that they occurred in the same region in both.

The seasonal total AOD is also deduced from Fig. 4.1. Spring has the maximum total AOD, followed by winter (Fig. 4.1). There is high AOD over this region during the southern African biomass burning season, which occurs between June and October (Lu *et al.*, 2018). Summer has the lowest total AOD, but autumn has lower than summer. In spring, the maximum total AOD is simulated in the northern region for the CCAM (0.25-0.30) and MODIS (0.55-0.6). Lower total AOD is simulated in the southern region for the CCAM (0.1-0.15) and over land for MODIS (0-0.05). Total AOD increases from south to north for all seasons. In winter, the maximum total AOD was simulated in the northern region for the CCAM (0.2-0.25) and MODIS (0.35-0.40). Lower total AOD is simulated in the southern region for the CCAM (0.05-0.1) and MODIS (0-0.05). In autumn, the maximum total AOD is simulated in the northern region for the CCAM (0.1-0.15) and MODIS (0.15-0.20). Lower total AOD is simulated in the southern region and over land for the CCAM (0.05-0.1) and MODIS (0-0.05). Autumn has the lowest total AOD compared to other seasons. In summer, the maximum total AOD is simulated in the northern region for the CCAM (0.15-0.20) and MODIS (0.20-0.25). Lower total AOD is simulated in the southern region for the CCAM (0.05-0.1) and over land for MODIS (0-0.05).

Results from this qualitative analysis suggest that the CCAM does simulate total AOD spatial patterns well when compared with satellite observations. The magnitude simulated by the CCAM was lower compared to MODIS observations for all seasons. The spatial patterns and peaks simulated by the CCAM are similar to MODIS observations for all seasons.

4.1.2 Compositional AOD: Black carbon

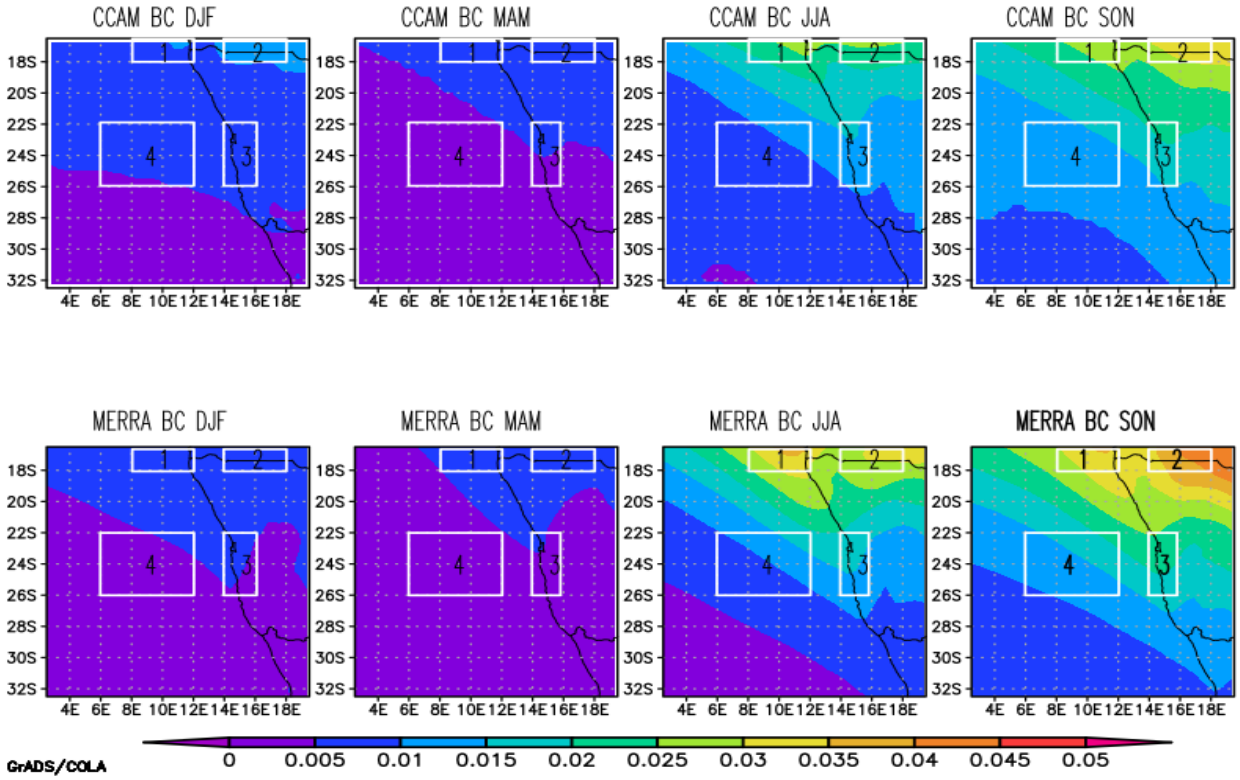

Figure 4.2: The multi-year (2002-2017) averaged compositional AOD of black carbon simulated by CCAM (top) and MERRA (bottom) over the Benguela Region

Fig. 4.2 shows the multi-year averaged magnitude of black carbon simulated by the CCAM and MERRA for all seasons. Compositional AOD of black carbon simulated by the CCAM is similar to that simulated by MERRA. Compositional AOD of black carbon simulated by the CCAM is lower (0-0.035) compared to reanalysis (0-0.045) for all seasons over the whole domain. There is lower compositional AOD of black carbon at the southern region of the study domain and higher compositional AOD of black carbon at the northern region for both the model and reanalysis. Fig. 4.2 also shows that compositional AOD of black carbon simulated by the CCAM has a similar spatial pattern compared to compositional AOD of black carbon simulated by MERRA. Furthermore, Fig. 4.2 shows that the peaks of compositional AOD of black carbon simulated by the CCAM

are in the similar area to those simulated in MERRA. Subdomains 1 to 4 (in white) in Fig. 4.2 are used in the subsequent sections studying the interactions between black carbon and cloud fraction, and liquid water path.

The seasonal magnitude of black carbon is also deduced from Fig. 4.2. Spring has the maximum black carbon followed by winter. Summer and autumn have the lower and lowest black carbon. In spring, the maximum black carbon is simulated in the northern region for the CCAM (0.03-0.035) and MERRA (0.04-0.045). Lower black carbon is simulated in the southern region for the CCAM (0.005-0.01) and MERRA (0.005-0.01). Black carbon increases from south-west to north-east in all seasons. In winter, the maximum black carbon is simulated in the northern region for the CCAM (0.02-0.025) and MERRA (0.03-0.035). Lower black carbon is simulated in the southern region for the CCAM (0.005-0.01) and MERRA (0.005-0.01). In autumn, the maximum black carbon is simulated in the northern region for the CCAM (0.005-0.01) and MERRA (0.005-0.01). Lower black carbon is simulated in the southern region for the CCAM (0-0.005) and MERRA (0-0.005). Autumn has the lowest black carbon compared to other seasons. This is because the main source of black carbon is biomass burning, which takes place between June and October (Choi *et al.*, 2020; Koch & Del Genio, 2010; Lu *et al.*, 2018). In summer, the maximum black carbon is simulated in the northern region for the CCAM (0.005-0.01) and MERRA (0.005-0.01). Lower black carbon is simulated in the southern region for the CCAM (0-0.005) and MERRA (0-0.005). These findings of spatial patterns and peaks in spring are the same as the total AOD, and we do see the peaks in biomass burning periods and areas impacted by biomass burning.

4.1.3 Compositional AOD: Organic carbon

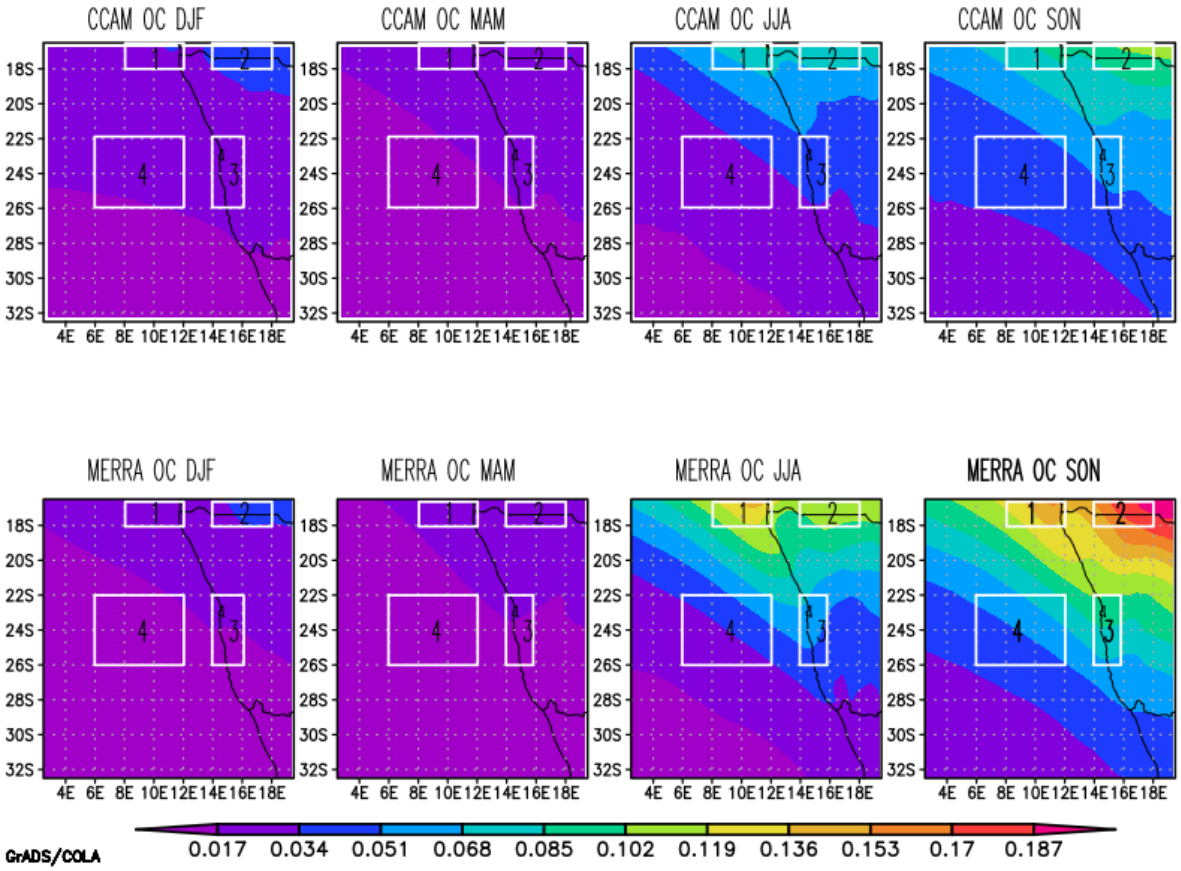

Figure 4.3: The multi-year (2002-2017) averaged compositional AOD of organic carbon simulated by CCAM (top) and MERRA (bottom) over the Benguela Region

Fig. 4.3 shows the multi-year averaged magnitude of simulated organic carbon for the CCAM and MERRA for all seasons. The CCAM simulation of organic carbon magnitude is similar to the simulation of MERRA (note: the simulations look different due to the scale size being small). The magnitude simulated by the CCAM is lower (0-0.119) compared to reanalysis (0-0.187) for all seasons over the whole domain. There is lower organic carbon at the southern region of the study domain and higher organic carbon at the northern region for both the model and reanalysis. Fig. 4.3 also shows that organic carbon simulated by the CCAM has a similar spatial pattern compared to organic carbon simulated by MERRA. Furthermore, Fig. 4.3 shows that the peaks of organic carbon

simulated by the CCAM are similar to those simulated by MERRA. Subdomains 1 to 4 (in white) in Fig. 4.3 are used in the subsequent sections studying the interactions between organic carbon and cloud fraction, and liquid water path.

The seasonal magnitude of organic carbon is also deduced from Fig. 4.3. Spring has the maximum organic carbon followed by winter. Summer and autumn have the lower and lowest organic carbon, respectively. In spring, the maximum organic carbon is simulated in the northern region for the CCAM (0.102-0.119) and MERRA (0.17-0.187). Lower organic carbon is simulated in the southern region for the CCAM (0.017-0.034) and MERRA (0.017-0.034). Organic carbon increases from south-west to north-east in all seasons. In winter, the maximum organic carbon is simulated in the northern region for the CCAM (0.068-0.085) and MERRA (0.119-0.136). Lower organic carbon is simulated in the southern region for the CCAM (0-0.017) and MERRA (0-0.017). In autumn, the maximum organic carbon is simulated in the northern region for the CCAM (0.017-0.034) and MERRA (0.017-0.034). Lower organic carbon is simulated in the southern region for the CCAM (0-0.017) and MERRA (0-0.017). Autumn has the lowest organic carbon compared to other seasons. In summer, the maximum organic carbon is simulated in the northern region for the CCAM (0.034-0.051) and MERRA (0.034-0.051). Lower organic carbon is simulated in the southern region for the CCAM (0-0.017) and MERRA (0-0.017). These findings of spatial patterns and peaks in spring are the same as the total AOD, and we can see the peaks in biomass burning periods and areas impacted by biomass burning.

4.1.4 Compositional AOD: Small dust

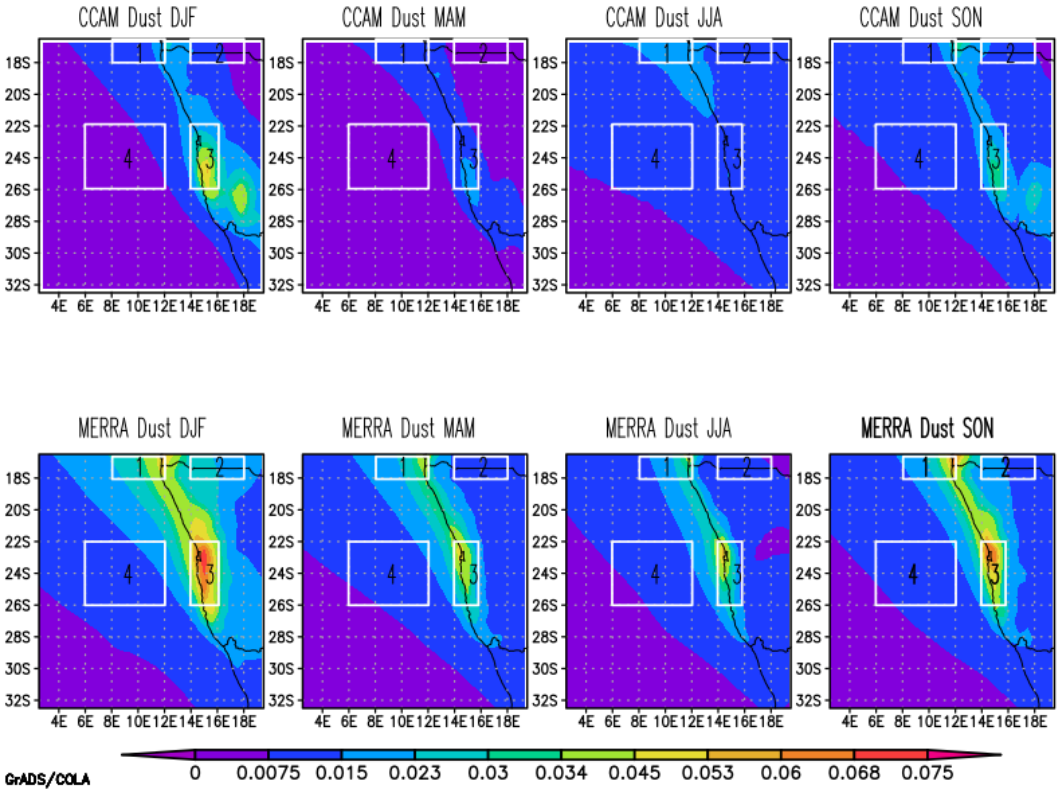

Figure 4.4: The multi-year (2002-2017) averaged compositional AOD of small dust simulated by CCAM (top) and MERRA (bottom) over the Benguela Region

Fig. 4.4 shows the multi-year averaged magnitude of simulated small dust for CCAM and MERRA for all seasons. Small dust is dust particles with a diameter of less than 50 μm. The CCAM simulation of small dust magnitude is similar to the simulation of MERRA. The magnitude simulated by the CCAM is lower (0-0.0075) compared to reanalysis (0-0.0075) for all seasons over the whole domain. There is lower small dust at the ocean compared to over the land for both the model and reanalysis. Fig. 4.4 also shows that dust simulated by the CCAM has a similar spatial pattern compared to small dust simulated by MERRA. Furthermore, Fig. 4.4 shows that the spatial peaks of dust simulated by the CCAM are similar to those simulated by MERRA. Subdomains 1 to 4 (in white) in Fig. 4.4 are used

in the subsequent sections studying the interactions between small dust and cloud fraction, and liquid water path.

The seasonal magnitude of small dust is also deduced from Fig. 4.4. Summer has the maximum small dust, followed by spring. Autumn and winter have the lower and lowest small dust respectively. MERRA simulations show that small dust occurs throughout the seasons. There is a small difference between the seasons, because the deviations of small dust between high- and low dust seasons are minor, indicating that dust activity remains constant during the year. In spring, the maximum small dust is simulated at the coast for the CCAM (0.045-0.053) and MERRA (0.068-0.075). Lower small dust is simulated over the ocean for the CCAM (0-0.0075) and MERRA (0-0.0075). Small dust increases at the coast and decreases towards the east on land and over the ocean in all seasons. In winter, the maximum small dust is simulated at the coast for the CCAM (0.02-0.025) and MERRA (0.03-0.035). Lower small dust is simulated over the ocean for the CCAM (0.005-0.01) and MERRA (0.005-0.01). In autumn, the maximum small dust is simulated at the coast for the CCAM (0.0075-0.015) and MERRA (0.03-0.034). Lower small dust is simulated in the ocean for the CCAM (0-0.0075) and MERRA (0-0.0075). Autumn has the least small dust compared to other seasons. In summer, the maximum small dust is simulated at the coast for the CCAM (0.0075-0.015) and MERRA (0.03-0.034). Lower small dust is simulated in the ocean for the CCAM (0-0.0075) and MERRA (0-0.0075). The findings show that the spatial patterns and peaks occur in summer, which is different to total AOD, and we can see that small dust is not impacted by the biomass burning period.

4.1.5 Compositional AOD: Sulphate

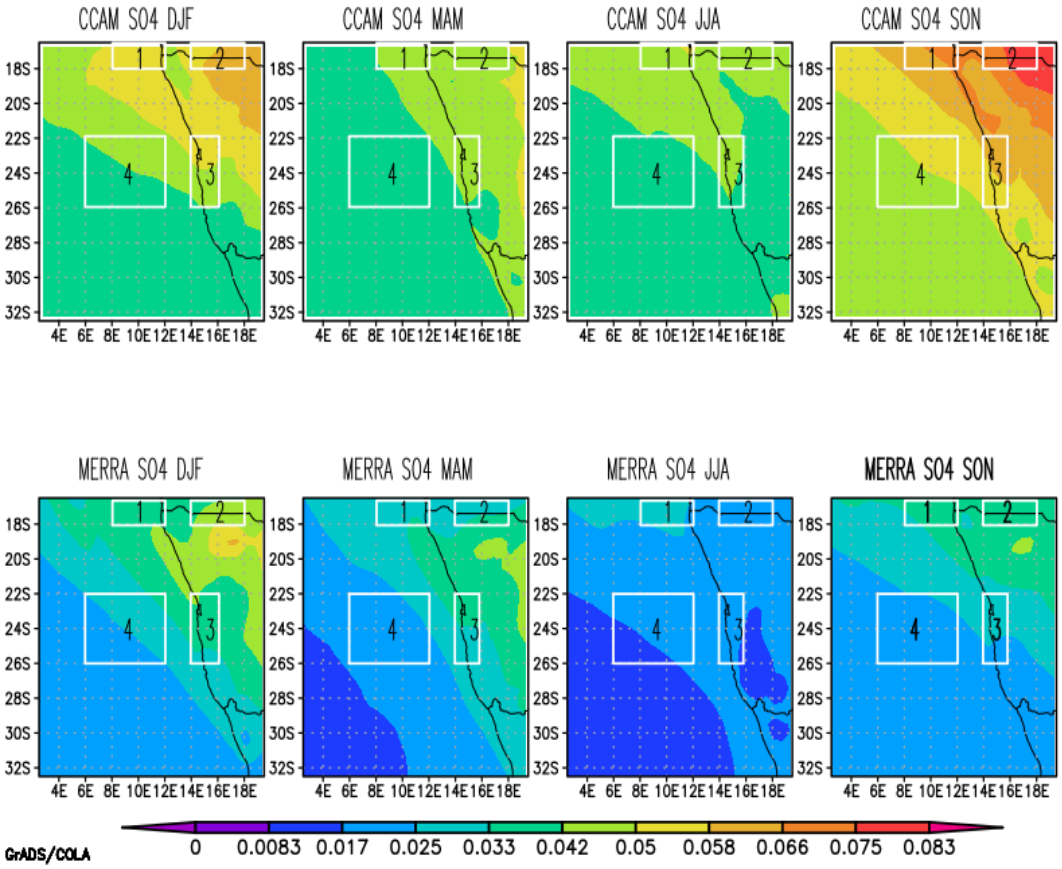

Figure 4.5: The multi-year (2002-2017) averaged compositional AOD of sulphate simulated by CCAM (top) and MERRA (bottom) over the Benguela Region

Fig. 4.5 shows multi-year averaged magnitude of simulated sulphate for the CCAM and MERRA for all seasons. The CCAM simulation of sulphate magnitude is similar to the simulation of MERRA. The magnitude simulated by the CCAM is higher (0.033-0.042) compared to reanalysis (0.0083-0.017) for all seasons over the whole domain. Sulphate is the first aerosol composition due to AOD where the CCAM is higher than MERRA. There is lower sulphate at the southern region of the study domain and higher sulphate at the northern region for both the model and reanalysis. Fig. 4.5 also shows that sulphate simulated by the CCAM has a similar spatial pattern compared to sulphate simulated by MERRA. Furthermore, Fig. 4.5 shows that the peaks of sulphate simulated by the CCAM

are similar to those simulated by MERRA. Subdomains 1 to 4 (in white) in Fig. 4.5 are used in the subsequent sections studying the interactions between sulphate and cloud fraction, and liquid water path.

The seasonal magnitude of sulphate is also deduced from Fig. 4.5. Spring has the maximum sulphate, followed by summer. Autumn and winter have the lower and lowest sulphate, respectively. In spring, the maximum sulphate is simulated in the northern region for the CCAM (0.075-0.083) and MERRA (0.042-0.05). Lower sulphate is simulated in the southern region for the CCAM (00.042-0.05) and MERRA (0.017-0.025). Sulphate increases from south-west to north-east in all seasons. In winter, the maximum sulphate is simulated in the northern region for the CCAM (0.042-0.05) and MERRA (0.025-0.033). Lower sulphate is simulated in the southern region for the CCAM (0.033-0.042) and MERRA (0.0083-0.017). Winter has the lowest sulphate compared to other seasons. In autumn, the maximum sulphate is simulated in the northern region for the CCAM (0.05-0.058) and MERRA (0.042-0.05). Lower sulphate is simulated in the southern region for the CCAM (0.033-0.042) and MERRA (0.0083-0.017). In summer, the maximum sulphate is simulated in the northern region for the CCAM (0.058-0.066) and MERRA (0.058-0.066). Lower sulphate is simulated in the southern region for the CCAM (0.033-0.042) and MERRA (0.017-0.025). The findings show that the spatial patterns and peaks occur in summer, which is different to total AOD, and we can see that sulphate is not impacted by the biomass burning period.

4.1.6 Compositional AOD: Sea salt

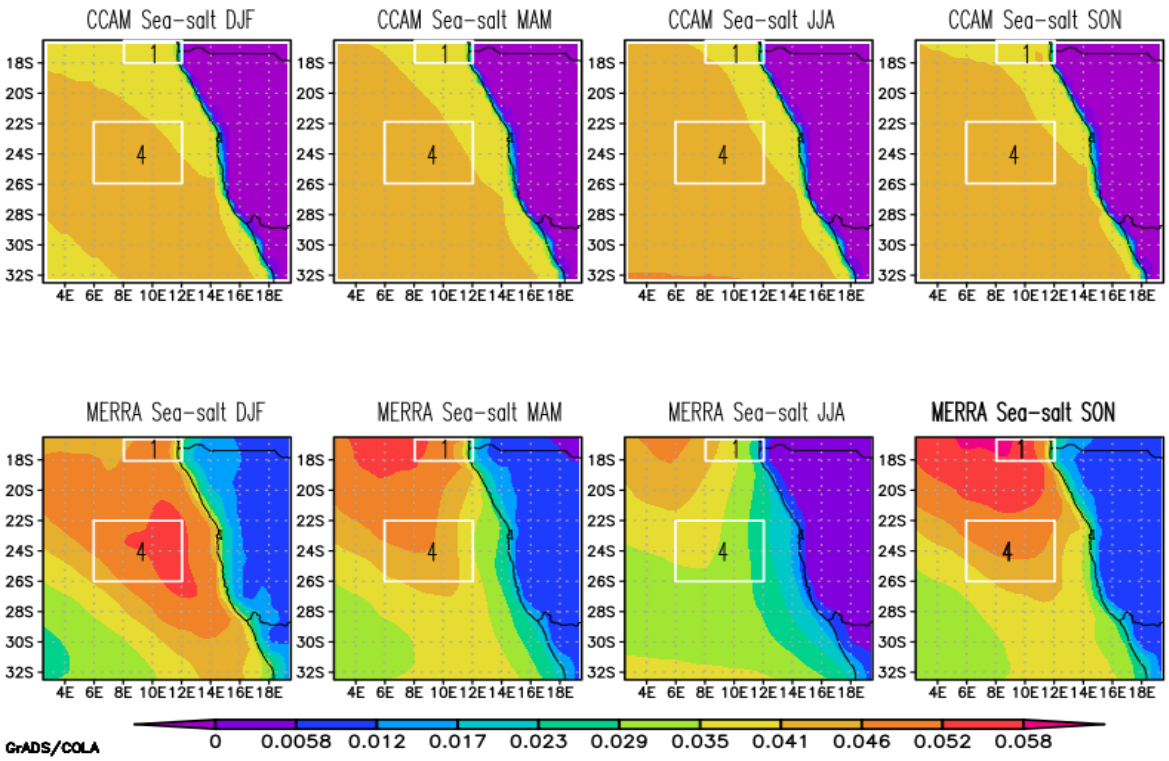

Figure 4.6: The multi-year (2002-2017) averaged compositional AOD of sea-salt simulated by CCAM (top) and MERRA (bottom) over the Benguela Region

Fig. 4.6 shows multi-year averaged magnitude of simulated sea salt for the CCAM and MERRA for all seasons. Sea-salt magnitude simulated by the CCAM is different from that simulated by MERRA. The CCAM does not simulate sea salt over land because the model does not transport sea salt as it is calculated at each timestep based on the strong wind speeds over the ocean surface (Rotstayn *et al.*, 2007). The magnitude simulated by the CCAM is lower (0-0.046) compared to reanalysis (0-0.058) for all seasons over the whole domain. There is lower sea salt on-shore and higher sea salt in the ocean as simulated by the CCAM. MERRA simulated lower sea salt at the south-west of the domain and higher sea salt is simulated at the northern region. Fig. 4.6 also shows that sea salt simulated by the CCAM does not have similar spatial patterns compared to MERRA. Fig. 4.6 shows the sea salt of the CCAM and MERRA on the same scale, so you cannot see

the spatial variation very well. However, if you look at the sea salt of the CCAM and MERRA with different scales (not shown), the spatial pattern of the CCAM has the maximum over the inner ocean and decreases towards the coast, while MERRA has the maximum over northern region and decreases towards the southern region with the minimum over the coast. Furthermore, the peaks of sea salt simulated by the CCAM are not similar to those simulated by MERRA, as the CCAM's peaks are located over the southern region and MERRA's peaks are located over the northern region. The findings show that the spatial patterns and peaks occur in spring, which is similar to total AOD; however, sea salt is not impacted by the biomass burning period. Subdomains 1 to 4 (in white) in Fig. 4.6 are used in the subsequent sections studying the interactions between sea salt and cloud fraction, and liquid water path.

The seasonal magnitude of sea salt is also deduced from Fig. 4.6. Spring has the maximum sea salt, followed by summer and autumn, respectively, as simulated by MERRA. Winter has the lowest sea salt. In spring, the maximum sea salt is simulated on-shore for the CCAM (0.041-0.046) and the northern region for MERRA (0.052-0.058). Lower sea salt is simulated in the south-west region for the CCAM (0.035-0.041) and the southern region for MERRA (0.029-0.035). Sea salt increases from the coast to the ocean for the CCAM. Sea salt increases from the north to the south for MERRA. In winter, the maximum sea salt is simulated on-shore for the CCAM (0.041-0.046) and northern region for MERRA (0.046-0.052). Lower sea salt is simulated in the south-west region for the CCAM (0.035-0.041) and at the coast for MERRA (0.012-0.017). Winter has the lowest sea salt compared to other seasons. In autumn, the maximum sea salt is simulated on-shore for CCAM (0.041-0.046) and northern region for MERRA (0.052-0.058). Lower sea salt is simulated in the southern region for the CCAM (0.035-0.041) and at the coast for MERRA (0.023-0.029). In summer, the maximum sea salt is simulated on-shore for the CCAM (0.041-0.046) and at the centre for MERRA (0.052-0.058). Lower sea salt is simulated in the southern region for the CCAM (0.035-0.041) and at the south-west region for MERRA (0.023-0.029).

4.1.7 Summary

The spatial variation from CCAM simulations of total AOD and compositional AOD (i.e. black carbon, organic carbon, sulphate, small dust and sea salt) has been evaluated against MODIS observations and MERRA. Results suggest that AOD attributable to black carbon and organic carbon simulated lower magnitudes in the CCAM compared to MODIS and MERRA. The spatial patterns and peaks simulated by the CCAM are similar to MODIS observations and MERRA, though there are slight differences. Peaks are seen during biomass burning periods, which highlights that the emissions and transport of these aerosols are captured in the CCAM. Aerosol optical depth attributable to sulphate simulated higher magnitudes in the CCAM compared to MERRA. The spatial patterns and peaks simulated by the CCAM are different to MERRA. Dust aerosols (i.e. small dust) simulated lower magnitudes in the CCAM compared to MERRA. The spatial patterns and peaks simulated by the CCAM are similar to MERRA, although they are slightly different. Peaks are seen throughout all seasons, which is expected because the transportation of dust depends on wind, which is omnipresent. Marine aerosols (i.e. sea salt) simulated lower magnitudes in the CCAM compared to MERRA. Sea-salt aerosols in CCAM are diagnosed at each time step and are a function of wind speeds at 10 m. Because sea-salt aerosols are diagnosed, it means vertical and horizontal transportation of these aerosols is not simulated. Sea salt simulated by the CCAM has different spatial patterns and peaks compared to MERRA, which is most likely due to the parameterisation of sea-salt emissions in the CCAM.

4.2 Quantitative verification between the CCAM and MODIS or MERRA

This section presents the results of the CCAM simulations and MODIS observations. We performed quantitative analysis between the CCAM simulations and MODIS observations (for total AOD) and MERRA (for compositional AOD). To carry out the analysis, statistical schemes (bias, RMSE and correlation) were used to evaluate the model. Bias is formulated as CCAM simulations minus MODIS observations or CCAM simulations minus MERRA simulations. The map colour bar scale of RMSE shares the same map colour

bar scale of the spatial maps that were used for magnitude (eyeball verification method). Keeping the map colour bar scale the same made it easier to see by what size the CCAM simulations differed from MODIS observations. The first focus was bias, followed by RMSE, and lastly correlation over the four subdomains.

4.2.1 Total aerosol optical depth

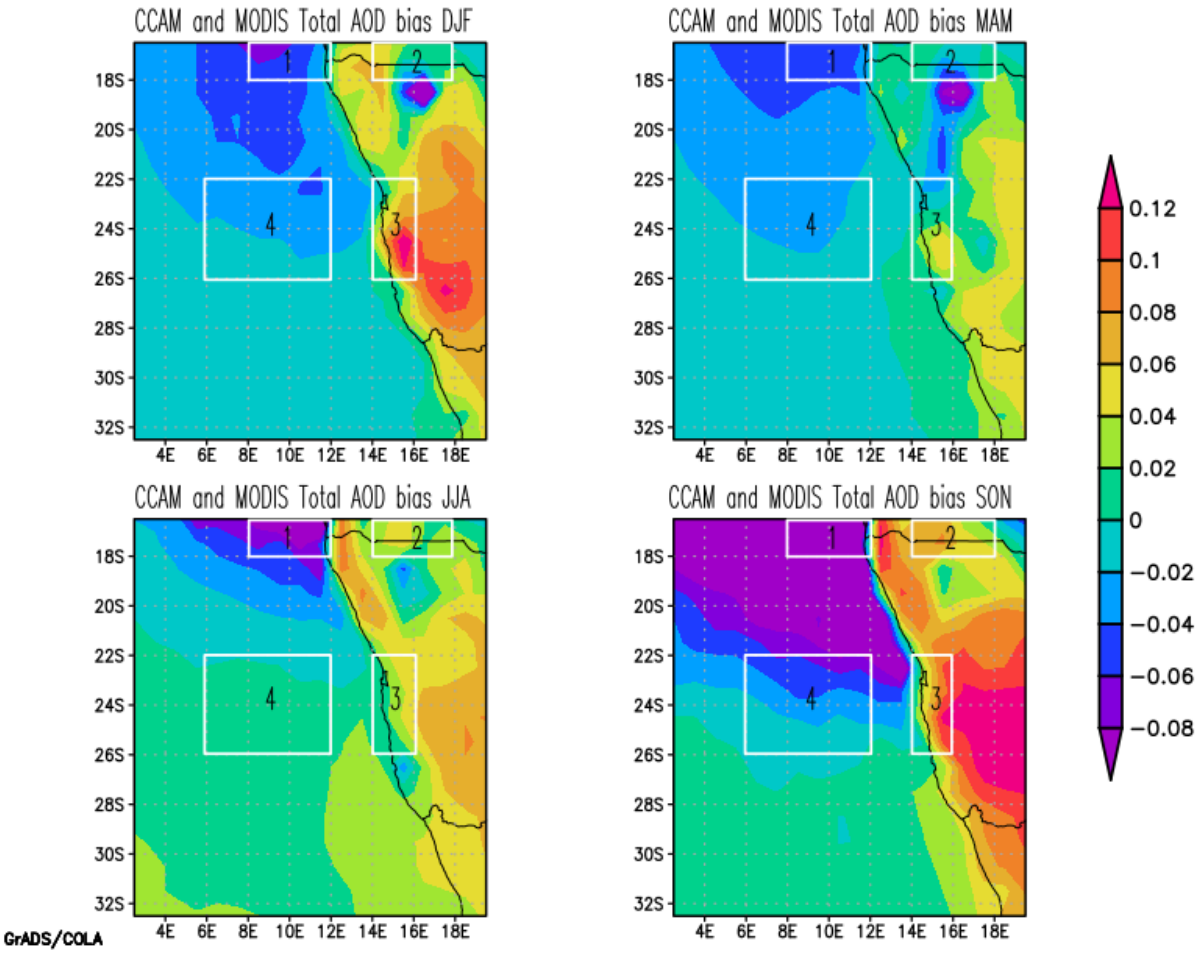

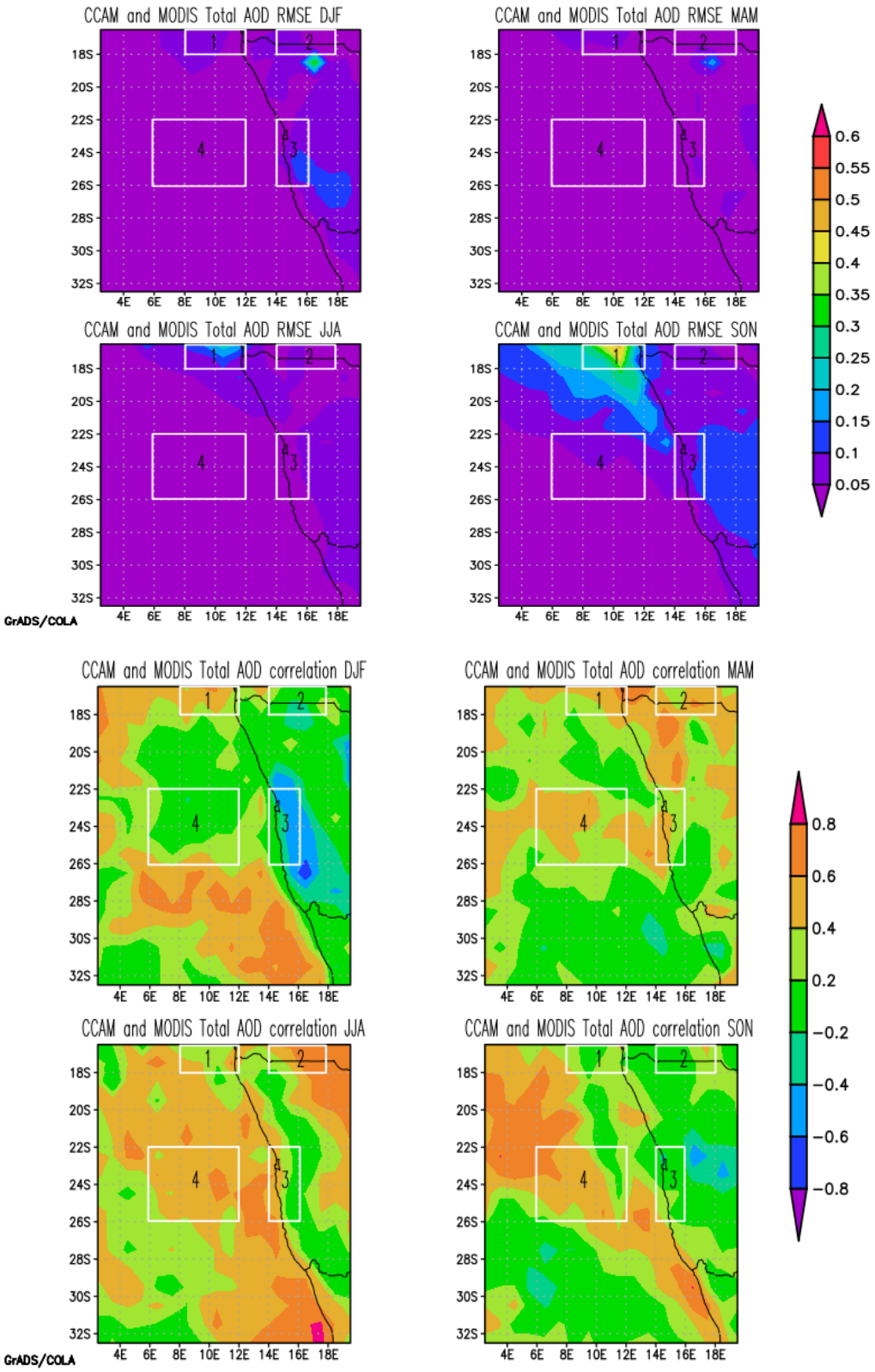

Figure 4.7: The multi-year (2002-2017) averaged bias (top), RMSE (middle) and correlation (bottom) of total AOD between CCAM and MODIS

Fig. 4.7 shows multi-year averaged statistical schemes of total AOD between the CCAM simulations and MODIS observations for the subdomains in all seasons. Subdomain 1 has a negative bias for total AOD in all seasons. The magnitude of error for total AOD calculated for subdomain 1 is lower (0-0.05) in autumn, and higher (0.05-0.3) in summer, winter and spring. Subdomain 1 has a moderate positive correlation in summer, autumn and winter, and a weak positive correlation in spring for total AOD.

Subdomain 2 has a positive bias for total AOD in summer, winter and spring, and has a negative bias in autumn. The magnitude of error for total AOD calculated for subdomain 2 is lower (0-0.05) in summer, autumn and winter, and higher (0.05-0.1) in spring. Subdomain 2 has no correlation for total AOD in summer and spring, and areas of moderate positive correlation in autumn, and strong positive correlation in winter.

Subdomain 3 has a positive bias for total AOD for all seasons. The magnitude of error for total AOD calculated for subdomain 3 is lower (0-0.05) in autumn and winter, and higher (0.05-0.1) in summer and spring. Subdomain 3 has moderate negative correlation for total AOD in summer, moderate positive correlation in autumn, weak positive correlation in winter and no correlation in spring.

Subdomain 4 has a negative bias for total AOD in summer, autumn and spring, and has a negative bias in winter. The magnitude of error calculated for subdomain 4 is lower (0-0.05) for all seasons. Subdomain 4 has no correlation for total AOD in summer, and a moderate positive correlation in autumn, winter and spring.

It was found that the CCAM underestimated AOD over the ocean except in the fourth subdomain in winter. The CCAM overestimated AOD on land except in the second subdomain in autumn. Also, the CCAM produced a lower magnitude of error compared to MODIS except in the first subdomain in spring. Furthermore, the CCAM had a moderate positive correlation over the ocean except in the fourth subdomain in summer and the first subdomain in spring. The CCAM had a moderate negative correlation in the third subdomain in summer.

The results of this study are in agreement with previous research. A previous study evaluated the performance of the GEOS-Chem-APM global aerosol model against MODIS observations and found that modelled AOD was lower than the observations over

southern Africa (Ma & Yu, 2015). ALADIN and RegCM models were in agreement with MERRA reanalysis, but are underestimated when compared to MODIS observations over the southeast Atlantic ocean (Mallet *et al.*, 2020). In another study, it was found that MODIS had a larger AOD compared to Oslo CTM2 and CAM-Oslo models globally (Myhre *et al.*, 2007). The low AOD simulations could be influenced by the emission inventory of the aerosols. Emission inventories are not entirely precise about the sources and emission rates, and as such models are bound to have lower values compared to observations (Van Aardenne & Pulles, 2002). In some instances, emission inventories are inaccurate because of incomplete emissions (Van Aardenne & Pulles, 2002).

It should also be noted that the difference between satellite and model AOD might be introduced by algorithms or model setup. Models estimate AOD every day and at every timestep, while the satellite measurements used here were from one overpass of Aqua. To equate the temporal resolution between the model and satellites, We averaged the data seasonally, then averaged the seasonal averages multi-year seasonally.

4.2.2 Compositional AOD: Black carbon

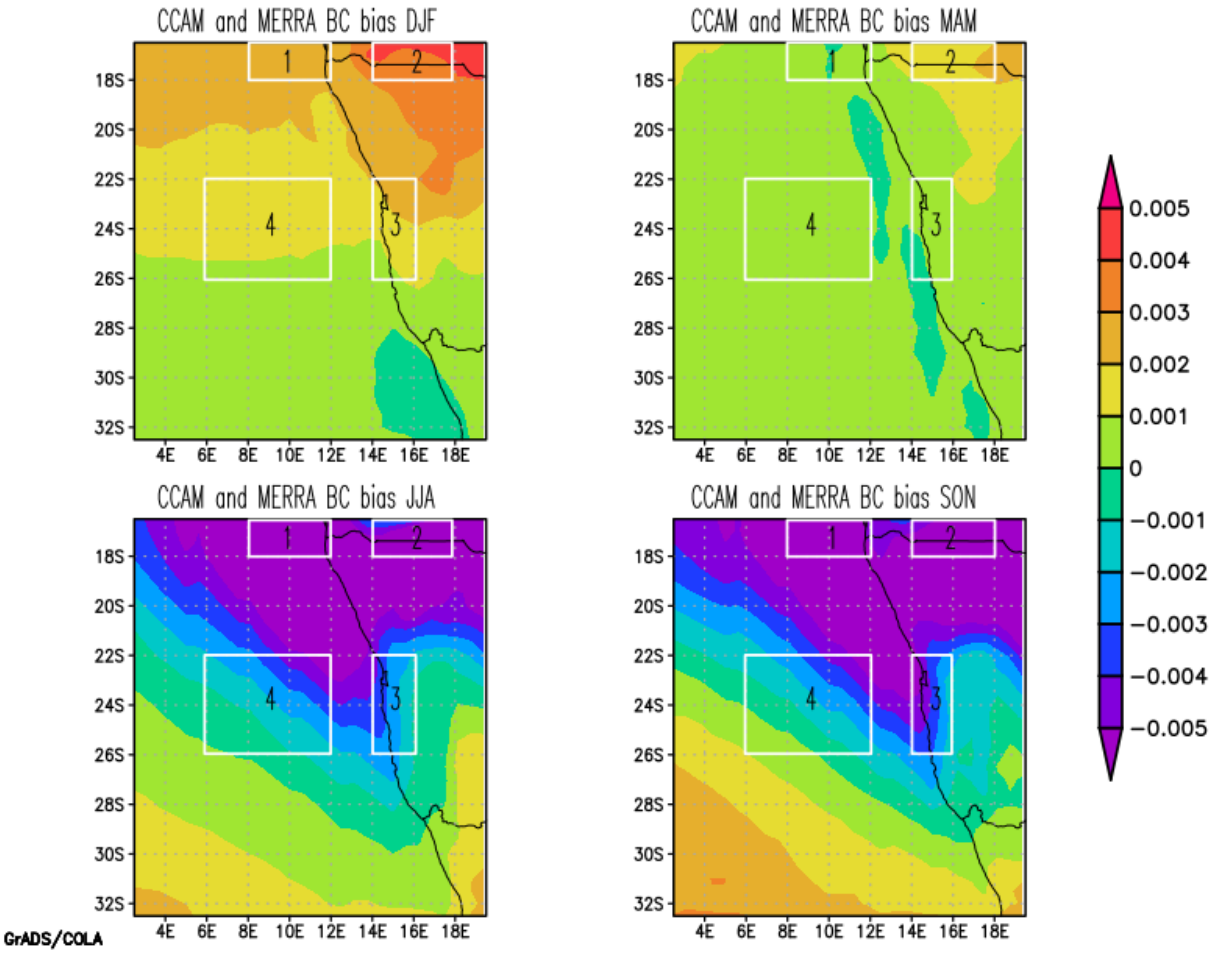

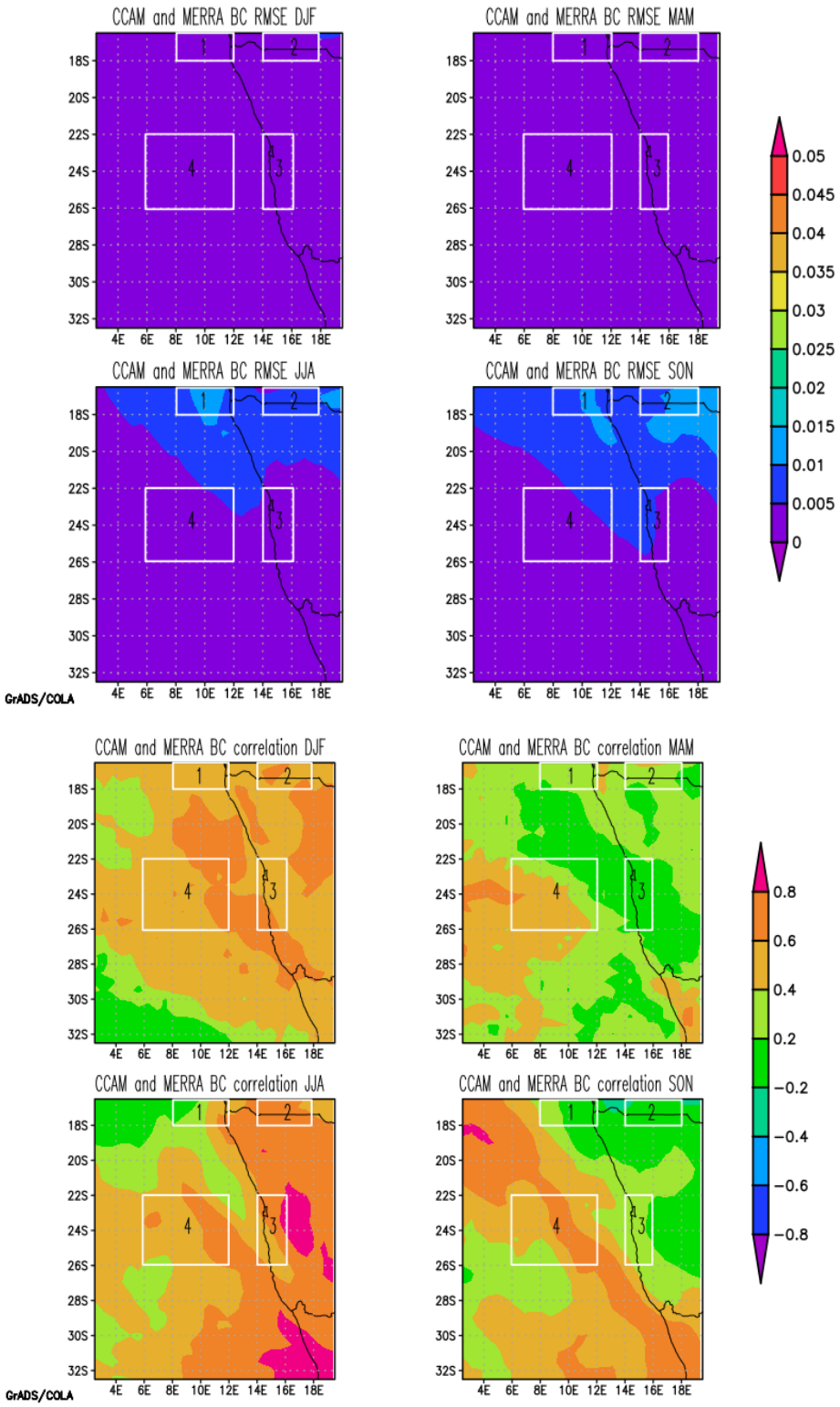

Figure 4.8: The multi-year (2002-2017) averaged bias (top), RMSE (middle) and correlation (bottom) of compositional AOD of black carbon between CCAM and MERRA

Fig. 4.8 shows multi-year averaged statistical schemes of compositional AOD of black carbon between the CCAM simulations and reanalysis for the subdomains in all seasons. Subdomain 1 had a positive bias for compositional AOD of black carbon in summer and autumn, and had a negative bias in winter and spring. The magnitude of error for compositional AOD of black carbon calculated for subdomain 1 was lower (0-0.005) in summer and autumn, and higher (0.005-0.01) in winter and spring. Subdomain 1 had moderate positive correlation (0.4-0.6) for compositional AOD of black carbon in summer, weak positive correlation (0.2-0.4) in autumn, winter, and no correlation (-0.2-0.2) in spring.

Subdomain 2 had a positive bias for compositional AOD of black carbon in summer and autumn, and had a negative bias in winter and spring. The magnitude of error for compositional AOD of black carbon calculated for subdomain 2 was lower (0-0.005) in summer and autumn, and higher (0.005-0.01) in winter and spring. Subdomain 2 had moderate positive correlation (0.4-0.6) for compositional AOD of black carbon in summer, weak positive correlation in autumn, strong positive correlation in winter, and no correlation in spring.

Subdomain 3 had a positive bias for compositional AOD of black carbon in summer and autumn, and had a negative bias in winter and spring. The magnitude of error for compositional AOD of black carbon calculated for subdomain 3 was lower (0-0.005) in all seasons. Subdomain 3 had a moderate positive correlation for compositional AOD of black carbon in summer, no correlation in autumn, strong positive correlation in winter, and weak positive correlation in spring.

Subdomain 4 had a positive bias for compositional AOD of black carbon in summer and autumn, and had a negative bias in winter and spring. The magnitude of error for compositional AOD of black carbon calculated for subdomain 4 was lower (0-0.005) in all seasons. Subdomain 4 had a moderate positive correlation for compositional AOD of black carbon in summer, winter and spring, and a weak positive correlation in autumn.

Results from both quantitative and qualitative analyses suggest that the CCAM simulations are similar to those of MERRA. The magnitude simulated by the CCAM is lower compared to MERRA simulations at the northern region in winter and spring.

However, the magnitude is similar for other seasons and over the southern region. The southern region has the lowest AOD from both models. The spatial pattern simulated by the CCAM is similar compared to MERRA simulations for all seasons. The peaks simulated by the CCAM are similar to MERRA simulations. Peaks are simulated at the northern region in winter and spring. It was also found that the CCAM overestimated black carbon in summer and autumn compared to MERRA. The CCAM underestimated black carbon in winter and spring. Also, the CCAM produced a lower magnitude of error except in the first and second subdomain in winter and spring. The bias and the magnitude of error are small (less than 0.005). Furthermore, the CCAM black carbon had a moderate positive correlation with MERRA in summer and winter. The CCAM had a weak positive correlation with MERRA in autumn except in the third subdomain. The CCAM had no correlation with MERRA over land in spring. Previous studies found that Community Earth System Model simulations were in agreement with MERRA reanalysis over the years over China and globally (Jeong & Wang, 2010; Luo *et al*., 2020).

4.2.3 Compositional AOD: Organic carbon

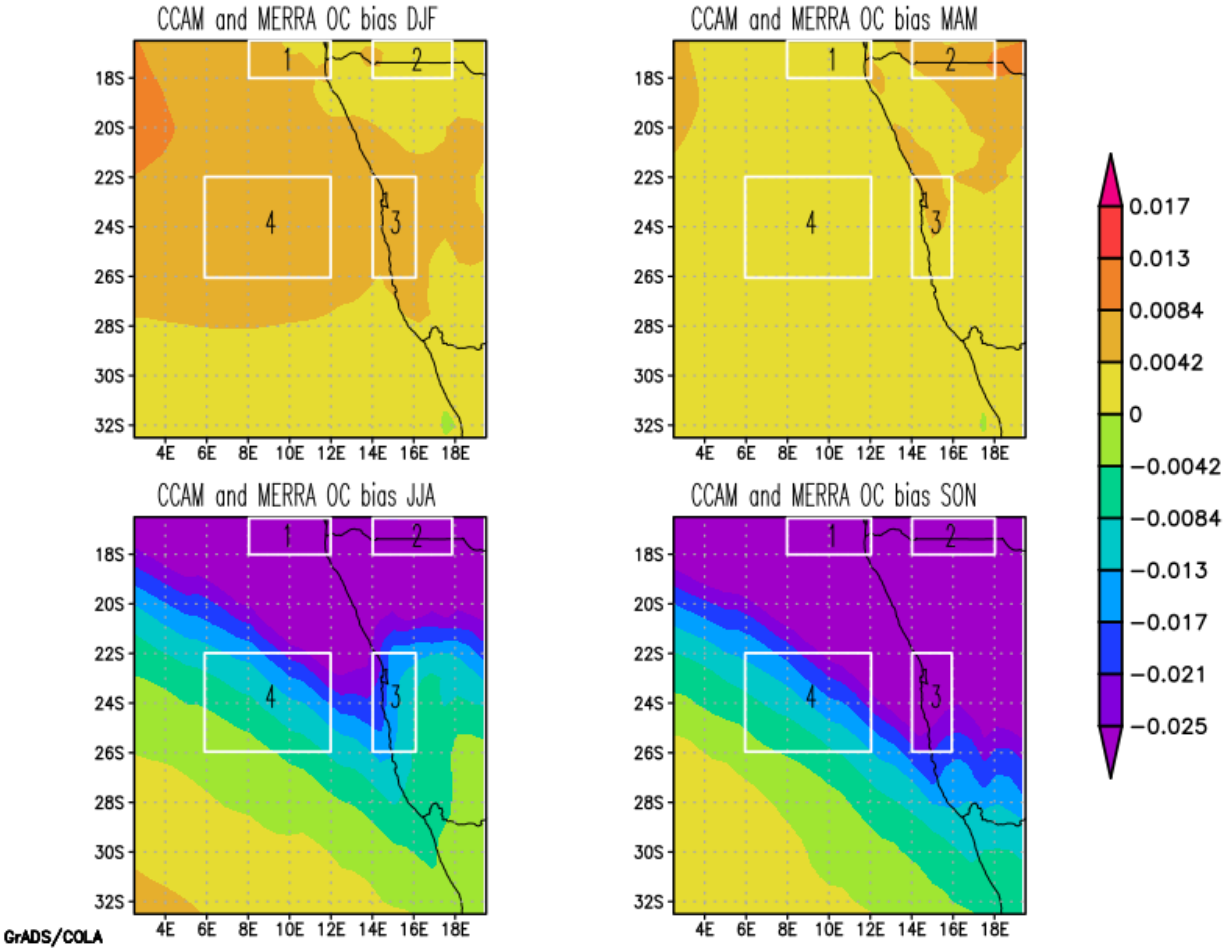

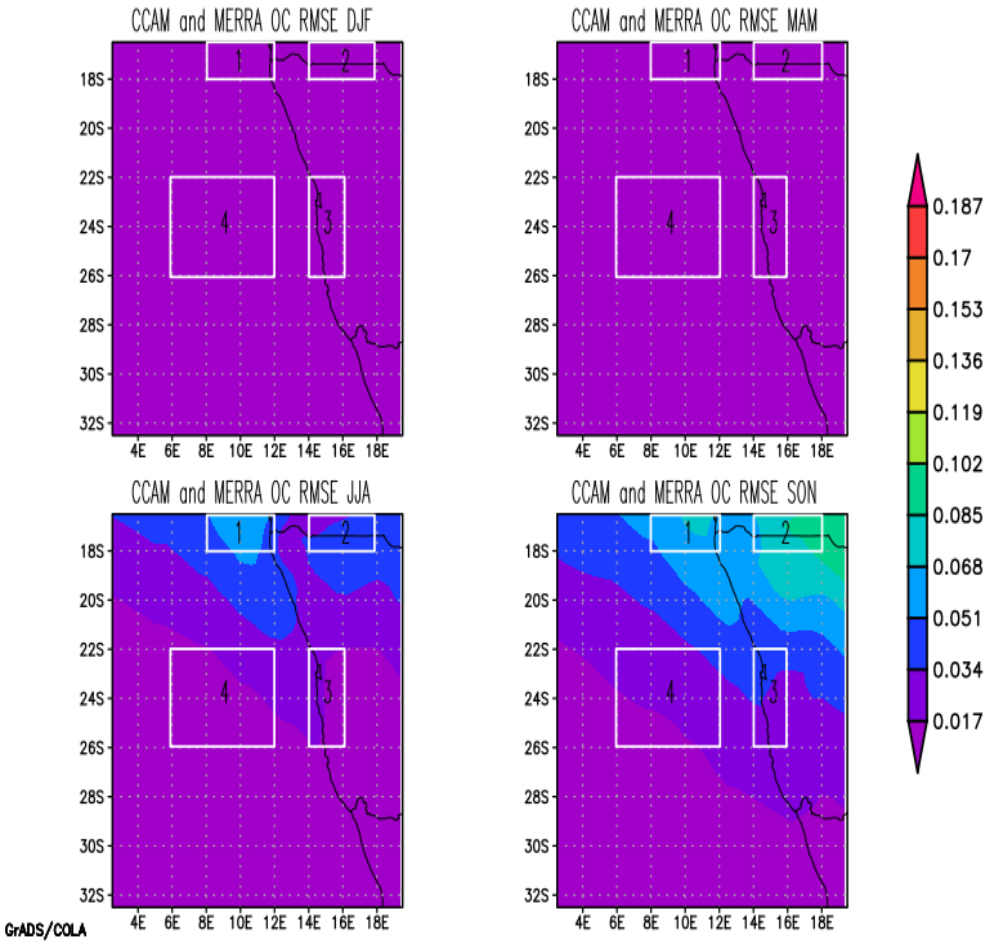
CCAM and MERRA OC RMSE DJF
CCAM and MERRA OC RMSE MAM
CCAM and MERRA OC RMSE JJA
CCAM and MERRA OC RMSE SON
18S
20S
22S
24S
26S
28S
30S
32S
4E 6E 8E 10E 12E 14E 16E 18E
1
2
3
4
0.187
0.17
0.153
0.136
0.119
0.102
0.085
0.068
0.051
0.034
0.017
GrADS/COLA

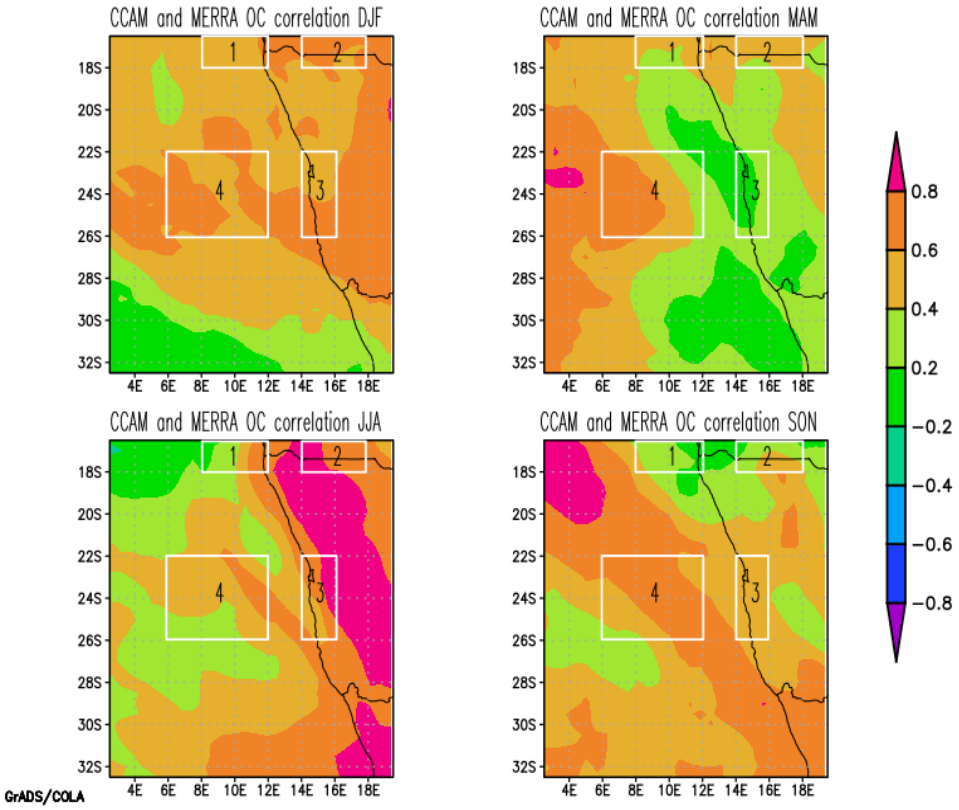

Figure 4.9: The multi-year (2002-2017) averaged bias (top), RMSE (middle) and correlation (bottom) of compositional AOD of organic carbon between CCAM and MERRA

Fig. 4.9 shows multi-year averaged statistical schemes of compositional AOD of organic carbon between the CCAM simulations and reanalysis for the subdomains in all seasons. Subdomain 1 had a positive bias for compositional AOD of organic carbon in summer and autumn, and a negative bias in winter and spring. The magnitude of error for compositional AOD of organic carbon calculated for subdomain 1 was (0-0.017) in summer and autumn, and higher (0.017-0.085) in winter and spring. Subdomain 1 had a moderate positive correlation for compositional AOD of organic carbon in summer, autumn and winter, and a weak positive correlation in spring. Subdomains 1 to 4 (in white) in Fig. 4.2 are used in the subsequent sections for linking organic carbon to cloud fraction and liquid water path.

Subdomain 2 had a positive bias for compositional AOD of organic carbon in summer and autumn, and a negative bias in winter and spring. The magnitude of error for

compositional AOD of organic carbon calculated for subdomain 2 was lower (0-0.017) in summer and autumn, and higher (0.017-0.085) in winter and spring. Subdomain 2 had a strong positive correlation for compositional AOD of organic carbon in summer and winter, a moderate positive correlation in autumn, and a weak positive correlation in spring.

Subdomain 3 had a positive bias for compositional AOD of organic carbon in summer and autumn, and a negative bias in winter and spring. The magnitude of error for compositional AOD of organic carbon calculated for subdomain 3 was lower (0-0.017) in summer and autumn, and higher (0.017-0.034) in winter and spring. Subdomain 3 had a strong positive correlation for compositional AOD of organic carbon in summer and winter, no correlation in autumn, and a moderate positive correlation in spring.

Subdomain 4 had a positive bias for compositional AOD of organic carbon in summer and autumn, and negative bias in winter and spring. The magnitude of error for compositional AOD of organic carbon calculated for subdomain 4 was lower (0-0.017) in summer and autumn, and higher (0.034) in winter and spring. Subdomain 4 had a strong positive correlation for compositional AOD of organic carbon in summer and spring, and a moderate positive correlation in autumn and winter.

Results from both quantitative and qualitative analysis suggest that the CCAM simulations are similar to those of MERRA, although they are smaller than MERRA. The magnitude simulated by the CCAM was lower compared to MERRA simulations. The southern region has the lowest AOD from both models. The spatial pattern simulated by the CCAM is similar compared to MERRA simulations for all seasons. The peaks simulated by the CCAM are similar to MERRA simulations. Peaks are simulated at the northern region in winter and spring. It was found that the CCAM overestimated compositional AOD of organic carbon in summer and autumn. The CCAM underestimated organic carbon in winter and spring. Also, the CCAM produced a lower magnitude of error except in summer and autumn. Furthermore, the CCAM had a moderate positive correlation except over the coast in autumn.

4.2.4 Compositional AOD: Small dust

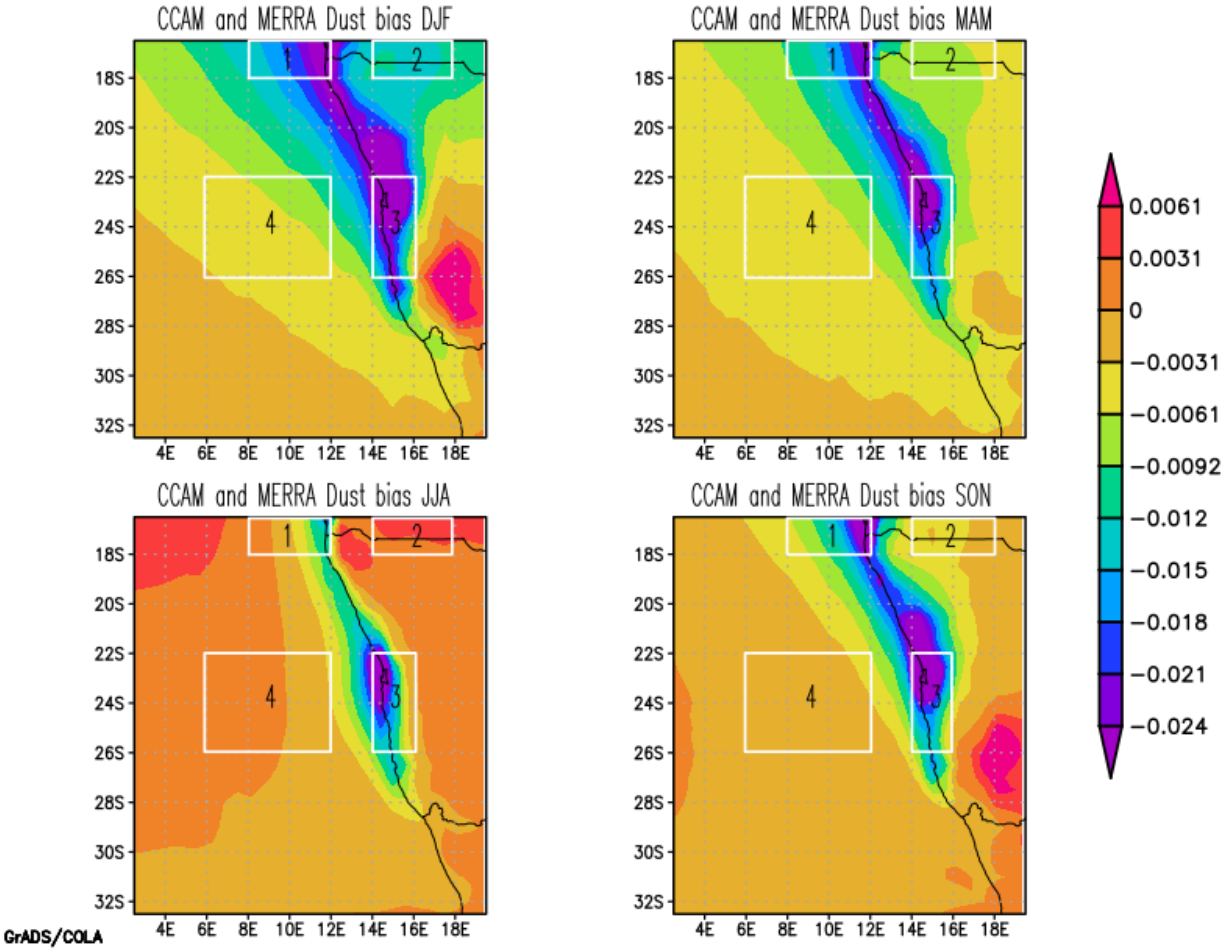

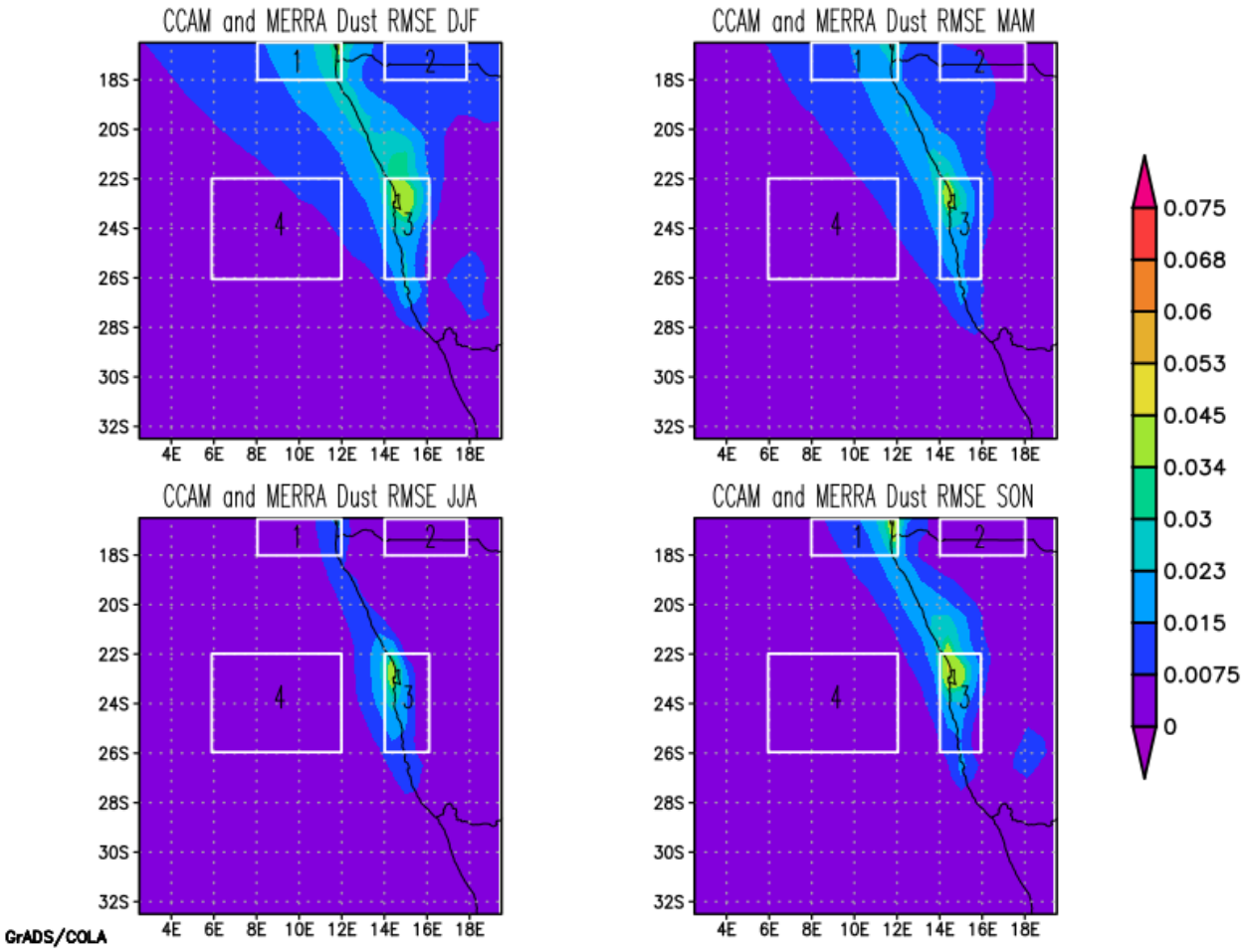
CCAM and MERRA Dust RMSE DJF
CCAM and MERRA Dust RMSE MAM
CCAM and MERRA Dust RMSE JJA
CCAM and MERRA Dust RMSE SON
1
2
3
4
18S
20S
22S
24S
26S
28S
30S
32S
4E
6E
8E
10E
12E
14E
16E
18E
0.075
0.068
0.06
0.053
0.045
0.034
0.03
0.023
0.015
0.0075
0
GrADS/COLA

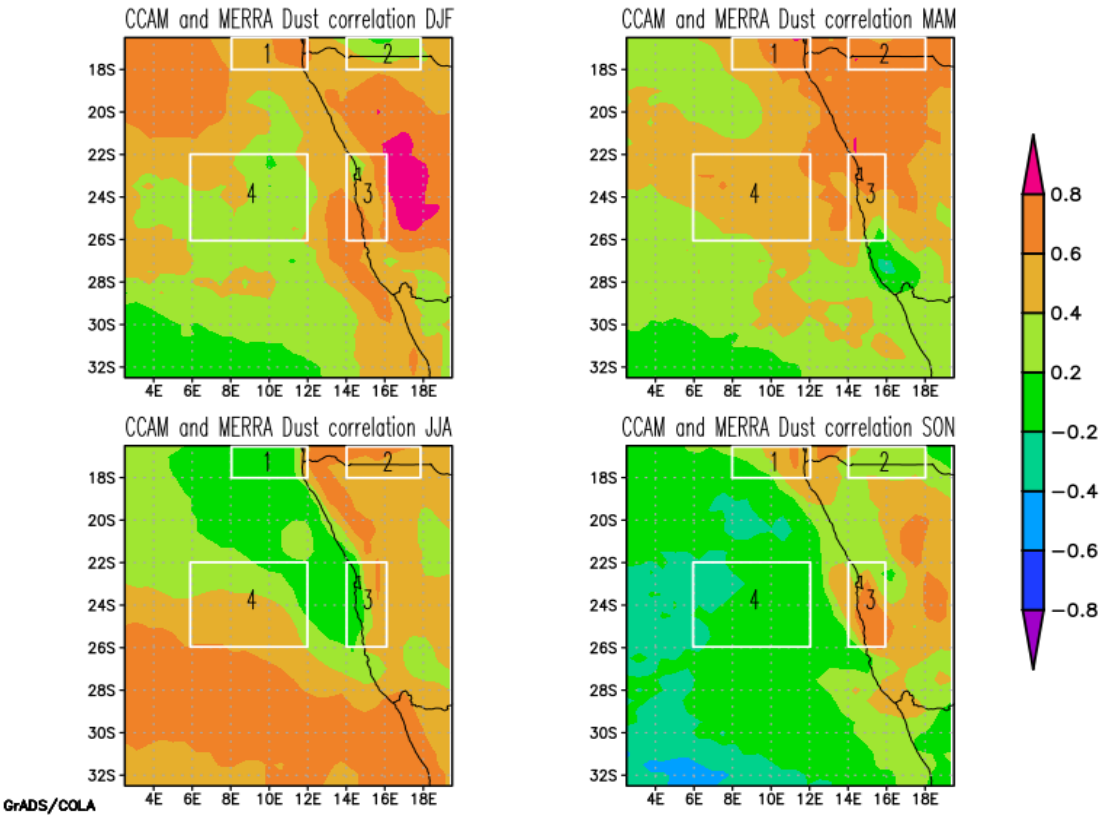

Figure 4.10: The multi-year (2002-2017) averaged bias (top), RMSE (middle) and correlation (bottom) of compositional AOD of small dust between CCAM and MERRA

Fig. 4.10 shows multi-year averaged statistical schemes of small dust between the CCAM simulations and reanalysis for the subdomains in all seasons. Subdomain 1 had a negative bias for compositional AOD of small dust in all seasons. The magnitude of error for compositional AOD of small dust calculated for subdomain 1 was lower (0-0.0075) in winter, and higher (0.0075-0.023) in summer, autumn and spring. Subdomain 1 had a strong positive correlation for compositional AOD of small dust in summer and autumn, no correlation in winter and a moderate positive correlation in spring.

Subdomain 2 had a negative bias for compositional AOD of small dust in summer, autumn and spring, and a positive bias in winter. The magnitude of error for compositional AOD of small dust calculated for subdomain 2 was lower (0-0.0075) in autumn, winter, and spring, and higher (0.0075-0.015) in summer. Subdomain 2 had a weak positive

correlation for compositional AOD of small dust in summer and spring, a strong positive correlation in autumn, and a moderate positive correlation in winter.

Subdomain 3 had a negative bias for compositional AOD of small dust in all seasons. The magnitude of error for compositional AOD of small dust calculated for subdomain 3 was higher (0.0075-0.03) in all seasons. Subdomain 3 had a moderate positive correlation for compositional AOD of small dust in summer and autumn, no correlation in winter, and a strong positive correlation in spring.

Subdomain 4 had a negative bias for compositional AOD of small dust in summer, autumn and spring, and a positive bias in winter. The magnitude of error for compositional AOD of small dust calculated for subdomain 4 was lower (0-0.0075) in all seasons. Subdomain 4 had a weak positive correlation for compositional AOD of small dust in summer and winter, moderate positive correlation in autumn, and no correlation in spring.

Results from both quantitative and qualitative analysis suggest that the CCAM simulations are similar to those of MERRA, although they are smaller compared to MERRA. The magnitude simulated by the CCAM is lower compared to MERRA simulations. The ocean and land have the lowest AOD from the model and reanalysis. The spatial pattern simulated by CCAM is similar compared to MERRA simulations for all seasons. The peaks simulated by CCAM are similar to MERRA simulations. Peaks are simulated at the coast for all seasons. It was found that the CCAM underestimated compositional AOD of small dust except in winter over land and the ocean. Also, the CCAM produced a lower magnitude of error in the third subdomain only. Furthermore, the CCAM had a moderate positive correlation in summer and winter. The CCAM had a weak positive correlation in autumn except in the third subdomain. The CCAM had a moderate positive correlation in summer and autumn. The CCAM had a weak positive correlation over land and southern parts of the ocean in winter. Previous studies found that the WRF-Chem model and ModIs Dust AeroSol (MIDAS) models are in agreement with spatial patterns of MERRA reanalysis and satellite observations in Sahel, but the magnitude is underestimated when compared to reanalysis (Gkikas *et al.*, 2022; Parajuli *et al.*, 2019).

4.2.5 Compositional AOD: Sulphate

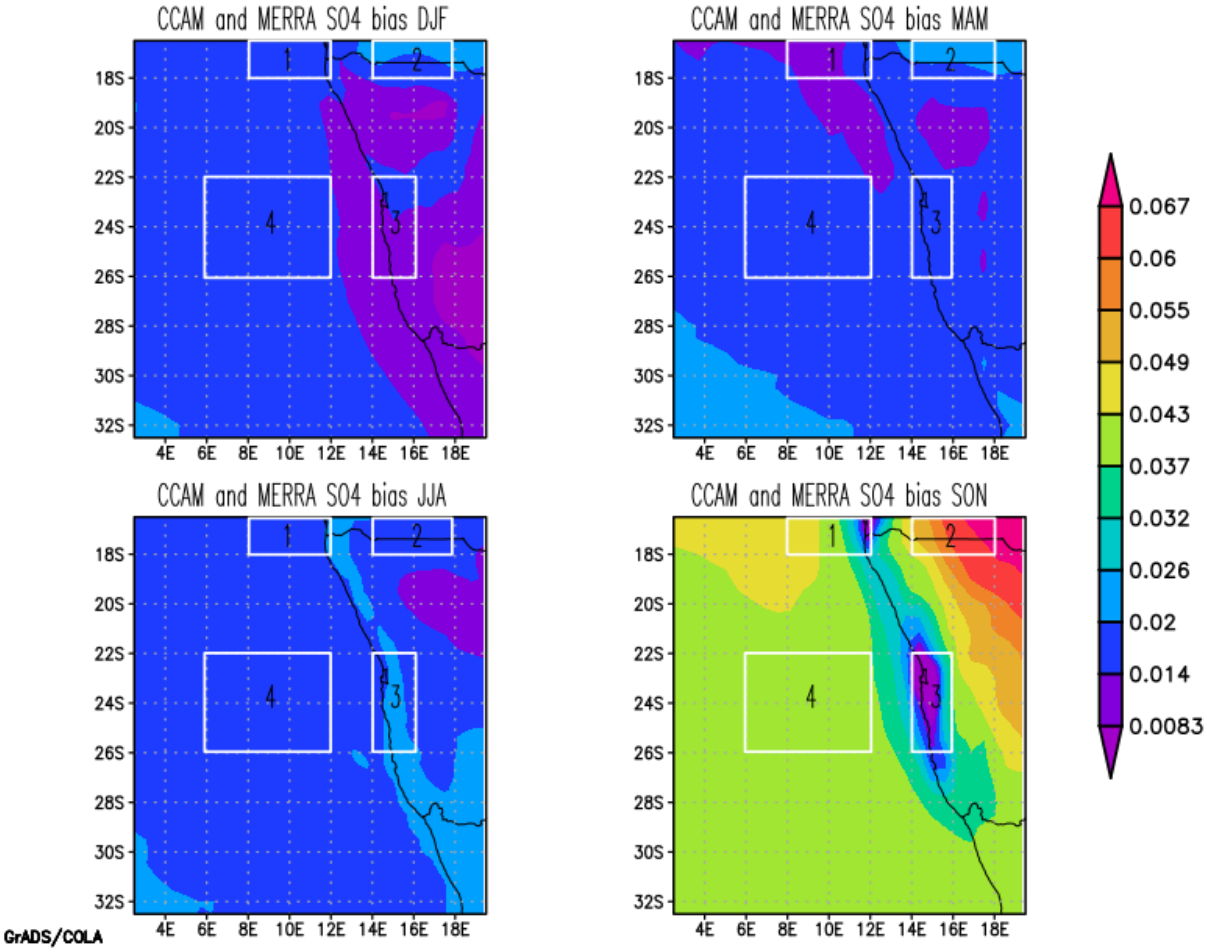

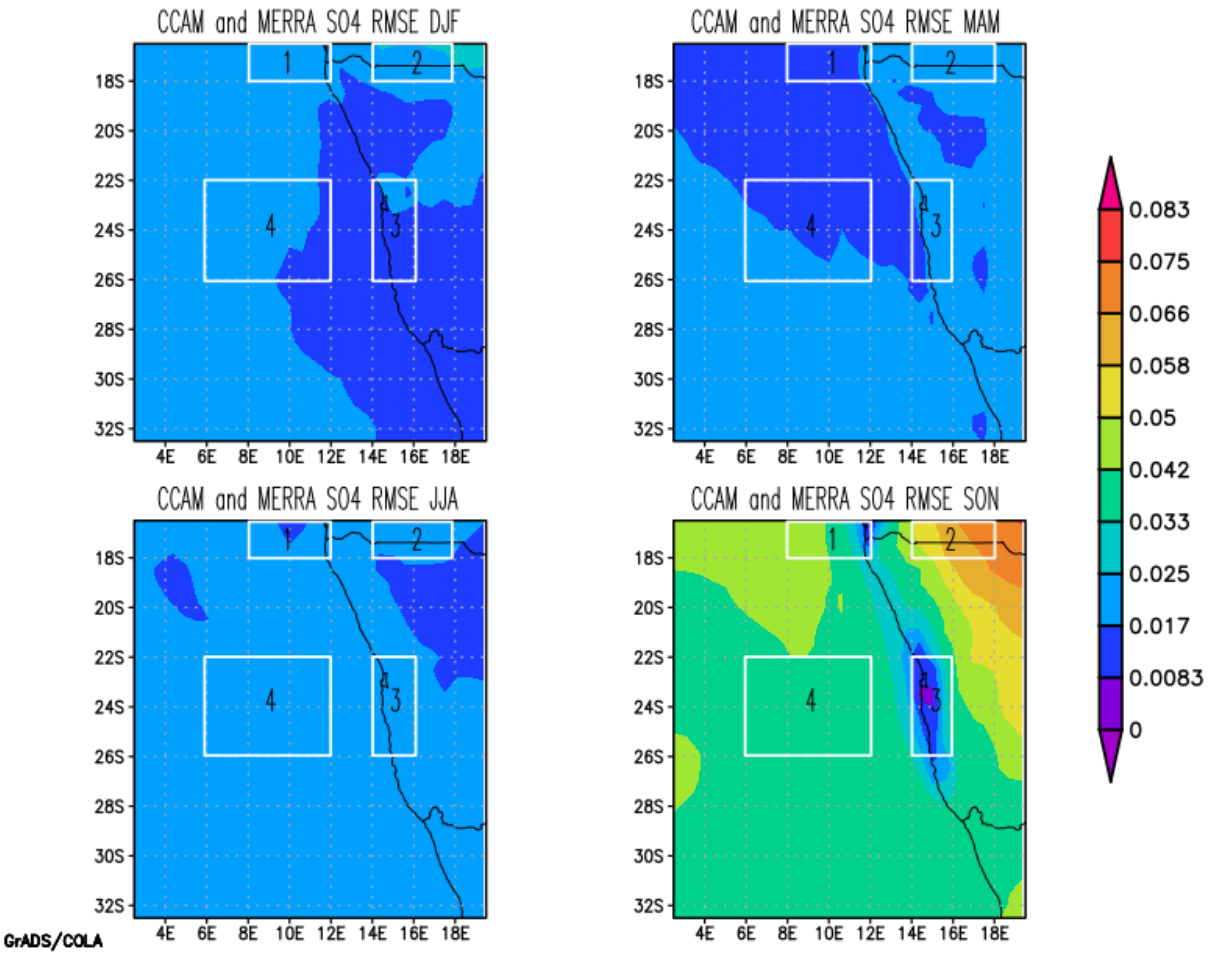
CCAM and MERRA SO4 RMSE DJF
CCAM and MERRA SO4 RMSE MAM
CCAM and MERRA SO4 RMSE JJA
CCAM and MERRA SO4 RMSE SON
18S
20S
22S
24S
26S
28S
30S
32S
4E
6E
8E
10E
12E
14E
16E
18E
1
2
3
4
0.083
0.075
0.066
0.058
0.05
0.042
0.033
0.025
0.017
0.0083
0
GrADS/COLA

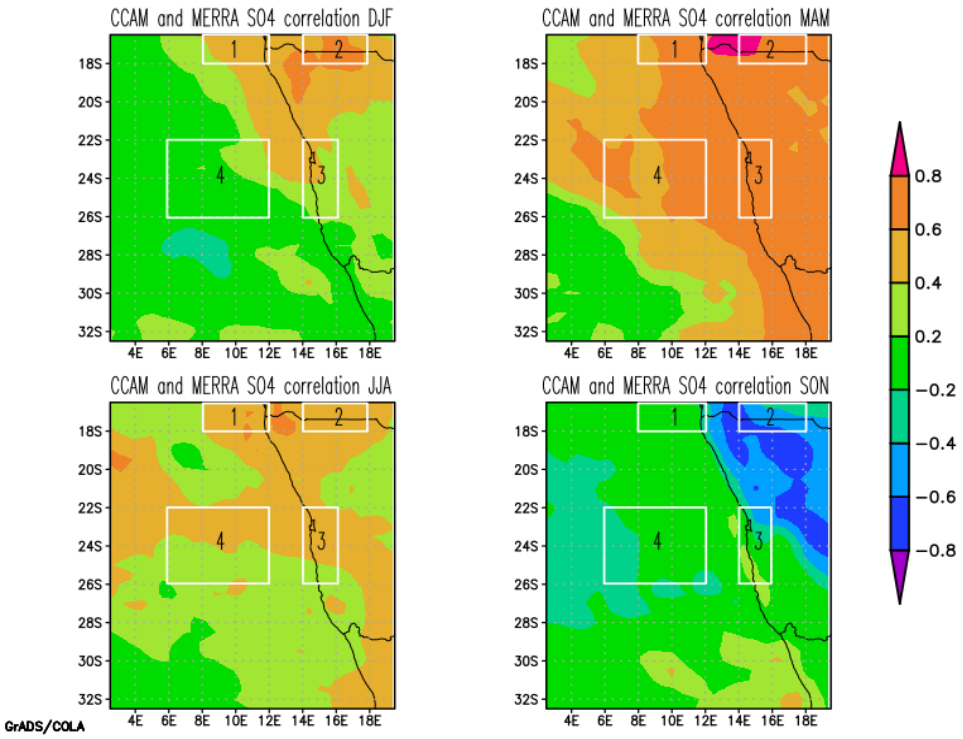

Figure 4.11: The multi-year (2002-2017) averaged bias (top), RMSE (middle) and correlation (bottom) of compositional AOD of sulphate between CCAM and MERRA

Fig. 4.11 shows multi-year averaged statistical schemes of compositional AOD of sulphate between the CCAM simulations and reanalysis for the subdomains in all seasons. Subdomain 1 had a positive bias for compositional AOD of sulphate in all seasons. The magnitude of error for compositional AOD of sulphate calculated for subdomain 1 was higher (0.0083-0.033) in all seasons. Subdomain 1 had a moderate positive correlation for compositional AOD of sulphate in summer and winter, a strong positive correlation in autumn, and no correlation in spring.

Subdomain 2 had a positive bias for compositional AOD of sulphate in all seasons. The magnitude of error for compositional AOD of sulphate calculated for subdomain 2 was higher (0.017-0.042) in all seasons. Subdomain 2 had a strong positive correlation for compositional AOD of sulphate in summer and autumn, a moderate positive correlation in winter, and no correlation in spring.

Subdomain 3 had a positive bias for compositional AOD of sulphate in all seasons. The magnitude of error for compositional AOD of sulphate calculated for subdomain 3 was higher (0.0083-0.025) in all seasons. Subdomain 3 had a weak positive correlation for compositional AOD of sulphate in summer, a strong positive correlation in autumn, moderate positive correlation in winter, and no correlation in spring.

Subdomain 4 had a positive bias for compositional AOD of sulphate in all seasons. The magnitude of error for compositional AOD of sulphate calculated for subdomain 4 was higher (0.0083-0.033) in all seasons. Subdomain 4 had no correlation for compositional AOD of sulphate in summer and spring, a strong positive correlation in autumn, and a moderate positive correlation in winter.

Results from both quantitative and qualitative analysis suggest that the CCAM simulations are similar to those of MERRA, although they are higher compared to MERRA. The magnitude simulated by the CCAM is higher compared to MERRA simulations. The southern region had the lowest AOD from both models. The spatial pattern simulated by the CCAM is similar compared to MERRA simulations for all seasons. The peaks simulated by the CCAM are similar to MERRA simulations. Peaks are simulated at the northern region in summer and spring. It was found that the CCAM overestimated compositional AOD of sulphate compared to MERRA. Also, the CCAM produced a lower magnitude of error in spring. Furthermore, the CCAM had a moderate positive correlation in autumn compared to MEERA. CCAM had a moderate negative correlation over land in spring.

4.2.6 Compositional AOD: Sea salt

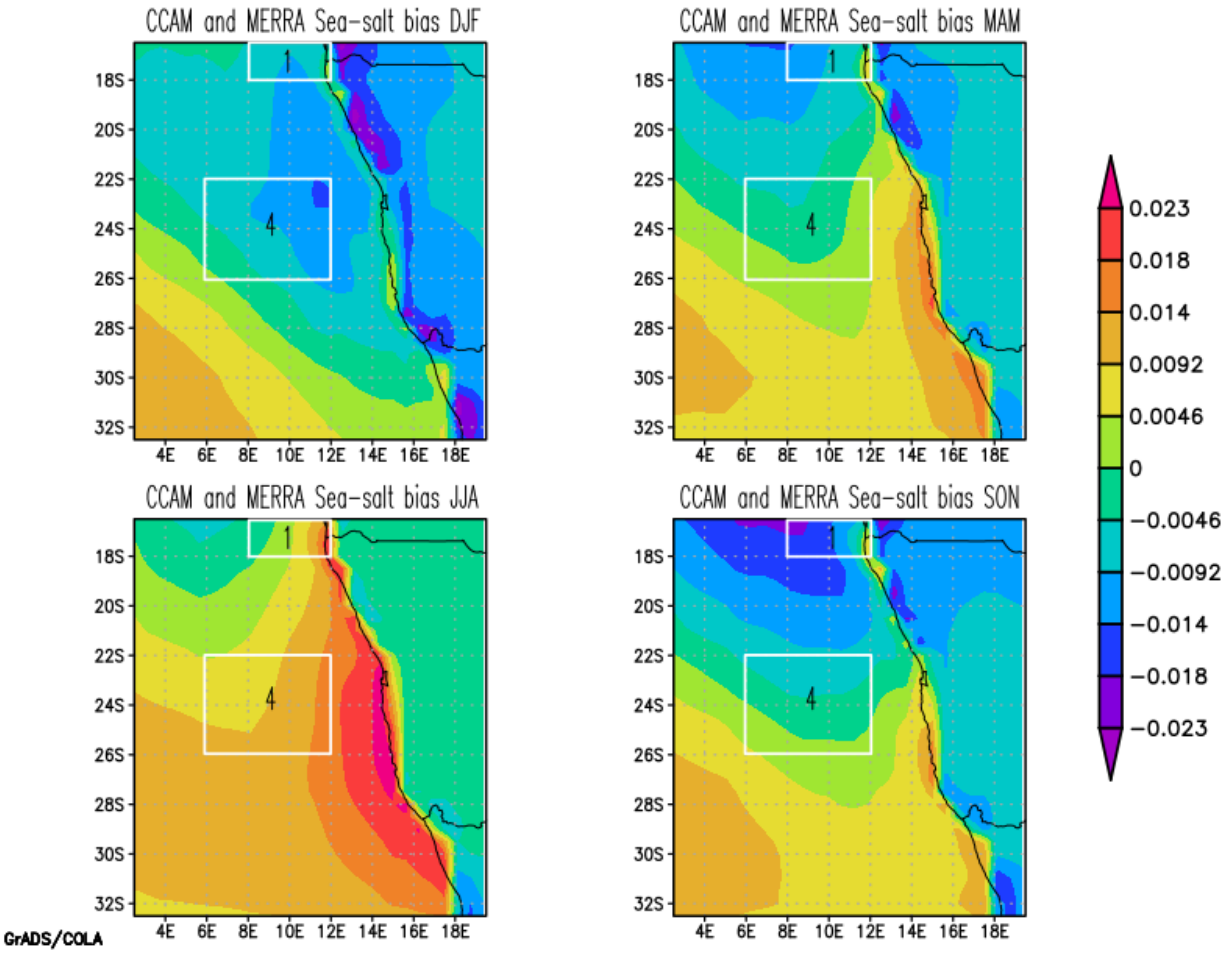

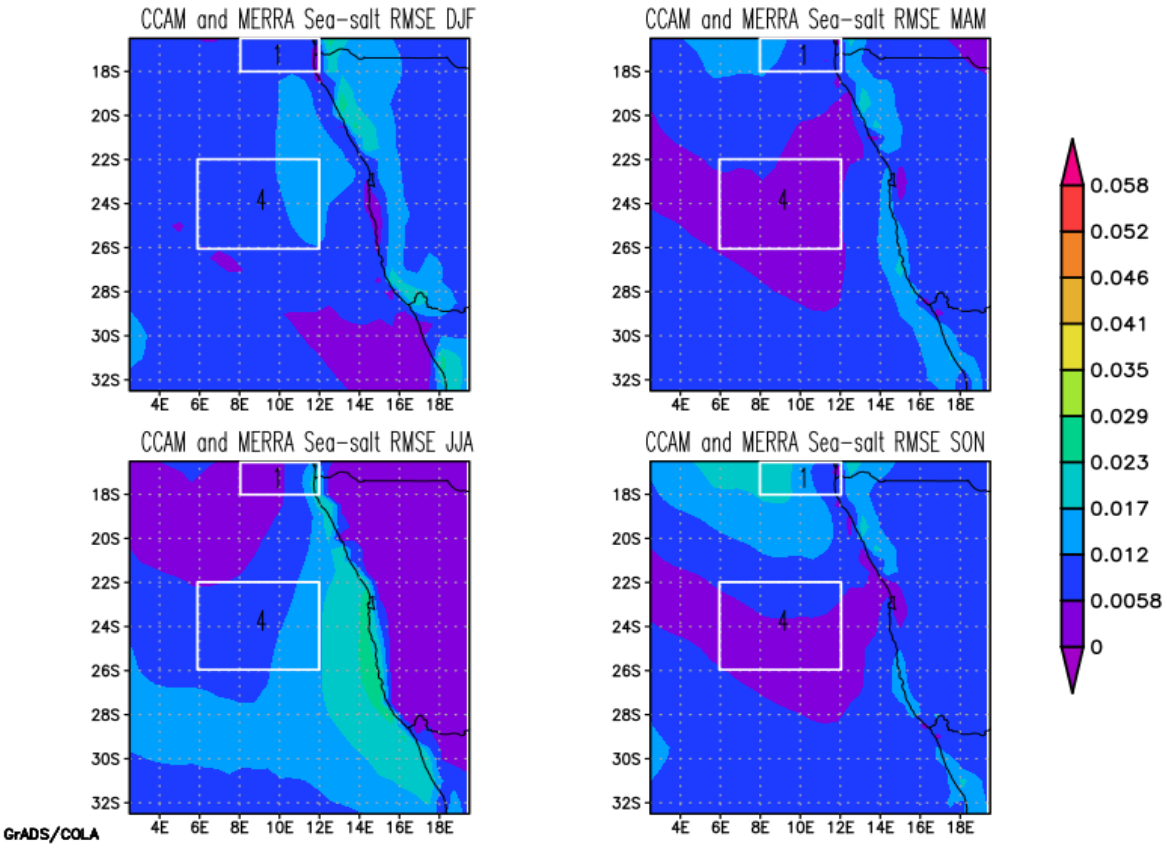
CCAM and MERRA Sea-salt RMSE DJF
CCAM and MERRA Sea-salt RMSE MAM
CCAM and MERRA Sea-salt RMSE JJA
CCAM and MERRA Sea-salt RMSE SON
18S
20S
22S
24S
26S
28S
30S
32S
4E
6E
8E
10E
12E
14E
16E
18E
1
4
0.058
0.052
0.046
0.041
0.035
0.029
0.023
0.017
0.012
0.0058
0
GrADS/COLA

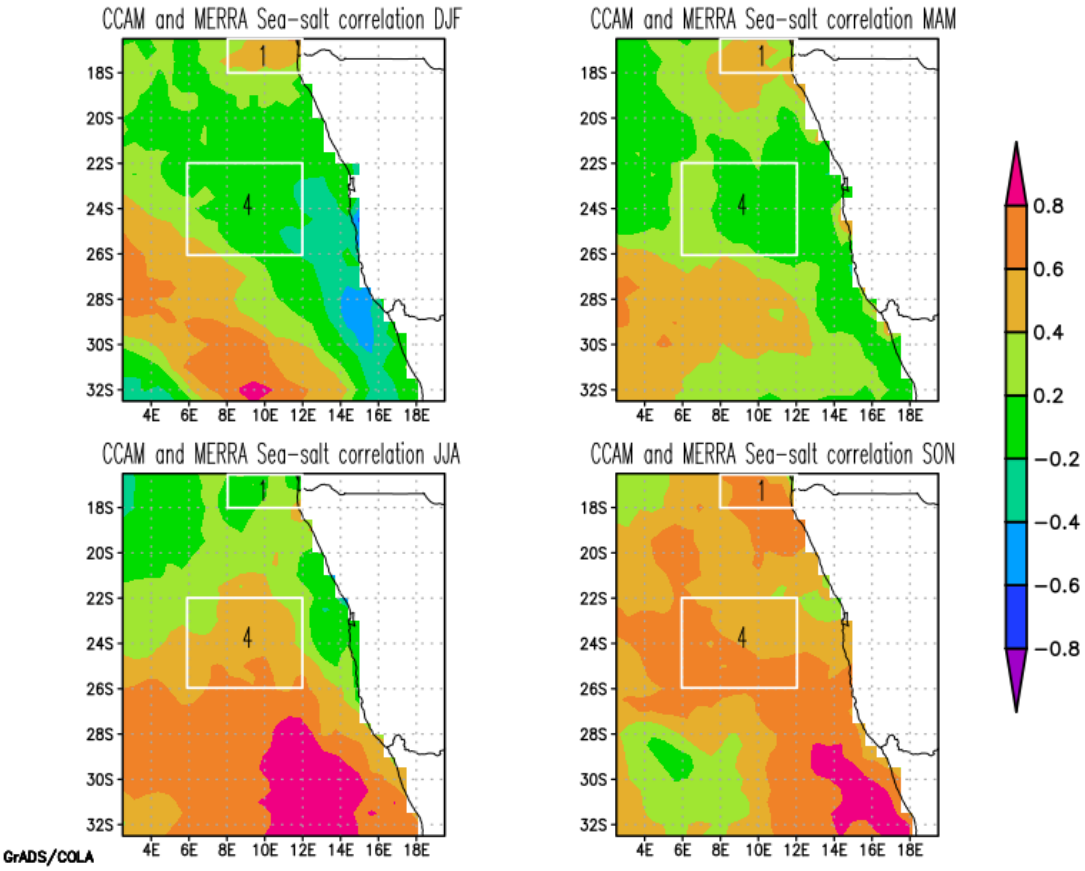

Figure 4.12: The multi-year (2002-2017) averaged bias (top), RMSE (middle) and correlation (bottom) of compositional AOD of sea-salt between CCAM and MERRA

Fig. 4.12 shows multi-year averaged statistical schemes of compositional AOD of sea-salt between the CCAM simulations and reanalysis for the subdomains in all seasons. Subdomain 1 had a negative bias for compositional AOD of sea-salt in summer, autumn and spring, and a positive bias in winter. The magnitude of error for compositional AOD of sea-salt calculated for subdomain 1 was higher (0.0058-0.017) in all seasons. Subdomain 1 had a moderate positive correlation for compositional AOD of sea-salt in summer and autumn, a weak positive correlation in winter, and a strong positive correlation in spring.

Subdomain 4 had a negative bias for compositional AOD of sea-salt in summer, autumn and spring, and positive bias in winter. The magnitude of error for compositional AOD of sea-salt calculated for subdomain 4 was lower (0-0.0058) in autumn and spring, and

higher (0.0058-0.012) in summer and winter. Subdomain 4 had no correlation for compositional AOD of sea-salt in summer and autumn, moderate positive correlation in winter, and a strong positive correlation in spring.

Results from both quantitative and qualitative analysis suggest that the CCAM simulations are different to those of MERRA, probably due to how they simulate sea salt. Simulated CCAM sea salt depicts two ranges of magnitude, while MERRA simulations show multiple degrees of magnitude arising at different parts of the domain. The spatial pattern simulated by the CCAM is not the same compared to MERRA simulations for all seasons. The peaks simulated by the CCAM are not similar to MERRA simulations. It was found that the CCAM underestimated the compositional AOD of sea salt except in winter. Also, the CCAM produced a higher magnitude of error except in the fourth subdomain of autumn and spring. Furthermore, the CCAM had a moderate positive correlation in winter and spring. The CCAM had no correlation in the fourth subdomain in summer and autumn.

4.2.7 Summary

Statistical scores (bias, RMSE, correlation) between the CCAM simulations of total AOD and compositional AOD (i.e. black carbon, organic carbon, sulphate, small dust and sea salt) have been evaluated against MODIS observations and MERRA. Results suggest that Aerosol optical depths attributable to black carbon and organic carbon were underestimated by the CCAM, particularly in areas where the maximum magnitude was simulated across all seasons. The highest magnitude of error occurs in areas where the maximum magnitude was simulated across all seasons, indicating that the CCAM has the largest errors over the peak areas. There is a positive correlation indicating that there is a linear association with how the CCAM simulates aerosols compared to MODIS or MERRA. Aerosol optical depth attributable to sulphate was overestimated by the CCAM, especially where the maximum magnitude was simulated across all seasons. The magnitude of error was low. Dust aerosols (i.e. small dust) and marine aerosols (i.e. sea salt) were underestimated by the CCAM, particularly in areas where the maximum magnitude was simulated across all seasons. The lower the magnitude of error, the more precise the CCAM is to the observed MODIS value. To get a broader view on aerosol

magnitude and spatial patterns, it is recommended that the CCAM and MERRA should be compared to ground/airplane measurements AOD (i.e. AERONET).

4.3 Seasonal cycles between the CCAM and MODIS or MERRA

This section presents the results of the CCAM simulations and MODIS observations. We evaluated the interannual seasonality (summer (December-January-February), autumn (March-April-May), winter (June-July-August) and spring (September-October-November)) from the CCAM simulations against observed total AOD and compositional AOD (i.e. black carbon, organic carbon, small dust, sulphate and sea salt) and MODIS observations or MERRA. To carry out the analysis, the timeseries of the seasonal cycles between CCAM simulations and MODIS observations and MERRA over the four domains are compared.

4.3.1 Total aerosol optical depth

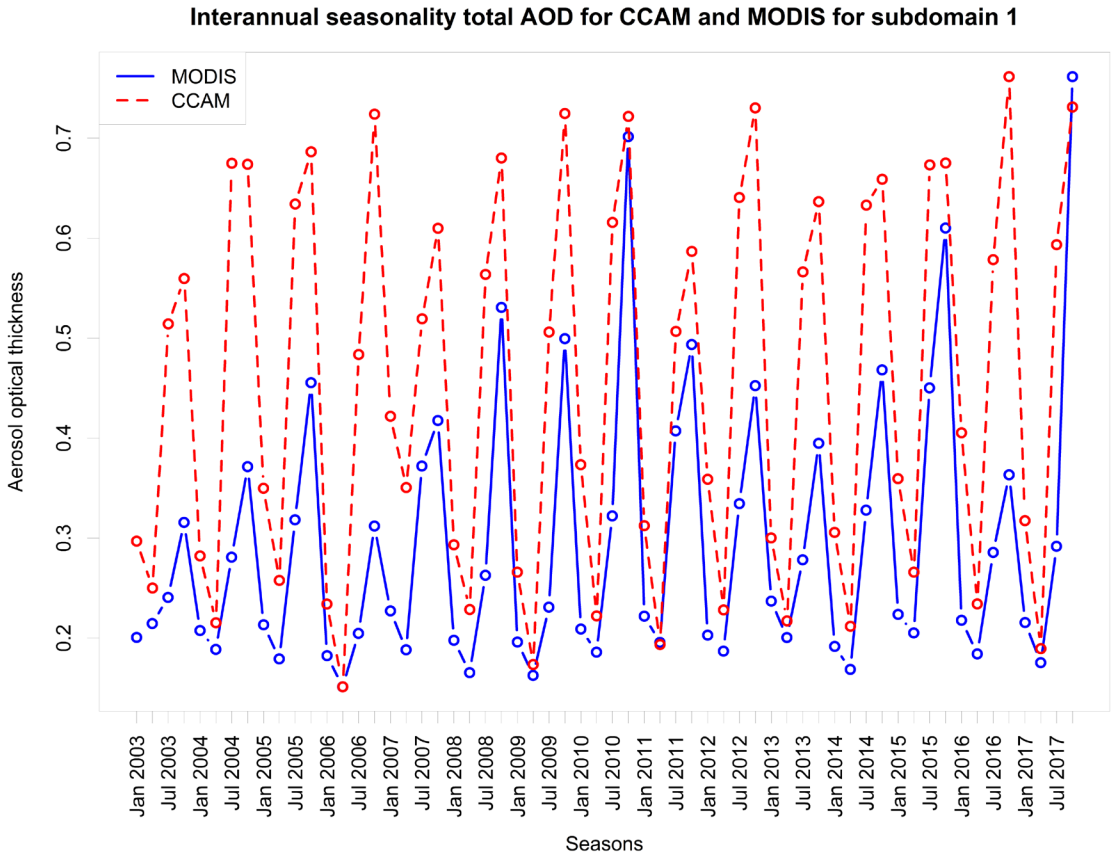

Figure 4.13: Area-averaged interannual seasonality of total AOD between CCAM simulations and MODIS observations for subdomain 1

Across all domains, the interannual seasonality of total AOD in the CCAM peaks in spring and MODIS also peaks in spring (Fig. 4.13). There are some exceptions, and these vary across the subdomains (see Fig. 4.13a, 4.13b and 4.13c in **Annexure A**). For example, in the third subdomain, the CCAM seasonal cycle of total AOD peaks in spring, except in 2007, where it peaked in summer, while MODIS' seasonal cycle peaks in spring, except 2004, where it was winter, and 2009, 2010 and 2016, where it was summer (Fig. 4.13b). The total AOD has its minimum in autumn for the CCAM as well as for MODIS.

4.3.2 Compositional AOD: Black carbon

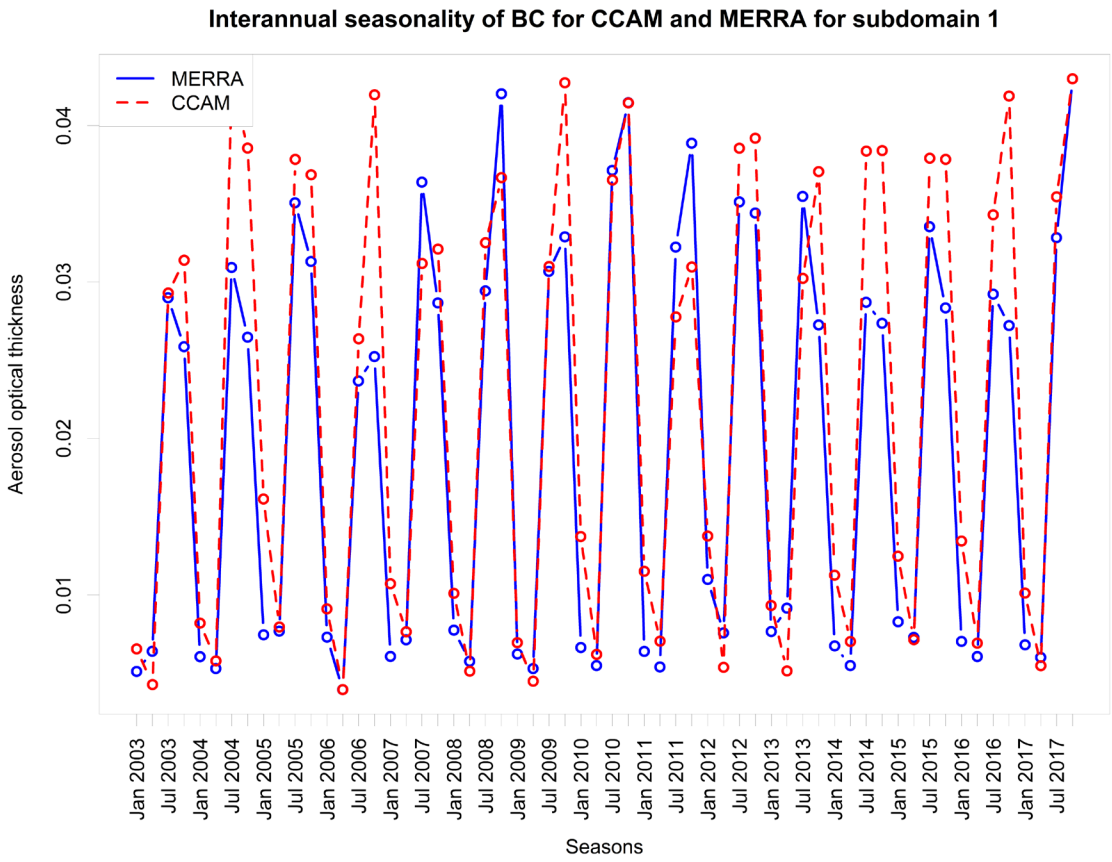

Figure 4.14: Area-averaged interannual seasonality of compositional AOD of black carbon between CCAM simulations and MERRA for subdomain 1

Across all domains, the interannual seasonality of compositional AOD of black carbon in the CCAM peaks in spring and MERRA peaks in spring as well (Fig. 4.14). There are some exceptions, and these vary across the subdomains (see Fig. 4.14a, 4.14b and 4.14c in **Annexure A**). For example, in the second subdomain, the CCAM seasonal cycle of compositional AOD of black carbon peaks in spring, except in 2015, where it peaked in winter, while MERRA's seasonal cycle peaks in spring, except in 2013 and 2015, when it peaked in winter (Fig. 4.14a). The compositional AOD of black carbon has its minimum in autumn for the CCAM as well as for MERRA. The main source of black carbon in the Benguela Region is biomass burning and it occurs between June and October, which is in spring.

4.3.3 Compositional AOD: Organic carbon

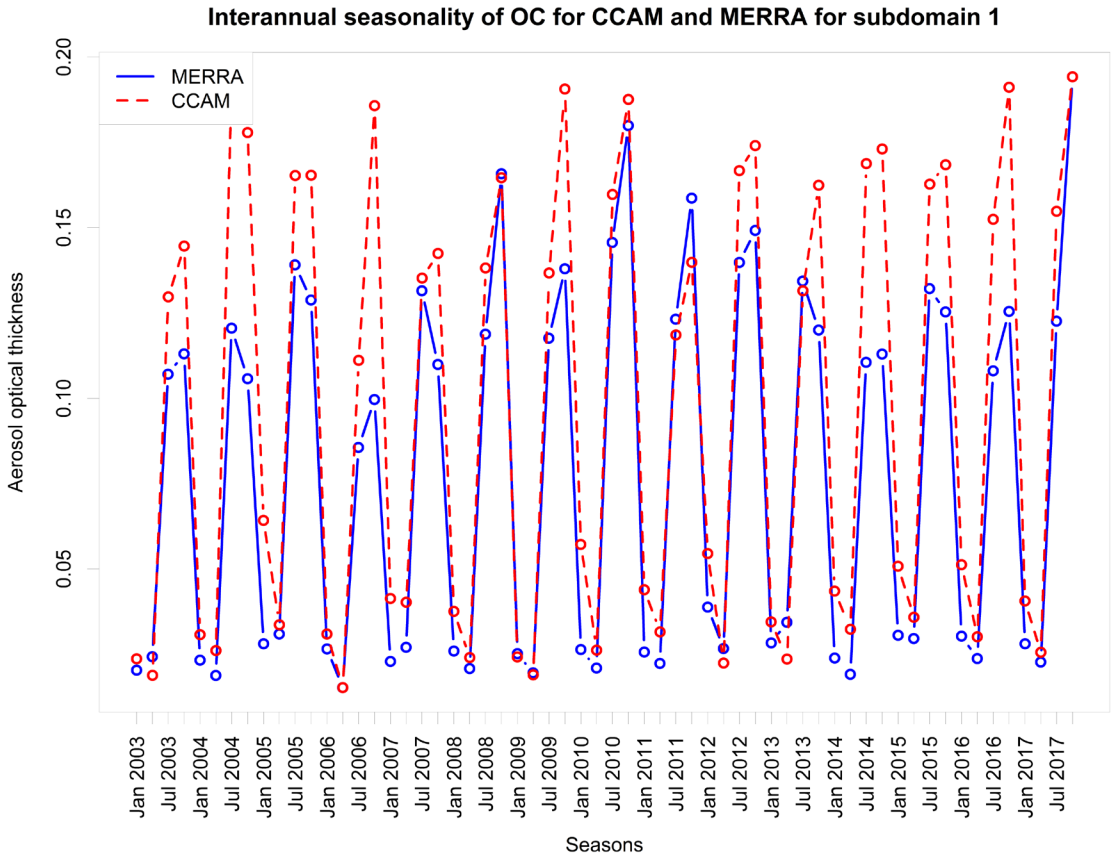

Figure 4.15: Area-averaged interannual seasonality of compositional AOD of organic carbon between CCAM simulations and MERRA for subdomain 1

Across all domains, the interannual seasonality of compositional AOD of organic carbon in the CCAM peaks in spring and MERRA peaks in spring as well (Fig. 4.15). There are some exceptions, and these vary across the subdomains (see Fig. 4.15a, 4.15b and 4.15c in **Annexure A**). For example, in the fourth subdomain, the MERRA seasonal cycle of compositional AOD of organic carbon peaks in spring, except in 2008 and 2009, when it peaked in winter (Fig. 4.15c). The compositional AOD of organic carbon has its minimum in autumn for the CCAM as well as for MERRA. The main source of organic carbon in the Benguela Region is biomass burning and it occurs between June and October, which is in spring.

4.3.4 Compositional AOD: Small dust

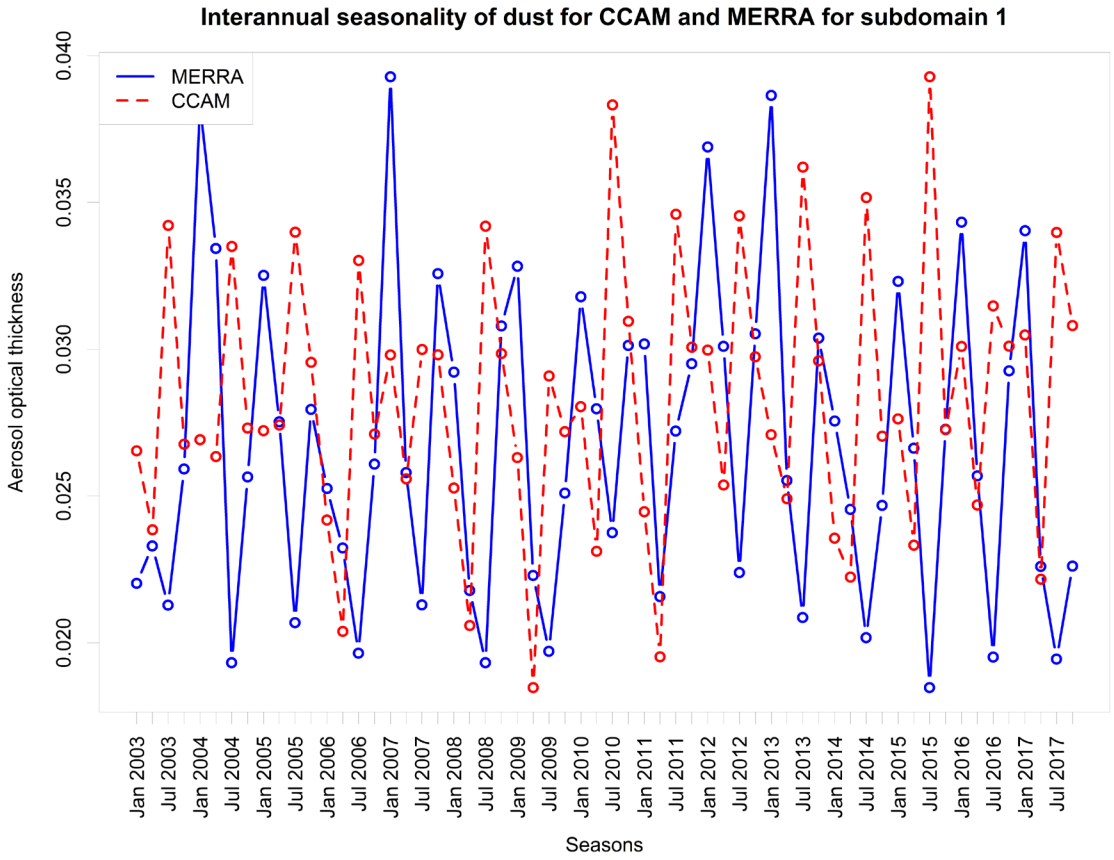

Figure 4.16: Area-averaged interannual seasonality of compositional AOD of small dust between CCAM simulations and MERRA for subdomain 1

Across all domains, the interannual seasonality of compositional AOD of small dust in the CCAM peaks in winter and MERRA peaks in summer (Fig. 4.16). There are some exceptions, and these vary across the subdomains (see Fig. 4.16a, 4.16b and 4.16c in **Annexure A**). For example, in the second subdomain, the MERRA seasonal cycle of compositional AOD of small dust peaks in summer, except in 2003 (Fig. 4.16a). The compositional AOD of small dust has its minimum in autumn for CCAM and winter for MERRA. This finding highlights that further research is needed to better understand the seasonal cycle and contribution of dust to the aerosol loading in this area.

4.3.5 Compositional AOD: Sulphate

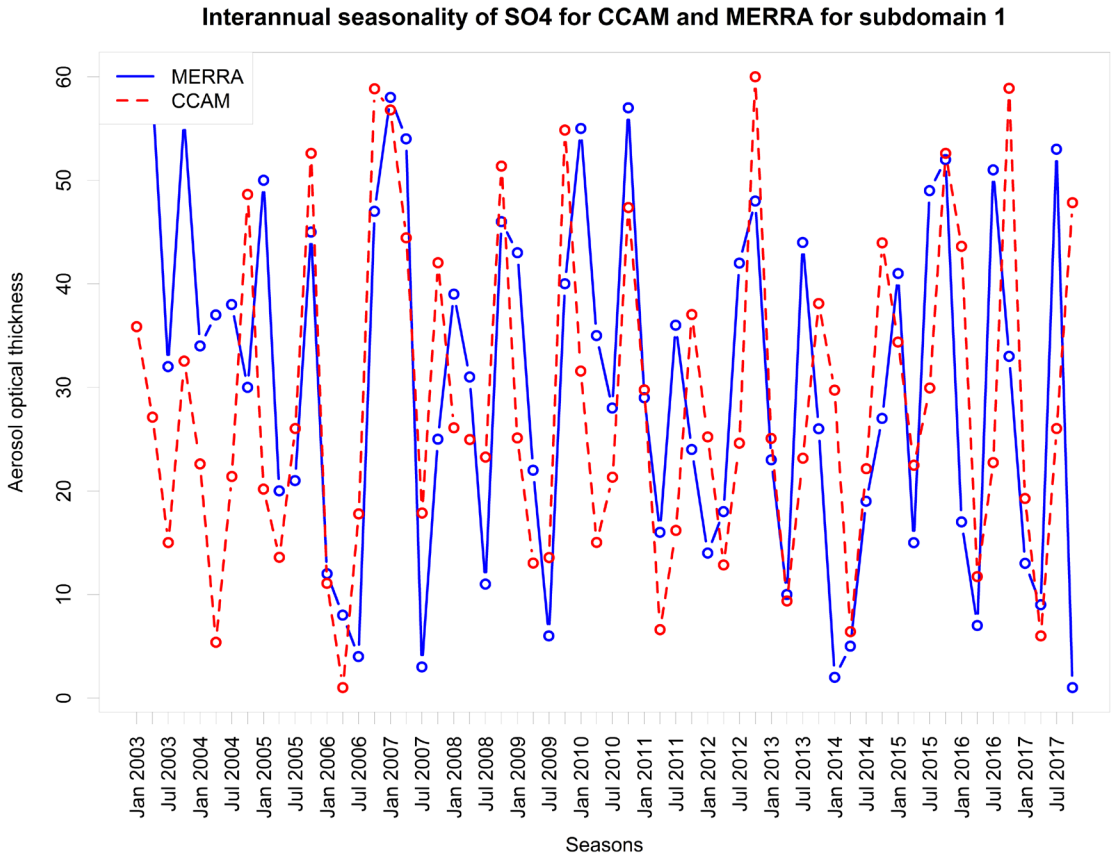

Figure 4.17: Area-averaged interannual seasonality of compositional AOD of sulphate between CCAM simulations and MERRA for subdomain 1

Across all domains, the interannual seasonality of compositional AOD of sulphate in the CCAM peaks in spring and MERRA peaks are not consistent in one season, but vary with peaks in winter, summer and spring (Fig. 4.17). There are some exceptions, and these vary across the subdomains (see Fig. 4.17a, 4.17b and 4.17c in **Annexure A**). The MERRA peaks in these three seasons over the study period (2002-2017) and they have equal numbers of peaks. The compositional AOD of sulphate has its minimum in autumn for the CCAM and summer, autumn and winter for MERRA. This highlights the potential complexity of the sulphate seasonal cycle. Measurements of compositional AOD of sulphate across this domain are needed to be compared to CCAM and MERRA.

4.3.6 Compositional AOD: Sea salt

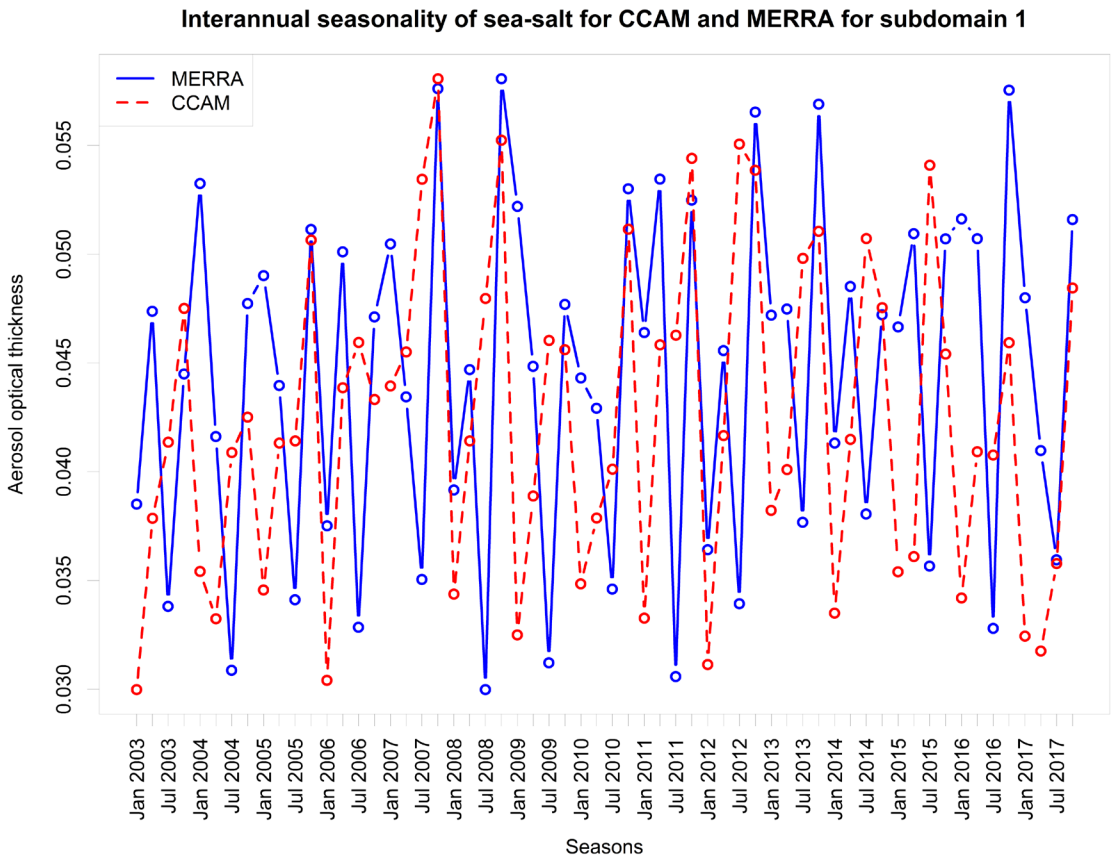

Figure 4.18: Area-averaged interannual seasonality of compositional AOD of sea salt between CCAM simulations and MERRA for subdomain 1

Across all domains, the interannual seasonality of compositional AOD of sea salt in the CCAM peaks in winter and spring, which differs from MERRA, as MERRA peaks in spring and summer (Fig. 4.18). The compositional AOD of sea salt has its minimum in summer for the CCAM and winter for MERRA (see Fig. 4.18a in **Annexure A**). The models simulate sea salt differently. In the CCAM, sea salt above the ocean's surface is diagnosed at each time step and as a function of wind speeds at 10 m. However, sea salt does not depend on wind speeds alone as the model is parametrised, but also on other atmospheric and oceanic parameters such as temperature, salinity and wave properties

(Grythe *et al.*, 2014). The temperature of ocean water has effects on surface tension, density and viscosity of water, which impact the production of sea salt through wave breaking (Grythe *et al.*, 2014). Salinity influences surface tension and density, which are responsible for the number of whitecaps produced (Grythe *et al.*, 2014). In addition, the amount of sea salt found in a sea-spray droplet and released depends on salinity. Wave properties such as wave direction, height and shape influence sea salt production (Grythe *et al.*, 2014). The model used to source data for assimilation for MERRA uses emissions inventory as well as aerosol schemes.

4.3.7 Summary

We evaluated interannual seasonality between the CCAM simulations of total AOD and compositional AOD (i.e. black carbon, organic carbon, sulphate, small dust and sea salt) against MODIS observations and MERRA. Results suggest that AOD attributable to black carbon and organic carbon has a peak interannual seasonality in spring and has the minimum in autumn in the CCAM, MODIS and MERRA. As stated above, biomass burning occurs between June and October in southern Africa, and therefore the maximum falls within the spring season. Dust aerosols (i.e. small dust) have different interannual seasonal peaks when simulated in the CCAM and MERRA. Marine aerosols (i.e. sea salt) have different interannual seasonal peaks when simulated in the CCAM and MERRA. Sea salt was expected to be different compared to MERRA because it is a diagnosed variable in the CCAM. The differences were profoundly clear, and it would be recommended to incorporate it in prognostic variables.

CHAPTER 5: INTERACTIONS BETWEEN AEROSOLS AND CLOUD PROPERTIES SIMULATED BY CCAM

This chapter presents the spatial and seasonal variations of the CCAM simulations of aerosols and cloud properties against satellite observations over the Benguela Region. Firstly, comparisons of spatial variation between CCAM simulations, and AIRS observations (for cloud fraction) and MODIS observations (for liquid water path) are performed using the eyeball verification method to determine the magnitude and spatial patterns. Secondly, statistical scores were calculated to quantify the comparison of spatial variation using bias, RMSE and correlation. Thirdly, the linear association between total AOD and compositional AOD (i.e. black carbon, organic carbon, sulphate, small dust and sea salt), and cloud properties (cloud fraction and liquid water path) using the CCAM model was determined. The first and fourth subdomains are the only used subdomains in this section because they consist of both the aerosols and marine stratocumulus.

The analysis methods applied are the eyeball verification method, bias, RMSE and correlation. Bias is formulated as CCAM minus AIRS or CCAM minus MODIS. The map colour bar scale of RMSE shares the same map colour bar scale of the spatial maps that were used for magnitude (eyeball verification method). Keeping the map colour bar scale the same made it easier to see by what size the CCAM simulations did differ from satellite observations.

5.1 Magnitude of cloud fraction between CCAM and AIRS

This section presents the results of the CCAM simulations and AIRS (ascending and descending) observations for cloud fraction. We evaluated the spatial variation from the CCAM simulations against observed cloud fractions from AIRS (ascending and descending) observations. To carry out the analysis, the eyeball verification method is used to compare the magnitude and spatial pattern between the CCAM simulations and AIRS (ascending and descending) observations. The first focus is magnitude, followed by

spatial patterns over the two subdomains. AIRS ascending passes across the equator at approximately 13:30 local solar time from south to north, and AIRS descending passes across the equator at approximately 01:30 local solar time from north to south. Due to the different passing times, the observed measurements are different. As such, AIRS ascending and AIRS descending are evaluated against the CCAM separately; and they are all averaged to multi-year seasonal temporal resolutions.

5.1.1 CCAM vs AIRS (ascending vs descending)

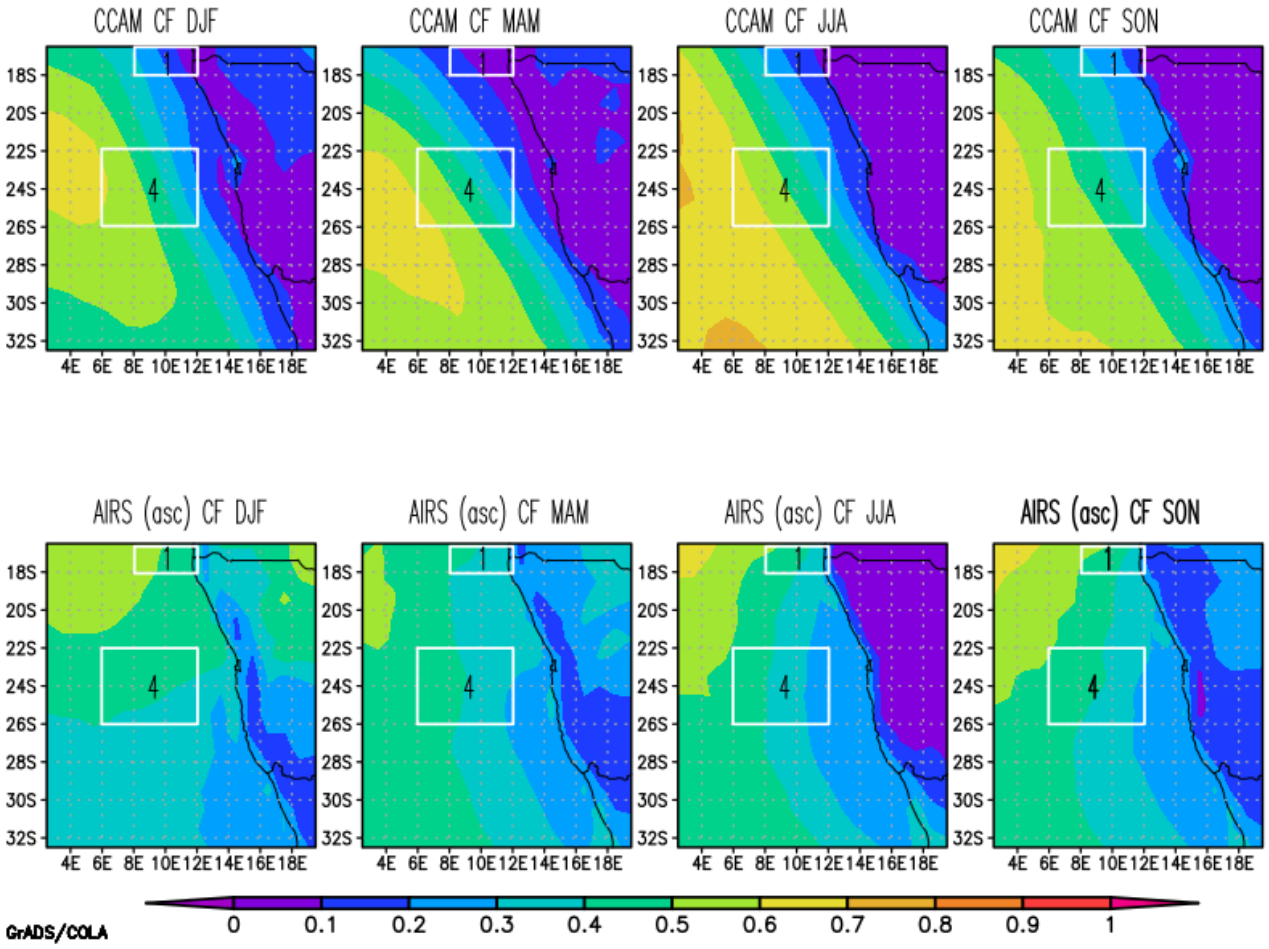

Figure 5.1: The multi-year (2002-2017) averaged magnitude of simulated CCAM (top) and measured AIRS (ascending) (bottom) cloud fraction over the Benguela Region

Fig. 5.1 and Fig. 5.2 show multi-year averaged magnitudes of cloud fraction for CCAM simulations and AIRS (ascending) and AIRS (descending) observations for all seasons. The magnitude of cloud fraction simulated by the CCAM is higher (0-0.9) compared to observations by AIRS (ascending) (0-0.7) for all seasons over the whole domain. Previous research found that low-level cloud fractions exist in all seasons and there is less variability of low-level cloud fraction within seasons over this study domain from using satellite observations (Adebiyi *et al.*, 2015; Zuidema, *et al.*, 2016). Estimated cloud fractions over this region range between 50 and 75% (Muhlbauer *et al.*, 2014). Higher cloud fractions are simulated over the ocean, and it decreases towards the coast in CCAM simulations, while AIRS (ascending) and AIRS (descending) observed higher cloud fractions at the northern region and lower at the south coast. Fig. 5.1 and Fig. 5.2 also show that cloud fractions simulated by the CCAM differ in magnitude from cloud fractions observed by AIRS (ascending) and AIRS (descending). The spatial pattern of cloud fraction becomes narrow as you approach the coast (0-0.7) as simulated by the CCAM compared to AIRS (ascending) and AIRS (descending) that the magnitude does not decrease as you approach the coast, but has higher magnitudes observed over the northern parts of the domain.

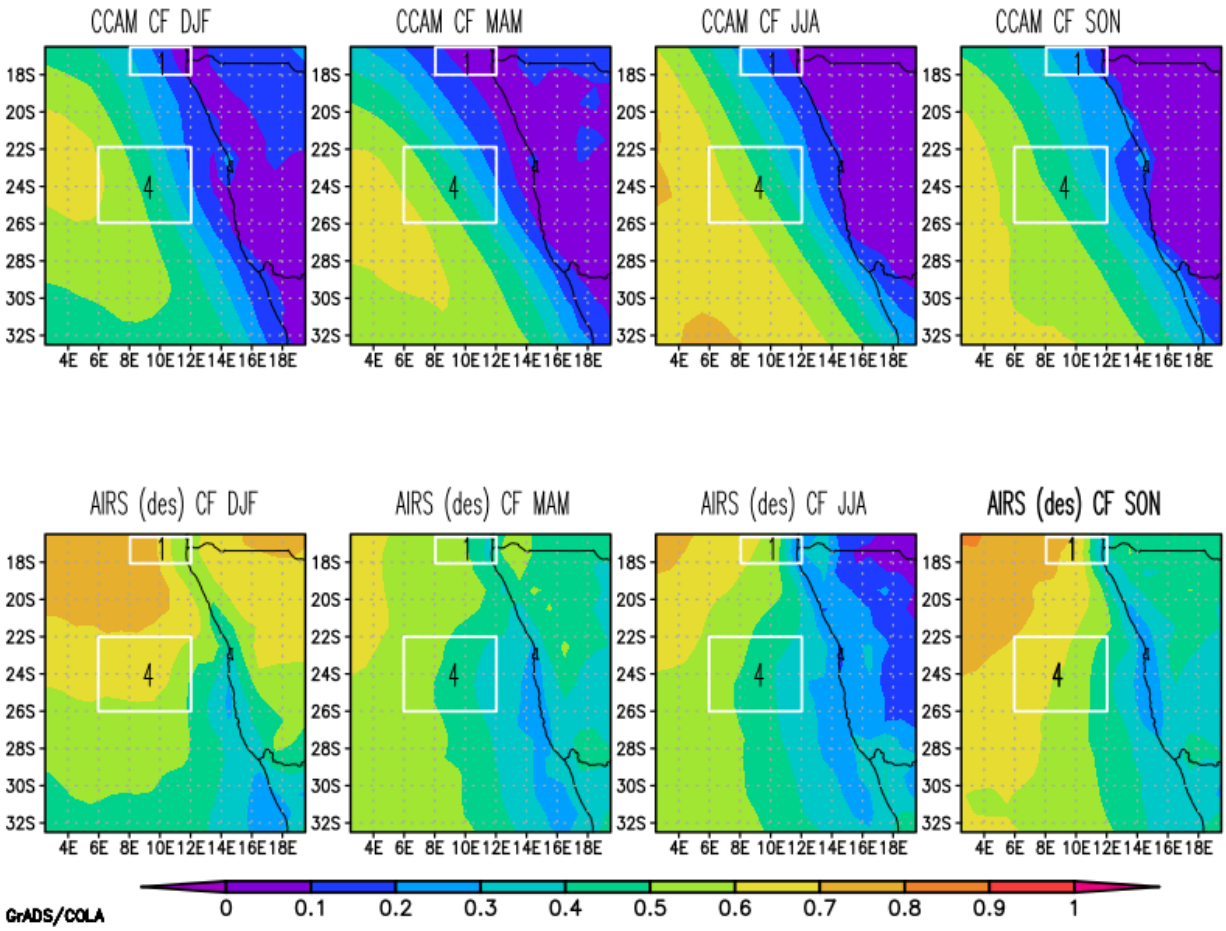

Figure 5.2: The multi-year (2002-2017) averaged magnitude of simulated CCAM (top) and measured AIRS (descending) (bottom) cloud fraction over the Benguela Region

5.2 Quantitative verification between CCAM and AIRS

This section presents the results of the CCAM simulations and AIRS observations for cloud fraction (CF). We evaluated the spatial variation from the CCAM simulations against observed cloud fractions from AIRS observations. To carry out the analyses, quantitative analyses (bias, RMSE and correlation) were used to evaluate the model. The first focus was bias, followed by RMSE, and lastly correlations over the two subdomains.

5.2.1 CCAM vs AIRS (ascending vs descending)

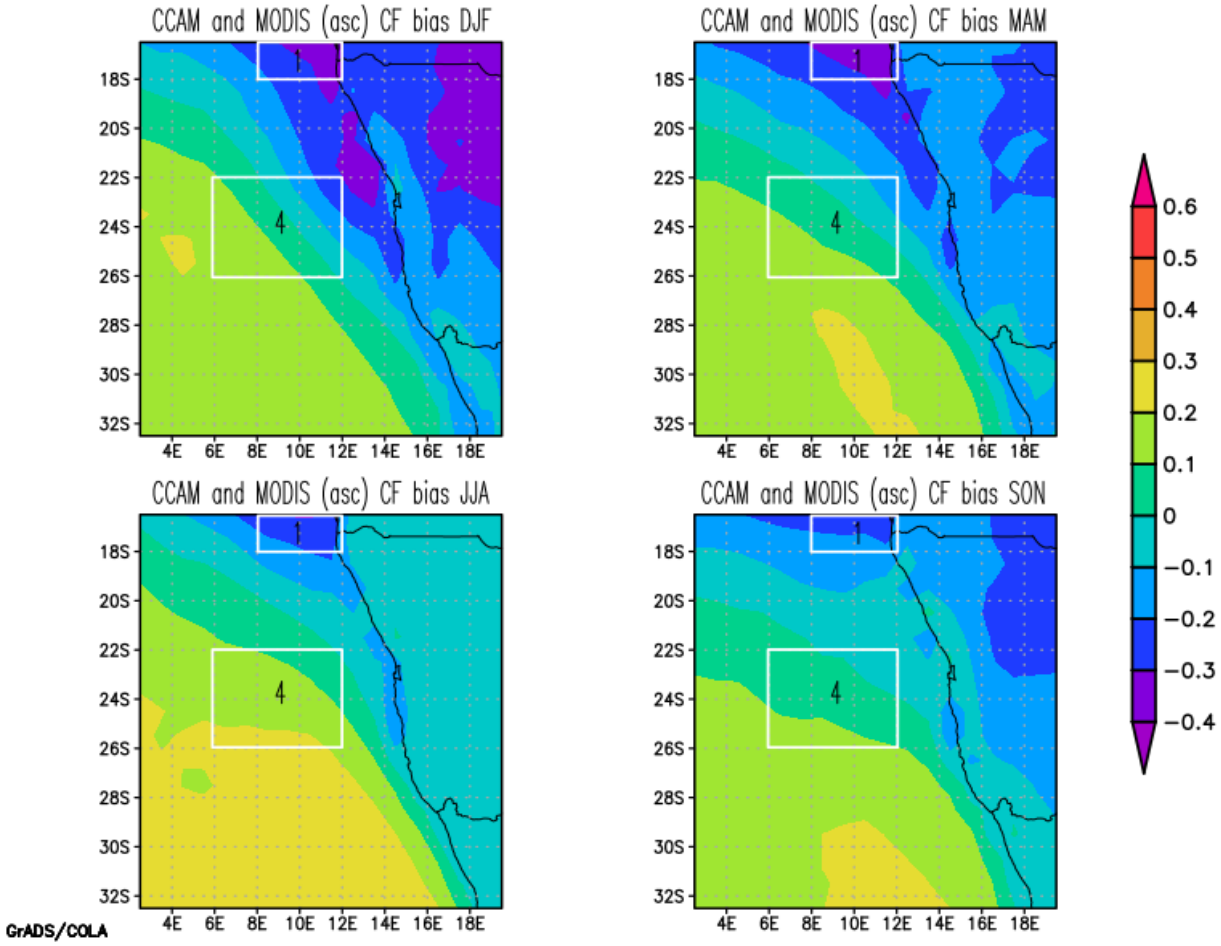

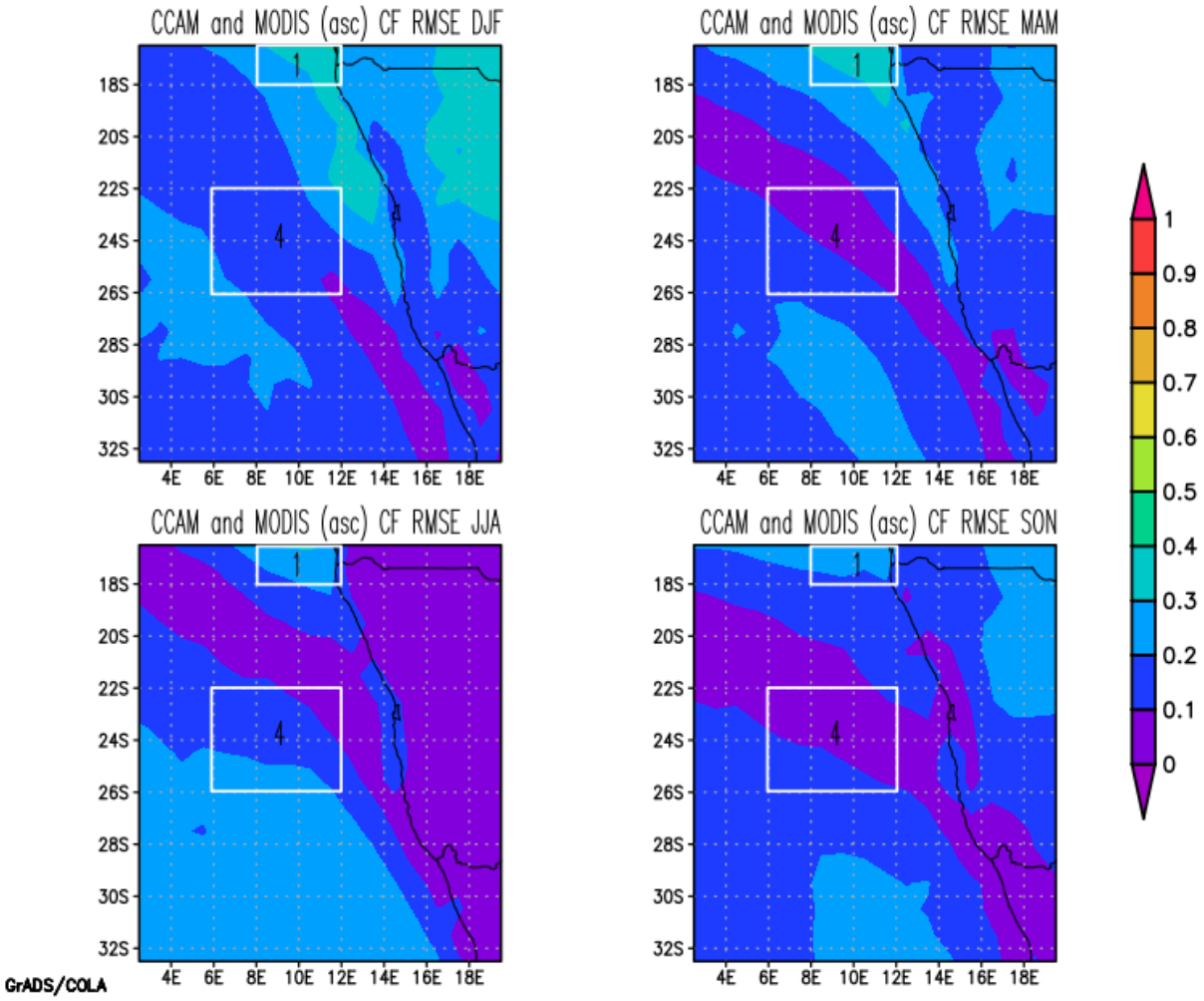
CCAM and MODIS (asc) CF RMSE DJF
CCAM and MODIS (asc) CF RMSE MAM
CCAM and MODIS (asc) CF RMSE JJA
CCAM and MODIS (asc) CF RMSE SON
1
4
18S
20S
22S
24S
26S
28S
30S
32S
4E
6E
8E
10E
12E
14E
16E
18E
1
0.9
0.8
0.7
0.6
0.5
0.4
0.3
0.2
0.1
0
GrADS/COLA

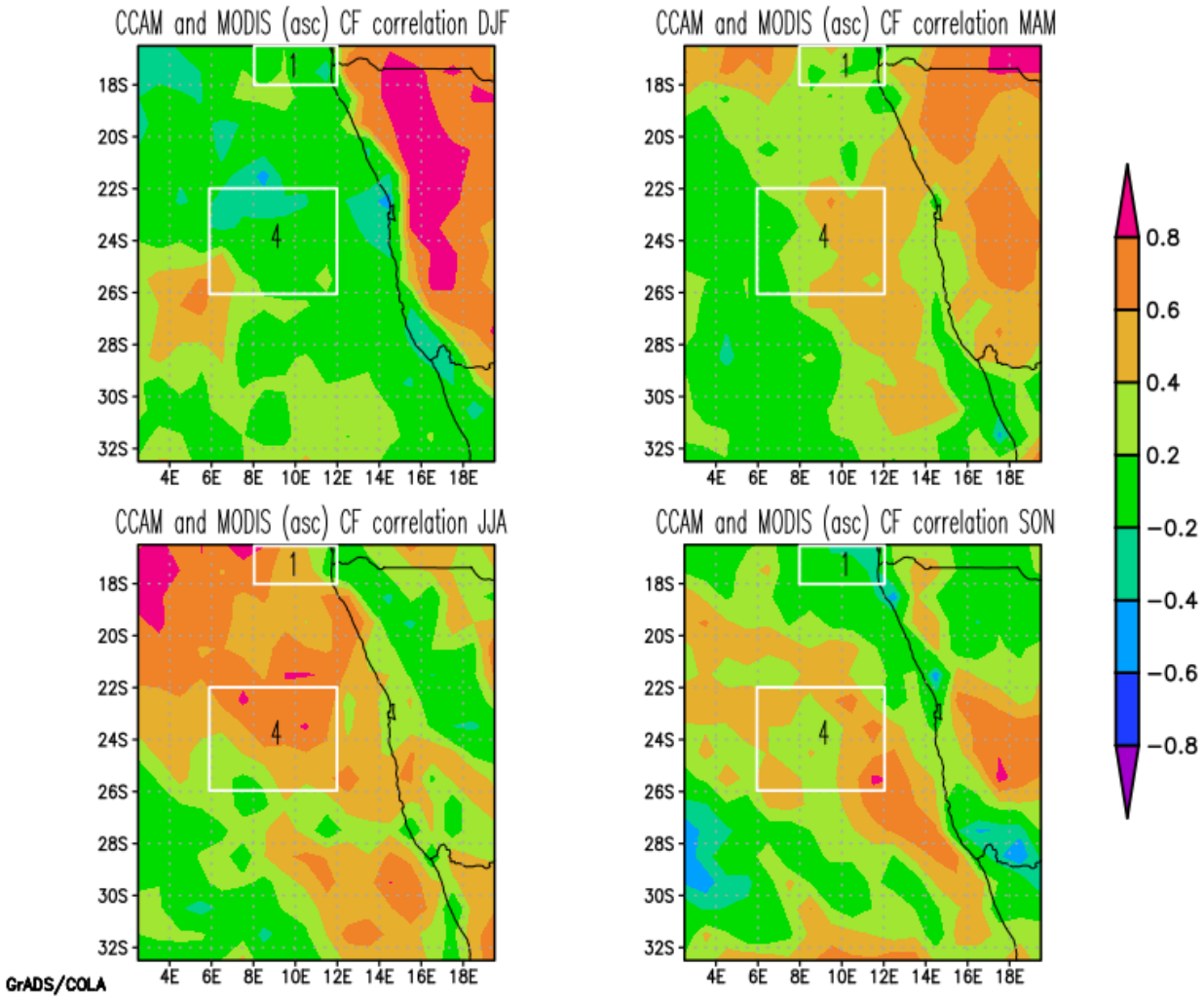

Figure 5.3: The multi-year (2002-2017) averaged bias (top), RMSE (middle) and correlation (bottom) of cloud fraction between the CCAM and AIRS (ascending)

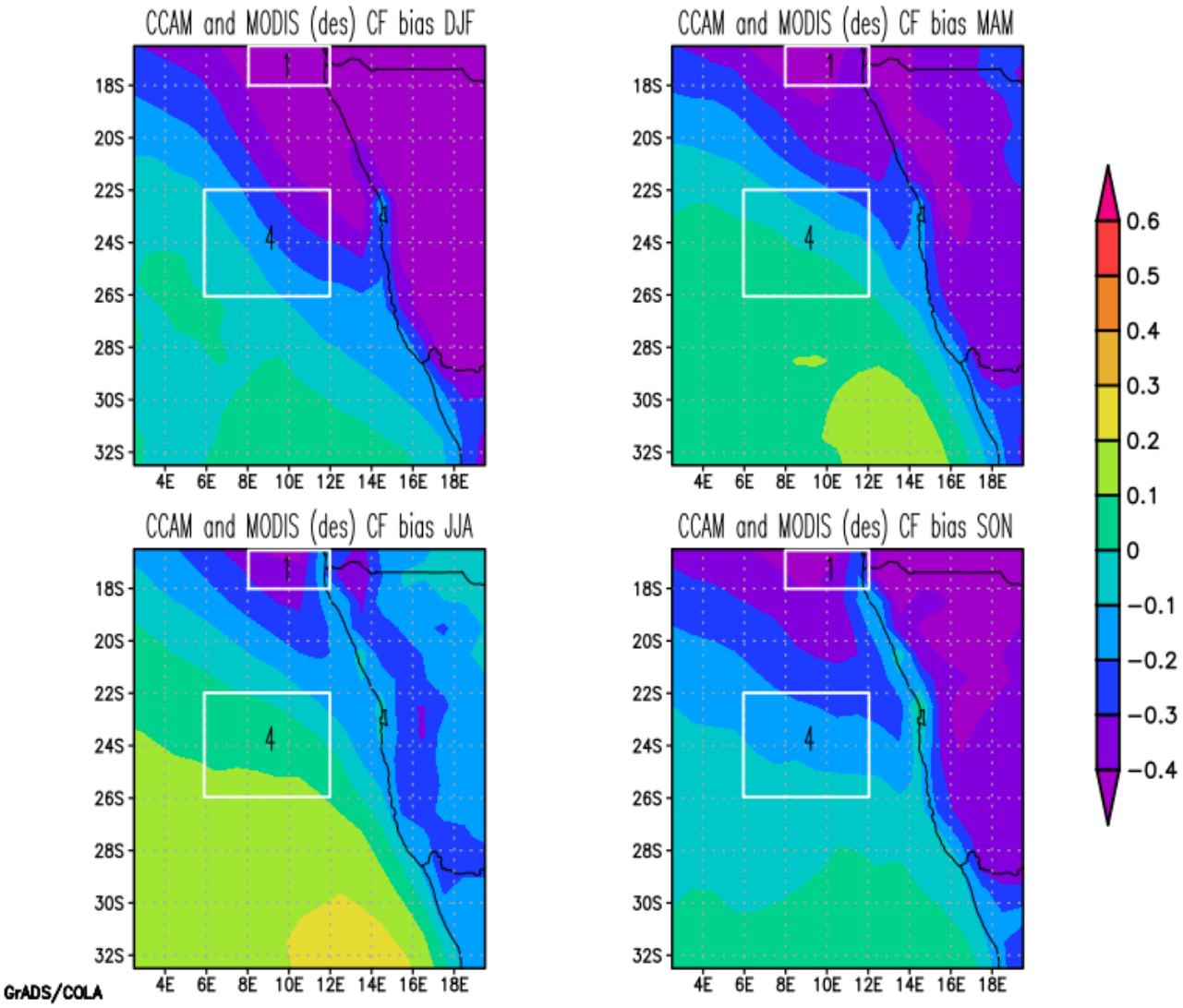
CCAM and MODIS (des) CF bias DJF
CCAM and MODIS (des) CF bias MAM
CCAM and MODIS (des) CF bias JJA
CCAM and MODIS (des) CF bias SON
1
4
18S
20S
22S
24S
26S
28S
30S
32S
4E
6E
8E
10E
12E
14E
16E
18E
0.6
0.5
0.4
0.3
0.2
0.1
0
−0.1
−0.2
−0.3
−0.4
GrADS/COLA

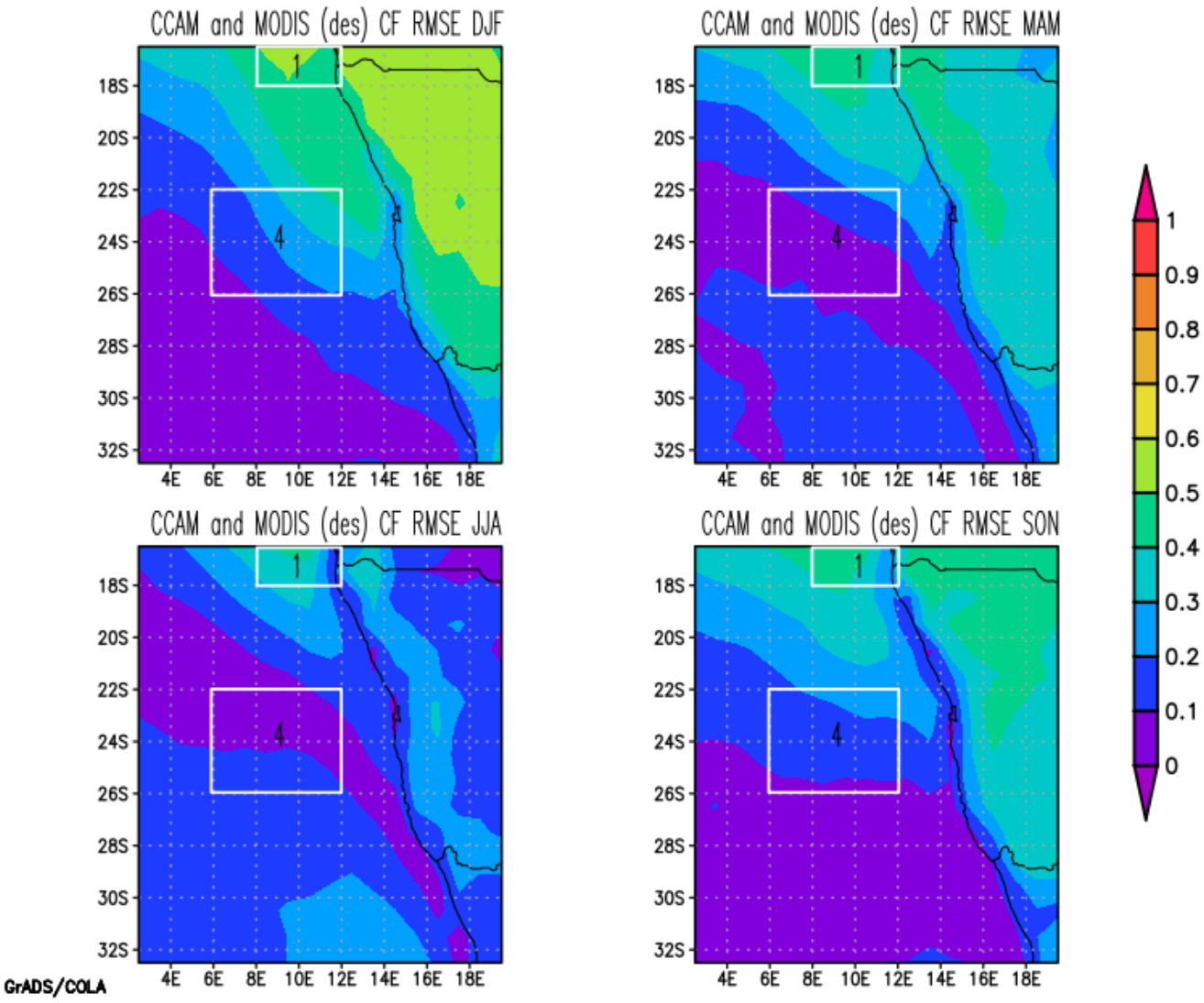
CCAM and MODIS (des) CF RMSE DJF
CCAM and MODIS (des) CF RMSE MAM
CCAM and MODIS (des) CF RMSE JJA
CCAM and MODIS (des) CF RMSE SON
18S
20S
22S
24S
26S
28S
30S
32S
4E
6E
8E
10E
12E
14E
16E
18E
1
4
1
0.9
0.8
0.7
0.6
0.5
0.4
0.3
0.2
0.1
0
GrADS/COLA

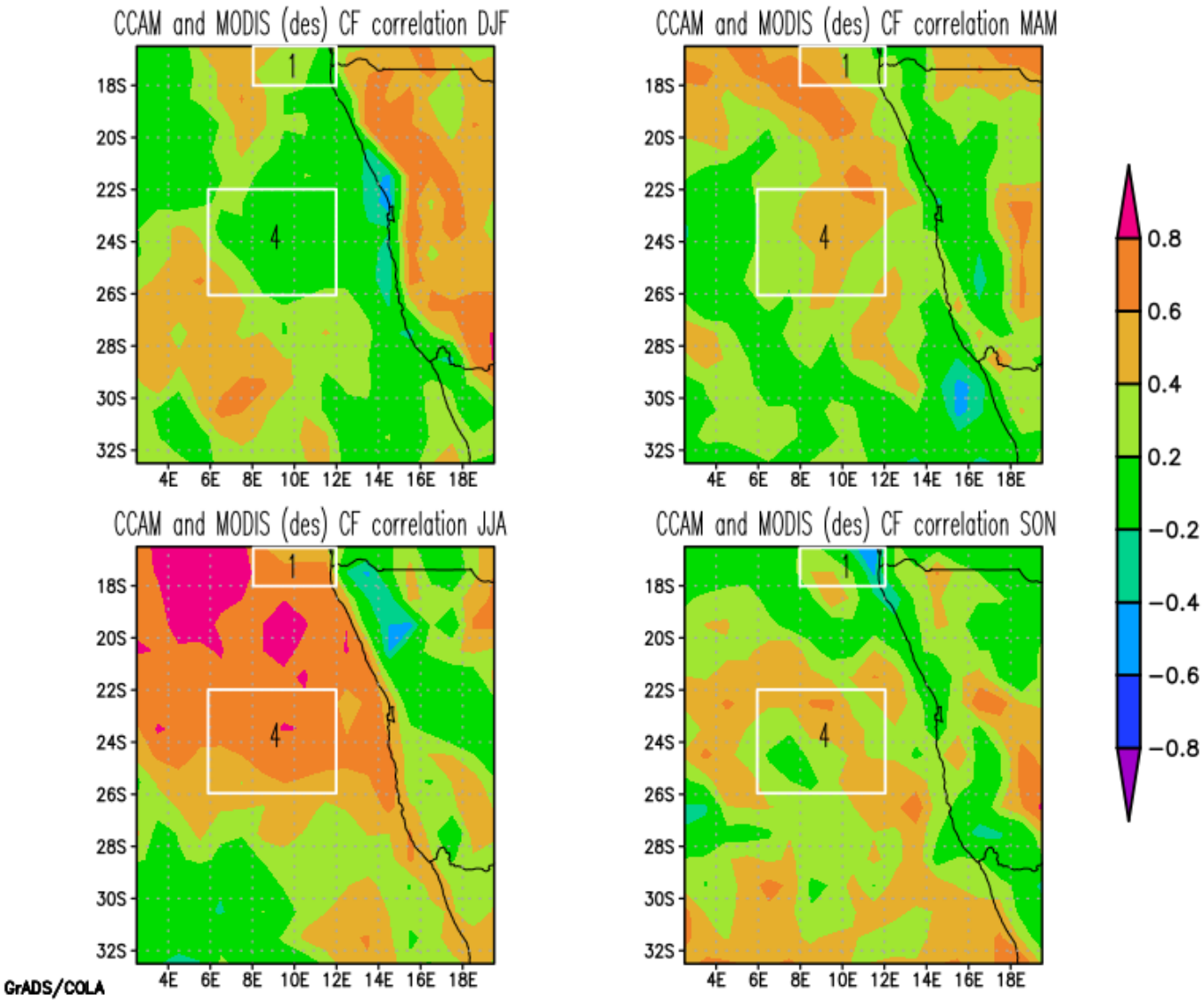

Figure 5.4: The multi-year (2002-2017) averaged bias (top), RMSE (middle) and correlation (bottom) of cloud fraction between the CCAM and AIRS (descending)

Fig. 5.3 and Fig. 5.4 show multi-year averaged quantitative analysis of cloud fraction between the CCAM simulations and AIRS (ascending) and AIRS (descending) observations for the subdomains in all seasons. The first subdomain has a negative bias for cloud fraction in all seasons. The magnitude of error for cloud fraction calculated for the first subdomain is higher (0.1-0.4 and 0.3-0.5) for all seasons for AIRS (ascending) and AIRS (descending), respectively. The first subdomain has no correlation for cloud

fraction in summer and spring, and has a weak positive correlation in autumn, and a moderate positive correlation in winter for AIRS (ascending). The first subdomain has a weak positive correlation for cloud fraction in summer and autumn, and a moderate positive correlation in winter, and no correlation in spring for AIRS (descending).

The fourth subdomain has a positive bias for cloud fraction in all seasons for AIRS (ascending). The fourth subdomain has negative bias for cloud fraction in all seasons except for winter for AIRS (descending). The magnitude of error for cloud fraction calculated for the fourth subdomain is lower (0-0.1) in autumn and spring, and higher (0.1-0.2) in summer and winter for AIRS (ascending) and AIRS (descending). The fourth subdomain has no correlation for cloud fraction in summer, and has moderate correlation in autumn and winter, and has a weak positive correlation in spring for AIRS (ascending). The fourth subdomain has no correlation for cloud fraction in summer and autumn, and strong positive correlation in winter, and weak positive correlation in spring for AIRS (descending).

Results from the quantitative analysis suggest that the CCAM underestimates cloud fraction at the northern region and the coast for all seasons. The CCAM overestimates cloud fraction in the south of the ocean for all seasons. Also, the CCAM produces a magnitude of error ranging between 20 and 30% in AIRS (ascending) and 40 and 60% at the northern region and 0 and 20% in the south of the ocean for AIRS (descending). The CCAM has no correlation to AIRS (ascending) for cloud fraction, except in winter.

In summary, the CCAM underestimates cloud fraction over the northern regions and overestimates cloud fraction over the southern regions in AIRS (both ascending and descending).

5.3 Relationship between aerosols and cloud fraction

This section presents the results of CCAM simulations for cloud fraction and aerosols. We evaluated the linear relationship between cloud fraction, total AOD and compositional AOD (black carbon, organic carbon, sulphate, small dust and sea salt) across the domain using spatial correlation. There is not much dust over the ocean in the CCAM, and as such, only values closer to land have dust but they have fewer clouds.

5.3.1 Total aerosol optical depth and cloud fraction

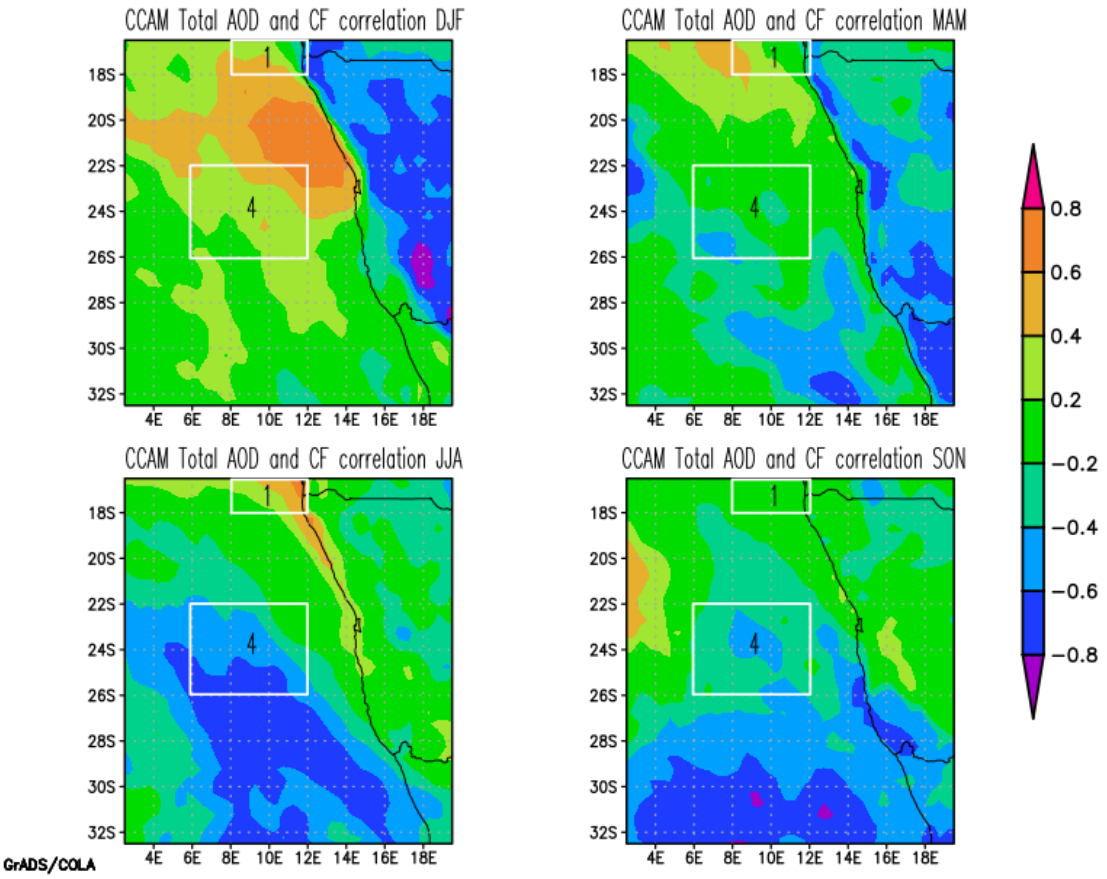

Figure 5.5: The multi-year (2002-2017) averaged spatial correlation between total AOD and cloud fraction

Fig. 5.5 shows the spatial correlation between total AOD and cloud fraction over the Benguela Region. The spatial correlation between total AOD and cloud fraction shows that winter and spring have a moderate negative correlation in the southern region of the domain. Summer has a weak positive correlation between total AOD and cloud fraction for the first subdomain and fourth subdomain. Autumn has a weak positive correlation between total AOD and cloud fraction for the first subdomain and a weak negative correlation for the fourth subdomain. Winter has a moderate positive correlation between total AOD and cloud fraction for the first subdomain and a moderate negative correlation

for the fourth subdomain. Spring has no correlation between total AOD and cloud fraction in the first subdomain and a moderate negative correlation for the fourth subdomain.

The results show that AOD is mostly negatively correlated with cloud fraction, indicating that when AOD increases, cloud fraction decreases in the southern domain. When AOD is >0.22 across the map, there is no correlation between AOD and cloud fraction. When AOD is <0.22 across the map, AOD and cloud fraction are positively correlated in the northern region of the domain. The 0.22 AOD level is not a standard figure; however, it is a point where total AOD in the CCAM shows the correlation relative to cloud fraction. The relationship between AOD and cloud fraction varies regionally. Some previous research conducted globally found that there is a positive relationship between AOD and cloud fraction (Adebiyi & Zuidema, 2018; Balakrishnaiah *et al.*, 2012; Grandey *et al.*, 2013; Gryspeerdt *et al.*, 2016; Myhre *et al.*, 2007). In contrast, other research from Asia found that when AOD is <0.3, it had a negative relationship to cloud fraction, and when AOD is >0.3, it had a positive relationship (Liu *et al.*, 2020). However, the other research from Kenya found that there is a negative relationship between AOD and cloud fraction (Nyasulu *et al.*, 2020). This shows that the relationship between total AOD and cloud fraction does not depend only on the aerosol loading of the region, but also on the prevailing meteorological conditions of that region (Kang *et al.*, 2015).

Interannual seasonal plots for area-averaged seasonal cycles between total AOD and cloud fraction for the first subdomain and fourth subdomain show that when total AOD increases, so does the cloud fraction (Fig. 5.6). Total AOD increases with an increase in cloud fraction in the fourth subdomain; however, it is not profound (Fig. 5.6a in **Annexure B**).

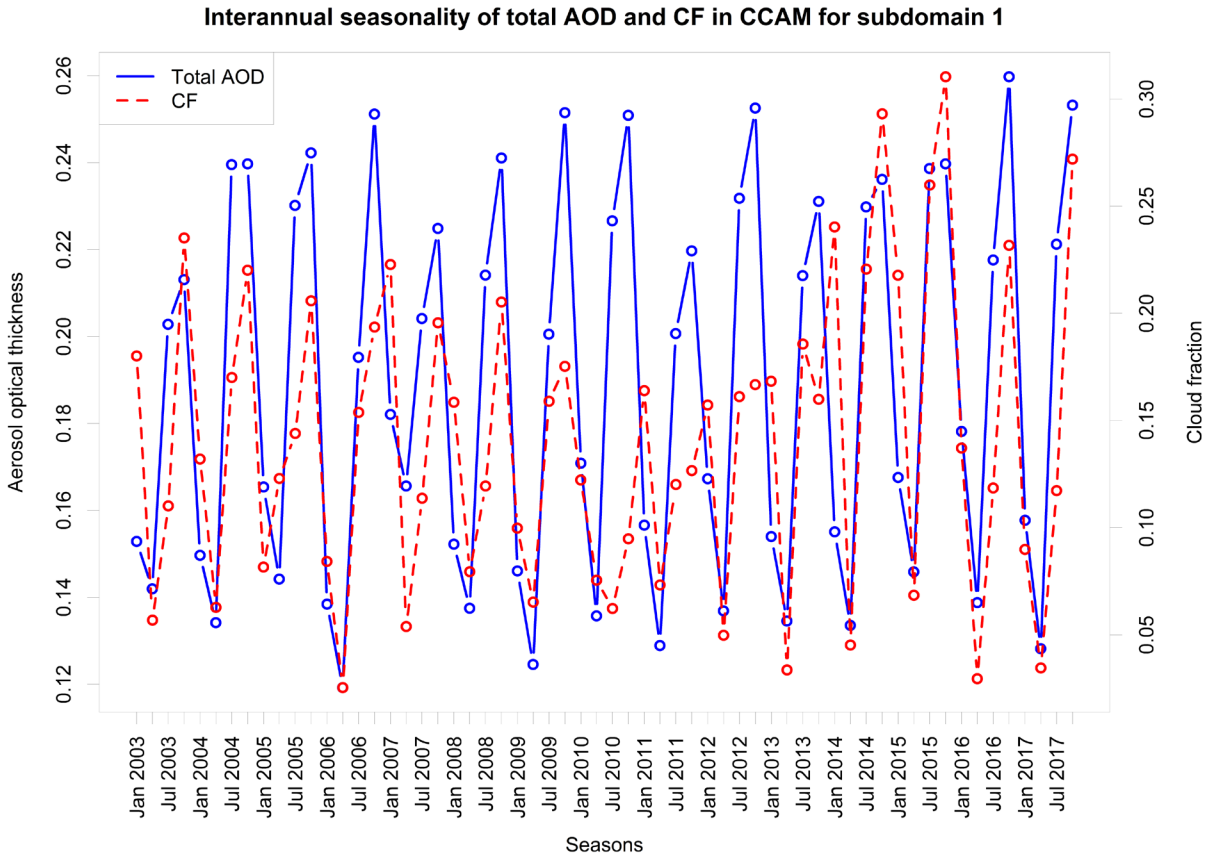

Figure 5.6: Area-averaged interannual seasonality between total AOD and cloud fraction for subdomain 1

5.3.2 Compositional AOD of black carbon and cloud fraction

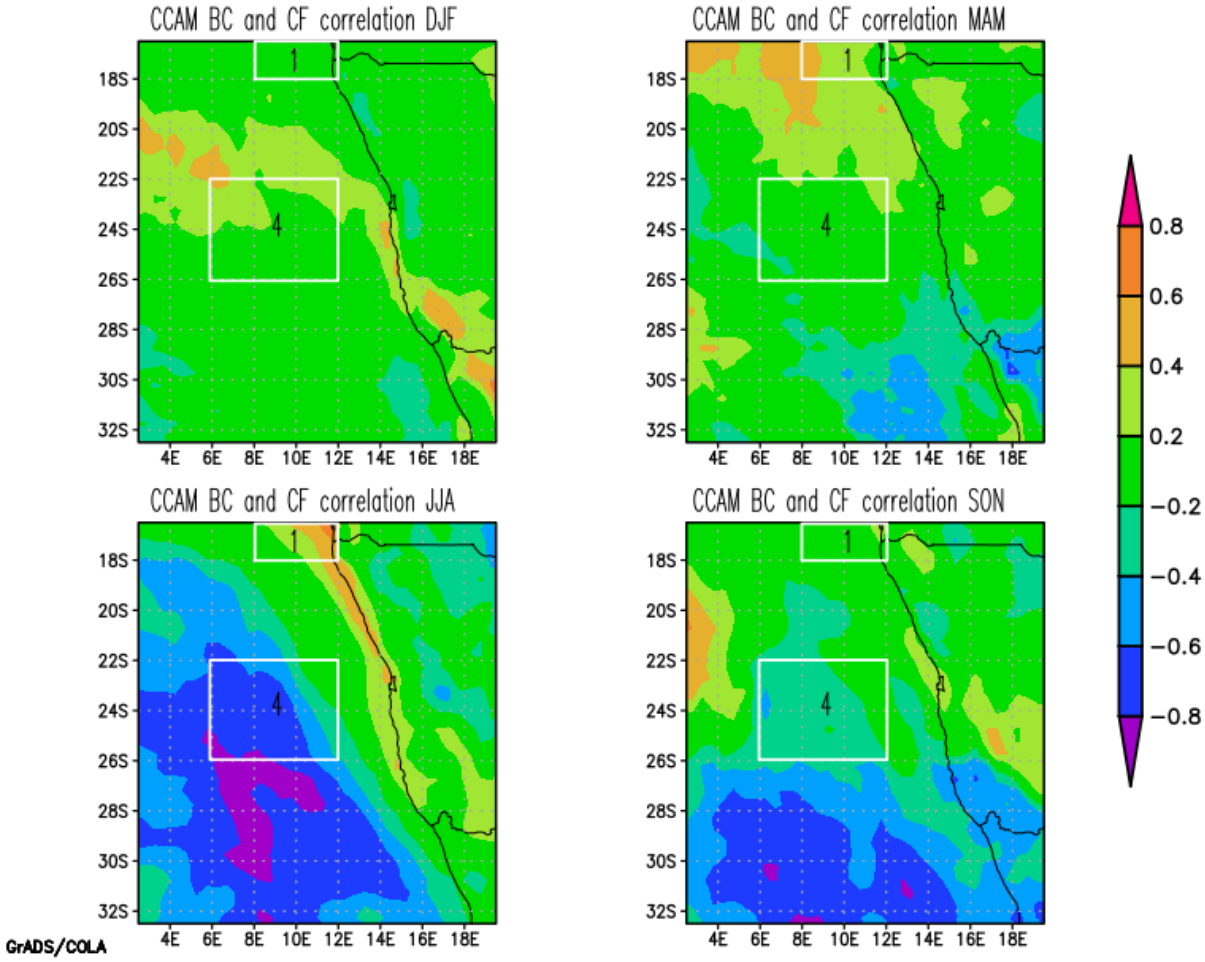

Figure 5.7: The multi-year (2002-2017) averaged spatial correlation between compositional AOD of black carbon and cloud fraction

Fig. 5.7 shows the spatial correlation between compositional AOD of black carbon and cloud fraction over the Benguela Region. The spatial correlation between compositional AOD of black carbon and cloud fraction shows winter and spring have a moderate negative correlation in the southern region of the domain. Summer has no correlation between compositional AOD of black carbon and cloud fraction for the first subdomain and fourth subdomain. Autumn has a moderate positive correlation between compositional AOD of black carbon and cloud fraction for the first subdomain and no correlation for the fourth subdomain. Winter has a weak positive correlation between

compositional AOD of black carbon and cloud fraction for the first subdomain and a strong negative correlation for the fourth subdomain. Spring has no correlation between compositional AOD of black carbon and cloud fraction for the first subdomain and a weak negative correlation for the fourth subdomain.

The results show that compositional AOD of black carbon is mostly negatively correlated with cloud fraction, indicating that when compositional AOD of black carbon increases, cloud fraction decreases in the southern domain. This is due to black carbon that absorbs solar radiation that can evaporate cloud droplets, which is decreasing cloud fraction with an increase in AOD (Adesina *et al.*, 2016). Compositional AOD of black carbon has a strong negative correlation with cloud fraction in winter, indicating that when compositional AOD of black carbon increases, cloud fraction decreases. It will be interesting to study this point further to understand what exactly is in play during the winter season.

Interannual seasonal plots for area-averaged seasonal cycles between compositional AOD of black carbon and cloud fraction for the first subdomain show that when compositional AOD of black carbon increases, so does the cloud fraction (Fig. 5.8). Compositional AOD of black carbon increases with an increase in cloud fraction in the fourth subdomain; however, it is not profound (Fig. 5.8a in **Annexure B**).

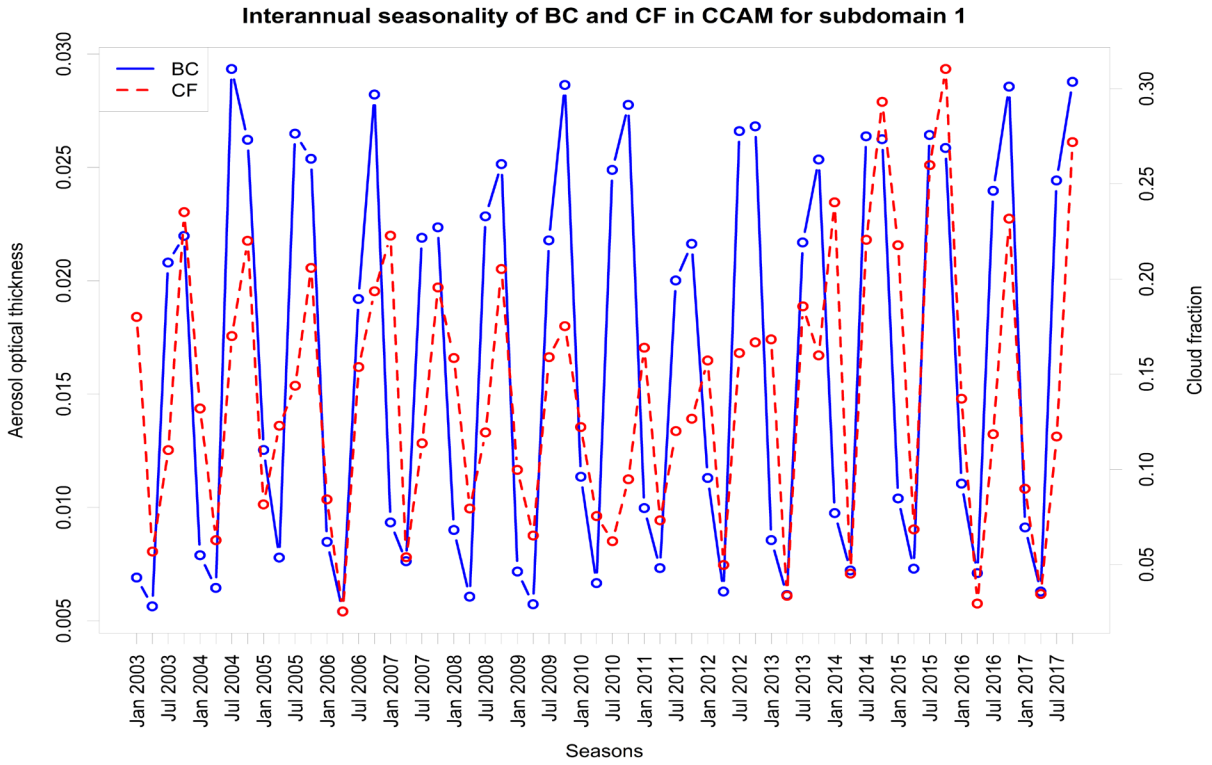

Figure 5.8: Area-averaged interannual seasonality between compositional AOD of black carbon and cloud fraction for subdomain 1

5.3.3 Compositional AOD of organic carbon and cloud fraction

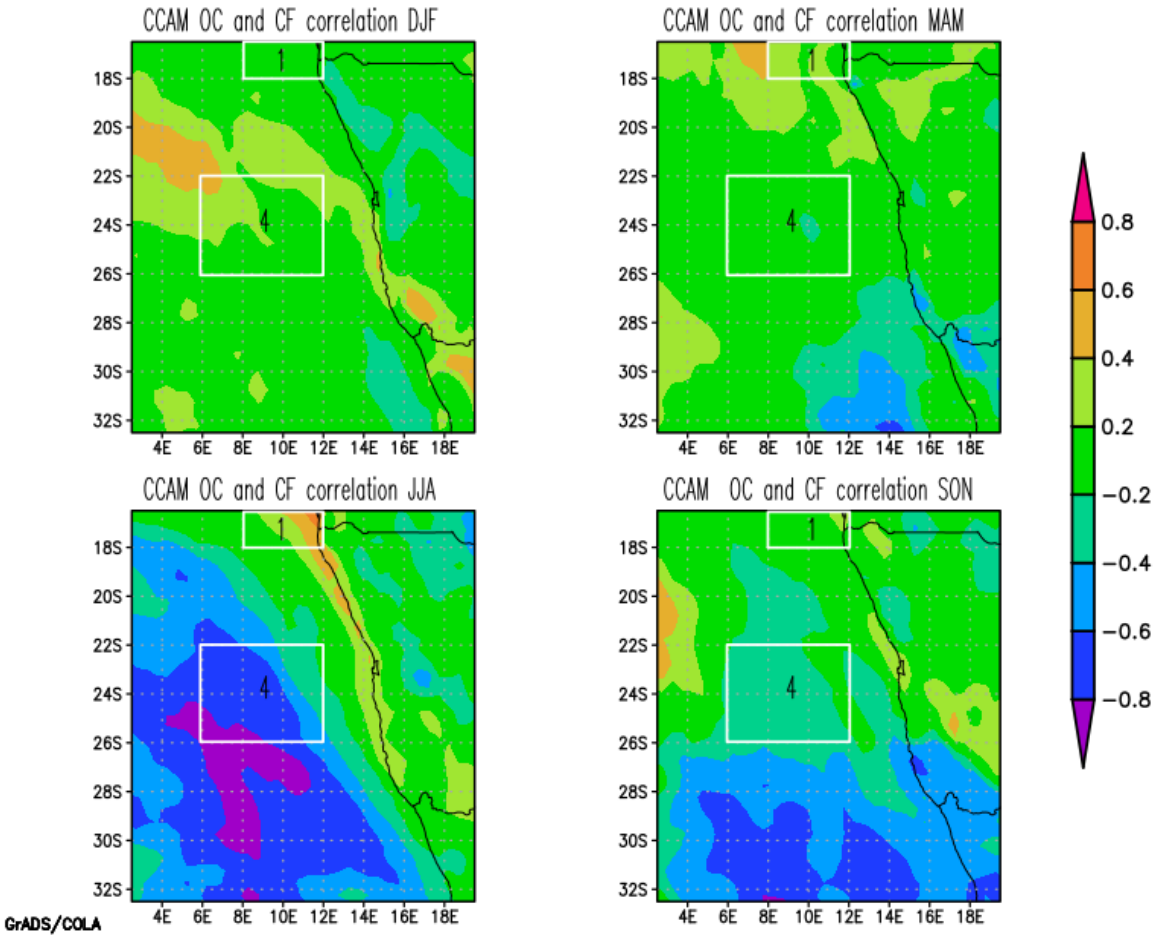

Figure 5.9: The multi-year (2002-2017) averaged spatial correlation between compositional AOD of organic carbon and cloud fraction

Fig. 5.9 shows the spatial correlation between the compositional AOD of organic carbon and cloud fraction over the Benguela Region. The spatial correlation between the compositional AOD of organic carbon and cloud fraction shows that winter and spring have a moderate negative correlation in the southern region of the domain. Summer has no correlation between the compositional AOD of organic carbon and cloud fraction for the first subdomain and fourth subdomain. Autumn has a weak positive correlation between the compositional AOD of organic carbon and cloud fraction for the first subdomain and no correlation for the fourth subdomain. Winter has a weak positive correlation between the compositional AOD of organic carbon and cloud fraction for the

first subdomain and a strong negative correlation for the fourth subdomain. Spring has no correlation between the compositional AOD of organic carbon and cloud fraction for the first subdomain and a weak negative correlation for the fourth subdomain.

The results show that the compositional AOD of organic carbon is mostly negatively correlated with cloud fraction, indicating that when the compositional AOD of organic carbon increases, cloud fraction decreases at the southern domain. Compositional AOD of organic carbon has a strong negative correlation with cloud fraction in winter, indicating that when the compositional AOD of organic carbon increases, cloud fraction decreases. This brings about the question as to why it is only strong in this season.

Interannual seasonal plots for area-averaged seasonal cycles between compositional AOD of organic carbon and cloud fraction for the first subdomain show that when compositional AOD of organic carbon increases, so does the cloud fraction (Fig. 5.10). Compositional AOD of organic carbon increases with the increase in cloud fraction in the fourth subdomain; however, it is not profound (Fig. 5.10a in **Annexure B**).

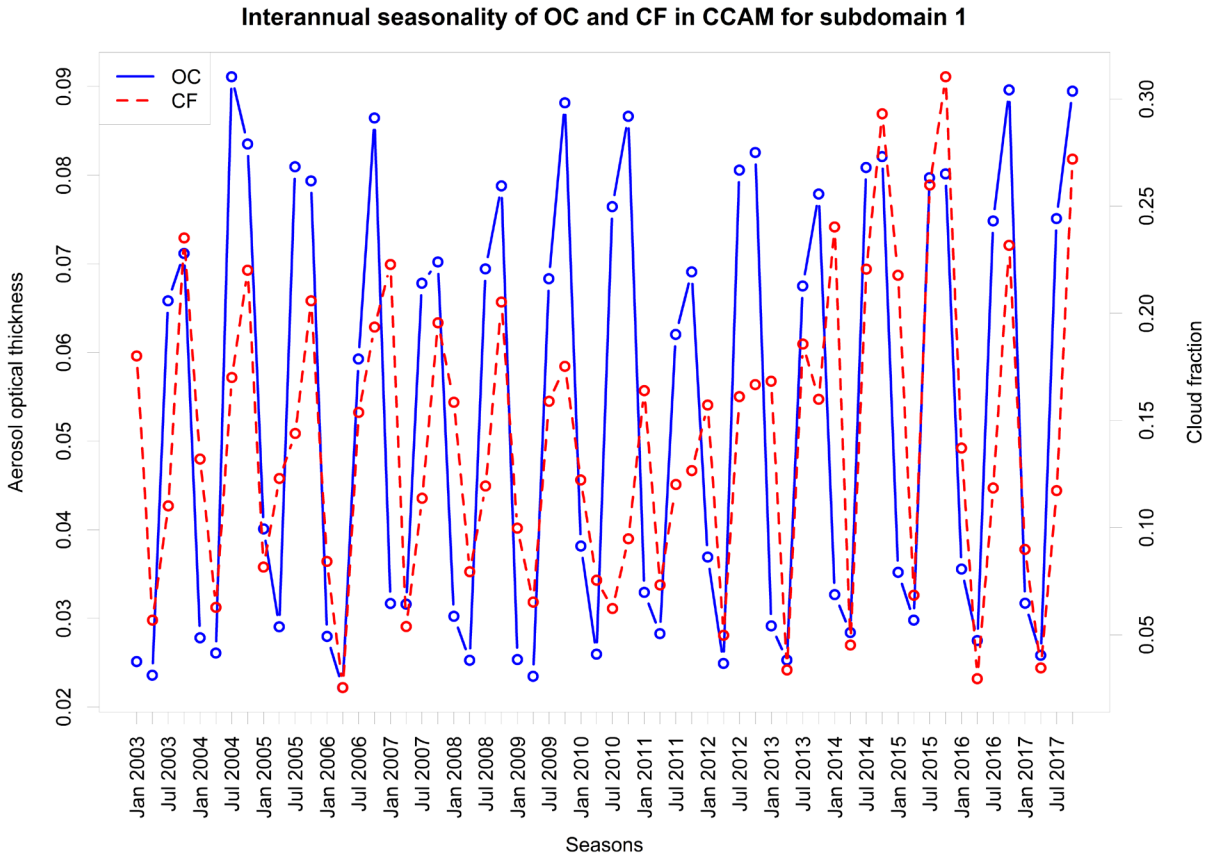

Figure 5.10: Area-averaged interannual seasonality between compositional AOD of organic carbon and cloud fraction for subdomain 1

5.3.4 Compositional AOD of small dust and cloud fraction

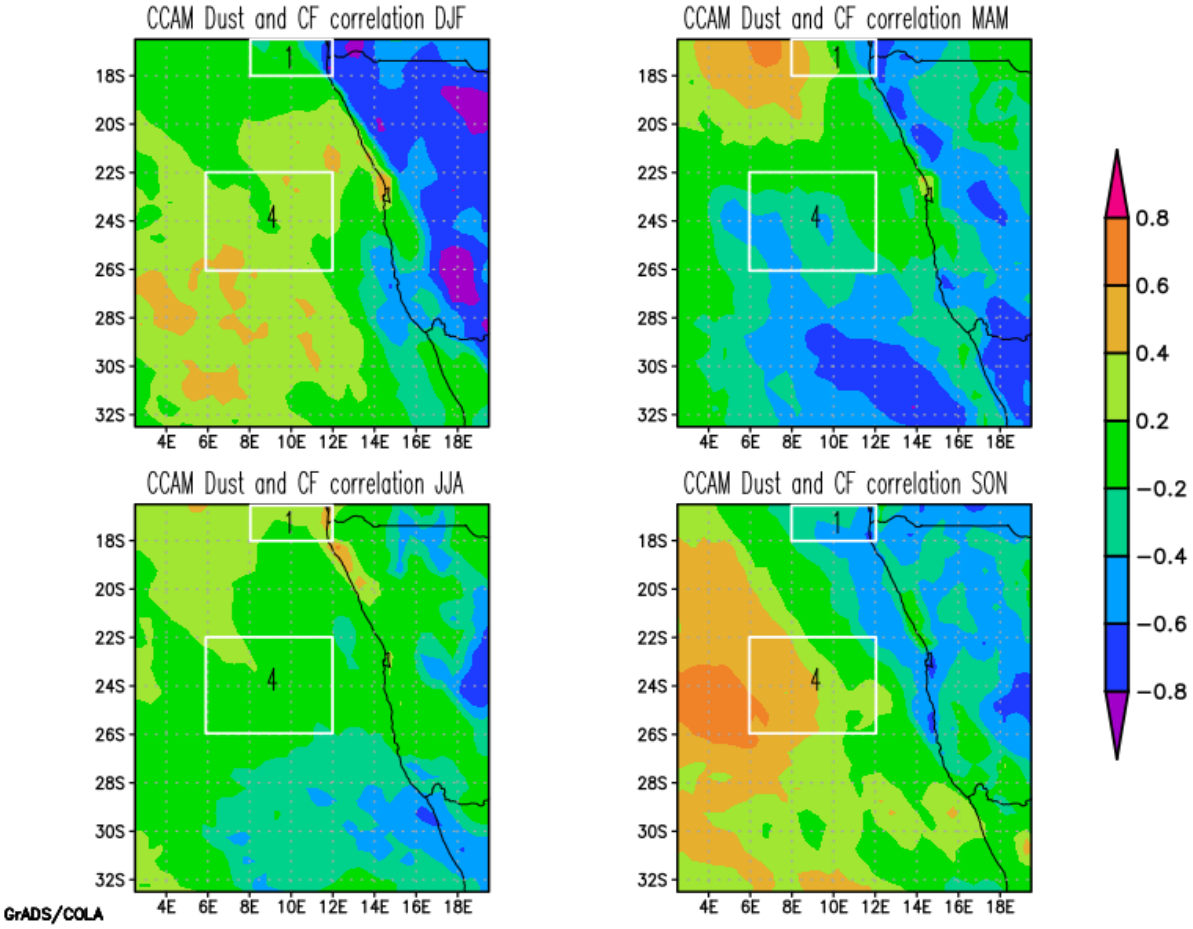

Figure 5.11: The multi-year (2002-2017) averaged spatial correlation between compositional AOD of small dust and cloud fraction

Fig. 5.11 shows the spatial correlation between the compositional AOD of small dust and cloud fraction over the Benguela Region. Summer has no correlation between the compositional AOD of small dust and cloud fraction for the first subdomain and a weak positive correlation for subdomain 4. Autumn has no correlation between the compositional AOD of small dust and cloud fraction for the first subdomain and a weak negative correlation for the fourth subdomain. Winter has a weak positive correlation

between the compositional AOD of small dust and cloud fraction for the first subdomain and no correlation for the fourth subdomain. Spring has a moderate negative correlation between the compositional AOD of small dust and cloud fraction for the first subdomain and a weak positive correlation for the fourth subdomain. It was expected that correlation was found near the coast, but that was not the coast. However, significant correlations were found in the inner ocean and the southern region of the domain.

Interannual seasonal plots for area-averaged seasonal cycles between compositional AOD of small dust and cloud fraction for the first subdomain and fourth subdomain show that when the compositional AOD of small dust increases, so does the cloud fraction (Fig. 5.12 and Fig. 5.12a in **Annexure B**). Dust aerosols originate from the Namib Desert and Etosha Pan, and were transported to the ocean by south-easterly winds (Gkikas *et al.*, 2022). Surface winds and precipitation play a key role in determining the transport and deposition processes of dust (Vickery *et al.*, 2013; Zhao *et al.*, 2022). An increase in surface winds leads to an increase in transportation of dust, while an increase in precipitation leads to a decrease in transportation of dust (Pu 2018). Dust aerosols peak in winter due to Bergwinds and reduced precipitation.

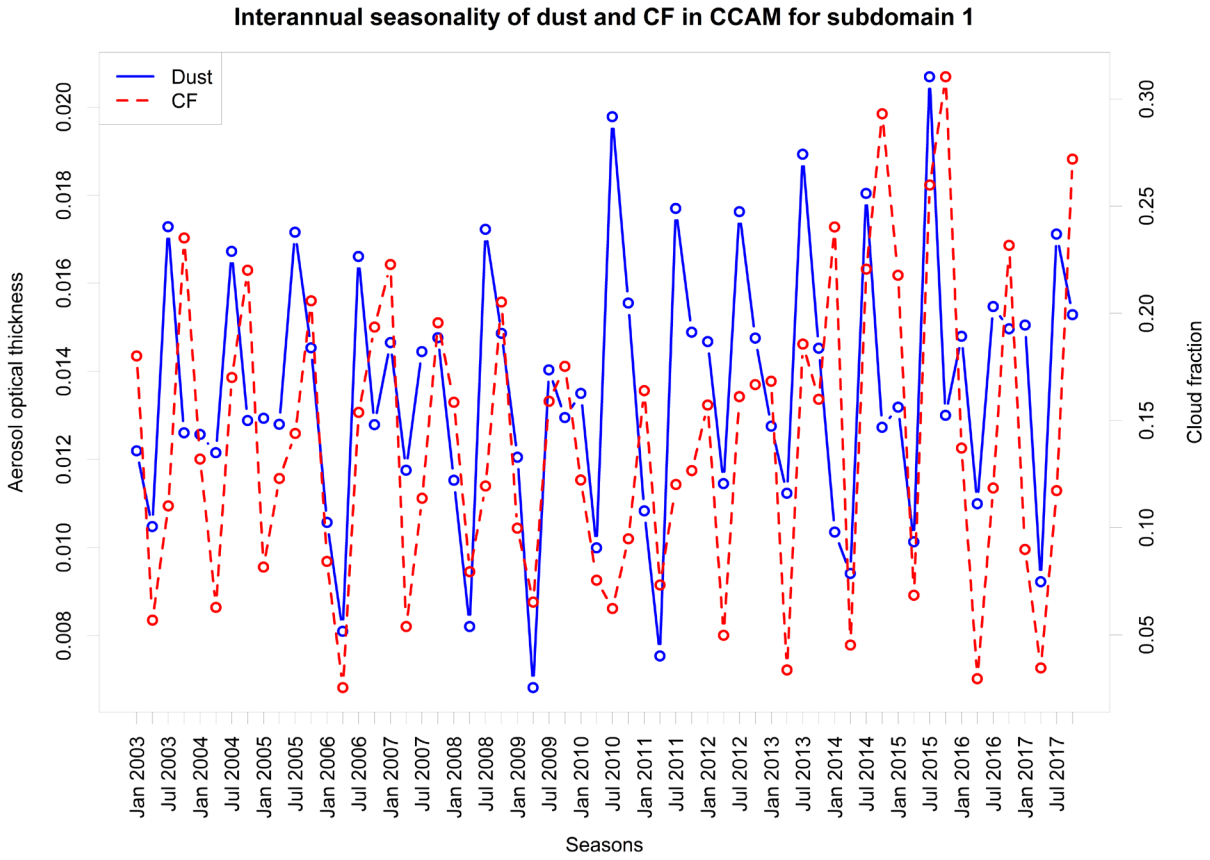

Figure 5.12: Area-averaged interannual seasonality between compositional AOD of small dust and cloud fraction for subdomain 1

5.3.5 Compositional AOD of sulphate and cloud fraction

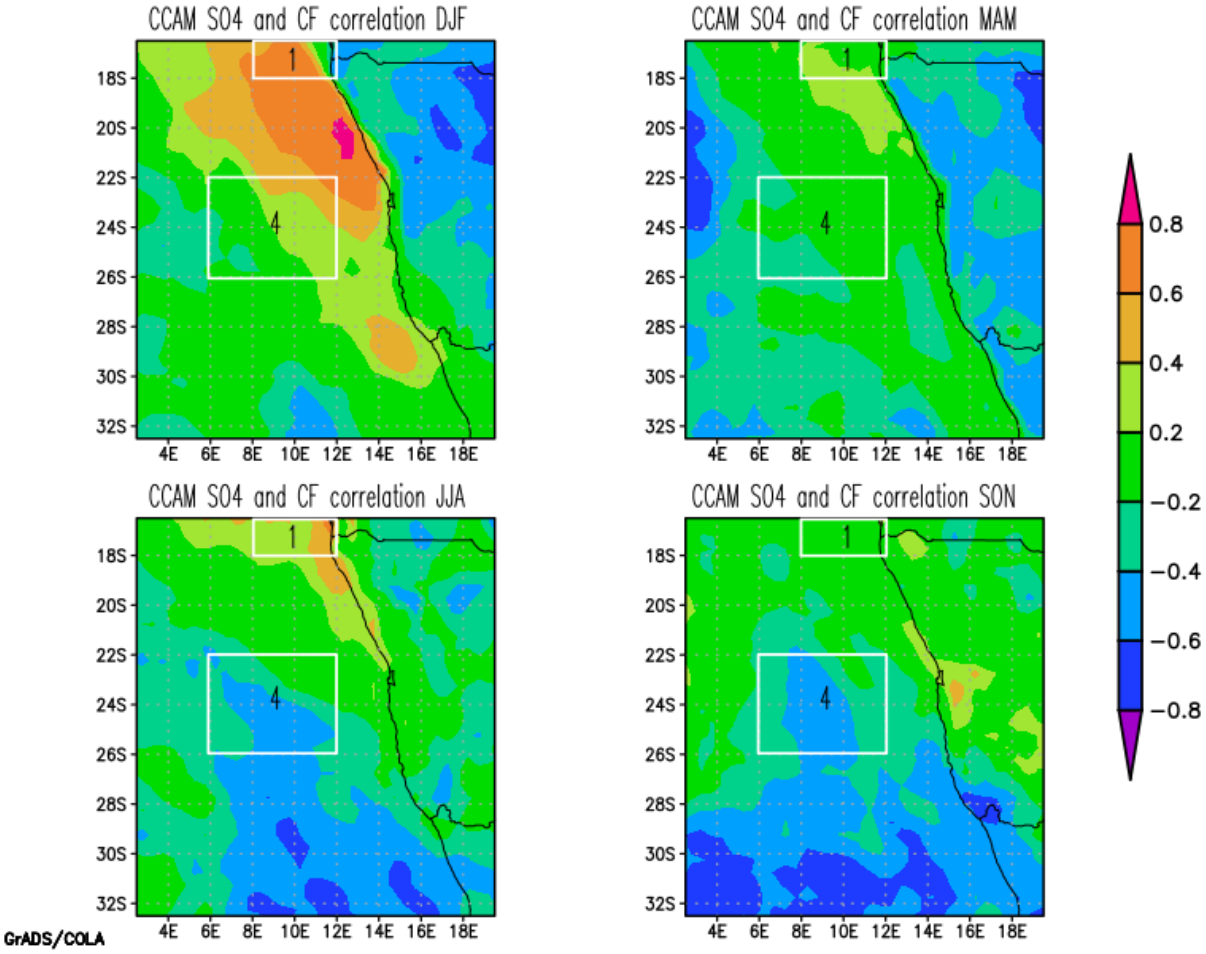

Figure 5.13: The multi-year (2002-2017) averaged spatial correlation between compositional AOD of sulphate and cloud fraction

Fig. 5.13 shows the spatial correlation between compositional AOD of sulphate and cloud fraction over the Benguela Region. The spatial correlation between compositional AOD of sulphate and cloud fraction shows that winter and spring have a moderate negative correlation in the southern region of the domain. Summer has a strong positive correlation between compositional AOD of sulphate and cloud fraction for the first subdomain and no correlation for the fourth subdomain. Autumn has a weak positive correlation between compositional AOD of sulphate and cloud fraction for the first subdomain and no correlation for the fourth subdomain. Winter has a moderate positive correlation between

compositional AOD of sulphate and cloud fraction for the first subdomain and a moderate negative correlation for the fourth subdomain. Spring has no correlation between compositional AOD of sulphate and cloud fraction for the first subdomain and a moderate negative correlation for the fourth subdomain.

The results show that the compositional AOD of sulphate mostly is negatively correlated with cloud fraction, indicating that when the compositional AOD of sulphate increases, cloud fraction decreases in the southern domain. Compositional AOD of sulphate has a positive strong correlation with cloud fraction in summer, indicating that when the compositional AOD of sulphate increases, so does the cloud fraction.

Interannual seasonal plots for area-averaged seasonal cycles between compositional AOD of sulphate and cloud fraction for the first subdomain and fourth subdomain show that when the compositional AOD of sulphate increases, so does the cloud fraction (Fig. 14 and Fig. 14a in **Annexure B**).

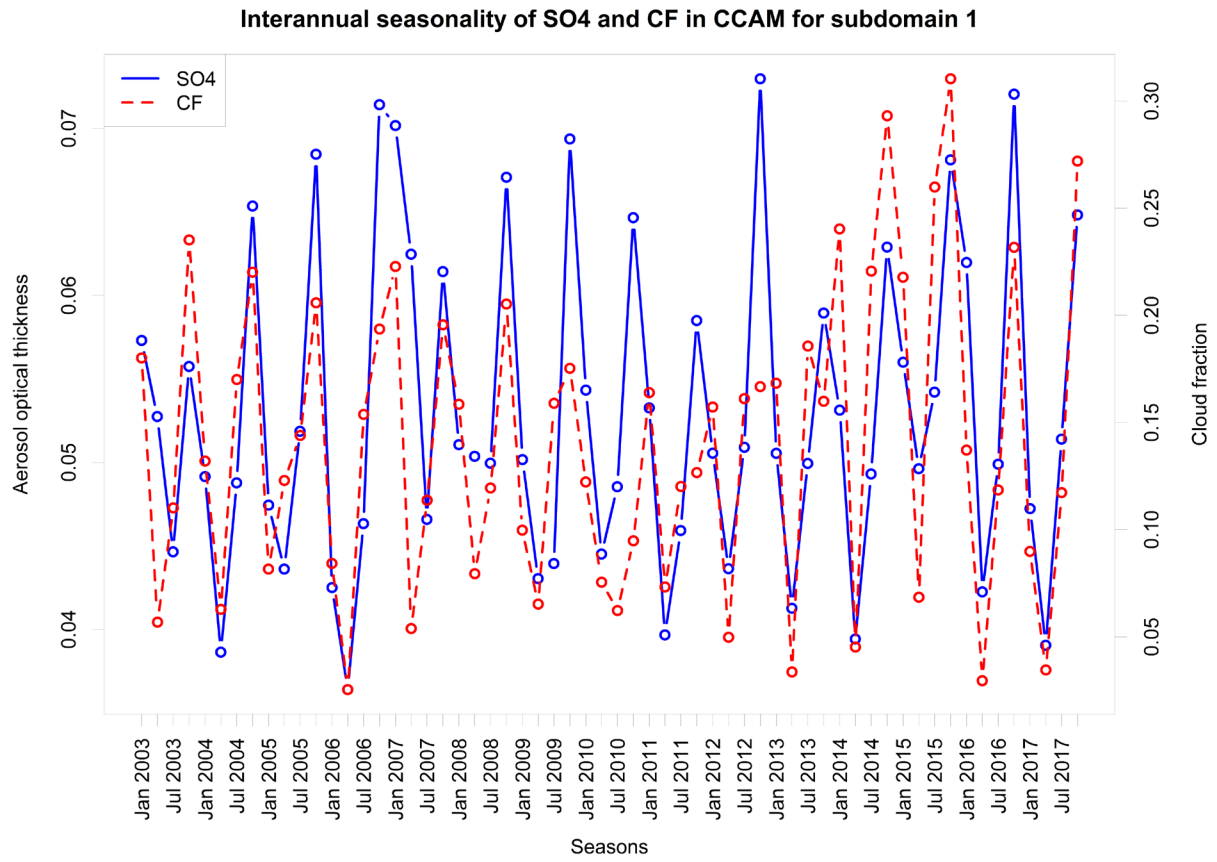

Figure 5.14: Area-averaged interannual seasonality between compositional AOD of sulphate and cloud fraction for subdomain 1

5.3.6 Compositional AOD of sea-salt and cloud fraction

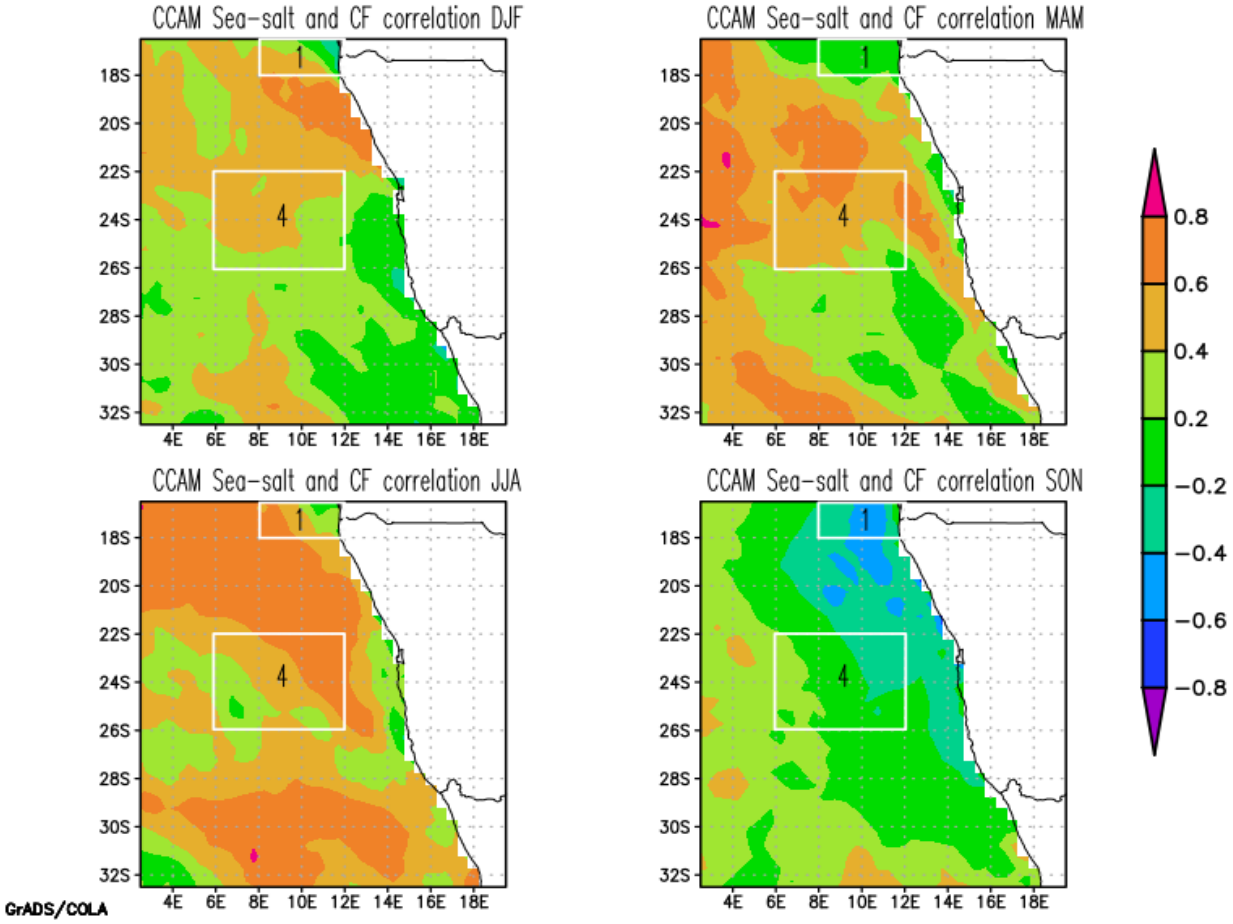

Figure 5.15: The multi-year (2002-2017) averaged spatial correlation between compositional AOD of sea-salt and cloud fraction

Fig. 5.15 shows the spatial correlation between compositional AOD of sea salt and cloud fraction over the Benguela Region. The spatial correlation between compositional AOD of sea salt shows that all seasons have a positive correlation in the whole domain except in spring. Summer has a weak positive correlation between compositional AOD of sea salt for the first subdomain and fourth subdomain. Autumn has no correlation between compositional AOD of sea salt for the first subdomain and a moderate positive correlation

for the fourth subdomain. Winter has a moderate positive correlation between compositional AOD of sea salt for the first subdomain and fourth subdomain. Spring has a moderate negative correlation between compositional AOD of sea salt for the first subdomain and no correlation for the fourth subdomain.

The results show that the compositional AOD of sea salt is positively correlated with cloud fraction, indicating that when the compositional AOD of sea-salt increases, cloud fraction increases.

Interannual seasonal plots for area-averaged seasonal cycles between compositional AOD of sea-salt and cloud fraction for the first subdomain and fourth subdomain show that when the compositional AOD of sea-salt increases, so does the cloud fraction, although it is not profound (Fig. 5.16 and Fig 5.16a in **Annexure B**).

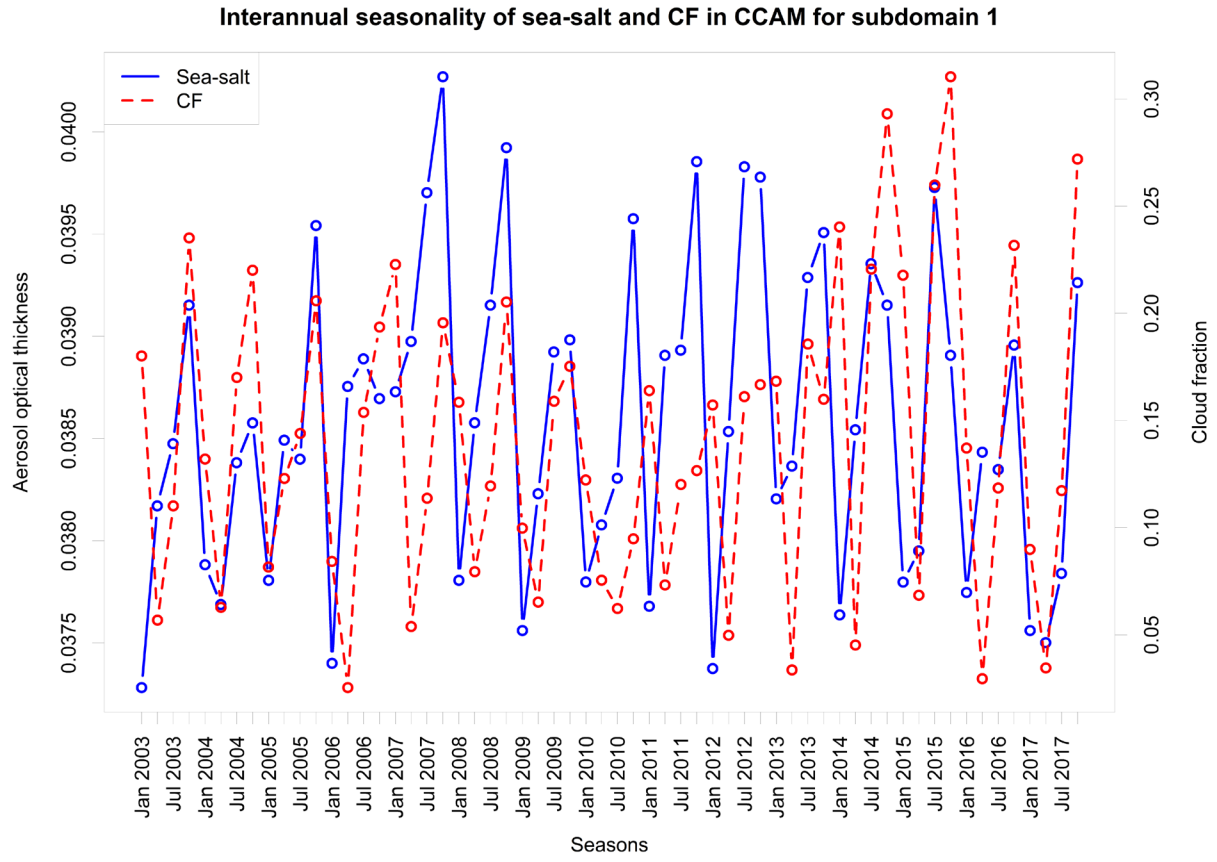

Figure 5.16: Area-averaged interannual seasonality between compositional AOD of sea-salt and cloud fraction for subdomain 1

5.3.7 Summary

We evaluated the linear association between cloud fraction, total AOD and compositional AOD (black carbon, organic carbon, sulphate, small dust and sea salt) seasonally using correlations. The results, as shown in Table 5.1, suggest that when any correlation was found, it was more often positive in the northern regions and negative in the southern domain. Aerosol optical depths attributable to black carbon and organic carbon have moderate or strong negative correlations with cloud fraction in winter. Aerosol optical depth attributable to sulphate has strong positive correlations with cloud fractions in summer. Dust aerosols (i.e. small dust) and marine aerosols (i.e. sea salt) had no strong correlations with cloud fraction. Interannual seasonal plots for total AOD and compositional AOD (black carbon, organic carbon, small dust, sulphate and sea salt) and cloud fraction are similar, though not always.

Table 5. 1: Correlation between cloud fraction total AOD and compositional AOD (i.e. black carbon, organic carbon, small dust, sulphate and sea salt).: Correlation between cloud fraction total AOD and compositional AOD (i.e. black carbon, organic carbon, small dust, sulphate and sea salt)

Cloud fraction to:	Subdomain	Summer	Autumn	Winter	Spring
Total AOD	1st	Weak positive	Weak positive	Moderate positive	No correlation
	4th	Weak positive	Weak negative	Moderate negative	Moderate negative
Compositional AOD of black carbon	1st	No correlation	Moderate positive	Weak positive	No correlation

	4th	No correlation	No correlation	Strong negative	Weak negative
Compositional AOD of organic carbon	1st	No correlation	Weak positive	Weak positive	No correlation
	4th	No correlation	No correlation	Strong negative	Weak negative
Compositional AOD of small dust	1st	No correlation	No correlation	Weak positive	Moderate negative
	4th	Weak positive	Weak negative	No correlation	Weak positive
Compositional AOD of sulphate	1st	Strong positive	Weak positive	Moderate positive	No correlation
	4th	No correlation	No correlation	Moderate negative	Moderate negative
Compositional AOD of sea-salt	1st	Weak positive	No correlation	Moderate positive	Moderate negative
	4th	Weak positive	Moderate positive	Moderate positive	No correlation

5.4 Magnitude of liquid water path between CCAM and MODIS

This section presents the results of the CCAM simulations and MODIS observations for liquid water path (LWP). We evaluated the spatial variation from the CCAM simulations against observed liquid water path from MODIS observations. To carry out the analysis, the eyeball verification method is used to compare the magnitude and spatial patterns

between the CCAM simulations and MODIS observations. The first focus is magnitude, followed by spatial patterns over the two subdomains. MODIS Terra passes across the equator at approximately 10:30 local solar time, and MODIS Aqua passes across the equator at approximately 13:30 local solar time. Due to the different passing times, the observed measurements are different. As such, MODIS Terra and MODIS Aqua are evaluated against the CCAM separately; and they are all averaged to multi-year seasonal temporal resolution. There is not much dust over the ocean in the CCAM, and as such, only values closer to land have dust, but they have less liquid water path.

5.4.1 CCAM vs MODIS (Aqua vs Terra)

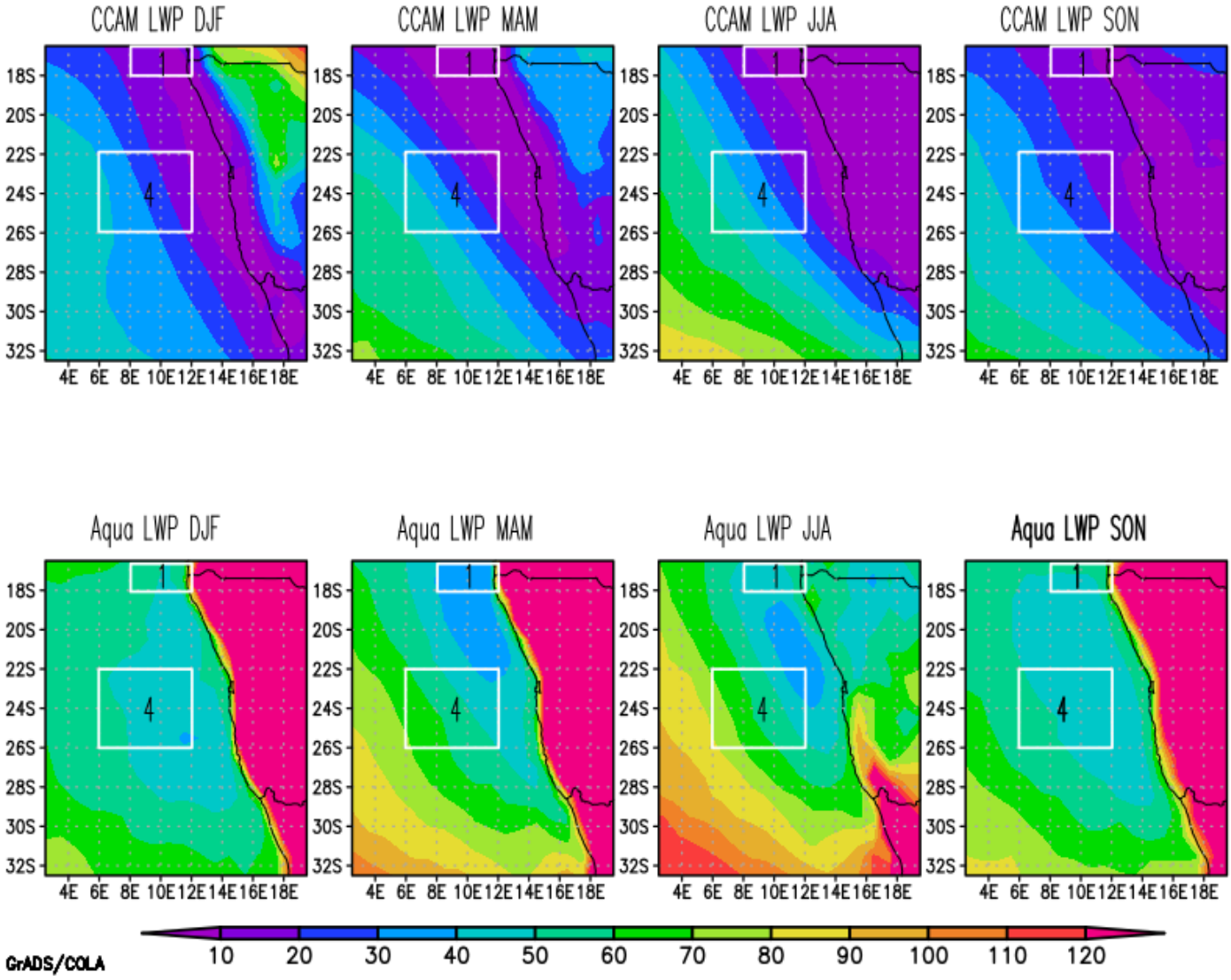

Figure 5.17: The multi-year (2002-2017) averaged magnitude of simulated CCAM (top) and measured Aqua (bottom) liquid water path in kg/m^2 over the Benguela Region

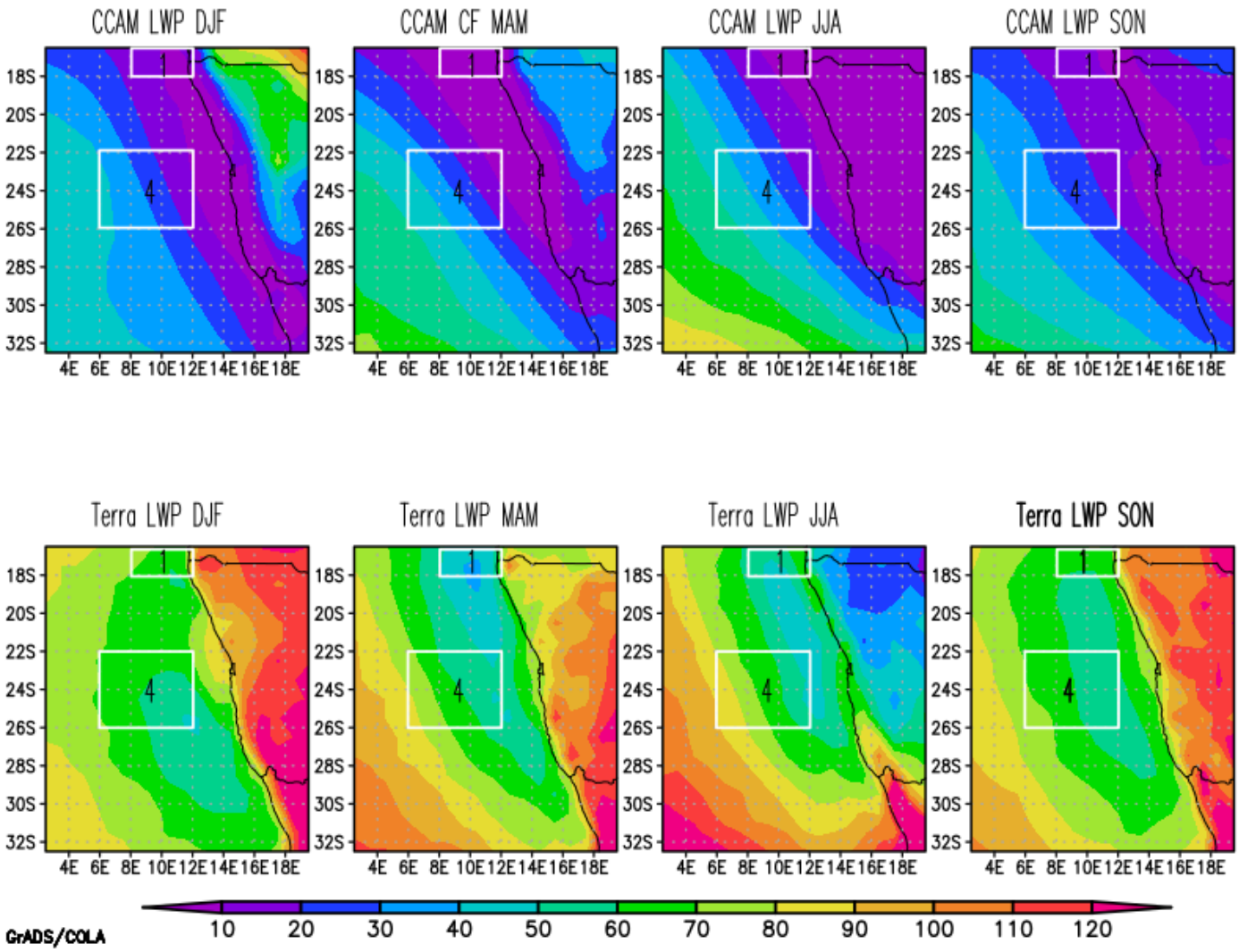

Figure 5.18: The multi-year (2002-2017) averaged magnitude of simulated CCAM (top) and measured Terra (bottom) liquid water path in kg/m^2 over the Benguela region

Fig. 5.17 and 5.18 show the multi-year averaged magnitude of the CCAM simulations, and Aqua and Terra observations for all seasons. The magnitude simulated by the CCAM was lower (0-90 kg/m^2) compared to observations (30-120 kg/m^2 and 30-120 kg/m^2) for Aqua and Terra for all seasons, respectively. A higher liquid water path was seen over

the inner ocean and it decreases when approaching the coastline in the CCAM. The spatial pattern was similar between the CCAM, and Aqua and Terra. The overpass times in Terra and Aqua are different, meaning that the clouds vary strongly diurnally, which could be studied in future research, specifically to compare the CCAM output only at satellite overpass times to see how much it changes.

5.5 Quantitative verification between CCAM and MODIS

This section presents the results of CCAM simulations and MODIS observations for liquid water path. We evaluated the spatial variation from the CCAM simulations against observed liquid water path from MODIS observations. To carry out the analyses, quantitative analyses (bias, RMSE and correlation) were used to evaluate the model. The first focus was bias, followed by RMSE, and lastly correlation over the two subdomains.

5.5.1 CCAM vs MODIS (Aqua vs Terra)

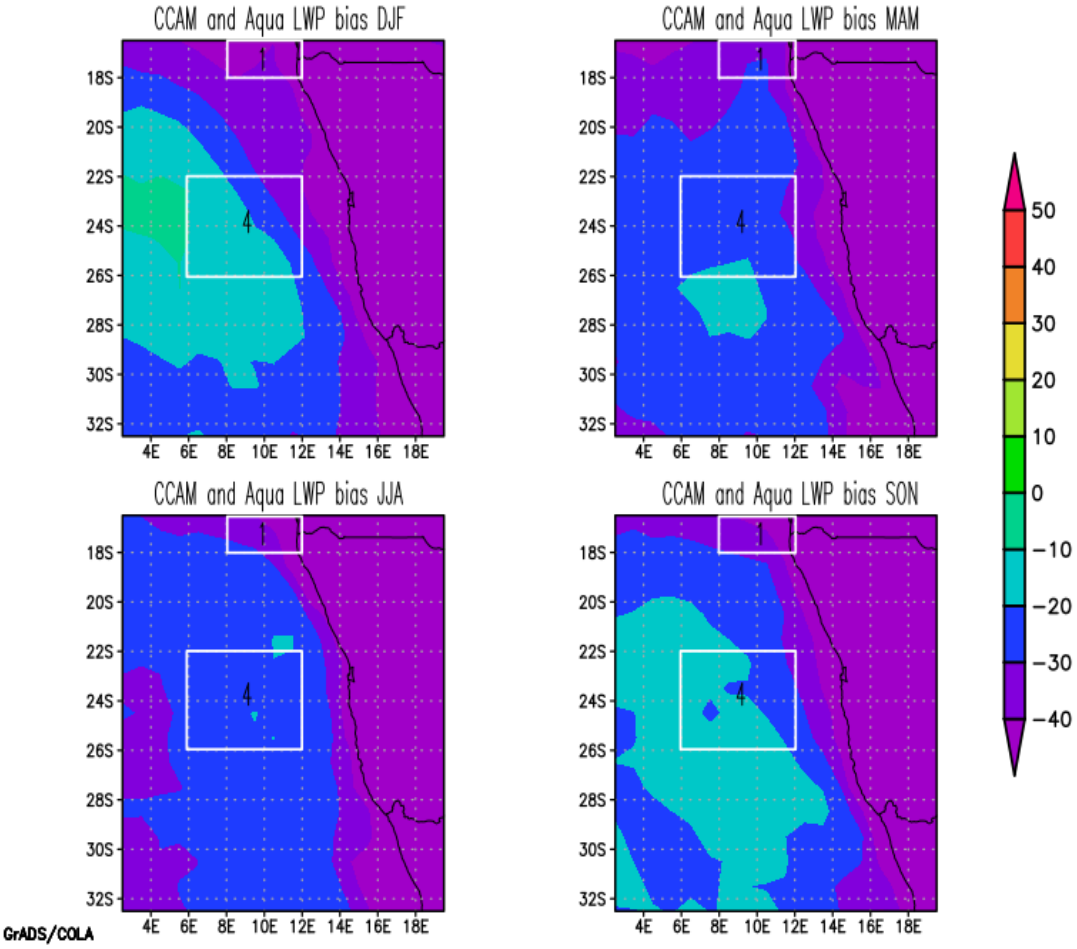

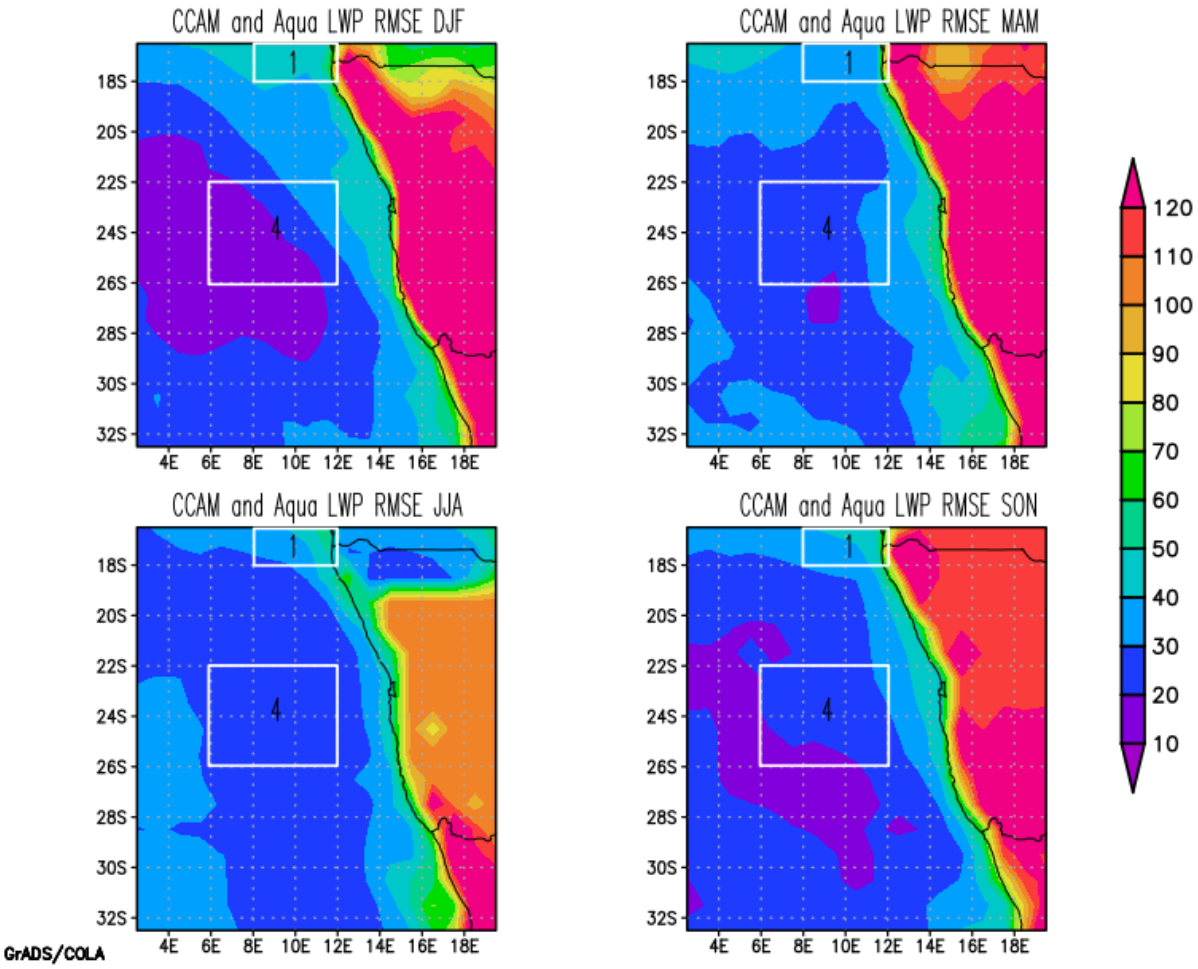
CCAM and Aqua LWP RMSE DJF
CCAM and Aqua LWP RMSE MAM
CCAM and Aqua LWP RMSE JJA
CCAM and Aqua LWP RMSE SON
1
4
18S
20S
22S
24S
26S
28S
30S
32S
4E
6E
8E
10E
12E
14E
16E
18E
120
110
100
90
80
70
60
50
40
30
20
10
GrADS/COLA

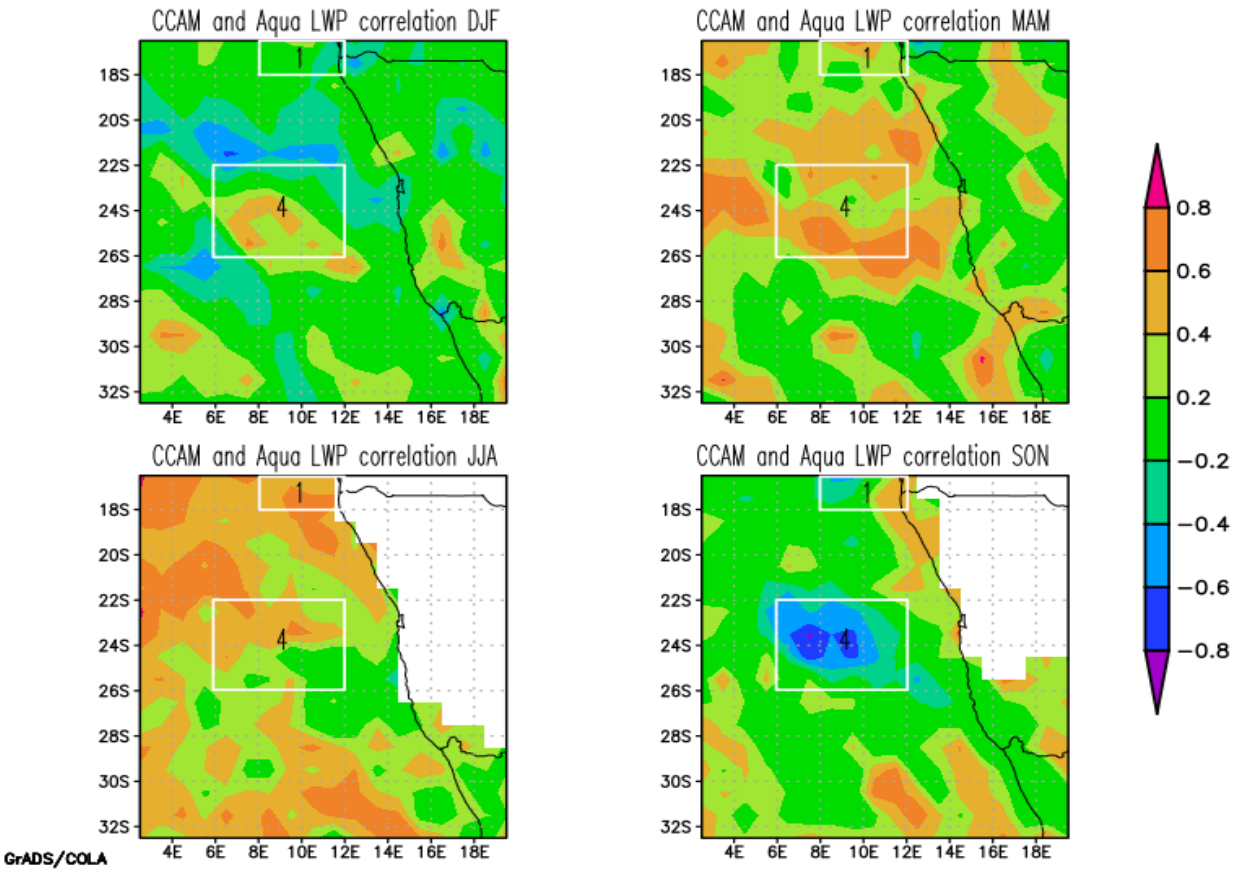

Figure 5.19: The multi-year (2002-2017) averaged bias (top), RMSE (middle) and correlation (bottom) of liquid water path between the CCAM and MODIS Aqua

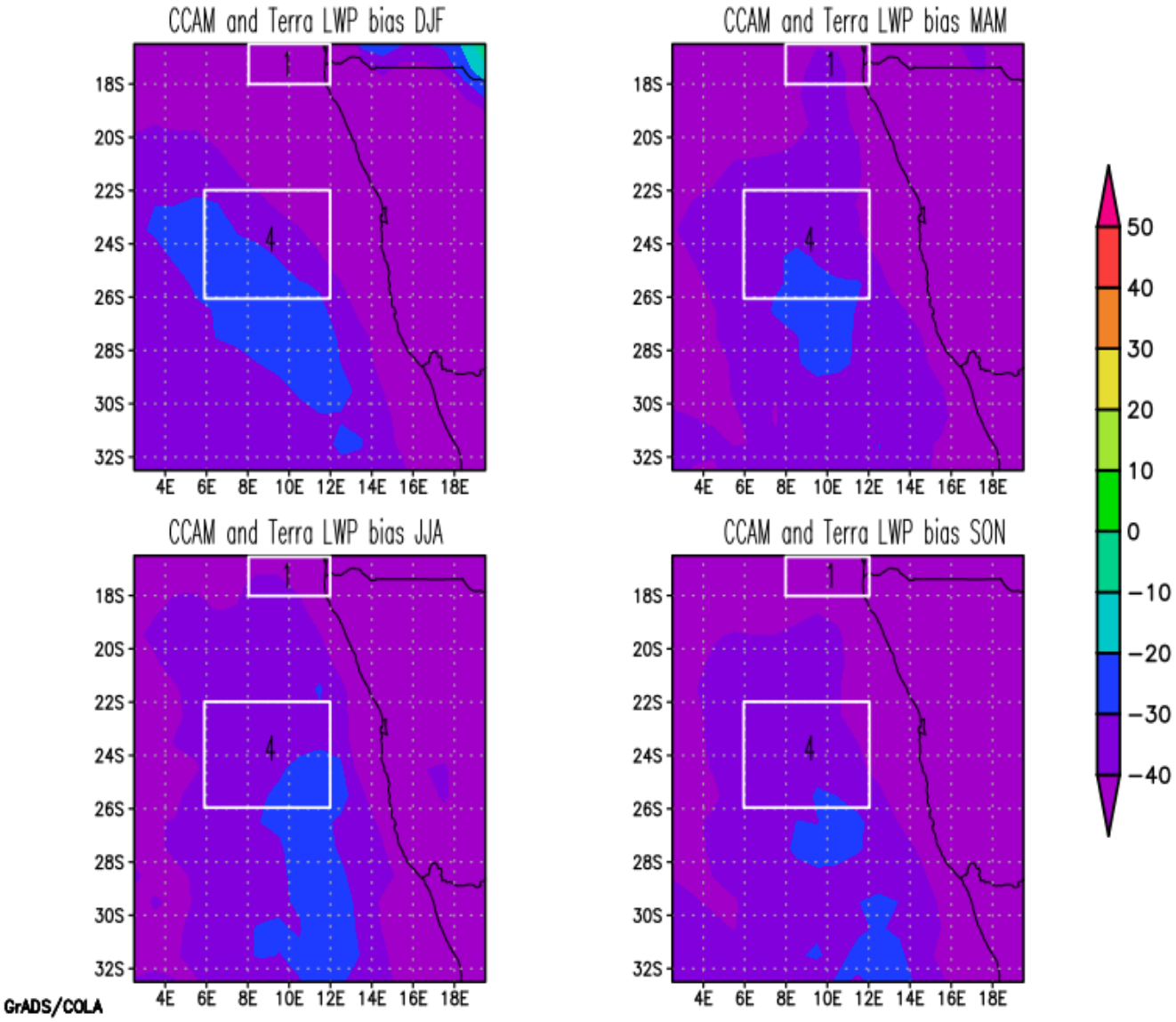
CCAM and Terra LWP bias DJF
CCAM and Terra LWP bias MAM
CCAM and Terra LWP bias JJA
CCAM and Terra LWP bias SON
18S
20S
22S
24S
26S
28S
30S
32S
4E
6E
8E
10E
12E
14E
16E
18E
1
4
50
40
30
20
10
0
−10
−20
−30
−40
GrADS/COLA

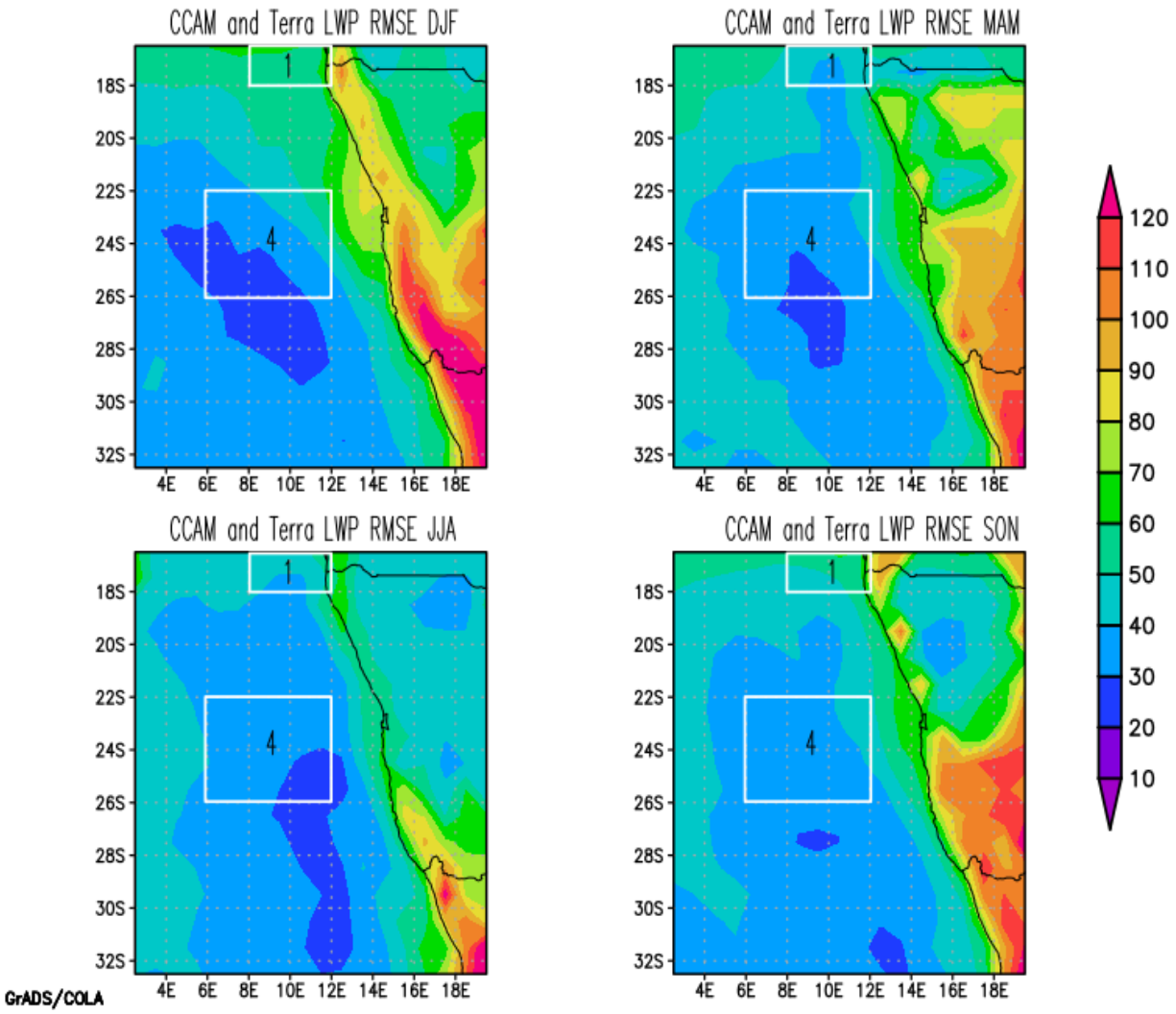
CCAM and Terra LWP RMSE DJF
CCAM and Terra LWP RMSE MAM
CCAM and Terra LWP RMSE JJA
CCAM and Terra LWP RMSE SON
1
4
18S
20S
22S
24S
26S
28S
30S
32S
4E
6E
8E
10E
12E
14E
16E
18E
120
110
100
90
80
70
60
50
40
30
20
10
GrADS/COLA

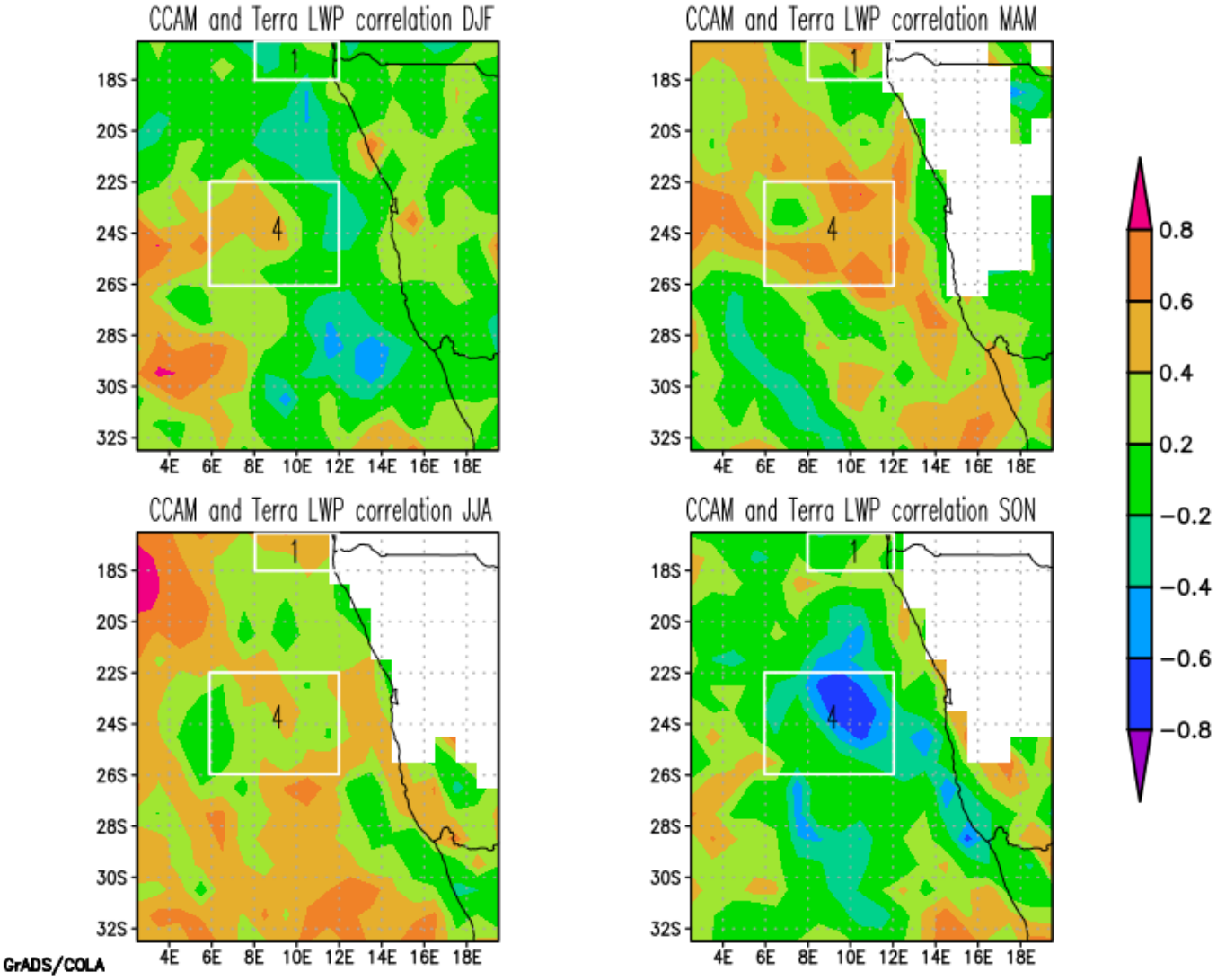

Figure 5.20: The multi-year (2002-2017) averaged bias (top), RMSE (middle) and correlation (bottom) of liquid water path between the CCAM and MODIS Terra

Fig. 5.19 and Fig. 5.20 show multi-year averaged quantitative analyses of liquid water path between the CCAM simulations, and Aqua and Terra observations for the subdomains in all seasons. The first subdomain had negative bias for liquid water path in all seasons. The magnitude of error for liquid water path calculated for the first subdomain was higher (30-40 kg/m^2 and 40-60 kg/m^2) in all seasons for Aqua and Terra, respectively. The first subdomain had no correlation for liquid water path in summer, and moderate positive correlation in winter, and weak positive correlation in autumn and spring. The

fourth subdomain had negative bias for liquid water path in all seasons. The magnitude of error for liquid water path calculated for the fourth subdomain was lower (10-30 kg/m^2) for Aqua in all seasons. The fourth subdomain had no correlation for liquid water path in summer, and weak positive correlation in autumn and winter, and weak negative correlation in spring in both Aqua and Terra.

It was found that the CCAM underestimated liquid water path over the ocean in Aqua and Terra. Also, the CCAM produced a magnitude of error of liquid water path ranging between 10 and 50 kg/m^2 and 10 and 60 kg/m^2 in Aqua and Terra, respectively. The CCAM had mostly weak positive correlations with liquid water path from Aqua and Terra.

5.6 Relationship between aerosols and liquid water path

This section presents the results of only the CCAM simulations for liquid water path and aerosols. We evaluated the linear relationship between liquid water path, total AOD and compositional AOD (black carbon (BC), organic carbon (OC), sulphate (SO_4), small dust and sea salt) using correlation.

5.6.1 Total aerosol optical depth and liquid water path

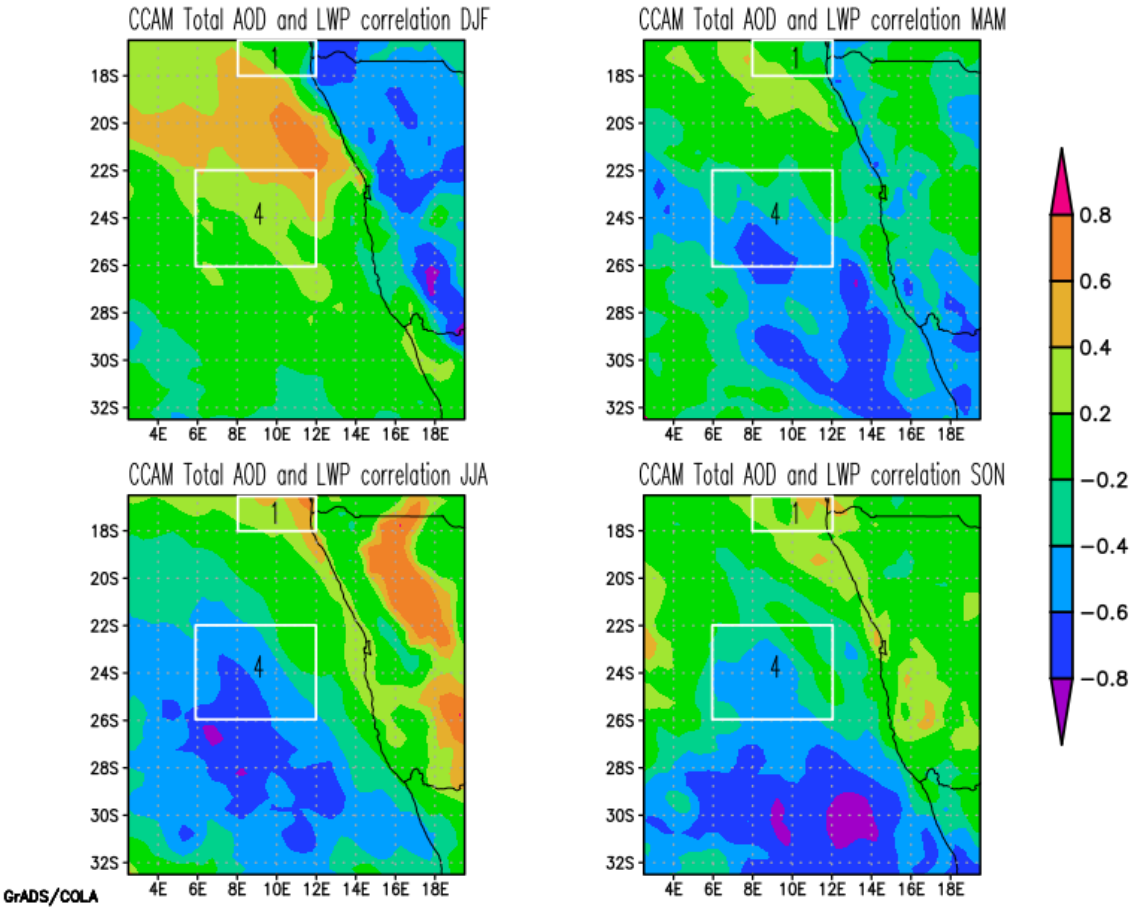

Figure 5.21: The multi-year (2002-2017) averaged spatial correlation between total AOD and liquid water path

Fig. 5.21 shows the spatial correlation between total AOD and liquid water path over the Benguela Region. The spatial correlation between total AOD and liquid water path shows winter and spring have a moderate negative correlation in the southern region of the domain. Summer has no correlation between total AOD and liquid water path for the first subdomain and a weak positive correlation for the fourth subdomain. Autumn has no correlation between total AOD and liquid water path for the first subdomain and moderate negative correlation for the fourth subdomain. Winter has a moderate positive correlation between total AOD and liquid water path for the first subdomain and a moderate negative correlation for the fourth subdomain. Spring has a weak positive correlation between total

AOD and liquid water path for the first subdomain and a moderate negative correlation for the fourth subdomain.

The results show that total AOD is more often negatively correlated with liquid water path, indicating that when total AOD increases, liquid water path decreases at the southern domain. Measurements in the South Atlantic Ocean (which my study area forms part of) found that an increase of AOD tends to decrease liquid water path (Gryspeerdt *et al.*, 2016). This finding is consistent with the southern region of my domain. This outcome may be due to dry air entrainment. Results in this study were not consistent with previous studies done in different regions and temporal resolutions, which found that an increase in AOD leads to an increase in liquid water path (Liu *et al.*, 2020a; Myhre *et al.*, 2007). This outcome may be the consequence of cool moist air flux from the Southern Ocean.

Interannual seasonal plots for area-averaged seasonal cycles between total AOD and liquid water path are similar. When total AOD increases, so does liquid water path, which does not occur across the full domain (Fig. 5.22 and Fig. 5.22a in **Annexure C**).

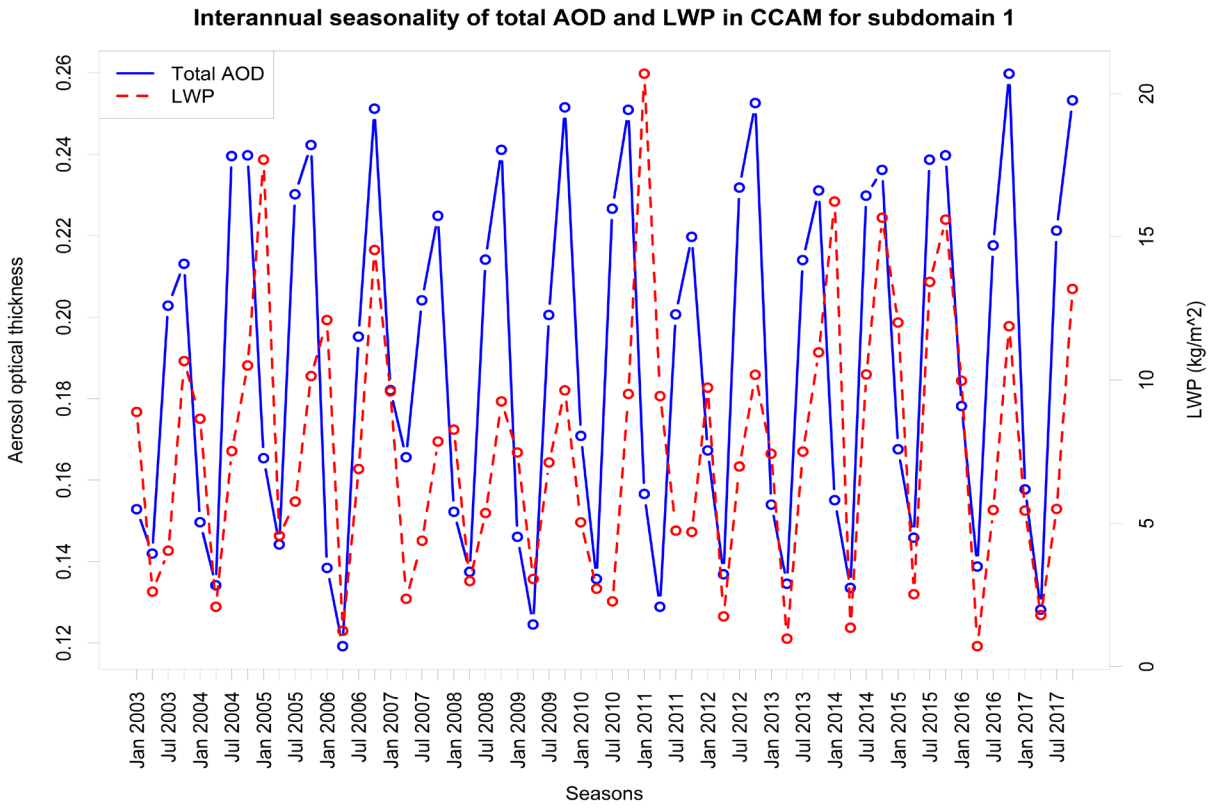

Figure 5.22: Area-averaged interannual seasonality between total AOD and liquid water path for subdomain 1

5.6.2 Compositional AOD of black carbon and liquid water path

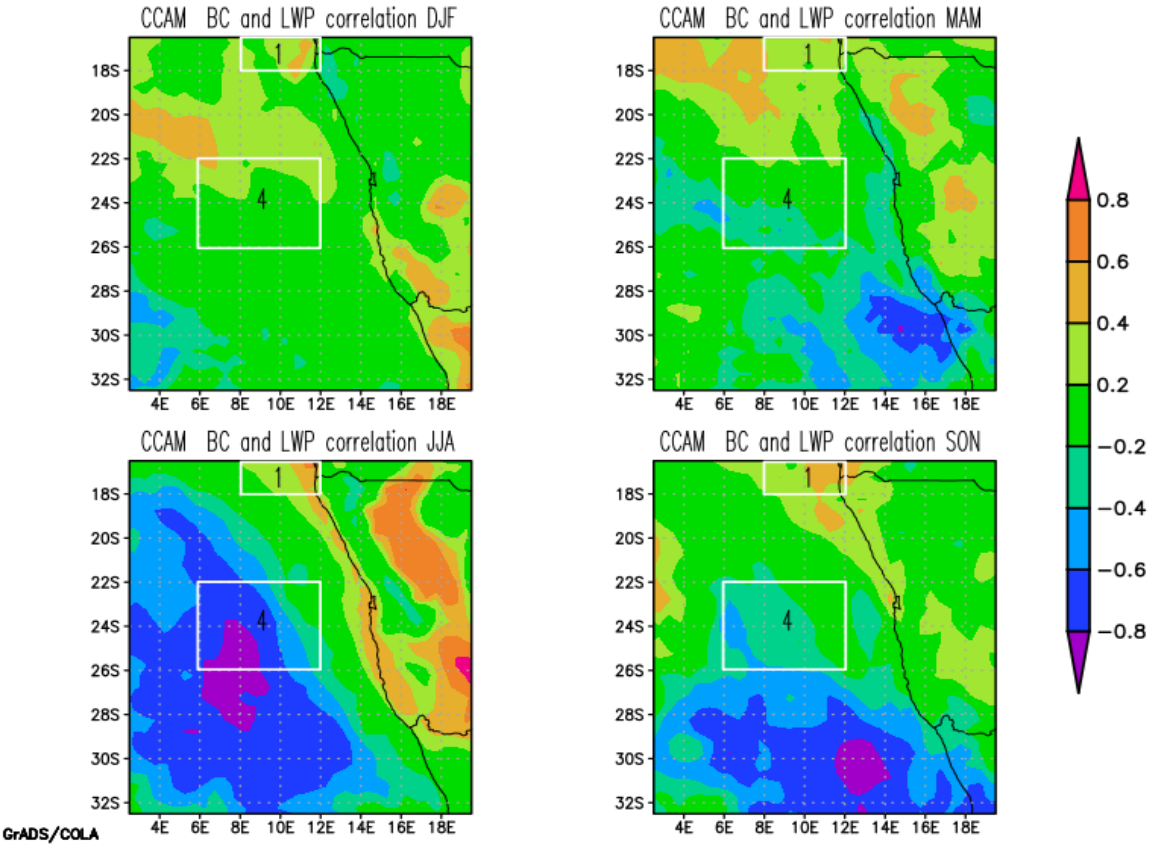

Figure 5.23: The multi-year (2002-2017) averaged spatial correlation between compositional AOD of black carbon and liquid water path

Fig. 5.23 shows the spatial correlation between the compositional AOD of black carbon and liquid water path over the Benguela Region. The spatial correlation between the compositional AOD of black carbon and liquid water path shows winter and spring have a moderate negative correlation in the southern region of the domain. Summer has a weak positive correlation between the compositional AOD of black carbon and liquid water path for the first subdomain and no correlation for the fourth subdomain. Autumn has a weak positive correlation between the compositional AOD of black carbon and liquid water path for the first subdomain and no correlation for the fourth subdomain. Winter has

a weak positive correlation between the compositional AOD of black carbon and liquid water path for the first subdomain and a strong negative correlation for the fourth subdomain. Spring has a moderate positive correlation between the compositional AOD of black carbon and liquid water path for the first subdomain and a weak negative correlation for the fourth subdomain.

Interannual seasonal plots for area-averaged seasonal between black carbon and liquid water path are similar. When black carbon increases, so does liquid water path, which does not occur across the full domain (Fig. 5.24 and Fig. 5.24a in **Annexure C**).

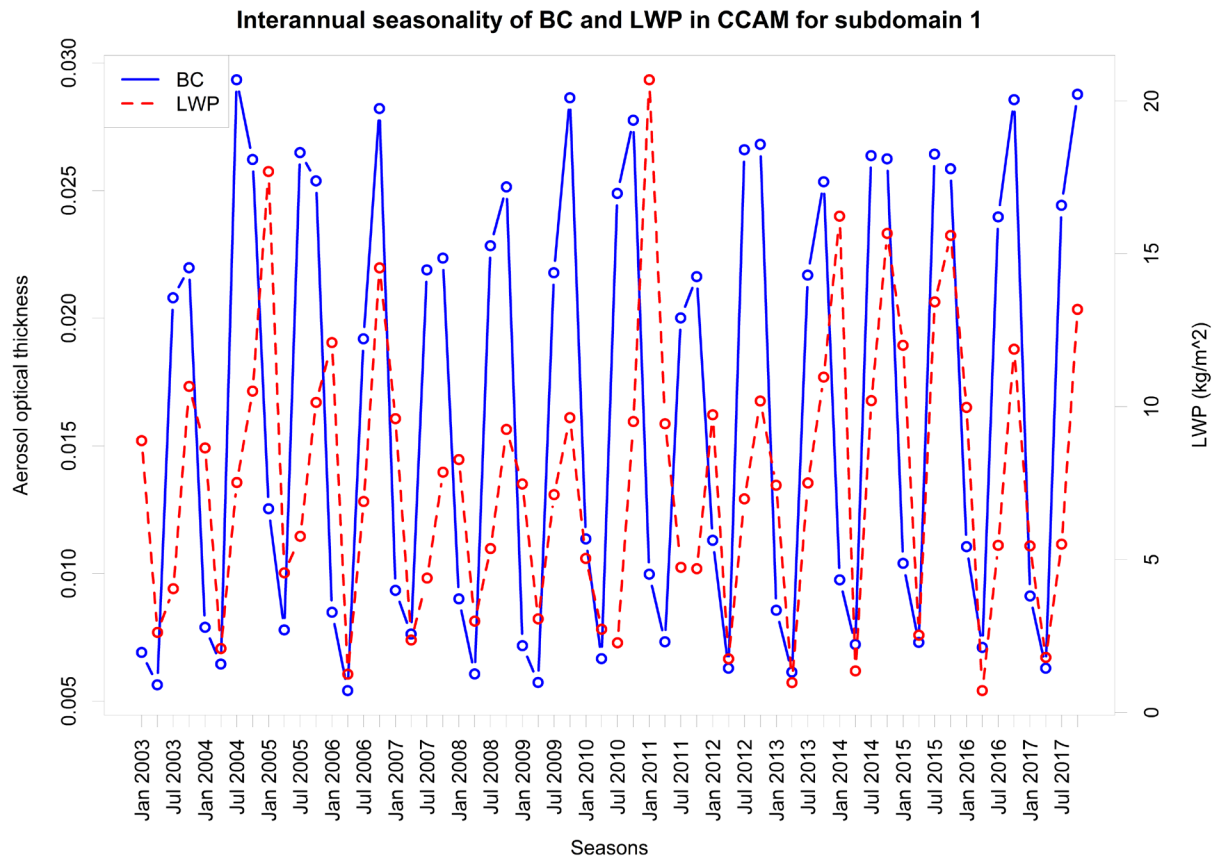

Figure 5.24: Area-averaged interannual seasonality between compositional AOD of black carbon and liquid water path for subdomain 1

5.6.3 Compositional AOD of organic carbon and liquid water path

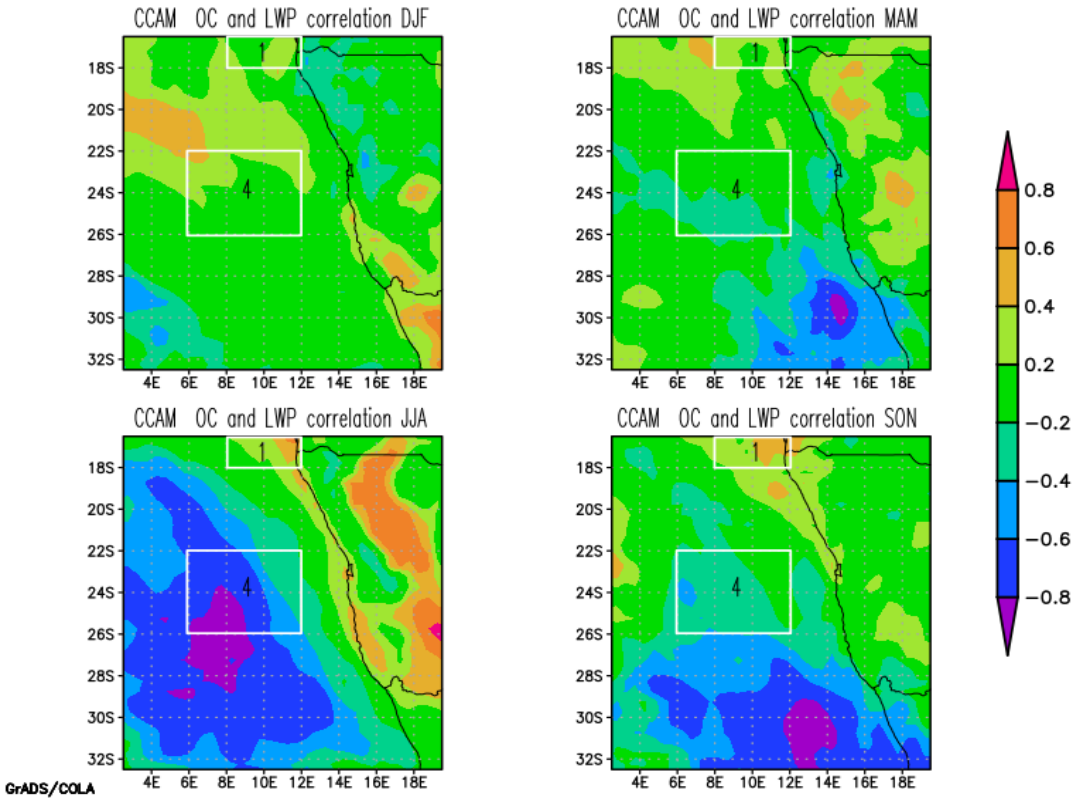

Figure 5.25: The multi-year (2002-2017) averaged spatial correlation between compositional AOD of organic carbon and liquid water path

Fig. 5.25 shows the spatial correlation between the compositional AOD of organic carbon and liquid water path over the Benguela Region. The spatial correlation between the compositional AOD of organic carbon and liquid water path shows winter and spring have a moderate negative correlation in the southern region of the domain. Summer has a weak positive correlation between the compositional AOD of organic carbon and liquid water path for the first subdomain and no correlation for the fourth subdomain. Autumn has a weak positive correlation between the compositional AOD of organic carbon and liquid water path for the first subdomain and no correlation for the fourth subdomain. Winter has a weak positive correlation between the compositional AOD of organic carbon and liquid water path for the first subdomain and a strong negative correlation for the fourth subdomain. Spring has a moderate positive correlation between the compositional

AOD of organic carbon and liquid water path for the first subdomain and a weak negative correlation for the fourth subdomain.

Interannual seasonal plots for area-averaged seasonal cycles between organic carbon and liquid water path are similar. When organic carbon increases, so does liquid water path, which does not occur across the full domain (Fig. 5.26 and Fig. 5.26 in **Annexure C)**.

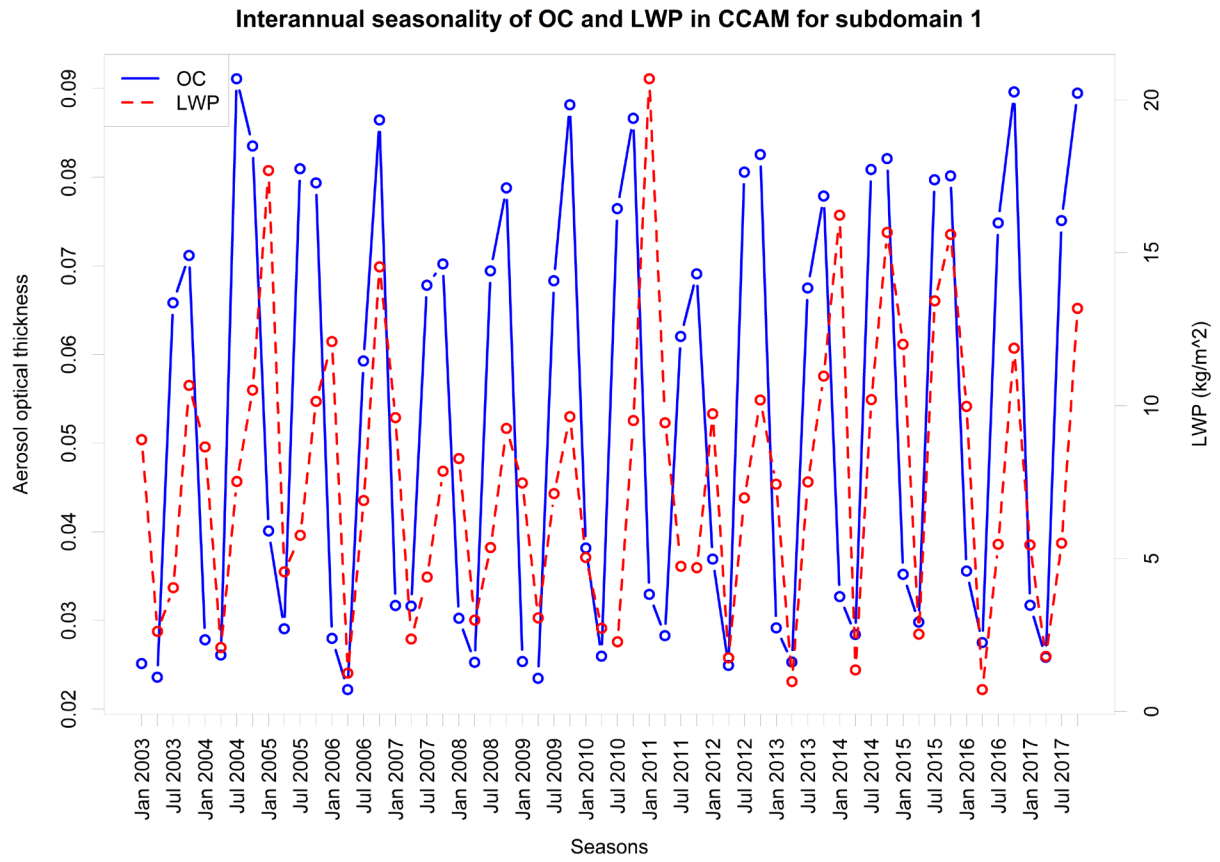

Figure 5.26: Area-averaged interannual seasonality between compositional AOD of organic carbon and liquid water path for subdomain 1

5.6.4 Compositional AOD of small dust and liquid water path

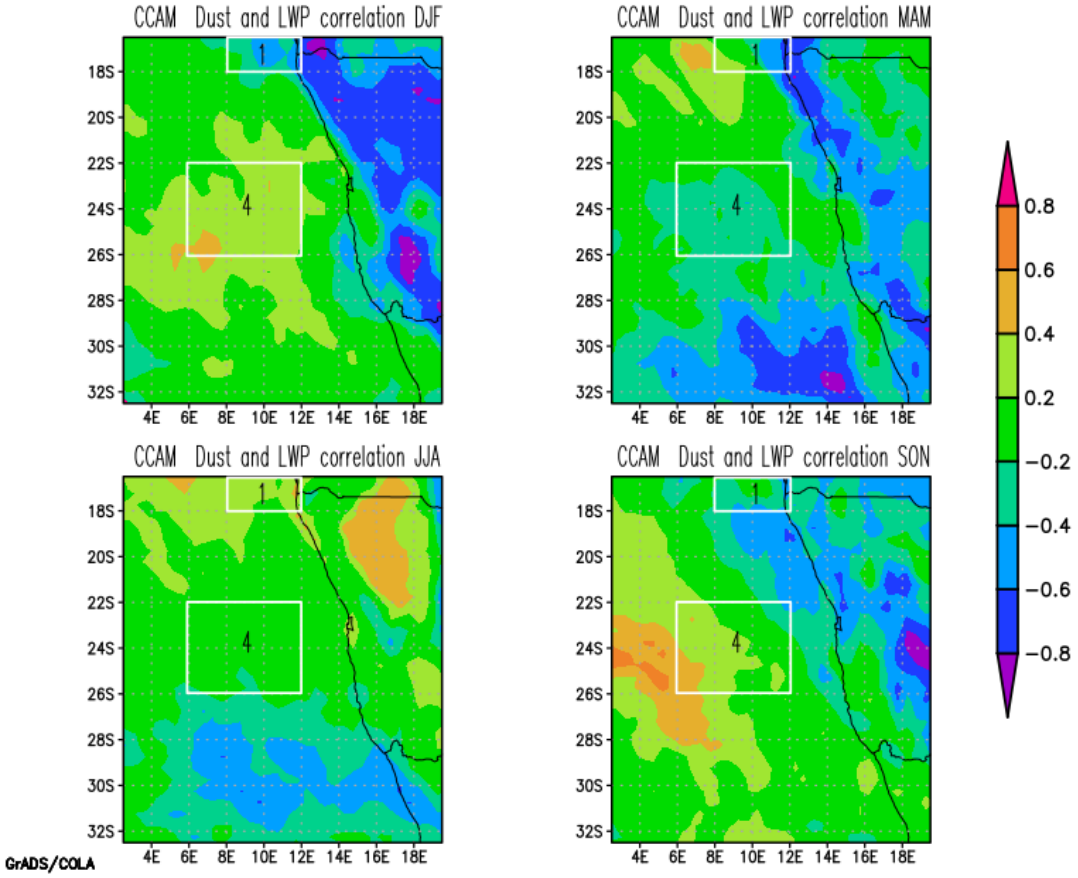

Figure 5.27: The multi-year (2002-2017) averaged spatial correlation between compositional AOD of small dust and liquid water path

Fig. 5.27 shows the spatial correlation between the compositional AOD of small dust and liquid water path over the Benguela Region. Summer has a moderate negative correlation between the compositional AOD of small dust and liquid water path for the first subdomain and a weak positive correlation for the fourth subdomain. Autumn has a weak negative correlation between the compositional AOD of small dust and liquid water path for the first subdomain and fourth subdomain. Winter has a weak positive correlation between the compositional AOD of small dust and liquid water path for the first subdomain and no correlation for the fourth subdomain. Spring has a moderate negative correlation between the compositional AOD of small dust and liquid water path for the first subdomain and a weak positive correlation for the fourth subdomain.

Interannual seasonal plots for area-averaged seasonal cycles between small dust and liquid water path are similar. When small dust increases, so does liquid water path, which does not occur across the full domain (Fig. 5.28 and Fig. 5.28a in **Annexure C**).

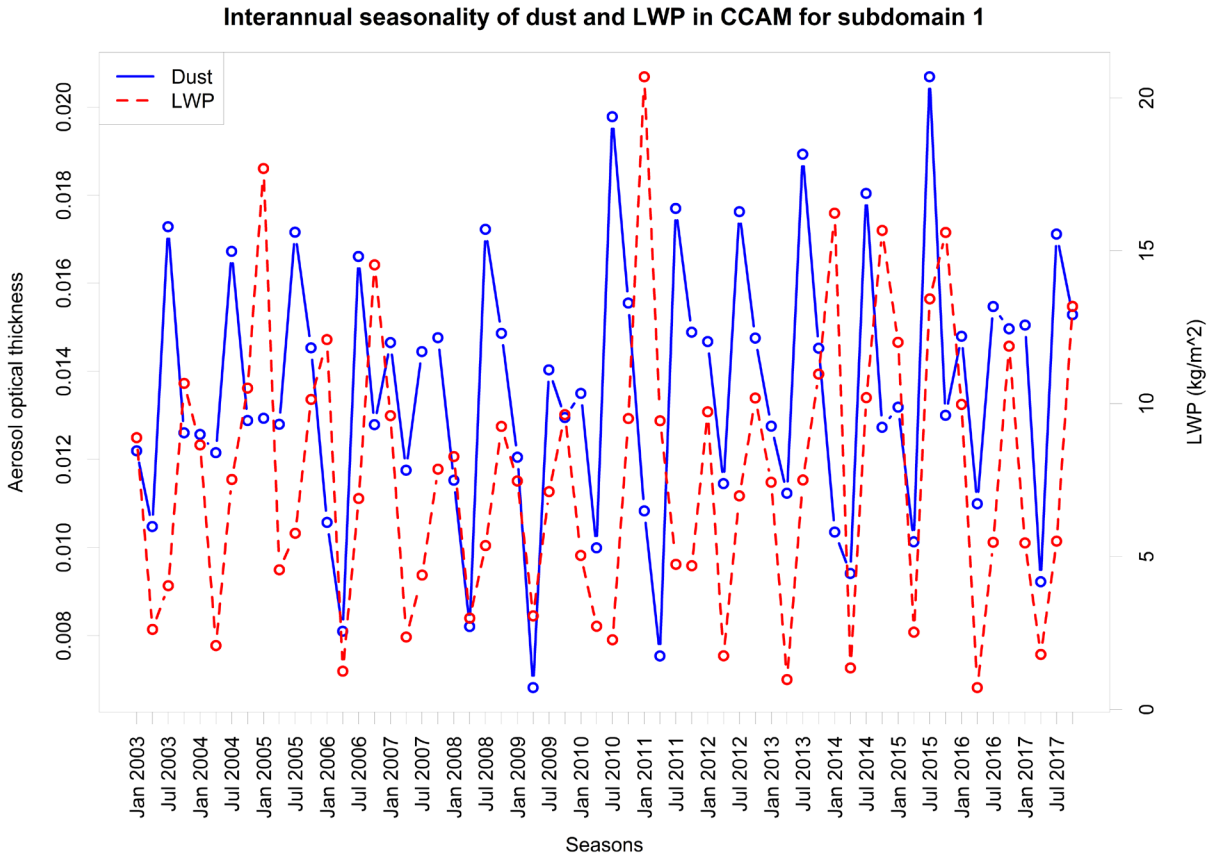

Figure 5.28: Area-averaged interannual seasonality between compositional AOD of small dust and liquid water path for subdomain 1

5.6.5 Compositional AOD of sulphate and liquid water path

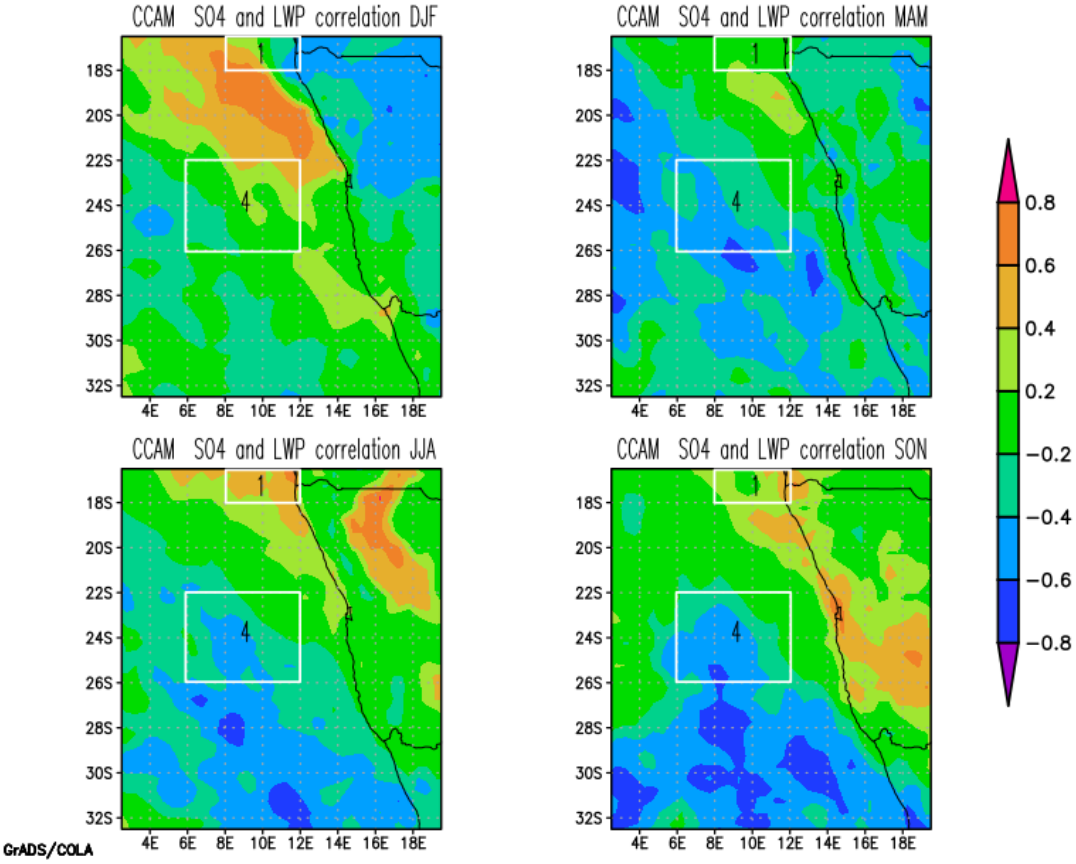

Figure 5.29: The multi-year (2002-2017) averaged spatial correlation between compositional AOD of sulphate and liquid water path

Fig. 5.29 shows the spatial correlation between the compositional AOD of sulphate and liquid water path over the Benguela Region. The spatial correlation between the compositional AOD of sulphate and liquid water path shows autumn, winter and spring have a negative correlation in the southern region of the domain. Summer has no correlation between the compositional AOD of sulphate and liquid water path for the first subdomain and the fourth subdomain. Autumn has no correlation between the compositional AOD of sulphate and liquid water path for the first subdomain and a moderate negative the fourth subdomain. Winter has a moderate positive correlation between the compositional AOD of sulphate and liquid water path for the first subdomain

and a weak negative correlation for the fourth subdomain. between the compositional AOD of sulphate and liquid water path

The results show that the compositional AOD of sulphate is negatively correlated with liquid water path, indicating that when the compositional AOD of sulphate increases, liquid water path decreases at the southern domain.

Interannual seasonal plots for area-averaged seasonal cycles between sulphate and liquid water path are similar. When sulphate increases, so does liquid water path, which does not occur across the full domain (Fig. 5.30 and Fig. 5.30a in **Annexure C**).

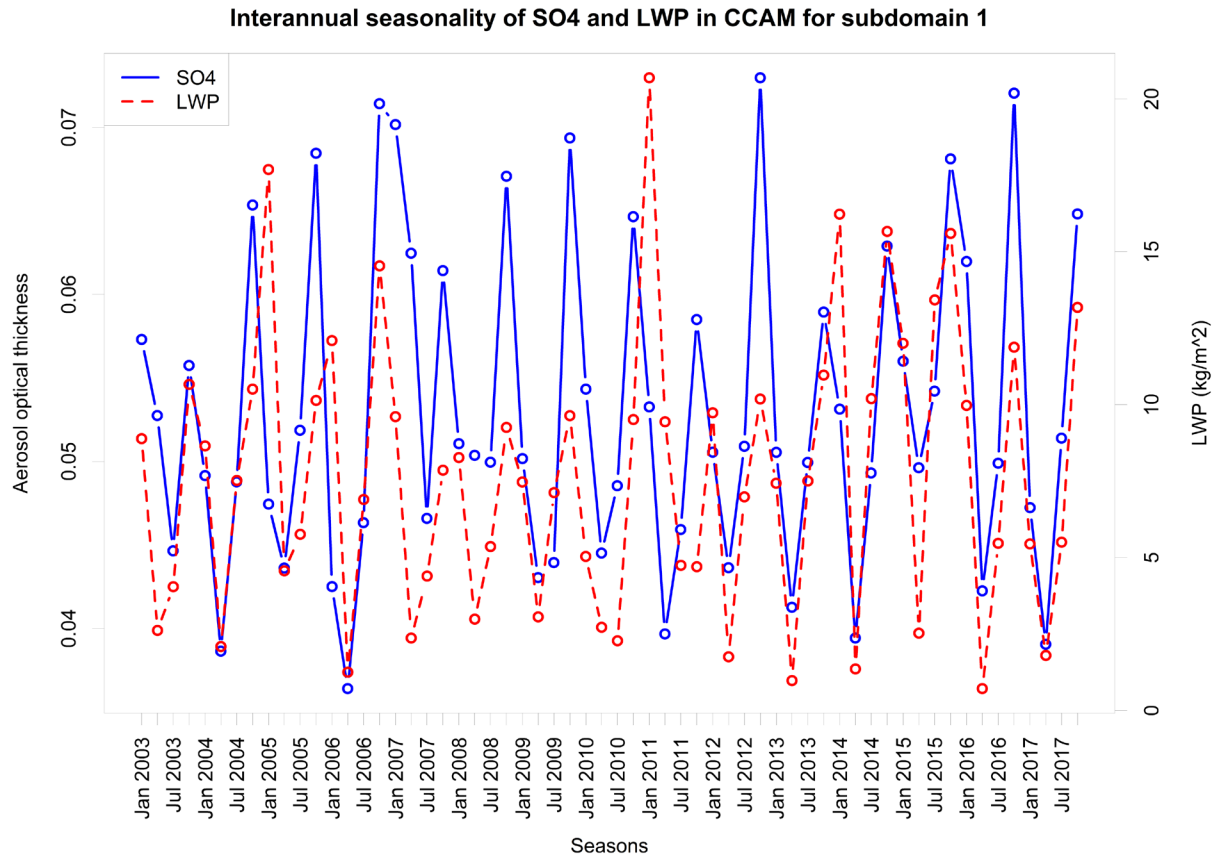

Figure 5.30: Area-averaged interannual seasonality between compositional AOD of sulphate and liquid water path for subdomain 1

5.6.6 Compositional AOD of sea-salt and liquid water path

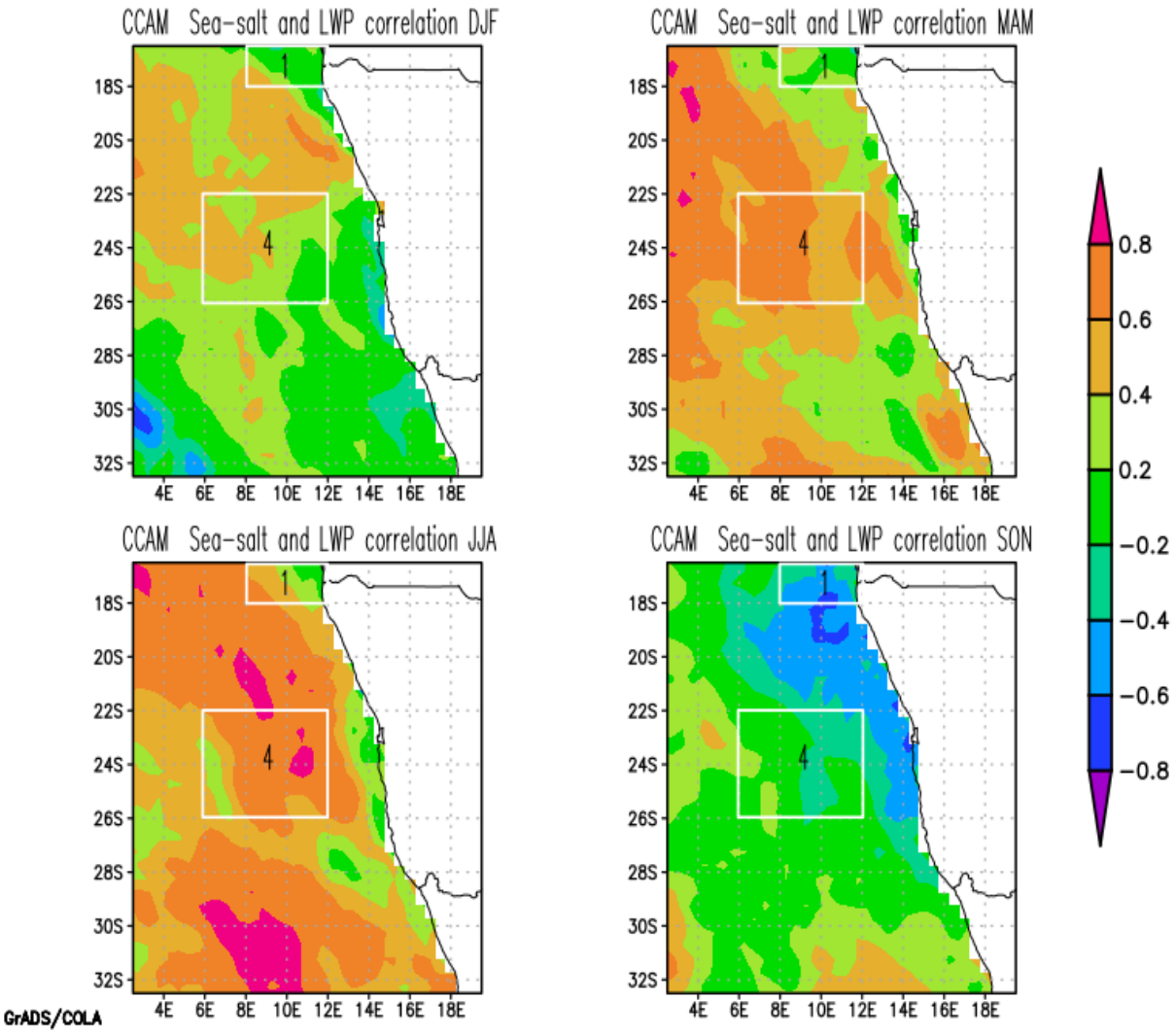

Figure 5.31: The multi-year (2002-2017) averaged spatial correlation between compositional AOD of sea-salt and liquid water path

Fig. 5.31 shows the spatial correlation between the compositional AOD of sea salt and liquid water path over the Benguela Region. The spatial correlation between the compositional AOD of sea salt and liquid water path shows that all seasons have a positive correlation in the whole domain except in spring. Summer has no correlation between the compositional AOD of sea salt and liquid water path for the first subdomain and a weak positive correlation for the fourth subdomain. Autumn has a weak positive

correlation between the compositional AOD of sea salt and liquid water path for the first subdomain and a strong positive correlation for the fourth subdomain. Winter has a moderate positive correlation between the compositional AOD of sea salt and liquid water path for the first subdomain and a strong positive correlation for the fourth subdomain. Spring has a strong negative correlation for the first subdomain and no correlation for the fourth subdomain.

Interannual seasonal plots for area-averaged seasonal cycle between sea salt and liquid water path are similar. When sea salt increases, so does liquid water path, which does not occur across the full domain (Fig. 5.32 and Fig. 5.32a in **Annexure C**).

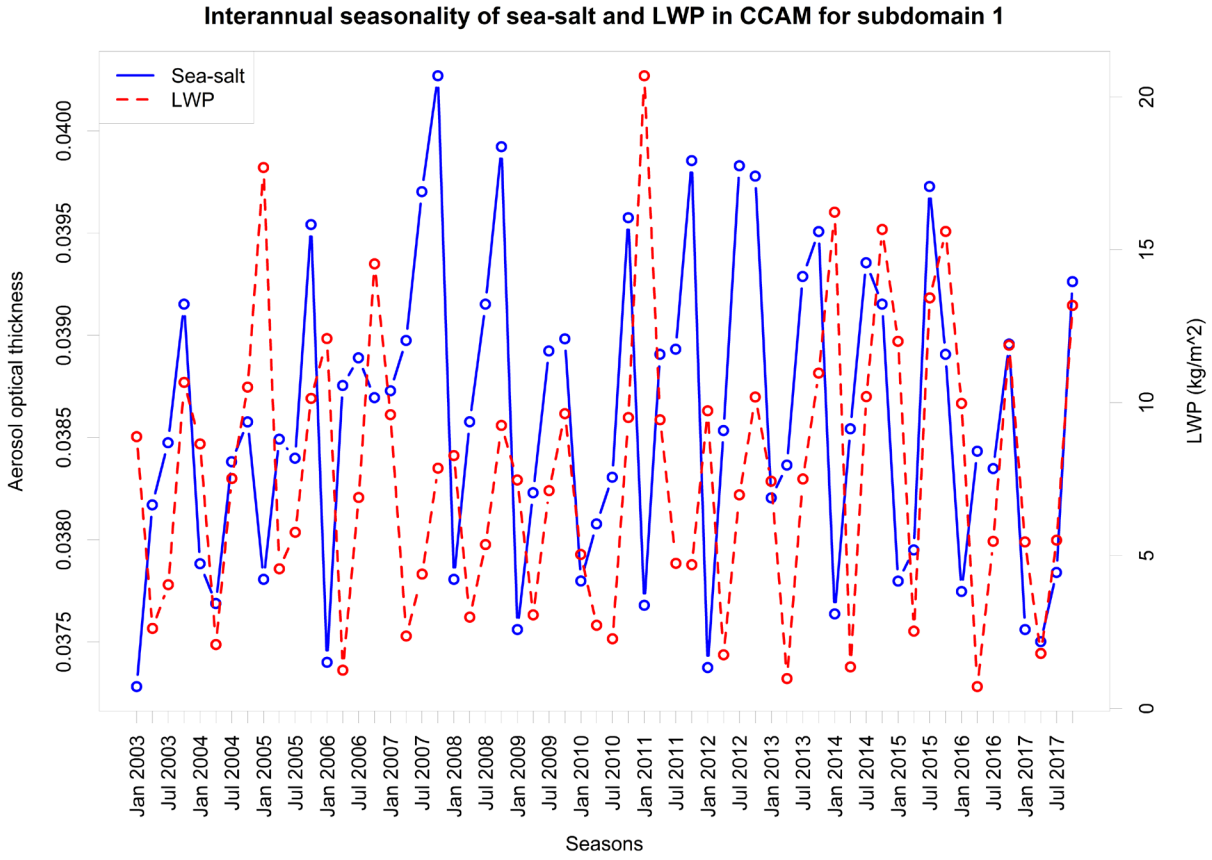

Figure 5.32: Area-averaged interannual seasonality between compositional AOD of sea-salt and liquid water path for subdomain 1

5.6.7 Summary

We evaluated the linear association between liquid water path, total AOD and compositional AOD (black carbon, organic carbon, sulphate, small dust and sea salt) using correlation. The results, as shown in Table 5.2, suggest that when any correlation was found, it was more often positive in the northern regions and negative in the southern domain. Aerosol optical depth attributable to black carbon and organic carbon have moderate or strong negative correlations with liquid water path in winter. Aerosol optical depth attributable to sulphate had no strong correlation with liquid water path. Dust aerosols (i.e. small dust) had no correlation with liquid water path, but this was expected due to a lack of interactions between the two variables. Marine aerosols (i.e. sea salt) have strong positive correlations in autumn and winter, and strong negative correlations in spring with liquid water path. Interannual seasonal plots for total AOD and compositional AOD (black carbon, organic carbon, small dust, sulphate and sea salt) and liquid water path are similar, though not always.

Table 5. 2: Correlation between liquid water path, total AOD and compositional AOD (i.e. black carbon, organic carbon, small dust, sulphate and sea salt).Table 5.1: Correlation between liquid water path, total AOD and compositional AOD (i.e. black carbon, organic carbon, small dust, sulphate and sea salt).

Liquid water path to:	Subdomain	Summer	Autumn	Winter	Spring
Total AOD	1st	No correlation	No correlation	Moderate positive	Weak positive
	4th	Weak positive	Moderate negative	Moderate negative	Moderate negative
Compositional AOD of black carbon	1st	Weak positive	Weak positive	Weak positive	Moderate positive

	4th	No correlation	No correlation	Strong negative	Weak negative
Compositional AOD of organic carbon	1st	Weak positive	Weak positive	Weak positive	Moderate positive
	4th	No correlation	No correlation	Strong negative	Weak negative
Compositional AOD of small dust	1st	Moderate negative	Weak negative	Weak positive	Moderate negative
	4th	Weak positive	Weak negative	No correlation	Weak positive
Compositional AOD of sulphate	1st	No correlation	No correlation	Moderate positive	Weak positive
	4th	No correlation	Moderate negative	Weak negative	Moderate negative
Compositional AOD of sea-salt	1st	No correlation	Weak positive	Moderate positive	Strong negative
	4th	Weak positive	Strong positive	Strong positive	No correlation

CHAPTER 6: CONCLUSIONS

The aim of this study was to evaluate the representation of simulated aerosols and its effect on stratocumulus clouds in the Benguela Region in the CCAM model. To achieve this goal, three objectives were set. These will be summarised individually, and then the results from the study will be synthesised.

6.1 Evaluation of aerosols in the CCAM model

Objective 1: To investigate the seasonal, temporal and spatial variations of simulated total AOD and compositional AOD (i.e. black carbon, organic carbon, sulphate, small dust and sea salt) against satellite observations over the Benguela Region.

This study evaluated of the simulated AOD from the CCAM model against satellite observations. The first aspect was to evaluate how the CCAM simulates total AOD by comparing CCAM simulations to measured AOD from MODIS satellite observations. An addition to the first aspect was to evaluate how the CCAM simulates compositional AOD (i.e. black carbon, organic carbon, sulphate, small dust and sea salt) by comparing CCAM simulations to compositional AOD from MERRA reanalysis. Comparisons of magnitude, spatial patterns and peaks between CCAM simulations and MODIS measurements (for total AOD) and MERRA simulations (for compositional AOD (i.e. black carbon, organic carbon, sulphate, small dust and sea-salt)) were done. Secondly, quantitative analysis of aerosols using bias, root mean square error and correlation was examined to compare how close the CCAM simulation outputs were to MODIS Aqua satellite observations and MERRA reanalysis.

This study found that AOD attributable to black carbon and organic carbon simulated lower magnitudes in the CCAM compared to MODIS and MERRA. The spatial patterns and peaks simulated by the CCAM are similar to MODIS observations and MERRA, though there are slight differences. The peak Aerosol optical depths are seen during biomass burning periods in the CCAM and measurements, which highlights that the emissions and transport of these aerosols are captured in the CCAM. Aerosol optical

depth attributable to sulphate simulated higher magnitudes in the CCAM compared to MERRA. The spatial patterns and peaks simulated by CCAM are different to MERRA. Dust aerosols (i.e. small dust) simulated lower magnitudes in the CCAM compared to MERRA. The spatial patterns and peaks simulated by the CCAM are similar to MERRA, though there are slight differences. Peaks are seen throughout all seasons, which is expected because the transportation of dust depends on wind, which is omnipresent. Marine aerosols (i.e. sea salt) simulated lower magnitudes in the CCAM compared to MERRA. Sea-salt aerosols in the CCAM are diagnosed at each time step and are a function of wind speeds at 10 m. Because sea-salt aerosols are diagnosed, it means vertical and horizontal transportation of these aerosols is neglected. Sea salt simulated by CCAM has different spatial pattern and peaks compared to MERRA, this is most likely due to the parameterisation of sea-salt emissions in CCAM.

This study also found that aerosols, during the biomass burning season, were underestimated by the CCAM, particularly in areas where the maximum AOD values were simulated. The highest magnitude of error occurred in areas where the maximum magnitude was simulated across all seasons, indicating that the CCAM has the largest errors over the peak areas. There is a positive correlation indicating that there is a linear association with how CCAM simulates aerosols compared to MODIS or MERRA. Aerosol optical depth attributable to sulphate were overestimated by CCAM. The magnitude of error was low. Dust aerosols (i.e. small dust) and marine aerosols (i.e. sea salt) were underestimated by the CCAM, particularly in areas where the maximum magnitude was simulated across all seasons. A lower magnitude of error means the more precise the CCAM is to the observed MODIS value. For most of the domain, the magnitude of error is significantly lower. Based on the qualitative and quantitative outcomes, it is concluded that the CCAM does simulate the distribution of aerosols well.

In addition, this study found that aerosols, during the biomass burning season, have a peak interannual seasonality in spring and have the minimum in autumn in the CCAM, MODIS and MERRA. The differences in interannual seasonality are due to different schemes in the CCAM and MERRA or lack of association with relative humidity. Dust aerosols (i.e. small dust) have different interannual seasonal peaks when simulated in the CCAM and MERRA. Marine aerosols (i.e. sea salt) have different interannual seasonal

peaks when simulated in the CCAM and MERRA. Sea salt was expected to be different compared to MERRA because it is a diagnosed variable in the CCAM.

6.2 Effects of aerosols on cloud fraction

Objective 2: To examine the effects of simulated total AOD and compositional AOD (i.e. black carbon, organic carbon, sulphate, small dust and sea salt) on stratocumulus cloud fraction.

This study evaluated simulated cloud fractions from the CCAM model against satellite observations. The first aspect was to evaluate how the CCAM simulates cloud fractions by comparing the CCAM simulations to measured cloud fractions from AIRS observations.

Comparisons of magnitude, spatial patterns and peaks of CCAM simulations against AIRS (ascending) and AIRS (descending) satellite observations were done. Secondly, quantitative analysis of cloud fraction using bias, root mean square error and correlation was examined to compare how close CCAM simulation outputs were to AIRS (ascending) and AIRS (descending) satellite observations. This study found that the CCAM underestimates cloud fraction at the northern region and the coast for all seasons and the CCAM overestimates cloud fraction in the southern region of the domain over the ocean when compared to satellite observations. Also, the CCAM has a magnitude of error ranging between 40 and 60% at the northern region and 0 and 30% in the southern region of the ocean against satellite observations. The correlation between the CCAM and satellite observations was more often positive although not strong.

This study also found that when any correlation between cloud fraction and aerosols was found, it was more often positive in the northern regions and negative in southern domain. In addition, it was found that when AOD was >0.22, there was no correlation ($r = -0.19 – 0.19$) between AOD and cloud fraction. When AOD was <0.22, AOD and cloud fraction were positively correlated ($r = 0.20 – 0.79$) in the northern region of the domain. Aerosols during the biomass burning season had moderate or strong negative correlations ($r = -0.70 - -0.59$) with cloud fraction in winter. Aerosol optical depth attributed to sulphate had

strong positive correlations (r = 0.60 – 0.79) with cloud fraction in summer. Dust aerosols (i.e. small dust) and marine aerosols (i.e. sea salt) had no strong correlations (r = -0.19 – 0.19) with cloud fraction. Interannual seasonal plots for total AOD and compositional AOD (black carbon, organic carbon, small dust, sulphate and sea salt) and cloud fraction are similar, though not always.

6.3 Effects of aerosols on liquid water path

Objective 3: To determine the effects of simulated total AOD and compositional AOD (i.e. black carbon, organic carbon, sulphate, small dust and sea-salt) on liquid water path stratocumulus clouds.

This study evaluated simulated liquid water path from the CCAM model against satellite observations. The first aspect was to evaluate how the CCAM simulates liquid water path by comparing the CCAM simulations to measured liquid water path from MODIS Terra and Aqua satellite observations. Comparisons of magnitude, spatial patterns and peaks of CCAM simulations against MODIS Terra and MODIS Aqua satellite observations of liquid water path were done. Secondly, quantitative analysis of liquid water path using mean error, magnitude of error and correlation was examined to compare how close the CCAM simulation outputs were to MODIS Terra and MODIS Aqua satellite observations.

This study found that the CCAM underestimated liquid water path over the ocean when compared to satellite observations. Also, the CCAM produced a magnitude of error ranging between 10 and 50 kg/m^2 and 10 and 60 kg/m^2 when compared to satellite observations, respectively. Comparing liquid water path from the CCAM and satellite observations, there was more often a positive correlation, though not strong.

This study also found that when any correlation between liquid water path and aerosols was found, it was more often positive in the northern regions and negative in the southern domain. Aerosols during the biomass burning season had moderate or strong negative correlation (r = -0.70 - -0.59) with liquid water path in winter. Aerosol optical depth attributable to sulphate had no strong correlation to liquid water path. Dust aerosols (i.e. small dust) had no correlation (r = -0.19 – 0.19) with liquid water path, but this was

expected due to lack of interactions between the two variables. Marine aerosols (i.e. sea salt) have strong positive correlations (r = 0.60 – 0.79) in autumn and winter, and strong negative correlations (r = -0.79 - -0.60) in spring with liquid water path. Interannual seasonal plots for total AOD and compositional AOD (black carbon, organic carbon, small dust, sulphate and sea salt) and liquid water path are similar, though not always.

6.4 Synthesised results

The CCAM simulates the spatial distribution and peaks of aerosols, cloud fraction and liquid water path well. This can be seen in the spatial distribution and seasonal cycles simulated across all seasons in the CCAM. However, CCAM simulates lower magnitudes for aerosols, cloud fraction and liquid water, is representative to such an extent that it could be used to study the atmospheric interactions and relationships between individual variables (i.e., compositional AOD of black carbon and cloud fraction), because it has advanced aerosol and cloud schemes. Aerosols do influence cloud fraction and liquid water path, either directly proportionally or indirectly proportionally. However, in most seasons, the relationship between aerosols and cloud fraction or liquid water path is not strongly correlated. These results suggest that the influence of cloud fraction and liquid water path is not due to aerosols only, but also other parameters, such as the meteorological variables (i.e. temperature, relative humidity, winds) and weather systems. In addition, this study focused on AOD only, but AOD is a full column not just where clouds are and AOD is not concentration – perhaps a different aerosol parameter would be better to work with.

6.5 Limitations and future research

This study found interesting results. In addition, the aerosol schemes and the attributes that feed the model such as emission inventories should be evaluated to determine whether any improvements on accuracy and precision could be developed. Emission inventories can be improved as it was found that there are differences between the model and measurements.

This study also found that when AOD was >0.22, there was no correlation between AOD and cloud fraction. When AOD was <0.22, AOD and cloud fraction were positively correlated in the northern region of the domain. This threshold 0.22 value raises multiple questions that We recommend future AOD and cloud fraction interactions studies could assess: (1) Can the 0.22 threshold be applied to the correlation against cloud fraction in all regions globally? (2) Can the 0.22 threshold be replicated in satellite and ground/airplane-based measurement studies? (3) Can this 0.22 threshold be standardised, or does the threshold value change based on location, temporal resolution, or model?

In addition, We would recommend further studies on the CCAM that use different aerosol-cloud parameterisations to compare the differences and similarities.

This study also found that marine aerosols (i.e. sea salt) simulated lower magnitudes in the CCAM compared to MERRA. Sea-salt aerosols in CCAM are diagnosed at each time step and are a function of wind speeds at 10 m. Because sea-salt aerosols are diagnosed, it means vertical and horizontal transportation of these aerosols is not simulated. Sea salt simulated by the CCAM has different spatial patterns and peaks compared to MERRA, which is most likely due to the parameterisation of sea salt emissions in CCAM. We recommend that sea salt be improved to a prognostic variable.

This study also found that marine aerosols (i.e. sea-salt) have strong positive correlations in autumn and winter, and strong negative correlations in spring to liquid water path. Aerosols have moderate or strong negative correlation with liquid water path in winter, which is questionable, because it is post-biomass burning season. Aerosols have moderate or strong negative correlations with cloud fractions in winter, which is questionable, because it is post-biomass burning season. Based on the previous sentences, We recommend that future studies should explore why correlations are strong in those particular seasons.

Annexure A

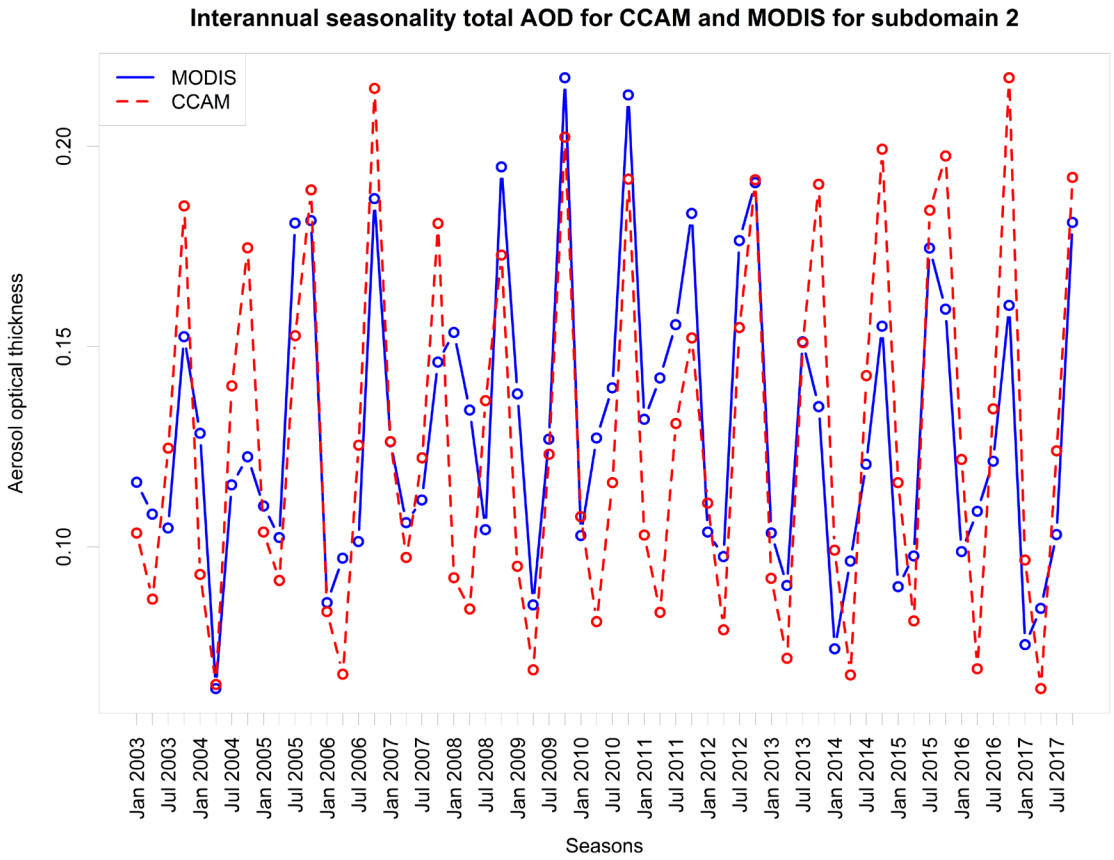

Figure 4.13a: Area-averaged interannual seasonality of total AOD between CCAM simulations and MODIS observations for subdomain 2

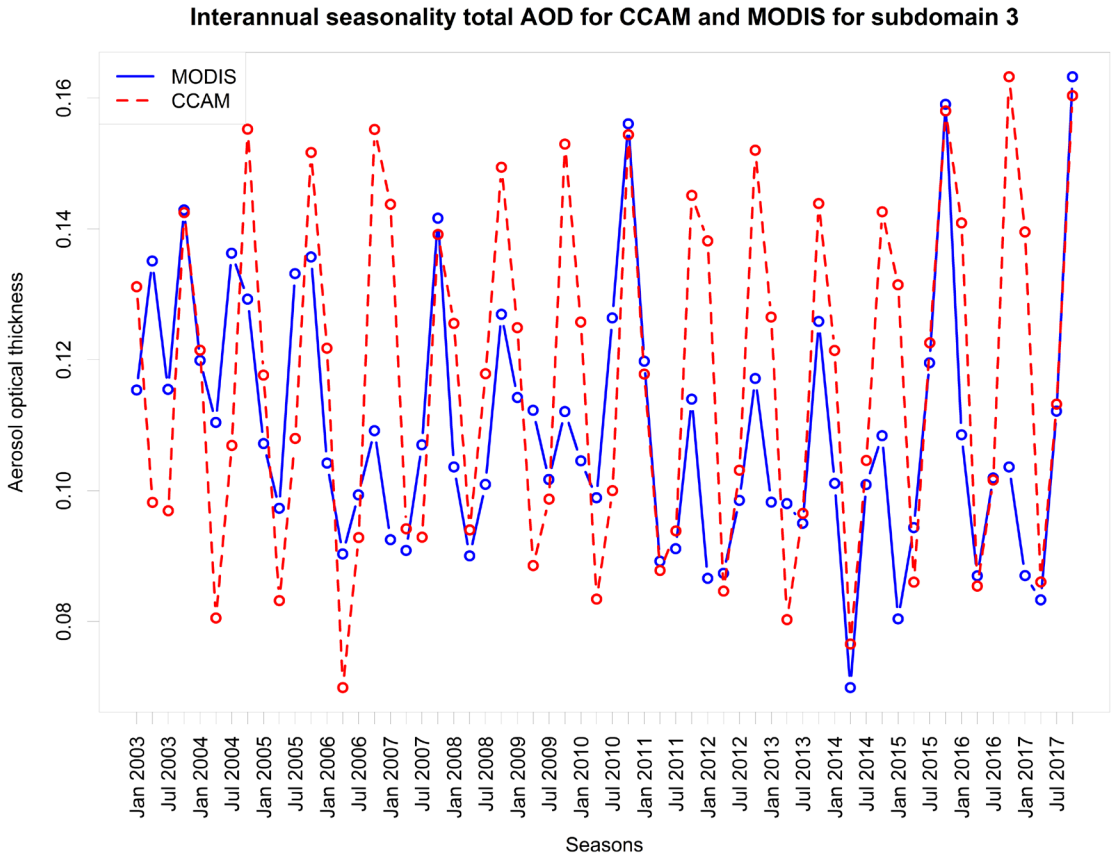

Figure 4.13b: Area-averaged interannual seasonality of total AOD between CCAM simulations and MODIS observations for subdomain 3

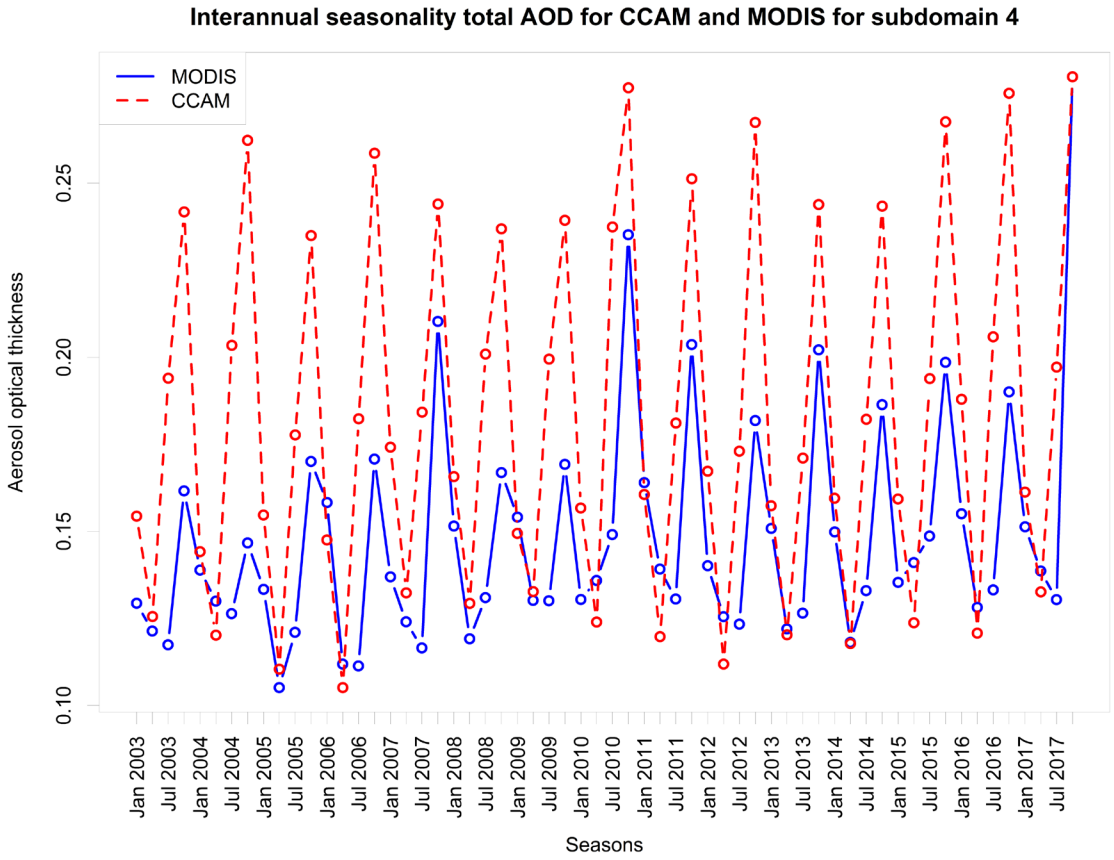

Figure 4.13c: Area-averaged interannual seasonality of total AOD between CCAM simulations and MODIS observations for subdomain 4

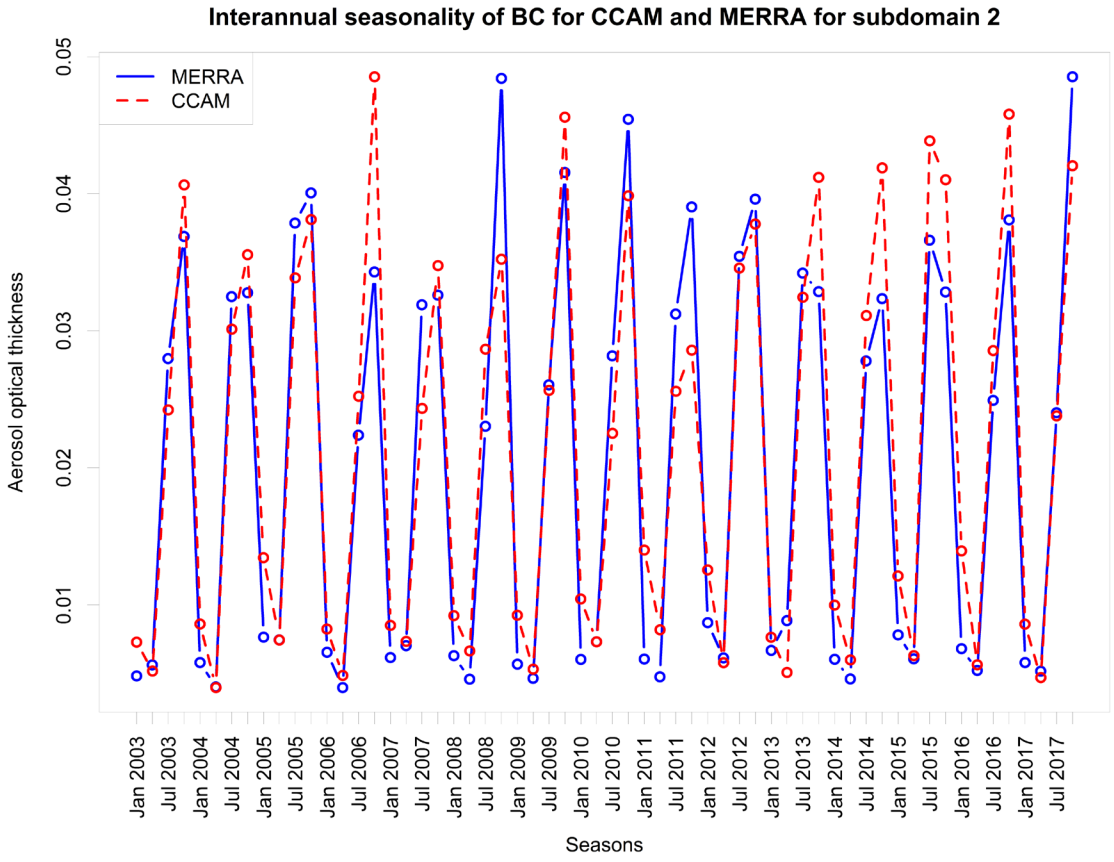

Figure 4.14a: Area-averaged interannual seasonality of compositional AOD of black carbon between CCAM simulations and MERRA for subdomain 2

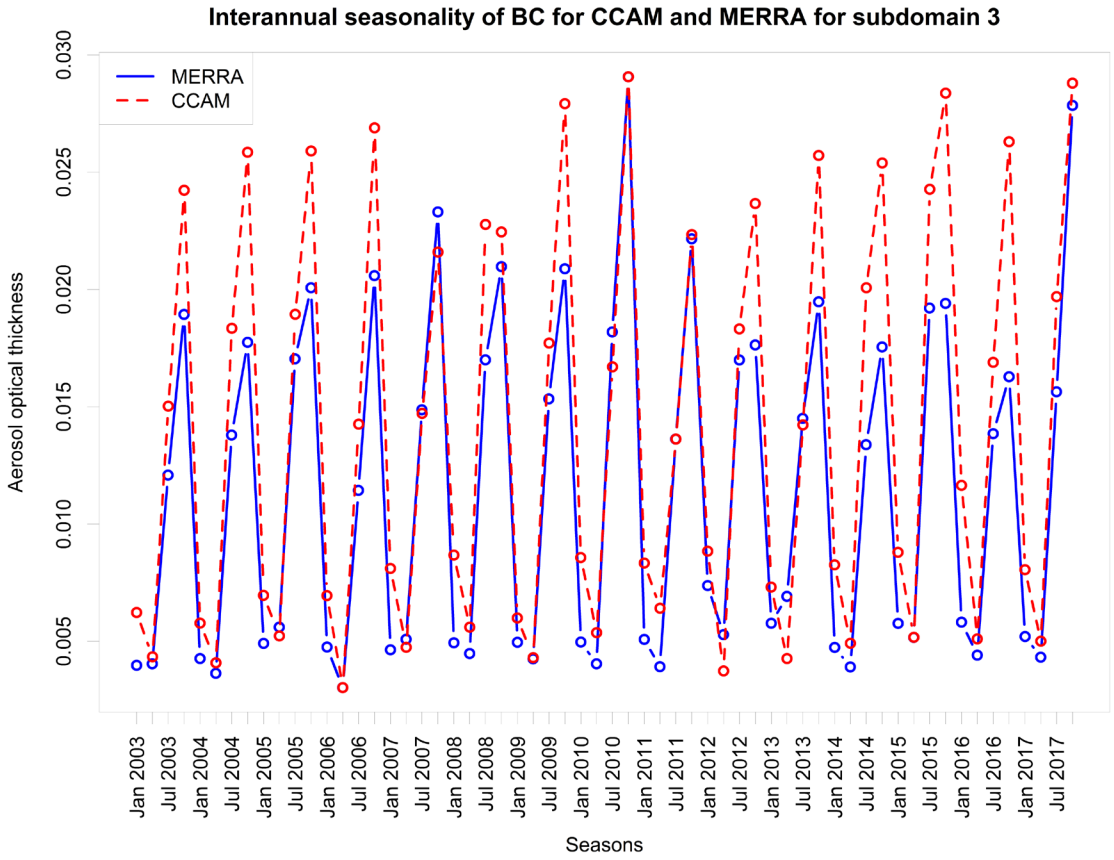

Figure 4.14b: Area-averaged interannual seasonality of compositional AOD of black carbon between CCAM simulations and MERRA for subdomain 3

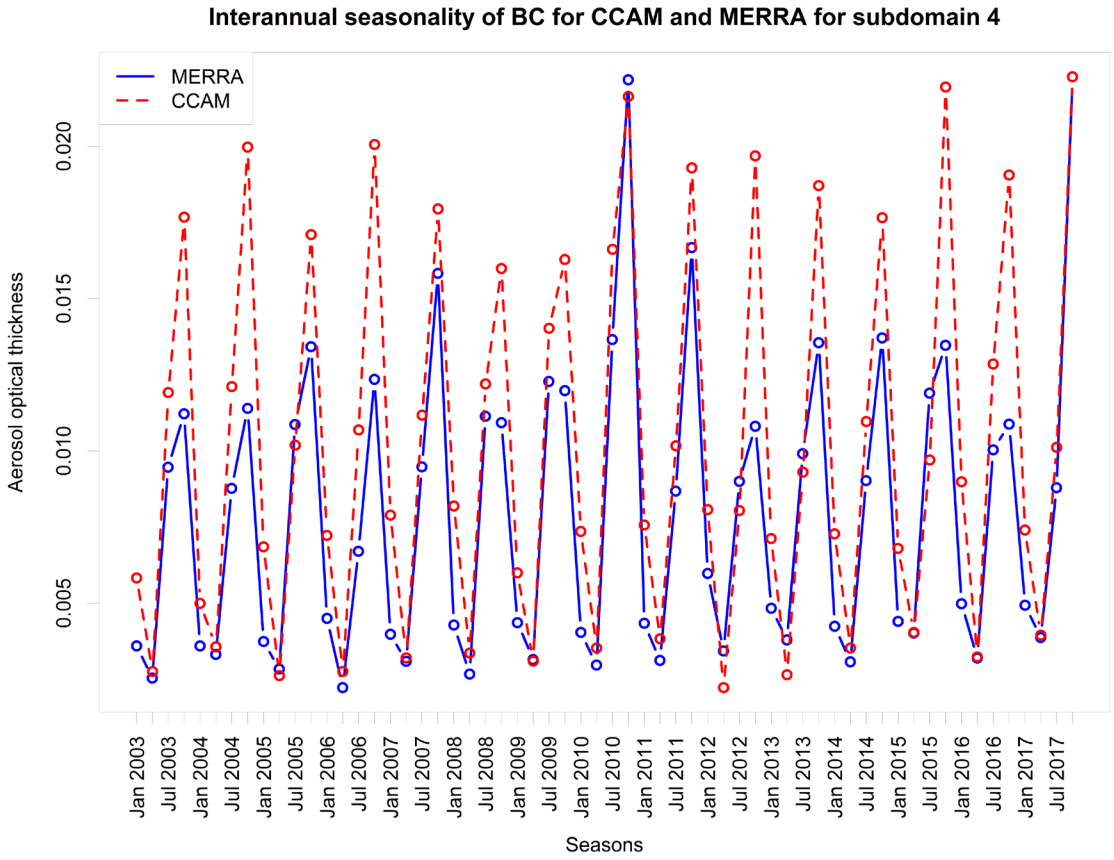

Figure 4.14c: Area-averaged interannual seasonality of compositional AOD of black carbon between CCAM simulations and MERRA for subdomain 4

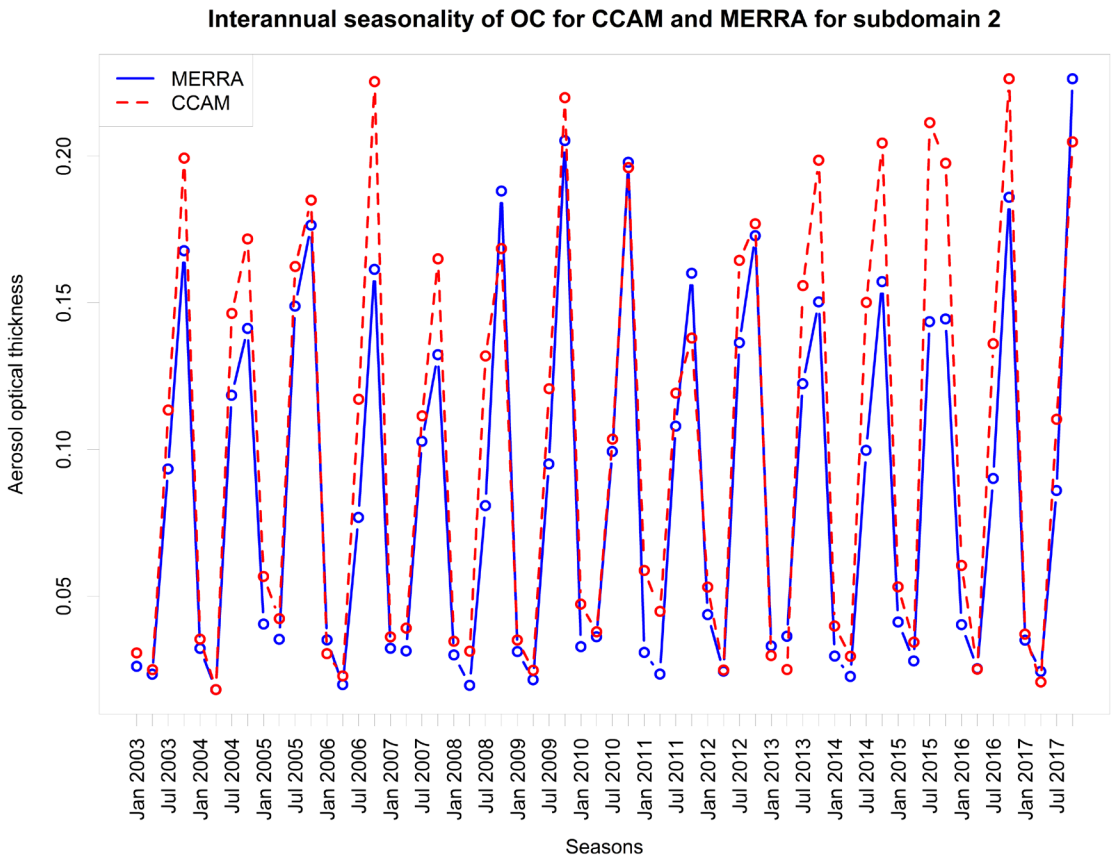

Figure 4.15a: Area-averaged interannual seasonality of compositional AOD of organic carbon between CCAM simulations and MERRA for subdomain 2

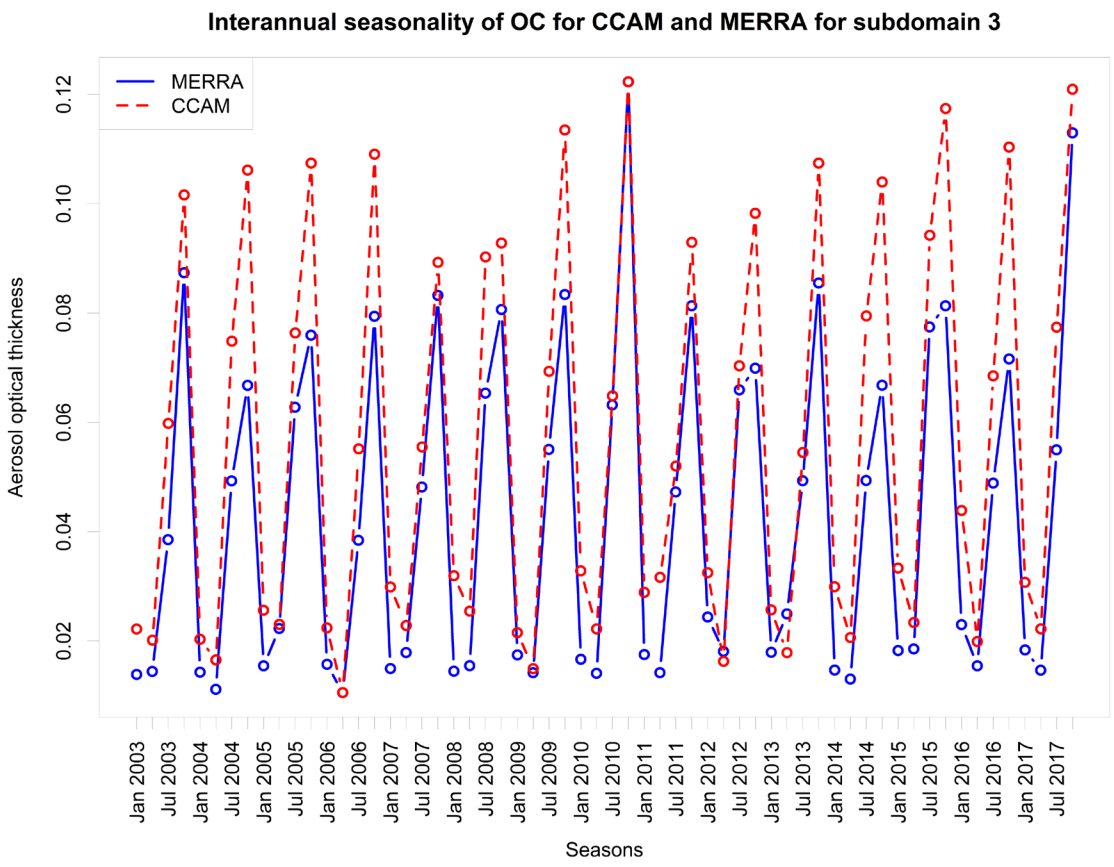

Figure 4.15b: Area-averaged interannual seasonality of compositional AOD of organic carbon between CCAM simulations and MERRA for subdomain 3

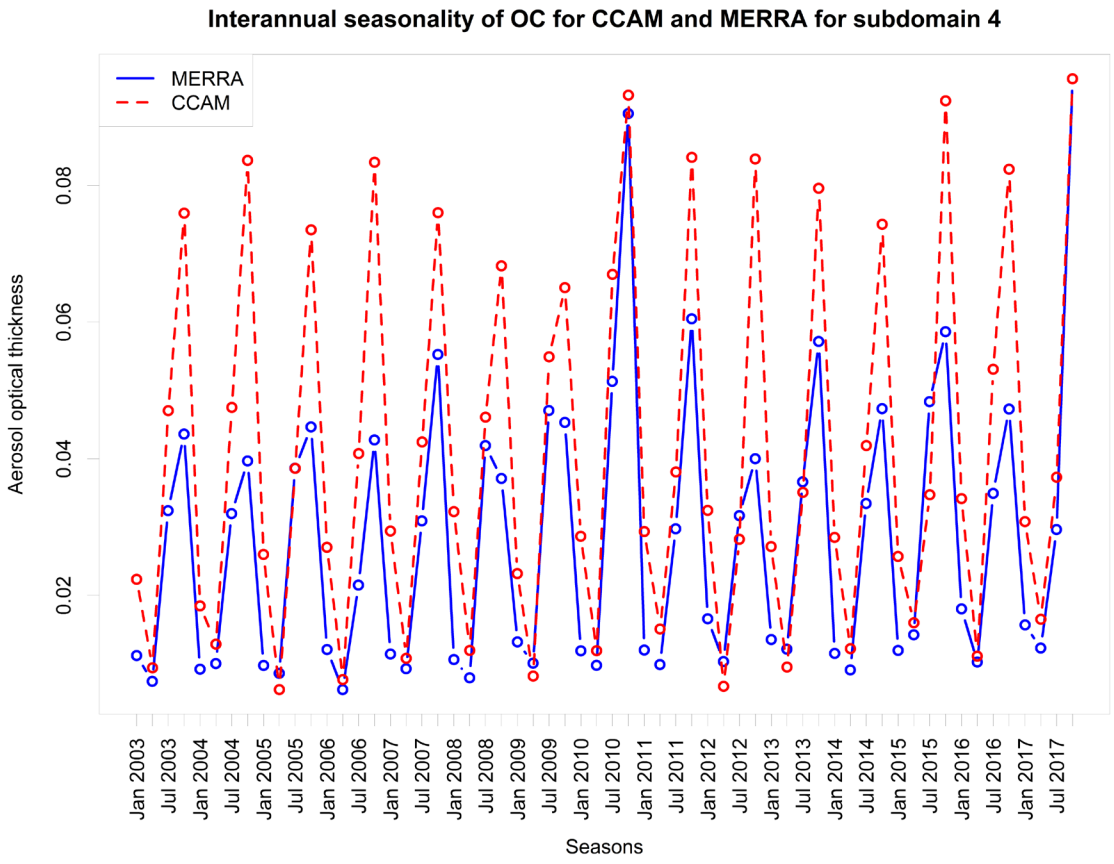

Figure 4.15c: Area-averaged interannual seasonality of compositional AOD of organic carbon between CCAM simulations and MERRA for subdomain 4

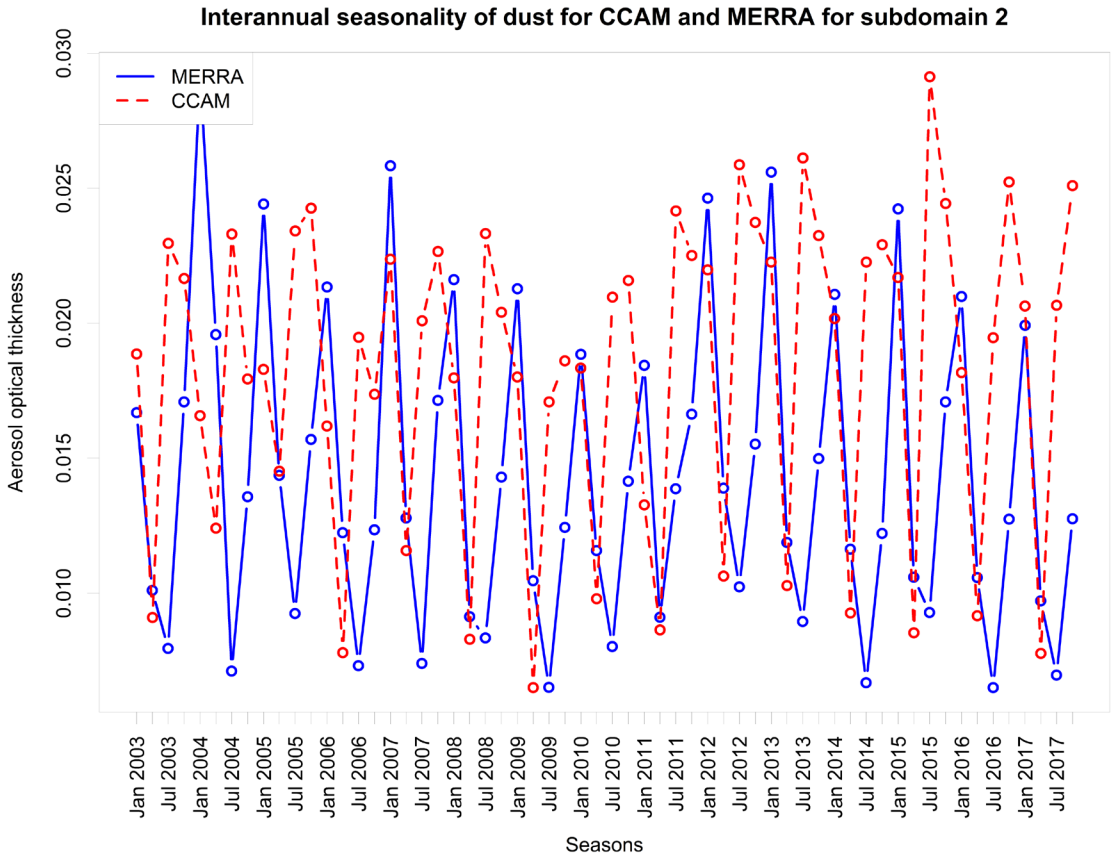

Figure 4.16a: Area-averaged interannual seasonality of compositional AOD of small dust between CCAM simulations and MERRA for subdomain 2

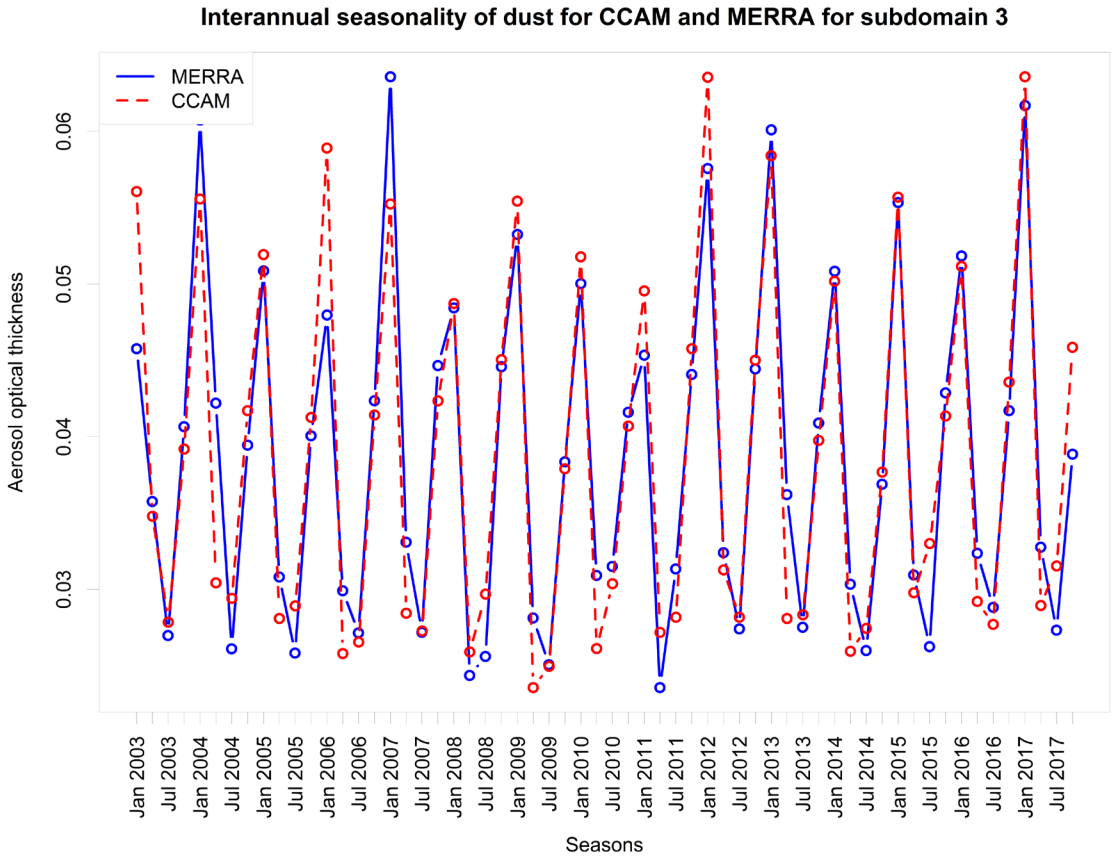

Figure 4.16b: Area-averaged interannual seasonality of compositional AOD of small dust between CCAM simulations and MERRA for subdomain 3

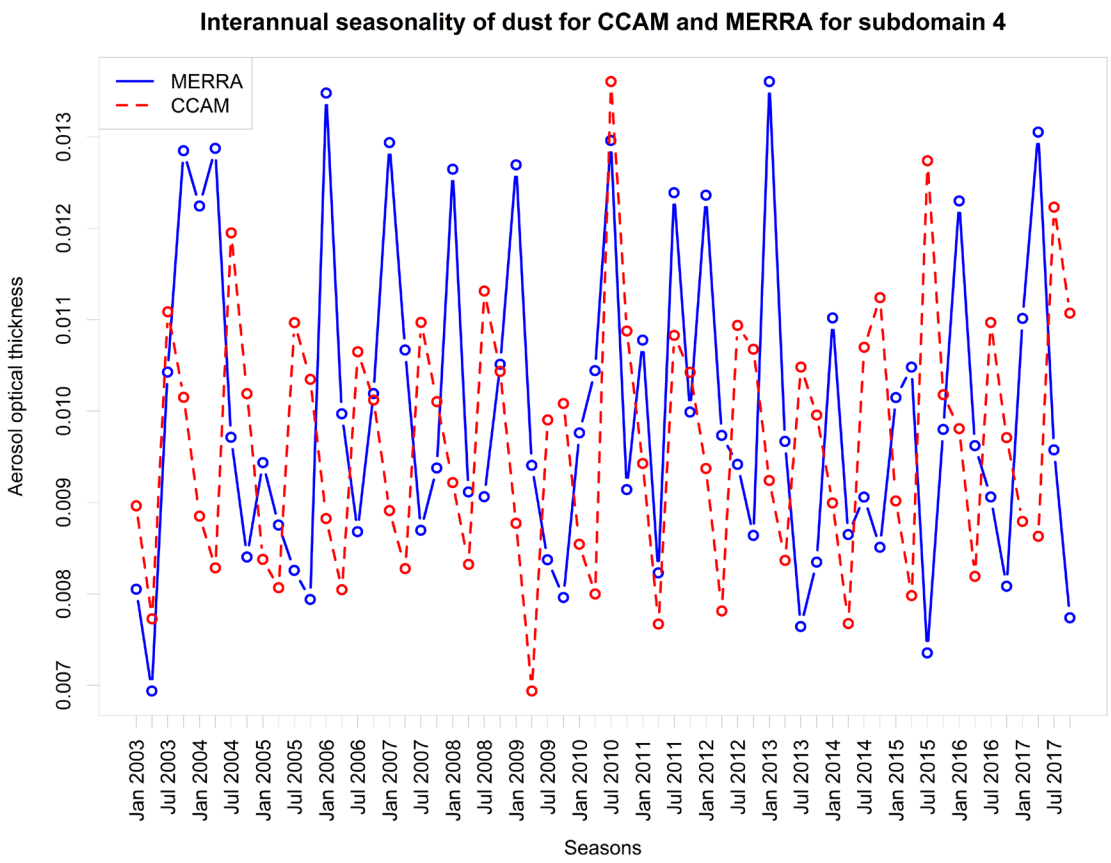

Figure 4.16c: Area-averaged interannual seasonality of compositional AOD of small dust between CCAM simulations and MERRA for subdomain 4

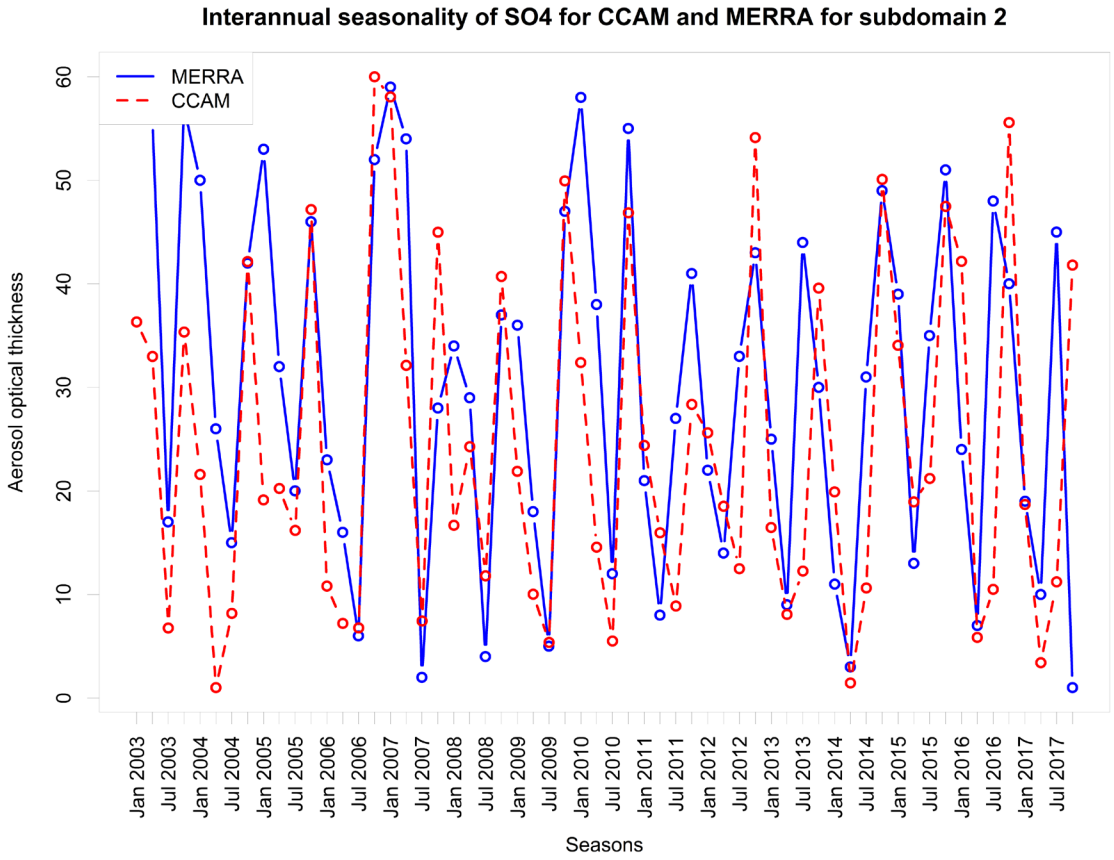

Figure 4.17a: Area-averaged interannual seasonality of compositional AOD of sulphate between CCAM simulations and MERRA for subdomain 2

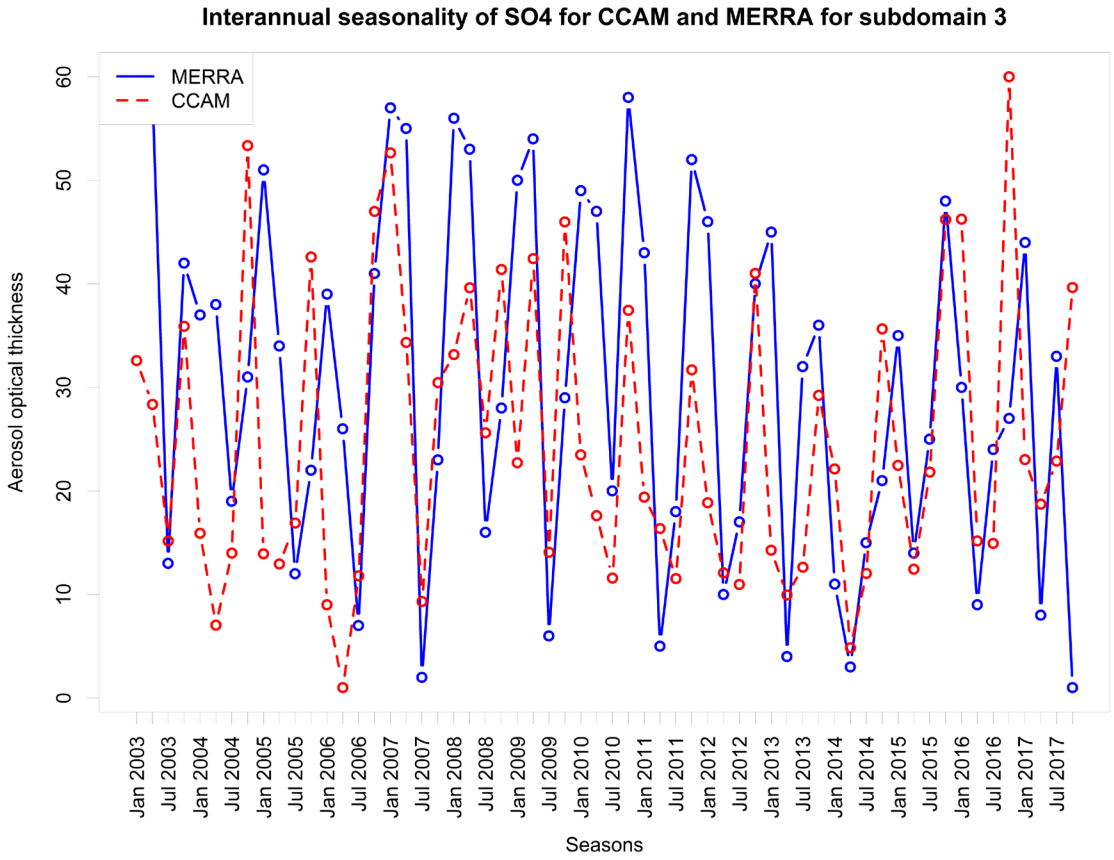

Figure 4.17b: Area-averaged interannual seasonality of compositional AOD of sulphate between CCAM simulations and MERRA for subdomain 3

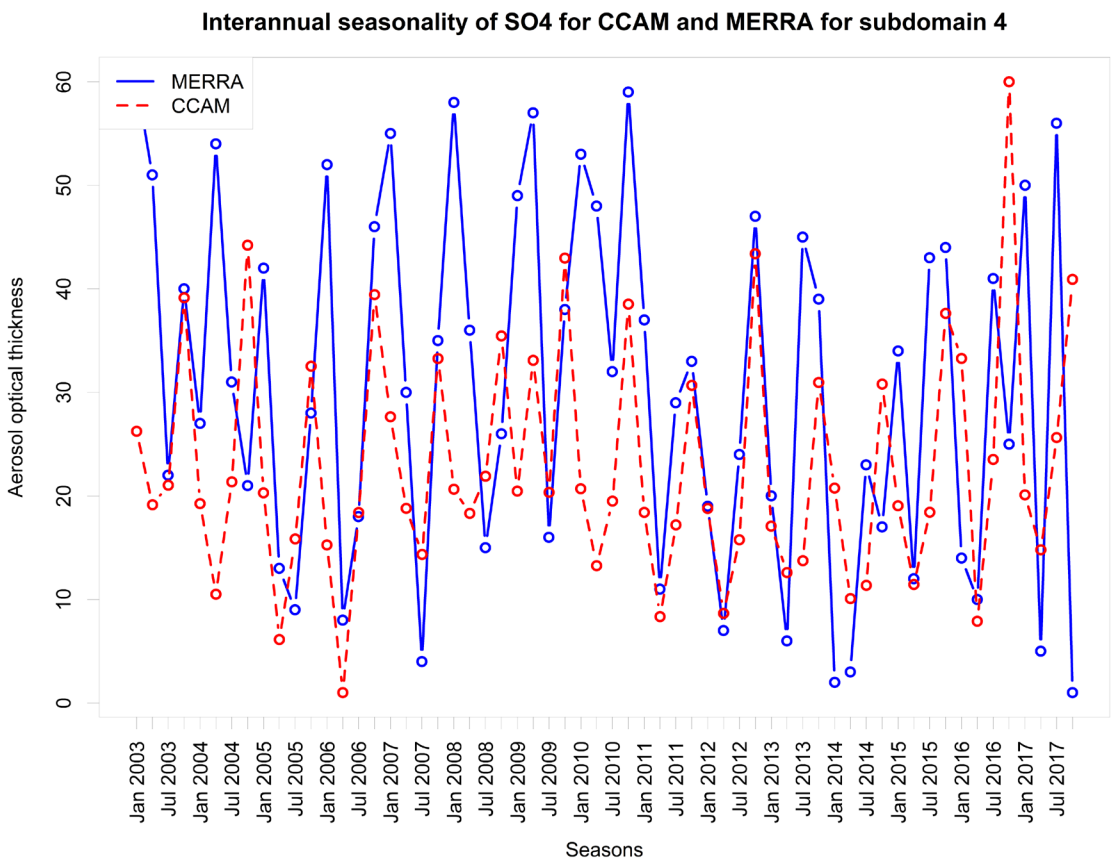

Figure 4.17c: Area-averaged interannual seasonality of compositional AOD of sulphate between CCAM simulations and MERRA for subdomain 4

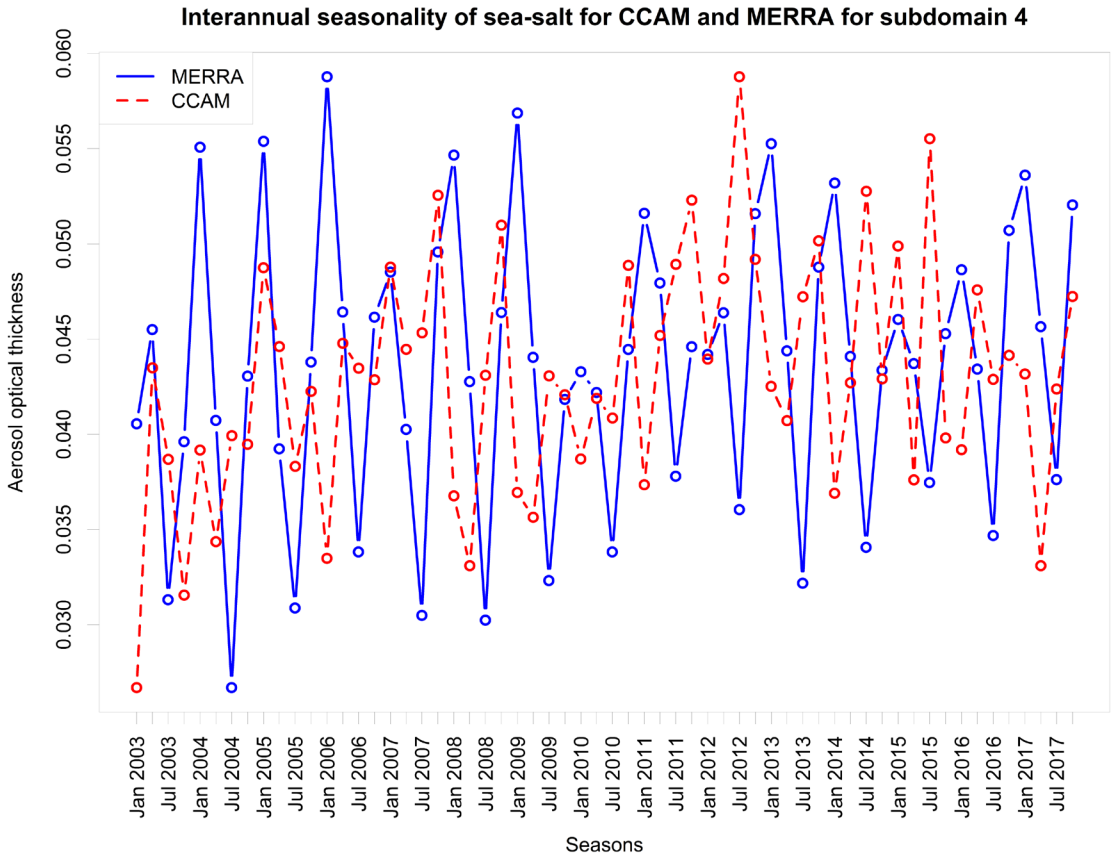

Figure 4.18a: Area-averaged interannual seasonality of compositional AOD of sea-salt between CCAM simulations and MERRA for subdomain 4

Annexure B

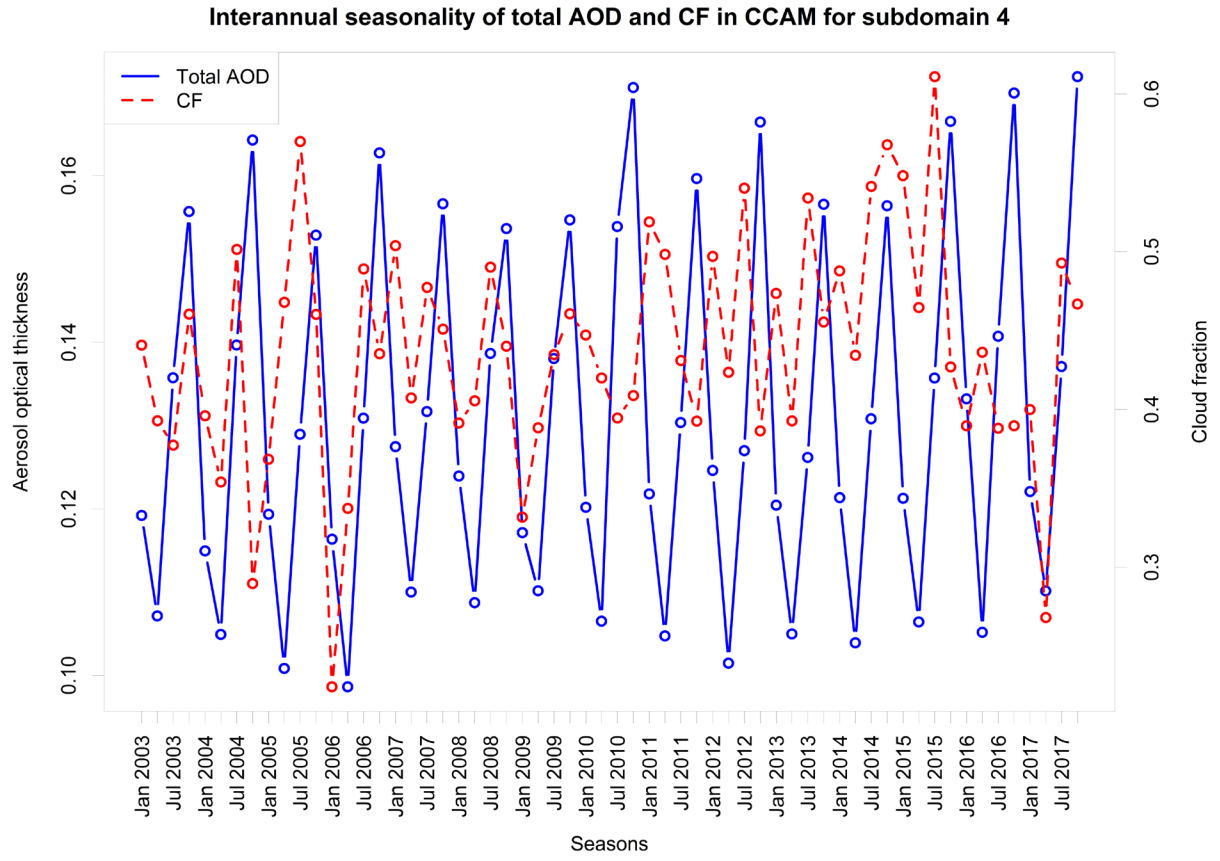

Figure 5.6a: Area-averaged interannual seasonality between total AOD and cloud fraction for subdomain 4

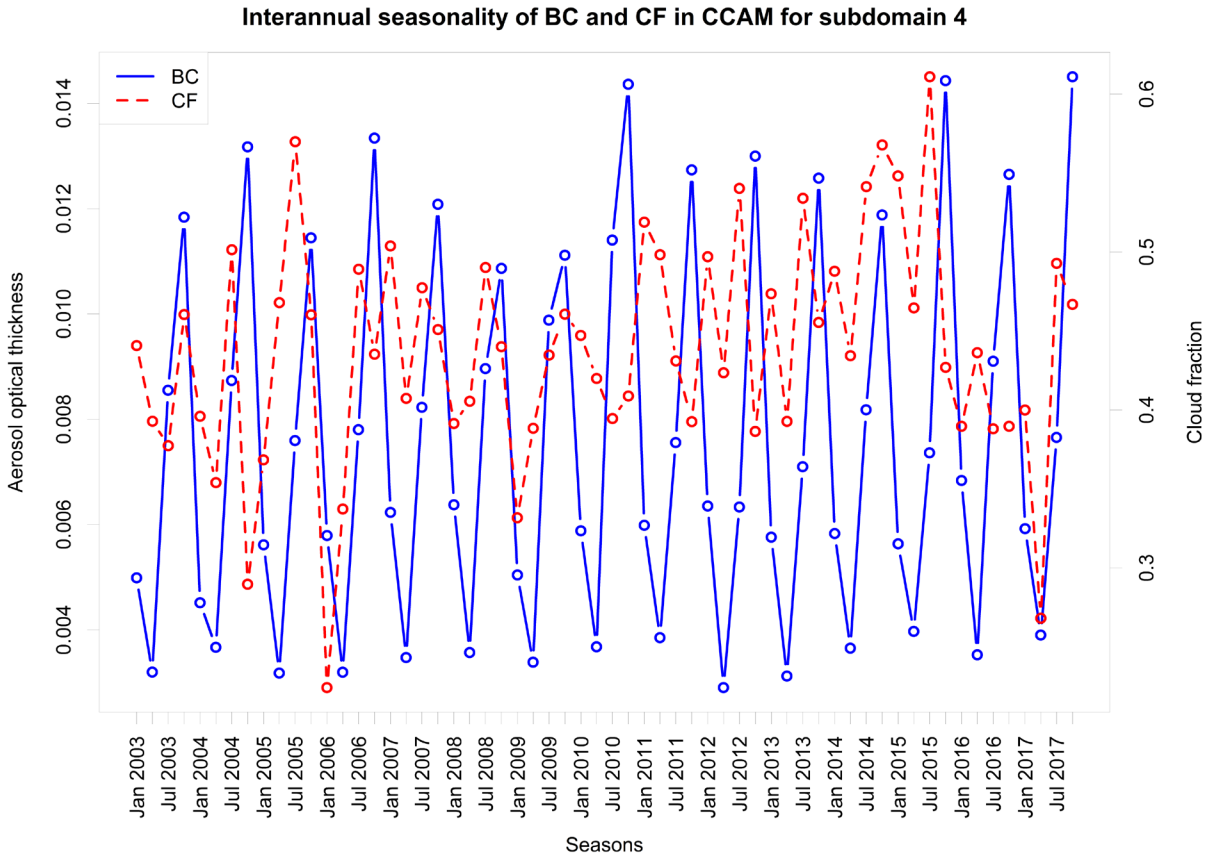

Figure 5.8a: Area-averaged interannual seasonality between compositional AOD of black carbon and cloud fraction for subdomain 4

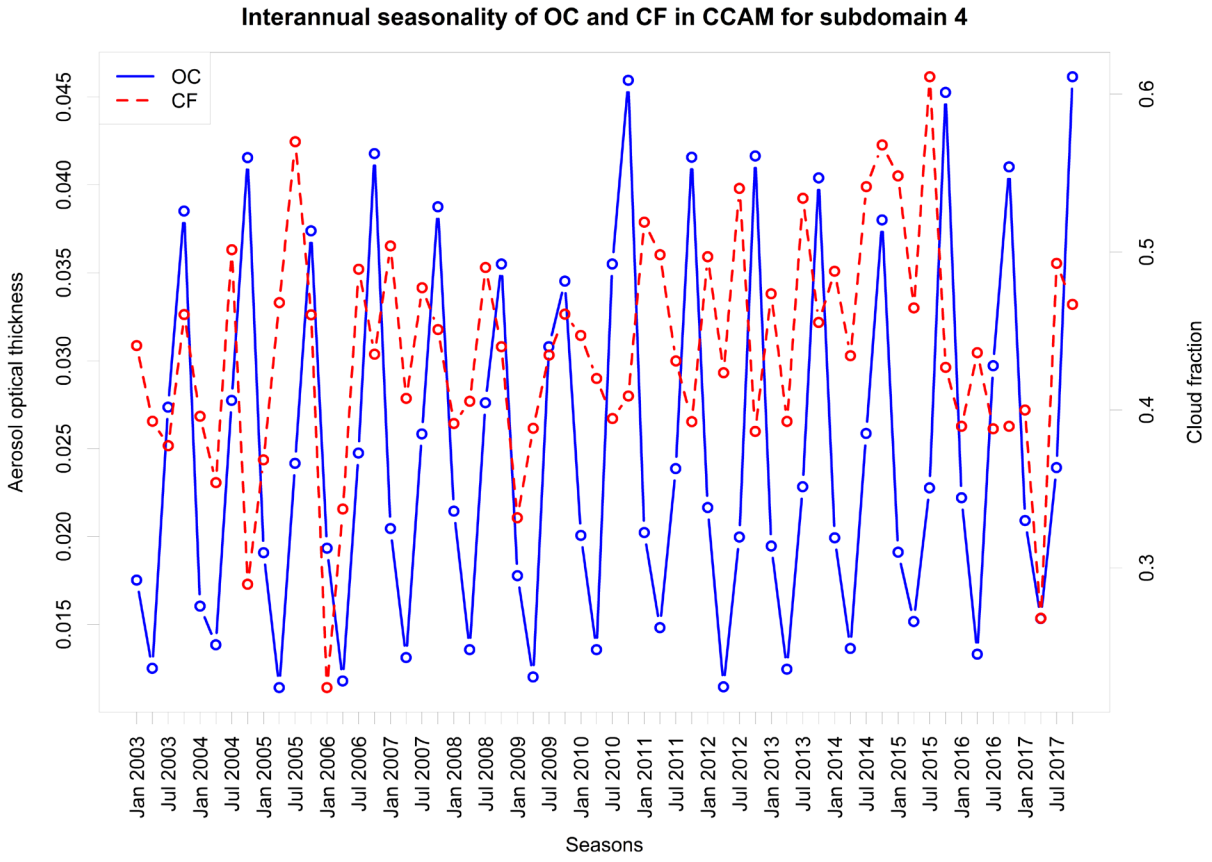

Figure 5.10a: Area-averaged interannual seasonality between compositional AOD of organic carbon and cloud fraction for subdomain 4

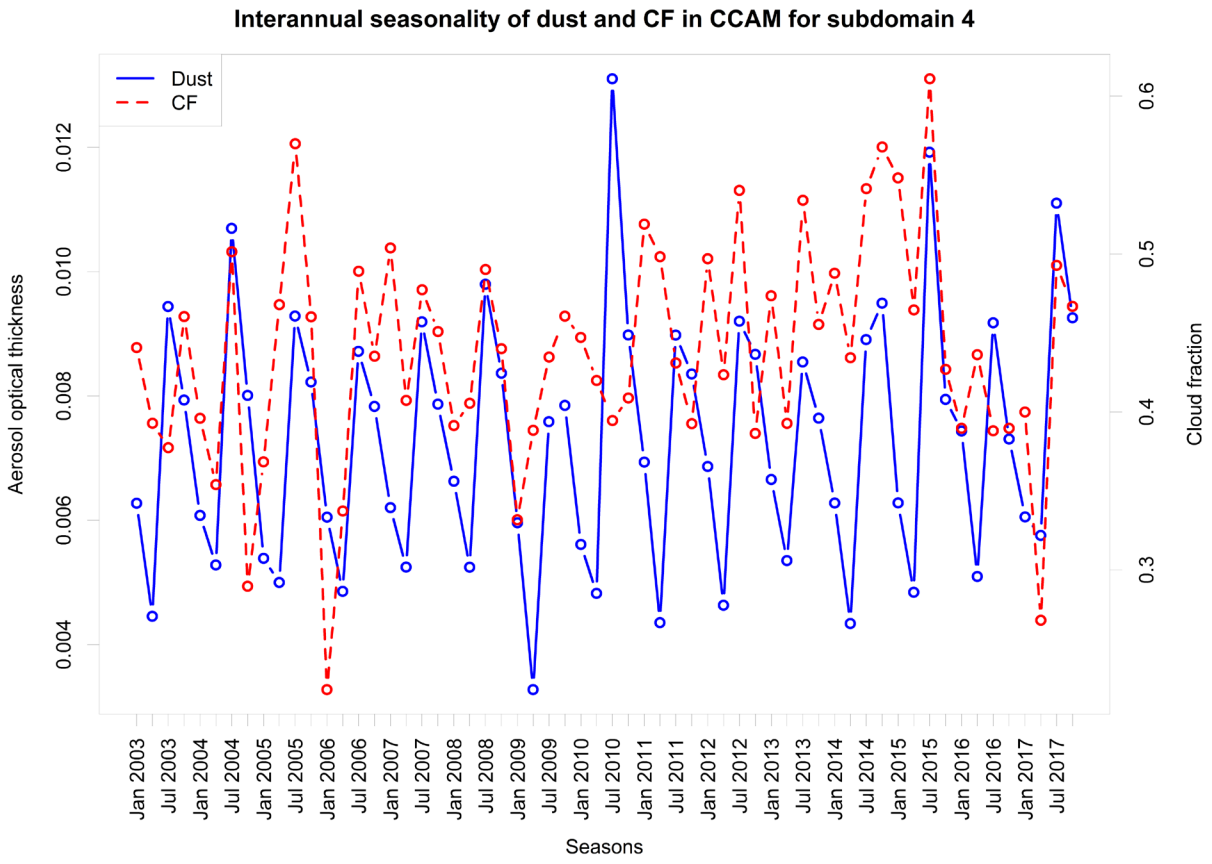

Figure 5.12a: Area-averaged interannual seasonality between compositional AOD of small dust and cloud fraction for subdomain 4

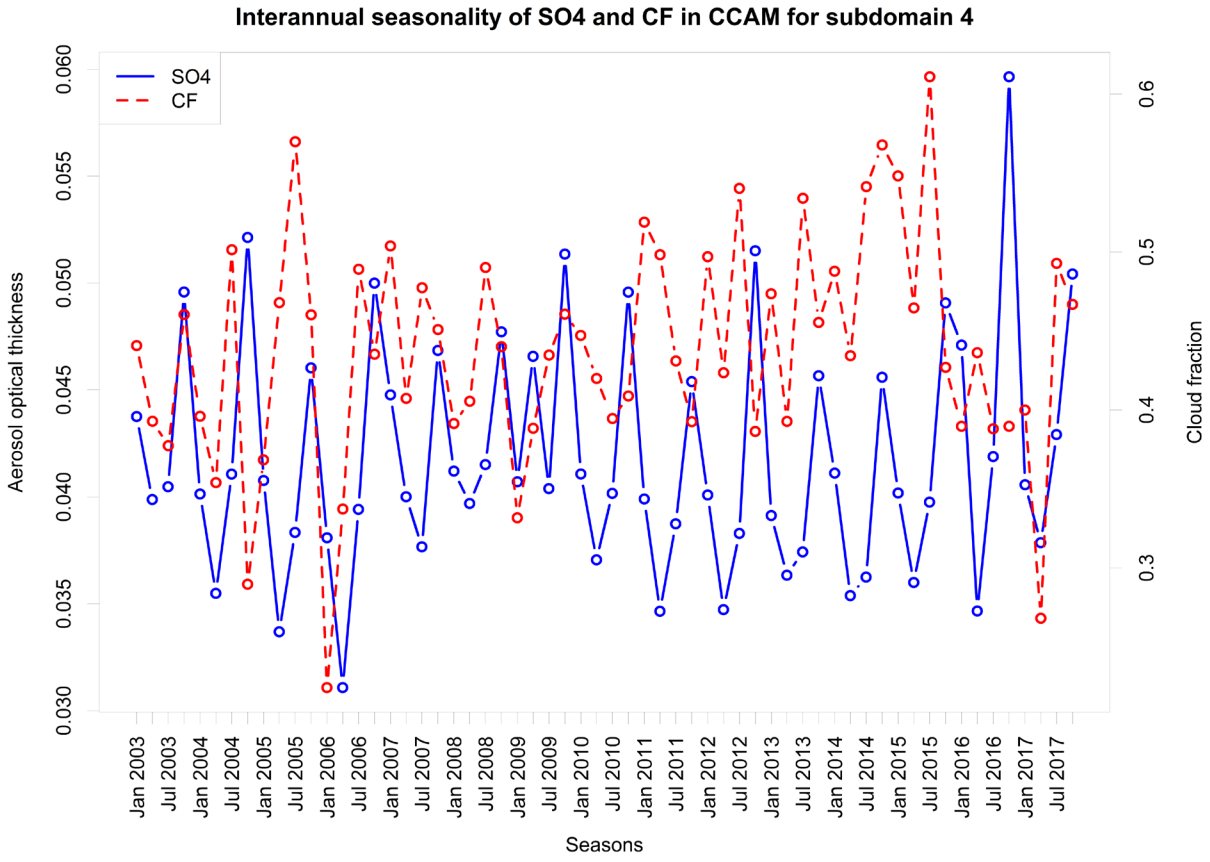

Figure 5.14a: Area-averaged interannual seasonality between compositional AOD of sulphate and cloud fraction for subdomain 4

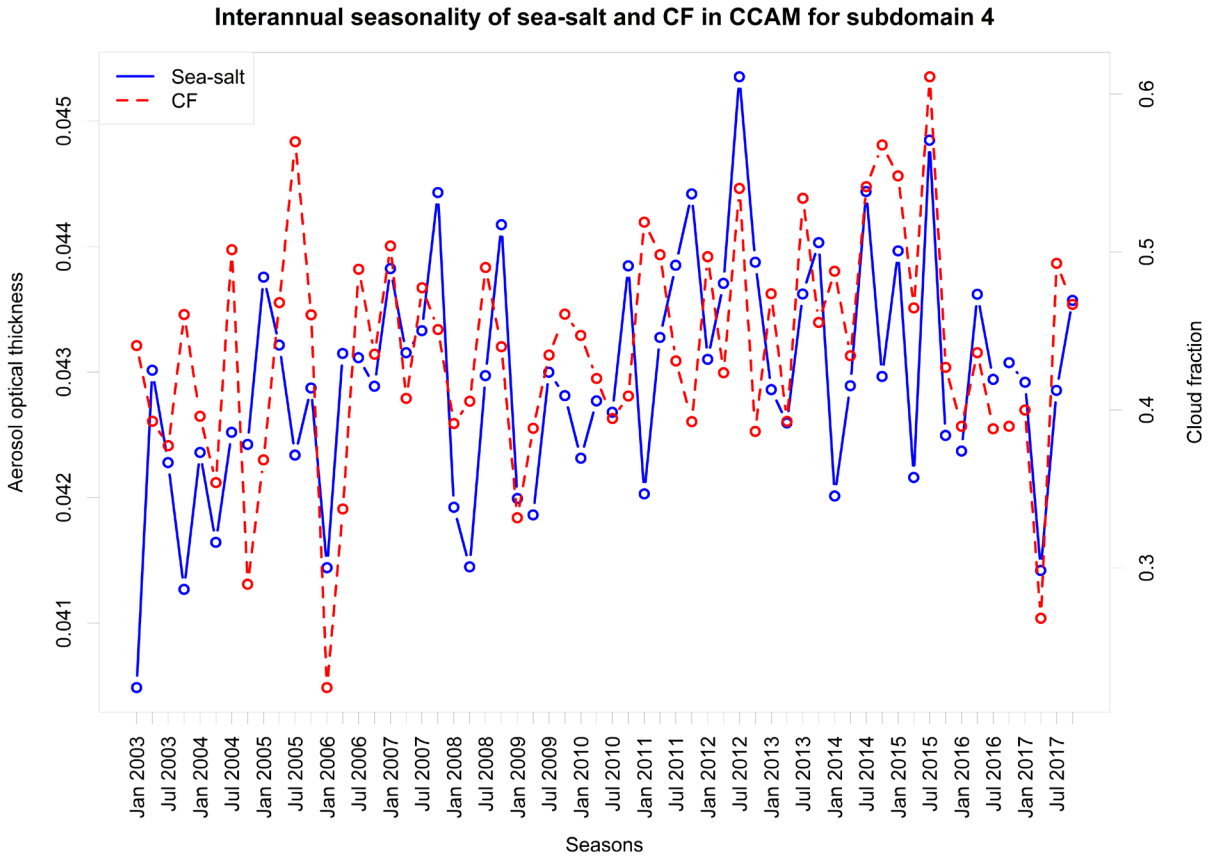

Figure 5.16a: Area-averaged interannual seasonality between compositional AOD of sea-salt and cloud fraction for subdomain 4

Annexure C

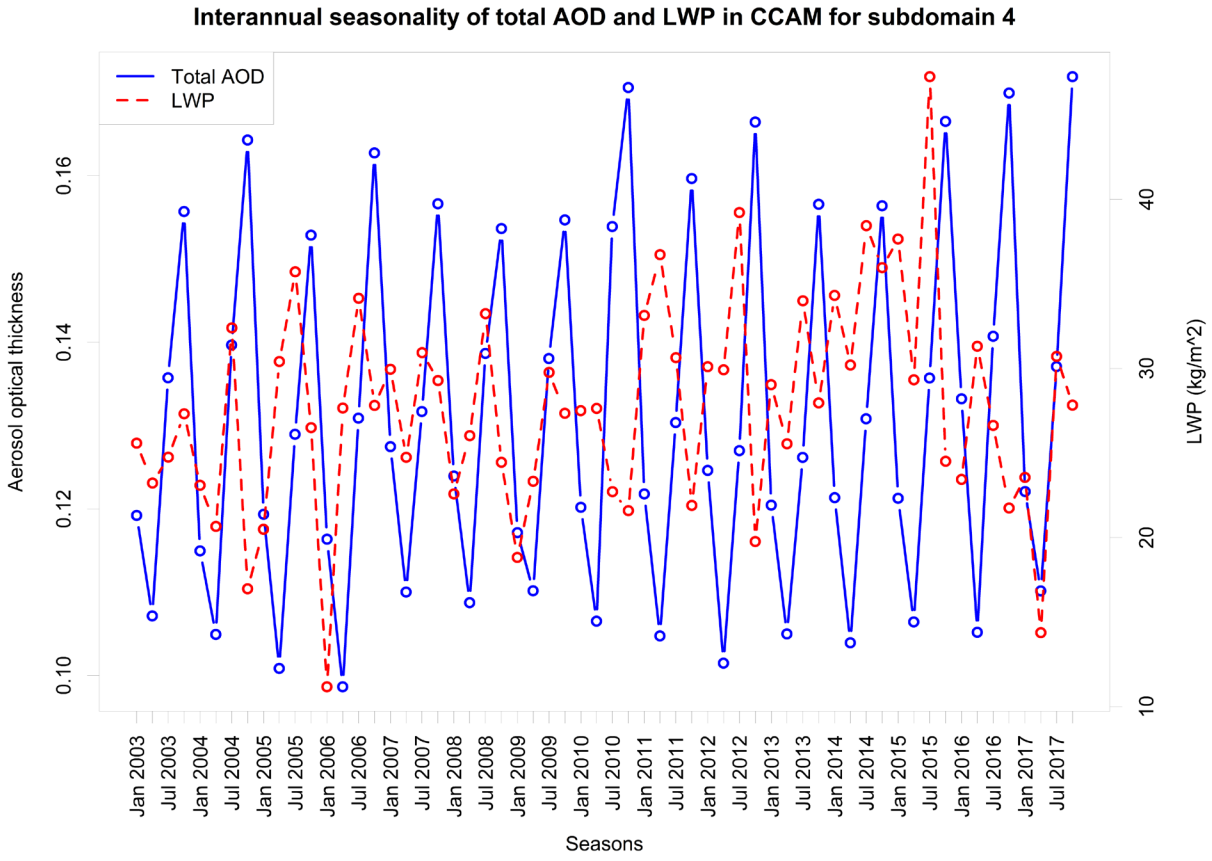

Figure 5.22a: Area-averaged interannual seasonality between total AOD and liquid water path for subdomain 4

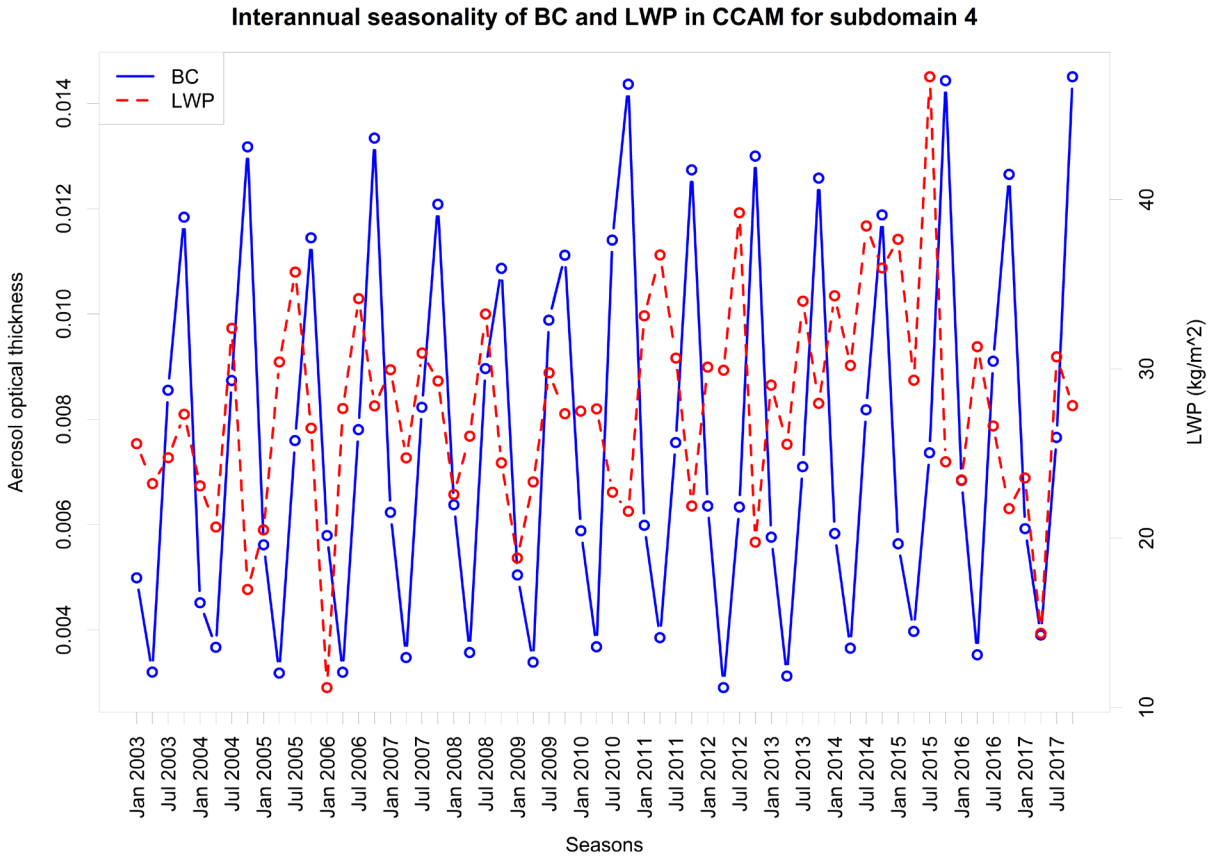

Figure 5.24a: Area-averaged interannual seasonality between compositional AOD of black carbon and liquid water path for subdomain 4

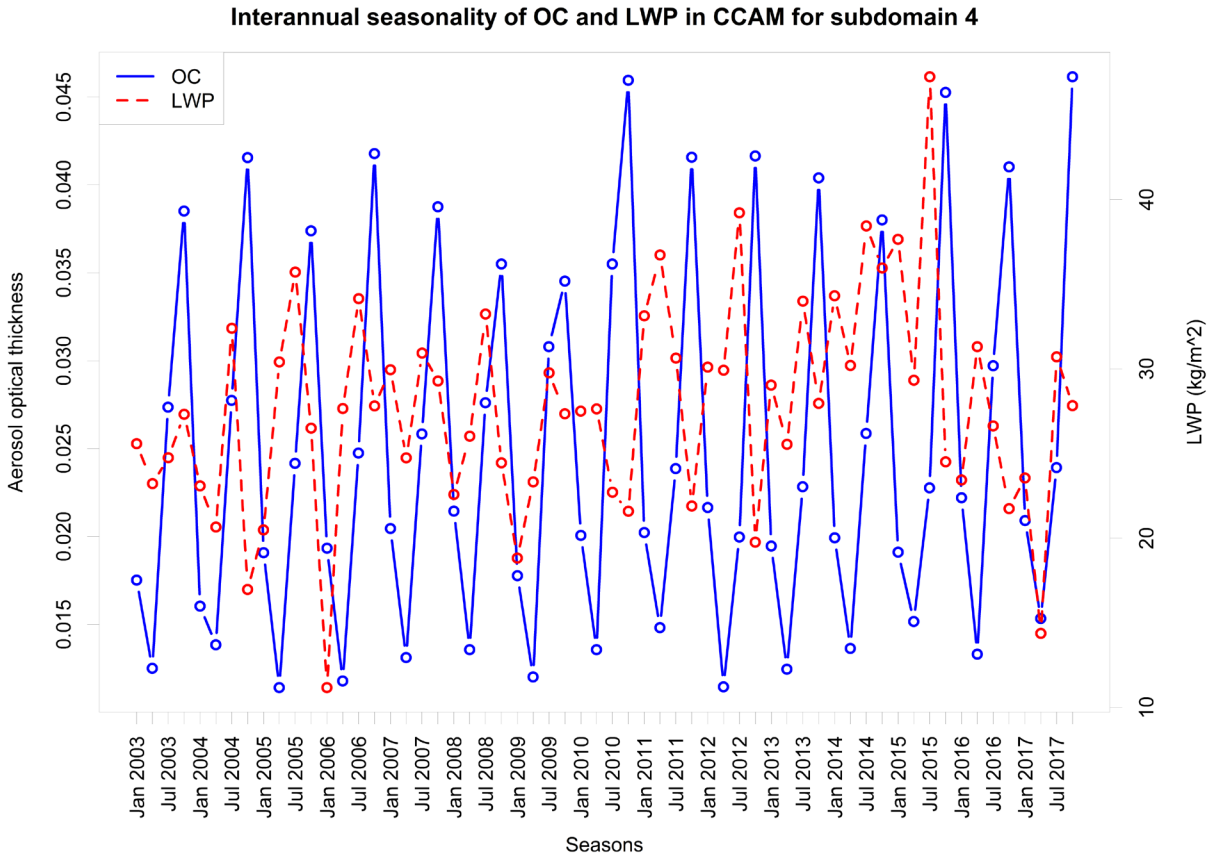

Figure 5.26a: Area-averaged interannual seasonality between compositional AOD of organic carbon and liquid water path for subdomain 4

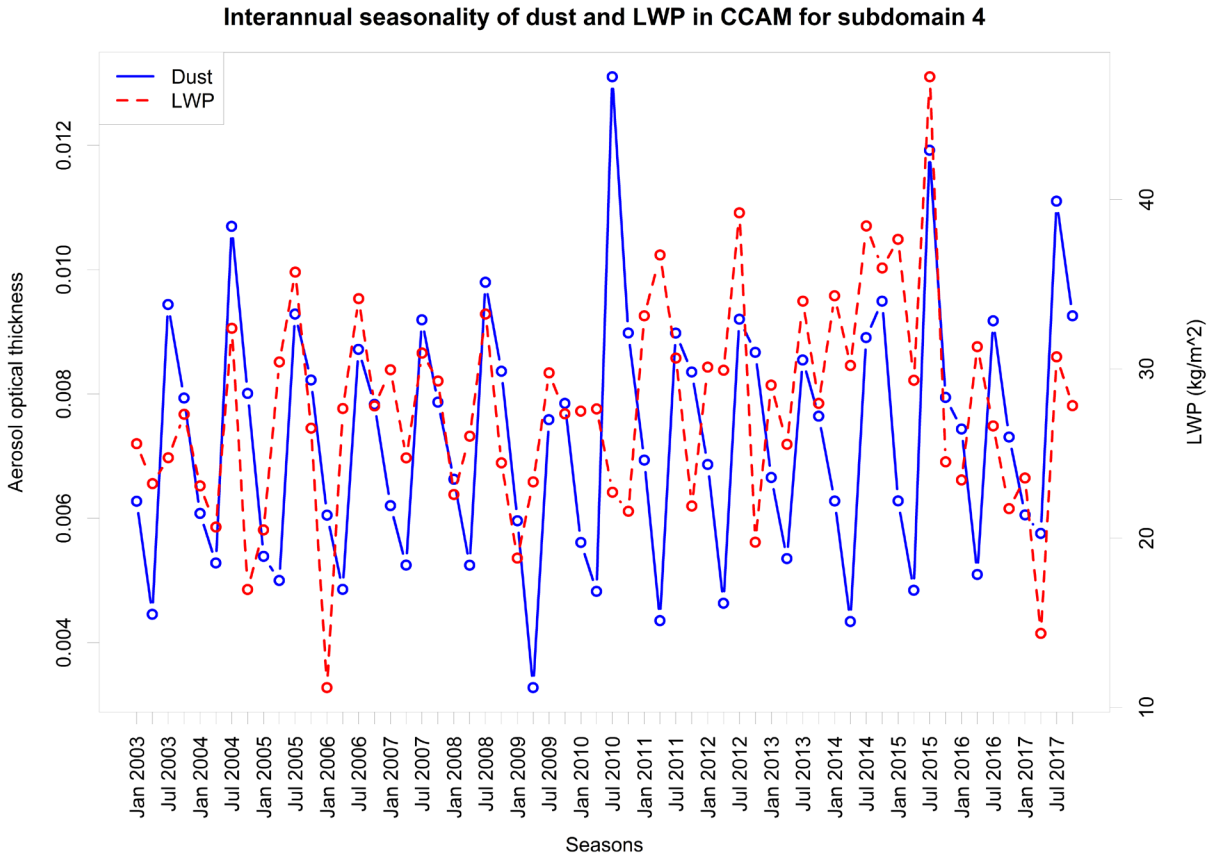

Figure 5.28a: Area-averaged interannual seasonality between compositional AOD of small dust and liquid water path for subdomain 4

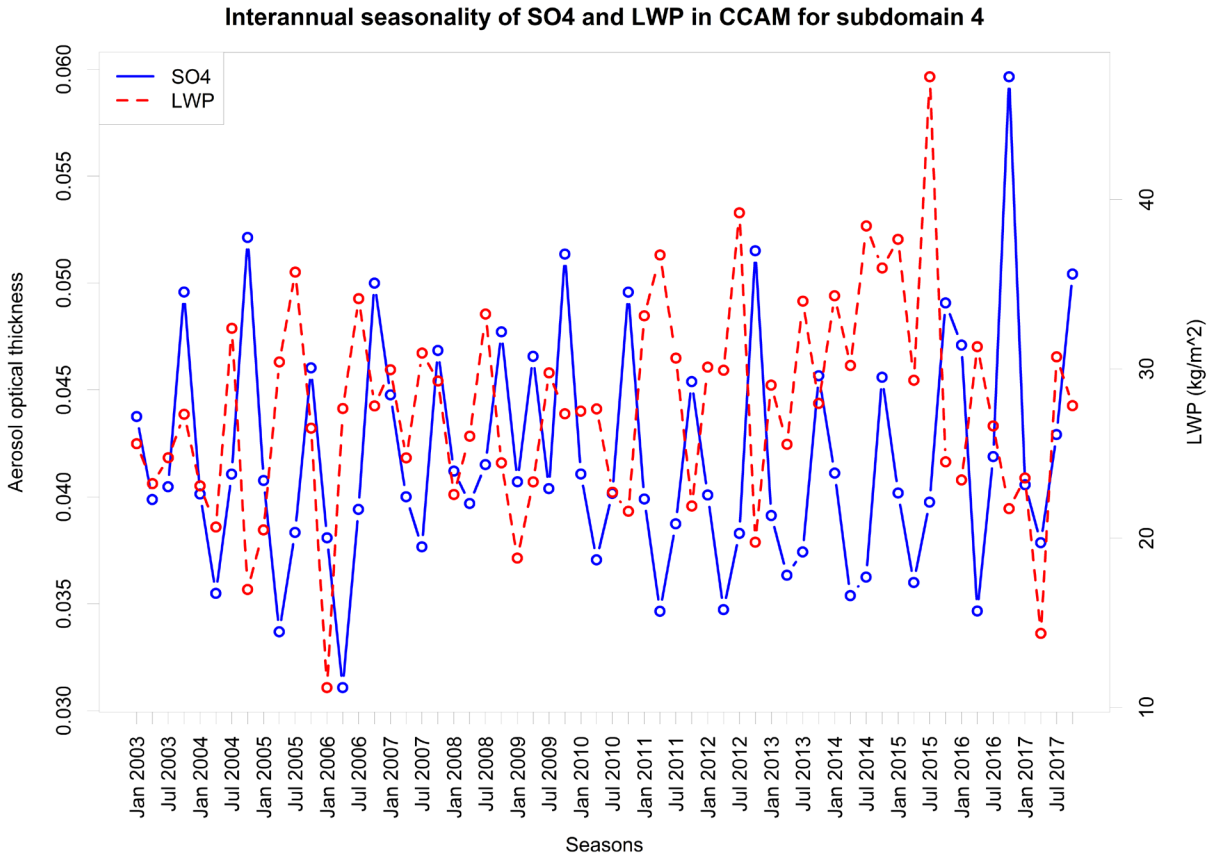

Figure 5.30a: Area-averaged interannual seasonality between compositional AOD of sulphate and liquid water path for subdomain 4

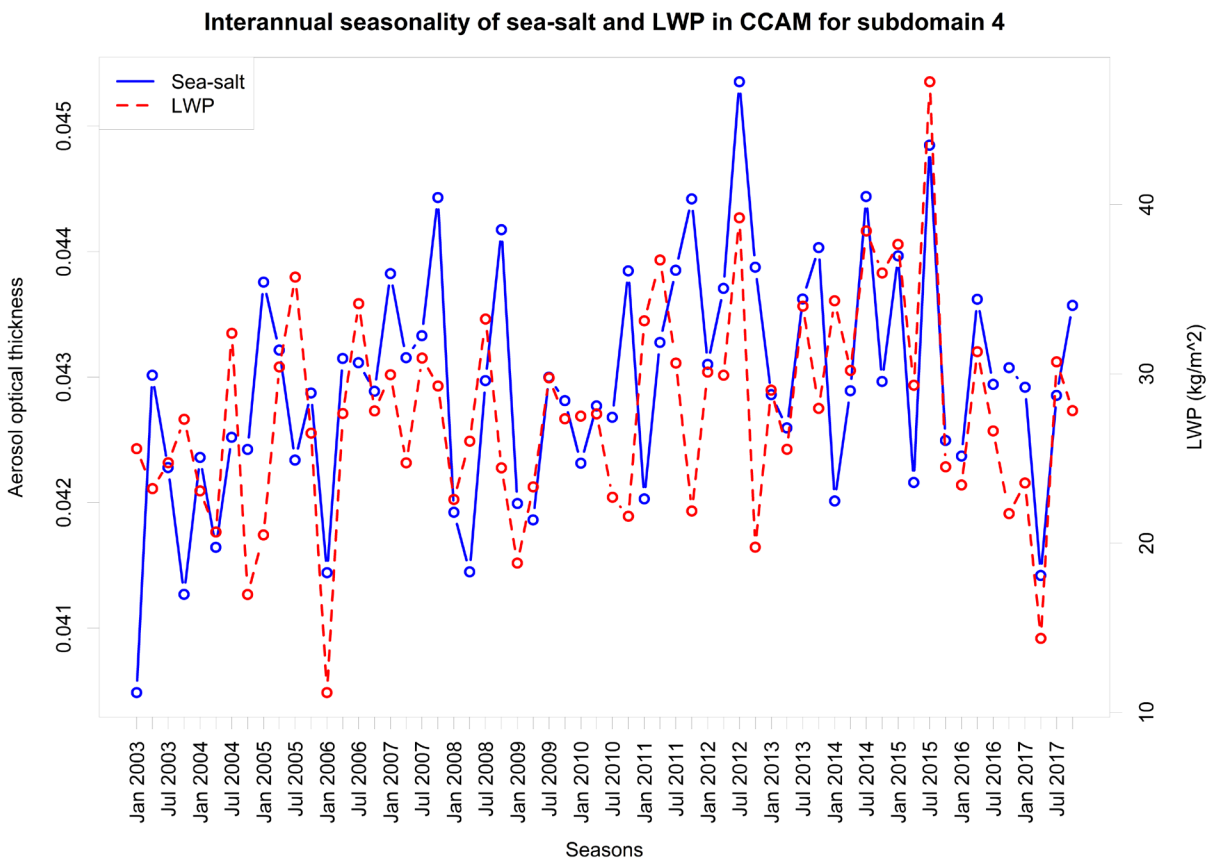

Figure 5.32a: Area-averaged interannual seasonality between compositional AOD of sea salt and liquid water path for subdomain 4

Bibliography

Van Aardenne, J. & Pulles, T. 2002. Uncertainty in emission inventories : What do we mean and how could we assess it ? **SOURCE?**

Adebiyi, A.A. & Zuidema, P. 2018. Low cloud cover sensitivity to biomass-burning aerosols and meteorology over the Southeast Atlantic. *Journal of Climate,* 31(11):4329-4346.

Adebiyi, A.A., Zuidema, P. & Abel, S.J. 2015. The convolution of dynamics and moisture with the presence of shortwave absorbing aerosols over the southeast Atlantic. *Journal of Climate,* 28(5):1997-2024.

Adesina, A.J., Kumar, K.R. & Sivakumar, V. 2016. Aerosol-cloud-precipitation interactions over major cities in south Africa: Impact on regional environment and climate change. *Aerosol and Air Quality Research,* 16(1):195-211.

Afeti, G.M. & Resch, F.J. 1990. Distribution of the liquid aerosol produced from bursting bubbles in sea and distilled water. *Tellus B: Chemical and Physical Meteorology*. 42(4):378-384.

Albrecht, B.A. 1989. Aerosols, cloud microphysics, and fractional cloudiness. *Science,* 245(4923):1227-1230.

Alfaro, S.C., Gaudichet, A., Gomes, L., Maille, M. 1998. Mineral aerosol production by wind erosion: aerosol particle sizes and binding energies. *Geophysical Research Letters,* 25:991-994.

Andreae, M. O., and P.M. 2001. Emission of trace gases and aerosol from biomass burning. *Global Biogeochemical Cycles*.,15:955-966.

Andreae, M.O. 1991. Biomass burning: its history, use and distribution and its impact on the environmental quality and global climate. *In*: J.S. Levine, ed. *Global Biomass Burning: Atmospheric, Climatic and Biospheric Implications*. Massachusetts: MIT Press. pp. 3-21.

Andreae, M.O. 2009. Correlation between cloud condensation nuclei concentration and aerosol optical thickness in remote and polluted regions. *Atmospheric Chemistry*

and Physics, 9(2):543-556.

Aumann, H.H., Chahine, M.T., Gautier, C., Goldberg, M.D., Kalnay, E., … Susskind, J. 2003. AIRS/AMSU/HSB on the aqua mission: design, science objectives, data products, and processing systems. *IEEE Transactions on Geoscience and Remote Sensing,* 41(2 PART 1):253-263.

Balakrishnaiah, G., Raghavendra kumar, K., Suresh Kumar Reddy, B., Rama Gopal, K., Reddy, R.R., … Suresh Babu, S. 2012. Spatio-temporal variations in aerosol optical and cloud parameters over Southern India retrieved from MODIS satellite data. *Atmospheric Environment,* 47:435-445.

Bates, T.S., Quinn, P.K., Frossard, A.A., Russell, L.M., Hakala, J., … Keene, W.C. 2012. Measurements of ocean derived aerosol off the coast of California. *Journal of Geophysical Research Atmospheres,* 117(12):1-13.

Betzer, P.R., Carder, K.L., Duce, R.A., Merrill, J.T., Tindale, N.W., … Greco, A.M. 1988. Long-range transport of giant mineral aerosol particles. *Nature,* 336(6199):568-571.

Bond, T.C., Bhardwaj, E., Dong, R., Jogani, R., Jung, S., … Trautmann, N.M. 2007. Historical emissions of black and organic carbon aerosol from energy-related combustion, 1850-2000. *Global Biogeochemical Cycles,* 21(2).

Botes, D., Mecikalski, J.R. & Jedlovec, G.J. 2012. Atmospheric Infrared Sounder (AIRS) sounding evaluation and analysis of the pre-convective environment. *Journal of Geophysical Research Atmospheres,* 117(9):1-22.

Bott, A. 1999. A numerical model of the cloud-topped planetary boundary-layer: Cloud processing of aerosol particles in marine stratus, *Environmental Modelling and Software,* 14(6):635-643.

Boyd, A.J. & Nelson, G. 1998. Variability of the Benguela Current off the Cape Peninsula, South Africa. *South African Journal of Marine Science,* (19):27-39.

Brown, P.C., Painting, S.J. & Cochrane, K.L. 1991. Estimates of phytoplankton and bacterial biomass and production in the northern and southern Benguela ecosystems. *South African Journal of Marine Science,* 11(1):537-564.

Buchard, V., Randles, C.A., da Silva, A.M., Darmenov, A., Colarco, P.R., … Yu, H. 2017. The MERRA-2 aerosol reanalysis, 1980 onward. Part II: Evaluation and case studies. *Journal of Climate,* 30(17):6851-6872.

Burleyson, C.D. & Yuter, S.E. 2015. Subdiurnal stratocumulus cloud fraction variability and sensitivity to precipitation. *Journal of Climate,* 28(8):2968-2985.

C.J.C. Reason, P. Florenchie, M. Rouault, J.V. 2006. 10 Influences of large scale climate modes and agulhas system variability on the BCLME region. *Large Marine Ecosystems,* 14:223-238.

Cecchini, M.A., MacHado, L.A.T., Andreae, M.O., Martin, S.T., Albrecht, R.I., … Wendisch, M. 2017. Sensitivities of Amazonian clouds to aerosols and updraft speed. *Atmospheric Chemistry and Physics,* 17(16):10037-10050.

Chahine, M.T., Pagano, T.S., Aumann, H.H., Atlas, R., Barnet, C., … Zhou, L. 2006. Improving weather forecasting and providing new data on greenhouse gases. *Bulletin of the American Meteorological Society,* 87(7):911-926.

Chauvigné, A., Waquet, F., Auriol, F., Blarel, L., Delegove, C., … Formenti, P. 2020. Aerosol and cloud properties in the Namibian region during AEROCLO-sA field campaign: 3MI airborne simulator and sun-photometer measurements. *Atmospheric Chemistry and Physics Discussions,* (October):1-21.

Choi, Y., Ghim, Y.S., Zhang, Y., Park, S.M. & Song, I.H. 2020. Estimation of surface concentrations of black carbon from long-term measurements at aeronet sites over korea. *Remote Sensing,* 12(23):1-24.

Costantino, L. & Bréon, F.M. 2013. Aerosol indirect effect on warm clouds over South-East Atlantic, from co-located MODIS and CALIPSO observations. *Atmospheric Chemistry and Physics,* 13(1):69-88.

Das, S., Harshvardhan, H., Bian, H., Chin, M., Curci, G., … Liu, X. 2017. Biomass burning aerosol transport and vertical distribution over the South African-Atlantic region. *Journal of Geophysical Research,* 122(12):6391-6415.

Dee, D.P., Uppala, S.M., Simmons, A.J., Berrisford, P., Poli, P., Kobayashi, S., Andrae, U., Balmaseda, M.A., Balsamo, G., Bauer, P., Bechtold, P., Beljaars, A.C.M., van

de Berg, L., Bidlot, J., Bormann, N., Delsol, C., Dragani, R., Fuentes, M., Geer, A.J, F. 2011. The ERA-Interim reanalysis: configuration and performance of the data assimilation system. *Quarterly Journal of the Royal Meteorological Society,* (7):553-597.

Ding, F., Savtchenko, A., Hearty, T., Wei, J., Theobald, M., … Fetzer, E. 2020. Assessing the impacts of two averaging methods on airs level 3 monthly products and multiyear monthly means. *Journal of Atmospheric and Oceanic Technology,* 37(6):1027-1050.

Duan, Y., Petters, M.D. & Barros, A.P. 2019. Understanding aerosol-cloud interactions through modeling the development of orographic cumulus congestus during IPHEx. *Atmospheric Chemistry and Physics,* 19(3):1413-1437.

Engelbrecht, F.A., Landman, W.A., Engelbrecht, C.J., Landman, S., Bopape, M.M., … Thatcher, M. 2011. Multi-scale climate modelling over Southern Africa using a variable-resolution global model. *Water SA,* 37(5):647-658.

Fauchereau, N., Trzaska, S., Rouault, M. & Richard, Y. 2003. Rainfall variability and changes in Southern Africa during the 20th century in the global warming context. *Natural Hazards,* 29(2):139-154.

Florenchie, P., Reason, C.J.C., Lutjeharms, J.R.E., Rouault, M., Roy, C. & Masson, S. 2004. Evolution of interannual warm and cold events in the Southeast Atlantic Ocean. *Journal of Climate,* 17(12):2318-2334.

Formenti, P., D'Anna, B., Flamant, C., Mallet, M., Piketh, S.J., … Holben, B. 2019. The aerosols, radiation and clouds in southern Africa field campaign in Namibia overview, illustrative observations, and way forward. *Bulletin of the American Meteorological Society,* 100(7):1277-1298.

France, O.B., France, C.G., Germany, C.H. & Uk, A.J. 2013. [IPCC WG1AR5] Clouds and Aerosols. **SOURCE?**

Fu, L.-L. 1981. The general circulation and meridional heat transport of the subtropical south atlantic determined by inverse methods. *Journal of Physical Oceanography,* 11(9):1171-1193.

Gao, M., Han, Z., Tao, Z., Li, J., Kang, J.E., … Carmichael, G.R. 2020. Air quality and climate change, Topic 3 of the Model Inter-Comparison Study for Asia Phase III (MICS-Asia III) - Part 2: Aerosol radiative effects and aerosol feedbacks. *Atmospheric Chemistry and Physics,* 20(2):1147-1161.

Gareth, R., Roberts, G., Wooster, M.J. & Lagoudakis, E. 2009. Annual and diurnal african biomass burning temporal dynamics. *Biogeosciences,* 6(5):849-866.

Garland, R.M., Horowitz, H.M., Engelbrecht, C.J., Dedkind, Z., Piketh, S.J. & Engelbrecht, F.A. 2013. Representation of aerosol particles and associated transport pathways in regional climate modelling in Africa. 40-44. **SOURCE?**

Garstang, M., Tyson, P.D., Swap, R., Edwards, M., Kållberg, P. & Lindesay, J.A. 1996. Horizontal and vertical transport of air over southern Africa. *Journal of Geophysical Research Atmospheres,* 101(19):23721-23736.

Garzoli, S.L. & Gordon, A.L. 1996. Origins and variability of the Benguela Current. *Journal of Geophysical Research C: Oceans,* 101(C1):897-906.

Gelaro, R., McCarty, W., Suárez, M.J., Todling, R., Molod, A., … Zhao, B. 2017. The modern-era retrospective analysis for research and applications, version 2 (MERRA-2). *Journal of Climate,* 30(14):5419-5454.

Ginoux, P., Chin, M., Tegen, I., Prospero, J.M., Holben, B., … Lin, S.J. 2001. Sources and distributions of dust aerosols simulated with the GOCART model. *Journal of Geophysical Research Atmospheres,* 106(D17):20255-20273.

Gkikas, A., Proestakis, E., Amiridis, V., Kazadzis, S., Di Tomaso, E., … García-Pando, C.P. 2022. Quantification of the dust optical depth across spatiotemporal scales with the MIDAS global dataset (2003-2017). *Atmospheric Chemistry and Physics,* 22(5):3553-3578.

Gopal, K.R., Obul Reddy, K.R., Balakrishnaiah, G., Arafath, S.M.D., Kumar Reddy, N.S., … Reddy, R.R. 2016. Regional trends of aerosol optical depth and their impact on cloud properties over Southern India using MODIS data. *Journal of Atmospheric and Solar-Terrestrial Physics,* 146:38-48.

Gordon, H.B. & Rotstayn LD, McGregor JL, Dix MR, Kowalczyk, O'Farrell SP,

Waterman LJ, HirstAC, Wilson SG, Collier MA, Watterson IG, E.T. 2002. The CSIRO Mk3 climate system model. *Asoendale: CSIRO Atmospheric Research Technical Paper,* (60):130. http://scholar.google.com/scholar?hl=en&btnG=Search&q=intitle:The+CSIRO+Mk3+Climate+System+Model#0.

Grandey, B.S., Stier, P. & Wagner, T.M. 2013. Investigating relationships between aerosol optical depth and cloud fraction using satellite, aerosol reanalysis and general circulation model data. *Atmospheric Chemistry and Physics,* 13(6):3177-3184.

Gregory, D. & Rowntree, P.R. 1990. A mass flux convection scheme with representation of cloud ensemble characteristics and stability-dependent closure. *Monthly Weather Review,* 118(7):1483-1506.

Grousset, F.E., Ginoux, P., Bory, A. & Biscaye, P.E. 2003. Case study of a Chinese dust plume reaching the French Alps. *Geophysical Research Letters,* 30(6):23-26.

Gryspeerdt, E., Quaas, J. & Bellouin, N. 2016. Constraining the aerosol influence on cloud fraction. *Journal of Geophysical Research,* 121(7):3566-3583.

Grythe, H., Ström, J., Krejci, R., Quinn, P. & Stohl, A. 2014. A review of sea-spray aerosol source functions using a large global set of sea salt aerosol concentration measurements. *Atmospheric Chemistry and Physics,* 14(3):1277-1297.

Haywood, J.M., Pelon, J., Formenti, P., Bharmal, N.A., Brooks, M.E., … Tulet, P. 2008. Overview of the dust and biomass-burning experiment and African monsoon multidisciplinary analysis special observing period-0. *Journal of Geophysical Research Atmospheres,* 113(23).

Hendricks, J., Righi, M. & Aquila, V. 2012. Global atmospheric aerosol modeling. 561-576. **SOURCE?**

Hermes, J.C. & Reason, C.J.C. 2005. Ocean model diagnosis of interannual coevolving SST variability in the South Indian and South Atlantic Oceans. *Journal of Climate,* 18(15):2864-2882.

Horowitz, H.M., Garland, R.M., Thatcher, M., Landman, W.A., Dedekind, Z., …

Engelbrecht, F.A. 2017. Evaluation of climate model aerosol seasonal and spatial variability over Africa using AERONET. *Atmospheric Chemistry and Physics,* 17(22):13999-14023.

Huang, J., Mendoza, B., Daniel, J.S., Nielsen, C.J., Rotstayn, L. & Wild, O. 2013. Anthropogenic and natural radiative forcing. *Climate Change 2013 the Physical Science Basis: Working Group We Contribution to the Fifth Assessment Report of the Intergovernmental Panel on Climate Change,* 9781107057:659-740.

Hutchings, L., van der Lingen, C.D., Shannon, L.J., Crawford, R.J.M., Verheye, H.M.S., … Monteiro, P.M.S. 2009. The Benguela Current: An ecosystem of four components. *Progress in Oceanography,* 83(1-4):15-32.

IPCC. 2014. *Climate Change 2014 Part A: Global and sectoral aspects*. *Climate Change 2014: Impacts, adaptation, and vulnerability. Part A: Global and sectoral aspects. contribution of Working Group II to the Fifth Assessment Report of the Intergovernmental Panel on Climate Change*. papers2://publication/uuid/B8BF5043-C873-4AFD-97F9-A630782E590D.

Jacob, M., Ament, F., Gutleben, M., Konow, H., Mech, M., … Crewell, S. 2019. Investigating the liquid water path over the tropical Atlantic with synergistic airborne measurements. *Atmospheric Measurement Techniques,* 12(6):3237-3254.

James N., H.J. 2011. Insights into impacts of climate change on the South African marine and coastal environment. Report prepared by the South African Environmental Observation Network (SAEON). 1-51.

Jeong, G.R. & Wang, C. 2010. Climate effects of seasonally varying Biomass Burning emitted Carbonaceous Aerosols (BBCA). *Atmospheric Chemistry and Physics,* 10(17):8373-8389.

Jerez, S., López-romero, J.M., Lajarin, B., Lorente-plazas, R., Palacios-peña, L., … Montávez, J.P. 2019. Effect of aerosol-radiation and aerosol-cloud interactions in the simulation of photovoltaic and wind power using regional climate models MOTIVATION: previous works. **SOURCE?**

Jolliffe, I.T., & D.B.S. 2012. *Forecast verification: a practitioner's guide in atmospheric*

science. 2nd ed. Wiley and Sons Ltd.

Kanakidou, M., Seinfeld, J.H., Pandis, S.N., Barnes, I., Dentener, F.J., … Wilson, J. 2005. Organic aerosol and global climate modelling: A review. *Atmospheric Chemistry and Physics,* 5(4):1053-1123.

Kang, N., Kumar, K.R., Yin, Y., Diao, Y. & Yu, X. 2015. Correlation analysis between AOD and cloud parameters to study their relationship over china using MODIS data (2003-2013): Impact on cloud formation and climate change. *Aerosol and Air Quality Research,* 15(3):958-973.

Kaufman, Y.J., Koren, I., Remer, L.A., Tanré, D., Ginoux, P. & Fan, S. 2005. Dust transport and deposition observed from the Terra-Moderate Resolution Imaging Spectroradiometer (MODIS) spacecraft over the Atlantic Ocean. *Journal of Geophysical Research D: Atmospheres,* 110(10):1-16.

Kidson, J.W. 1988. Interannual Variations in the Southern Hemisphere Circulation. *Journal of Climate,* 1(12):1177-1198.

Kim, M., Cermak, J., Andersen, H., Fuchs, J. & Stirnberg, R. 2020. A new satellite-based retrieval of low-cloud liquid-water path using machine learning and meteosat seviri data. *Remote Sensing,* 12(21):1-16.

King, M.D., Menzel, W.P., Kaufman, Y.J., Tanré, D., Gao, B.C., … Hubanks, P.A. 2003. Cloud and aerosol properties, precipitable water, and profiles of temperature and water vapor from MODIS. *IEEE Transactions on Geoscience and Remote Sensing,* 41(2 PART 1):442-456.

Koch, D. & Del Genio, A.D. 2010. Black carbon semi-direct effects on cloud cover: Review and synthesis. *Atmospheric Chemistry and Physics,* 10(16):7685-7696.

Kroll, J.H. & Seinfeld, J.H. 2008. Chemistry of secondary organic aerosol: Formation and evolution of low-volatility organics in the atmosphere. *Atmospheric Environment,* 42(16):3593-3624.

Kuik, F., Lauer, A., Beukes, J.P., Van Zyl, P.G., Josipovic, M., … Feig, G.T. 2015. The anthropogenic contribution to atmospheric black carbon concentrations in southern Africa: A WRF-Chem modeling study. *Atmospheric Chemistry and Physics,*

15(15):8809-8830.

Lambrigtsen, B., Fetzer, E., Fishbein, E., Lee, S.Y. & Pagano, T. 2004. AIRS: The Atmospheric Infrared Sounder. *International Geoscience and Remote Sensing Symposium (IGARSS),* 3(June):2204-2207.

Lau, K.M., Kim, M.K. & Kim, K.M. 2006. Asian summer monsoon anomalies induced by aerosol direct forcing: The role of the Tibetan Plateau. *Climate Dynamics,* 26(7-8):855-864.

Van Leer, B. 1977. Towards the ultimate conservative difference scheme. IV. A new approach to numerical convection. *Journal of Computational Physics,* 23(3):276-299.

Levy, R.C., Remer, L.A. & Dubovik, O. 2007. Global aerosol optical properties and application to Moderate Resolution Imaging Spectroradiometer aerosol retrieval over land. *Journal of Geophysical Research Atmospheres,* 112(13):1-15.

Li, J., Carlson, B.E., Yung, Y.L., Lv, D., Hansen, J., … Dong, Y. 2022. Scattering and absorbing aerosols in the climate system. *Nature Reviews Earth & Environment,* 3(6):363-379.

Lima, D.C.A., Soares, P.M.M., Semedo, A., Cardoso, R.M., Cabos, W. & Sein, D. V. 2019. A Climatological Analysis of the Benguela Coastal Low-Level Jet. *Journal of Geophysical Research: Atmospheres,* 124(7):3960-3978.

Lindesay, J.A., Andreae, M.O., Goldammer, J.G., Harris, G., Annegarn, H.J., … Van Wilgen, B.W. 1996. International geosphere-biosphere programme/international global atmospheric chemistry SAFARI-92 field experiment: Background and overview. *Journal of Geophysical Research Atmospheres,* 101(19):23521-23530.

Liu, T., Liu, Q., Chen, Y., Wang, W., Zhang, H., … Sheng, J. 2020a. Effect of aerosols on the macro- and micro-physical properties of warm clouds in the Beijing-Tianjin-Hebei region. *Science of the Total Environment,* 720:137618.

Liu, T., Liu, Q., Chen, Y., Wang, W., Zhang, H., … Sheng, J. 2020b. Effect of aerosols on the macro- and micro-physical properties of warm clouds in the Beijing-Tianjin-Hebei region. *Science of the Total Environment,* 720.

Louis, J.F. 1979. A parametric model of vertical eddy fluxes in the atmosphere. *Boundary-Layer Meteorology,* 17(2):187-202.

Lu, Z., Liu, X., Zhang, Z., Zhao, C., Meyer, K., … Penner, J.E. 2018. Biomass smoke from southern Africa can significantly enhance the brightness of stratocumulus over the southeastern Atlantic Ocean. *Proceedings of the National Academy of Sciences of the United States of America,* 115(12):2924-2929.

Luo, M., Liu, Y., Zhu, Q., Tang, Y. & Alam, K. 2020. Role and mechanisms of black carbon affecting water vapor transport to Tibet. *Remote Sensing,* 12(2).

Ma, X. & Yu, F. 2015. Seasonal and spatial variations of global aerosol optical depth: Multi-year modelling with GEOS-Chem-APM and comparisons with multiple-platform observations. *Tellus, Series B: Chemical and Physical Meteorology,* 67(1).

Mahowald, N., Albani, S., Kok, J.F., Engelstaeder, S., Scanza, R., … Flanner, M.G. 2014. The size distribution of desert dust aerosols and its impact on the Earth system. *Aeolian Research,* 15(November):53-71.

Mallet, M., Solmon, F., Nabat, P., Elguindi, N., Waquet, F., … Formenti, P. 2020. Direct and semi-direct radiative forcing of biomass-burning aerosols over the southeast Atlantic (SEA) and its sensitivity to absorbing properties: a regional climate modeling study. *Atmospheric Chemistry and Physics,* 20(21):13191-13216.

Mandailina, V., Saddam, S., Ibrahim, M. & Syaharuddin, S. 2019. UTAUT: Analysis of Usage Level of Android Applications as Learning Media in Indonesian Educational Institutions. *IJECA (International Journal of Education and Curriculum Application),* 2(3):16.

Mardesci, H. 2020. The Effect of Online Learning on University Students' Learning Motivation. *JPP (Jurnal Pendidikan dan Pembelajaran),* 27(1):42-47.

Martín, A., Romero, R., Homar, V., De Luque, A., Alonso, S., … Llasat, M.C. 2007. Sensitivities of a flash flood event over Catalonia: A numerical analysis. *Monthly Weather Review,* 135(2):651-669.

Masuoka, E., Fleig, A., Wolfe, R.E. & Patt, F. 1998. Key characteristics of MODIS data products. *IEEE Transactions on Geoscience and Remote Sensing,* 36(4):1313-

1323.

Mayer, K.J., Wang, X., Santander, M. V., Mitts, B.A., Sauer, J.S., … Prather, K.A. 2020. Secondary Marine Aerosol Plays a Dominant Role over Primary Sea Spray Aerosol in Cloud Formation. *ACS Central Science,* 6(12):2259-2266.

McGregor, J.L. 2005. C-CAM geometric aspects and dynamical formulation. 70. **SOURCE?**

Mo, K.C. & Paegle, J.N. 2001. The Pacific-South American modes and their downstream effects. *International Journal of Climatology,* 21(10):1211-1229.

Monahan, E.C. 1988. Modelling the generation of marine aerosols at the sea surface. *Oceanologia,* 26:19-22.

Muhlbauer, A., McCoy, I.L. & Wood, R. 2014. Climatology of stratocumulus cloud morphologies: Microphysical properties and radiative effects. *Atmospheric Chemistry and Physics,* 14(13):6695-6716.

Myhre, G., Stordal, F., Johnsrud, M., Kaufman, Y.J., Rosenfeld, D., … Isaksen, I.S.A. 2007. Aerosol-cloud interaction inferred from MODIS satellite data and global aerosol models. *Atmospheric Chemistry and Physics,* 7(12):3081-3101.

Nakajima, T., Higurashi, A., Kawamoto, K. & Penner, J.E. 2001. A possible correlation between satellite-derived cloud and aerosol microphysical parameters. *Geophysical Research Letters,* 28(7):1171-1174.

Nakajima T., Higurashi K., and P.J. 2001. A study of correlation between satellite-derived cloud and aerosol microphysical parameters. *Geophysical Research Letters,* 28:1171-1174.

Nyasulu, M., Haque, M.M., Boiyo, R., Kumar, K.R. & Zhang, Y.L. 2020. Seasonal climatology and relationship between AOD and cloud properties inferred from the MODIS over Malawi, Southeast Africa. *Atmospheric Pollution Research,* 11(11):1933-1952.

O' Toole, M.J., Shannon, L.V., De Barros Netos, V. & Malan, D.E. 2001. Integrated Management of the Benguela Current Region. *Science and Integrated Coastal*

Management, (January):229-251. %5C%5CS9%5Cseparatas%5CLUIS%5COTooleetal.pdf.

O'Dowd, C. D., and M.H.S. 1993. O'Dowd, C. D., and M. H. Smith sub-micron sea-salt aerosol production. *Journal of Geophysical Research*. (98):1137-1149.

Ou, Y., Li, Z., Chen, C., Zhang, Y., Li, K., … Luo, J. 2022. Evaluation of MERRA-2 Aerosol Optical and Component Properties over China Using SONET and PARASOL/GRASP Data. *Remote Sensing,* 14(4).

Parajuli, S.P., Stenchikov, G.L., Ukhov, A. & Kim, H. 2019. Dust emission modeling using a new high-resolution dust source function in WRF-Chem With Implications for Air Quality. *Journal of Geophysical Research: Atmospheres,* 124(17-18):10109-10133.

Parkinson, C.L. 2003. Aqua: an Earth-Observing Satellite mission to examine water and other climate variables. *IEEE Transactions on Geoscience and Remote Sensing,* 41(2):173-183.

Peterson, R.G. & Stramma, L. 1991. Upper-level circulation in the South Atlantic Ocean. *Progress in Oceanography,* 26(1):1-73.

Piketh, S.J., Annegarn, H.J. & Tyson, P.D. 1999. Lower tropospheric aerosol loadings over South Africa: The relative contribution of aeolian dust, industrial emissions, and biomass burning. *Journal of Geophysical Research Atmospheres,* 104(D1):1597-1607.

Platnick, S., King, M.D., Ackerman, S.A., Menzel, W.P., Baum, B.A., … Frey, R.A. 2003. The MODIS cloud products: Algorithms and examples from terra. *IEEE Transactions on Geoscience and Remote Sensing,* 41(2 PART 1):459-472.

Prospero, J.M. 1996. Saharan dust transport over the North Atlantic Ocean and Mediterranean: an overview. 133-151. **SOURCE?**

Quinn, P.K., Coffman, D.J., Kapustin, V.N., Bates, T.S. & Covert, D.S. 1998. Aerosol optical properties in the marine boundary layer during the First Aerosol Characterization Experiment (ACE 1) and the underlying chemical and physical aerosol properties. *Journal of Geophysical Research Atmospheres,*

103(D13):16547-16563.

Reason, C.J.C. & Jury, M.R. 1990. On the generation and propagation of the southern African coastal low. *Quarterly Journal of the Royal Meteorological Society,* 116(495):1133-1151.

Redemann, J., Wood, R., Zuidema, P., Doherty, S.J., Luna, B., … Gao, L. 2021. An overview of the ORACLES (ObseRvations of aerosols above CLouds and their intEractionS) project: Aerosol-cloud-radiation interactions in the southeast Atlantic basin. *Atmospheric Chemistry and Physics,* 21(3):1507-1563.

Remer, L.A., Kaufman, Y.J., Tanré, D., Mattoo, S., Chu, D.A., … Holben, B.N. 2005. The MODIS aerosol algorithm, products, and validation. *Journal of the Atmospheric Sciences,* 62(4):947-973.

Rienecker, M.M., Suarez, M.J., Gelaro, R., Todling, R., Bacmeister, J., … Woollen, J. 2011. MERRA: NASA's modern-era retrospective analysis for research and applications. *Journal of Climate,* 24(14):3624-3648.

Ringer, M.A., Martin, G.M., Greeves, C.Z., Hinton, T.J., James, P.M., … Yang, G.Y. 2006. The physical properties of the atmosphere in the new Hadley Centre Global Environmental Model (HadGEM1). Part II: Aspects of variability and regional climate. *Journal of Climate,* 19(7):1302-1326.

Rizza, U., Mancinelli, E., Morichetti, M., Passerini, G. & Virgili, S. 2019. Aerosol optical depth of the main aerosol species over italian cities based on the NASA/MERRA-2 model reanalysis. *Atmosphere,* 10(11).

Rosenfeld, D., Zhu, Y., Wang, M., Zheng, Y., Goren, T. & Yu, S. 2019. Aerosol-driven droplet concentrations dominate coverage and water of oceanic low-level clouds. *Science,* 363(6427).

Rotstayn, L.D. 1997. A physically based scheme for the treatment of stratiform clouds and precipitation in large-scale models. I: Description and evaluation of the microphysical processes. *Quarterly Journal of the Royal Meteorological Society,* 123(541):1227-1282.

Rotstayn, L.D. & Lohmann, U. 2002. Simulation of the tropospheric sulfur cycle in a

global model with a physically based cloud scheme. *Journal of Geophysical Research Atmospheres,* 107(21).

Rotstayn, L.D., Collier, M.A., Dix, M.R., Feng, Y., Gordon, H.B., … Syktus, J. 2010. Improved simulation of Australian climate and ENSO-related rainfall variability in a global climate model with an interactive aerosol treatment. *International Journal of Climatology,* 30(7):1067-1088.

Rotstayn, L.D., Cai, W., Dix, M.R., Farquhar, G.D., Feng, Y., … Wang, M. 2007. Have Australian rainfall and cloudiness increased due to the remote effects of Asian anthropogenic aerosols? *Journal of Geophysical Research Atmospheres,* 112(9):1-28.

Roux, J.P., Van Der Lingen, C.D., Gibbons, M.J., Moroff, N.E., Shannon, L.J., … Cury, P.M. 2013. Jellyfication of marine ecosystems as a likely consequence of overfishing small pelagic fishes: Lessons from the Benguela. *Bulletin of Marine Science,* 89(1):249-284.

Sakaeda, N., Wood, R. & Rasch, P.J. 2011. Direct and semidirect aerosol effects of southern African biomass burning aerosol. *Journal of Geophysical Research Atmospheres,* 116(12):1-19.

Savane, O.S., Vant-Hull, B., Mahani, S. & Khanbilvardi, R. 2015. Effects of aerosol on cloud liquid water path: Statistical method a potential source for divergence in past observation based correlative studies. *Atmosphere,* 6(3):273-298.

Savtchenko, A., Ouzounov, D., Ahmad, S., Acker, J., Leptoukh, G., … Nickless, D. 2004. Terra and Aqua MODIS products available from NASA GES DAAC. *Advances in Space Research,* 34(4):710-714.

Scholes, M., and M.O.A. 2000. Biogenic and pyrogenic emissions from Africa and their impact on the global atmosphere. *Ambio,* 29:23-29.

Sekiguchi, M., Nakajima, T., Suzuki, K., Kawamoto, K., Higurashi, A., … Mukai, S. 2003. A study of the direct and indirect effects of aerosols using global satellite data sets of aerosol and cloud parameters. *Journal of Geophysical Research: Atmospheres,* 108(22).

Selvanathan, M., Jayabalan, N., Kaur, S., Supramaniam, M. & Hussin, N. 2020. Employee productivity in Malaysian private higher. *Palarch's Journal of Archaraology of Egypt,* 17(3):66-79.

Shannon, L. 1985. The Benguela ecosystem. Part I. Evolution of the Benguela, physical features and processes. *Oceanographic and Marine Biology. An Annual Review,* 23:105-182.

Shillington, F.A., Reason, C.J.C., Rae, C.M.D., Florenchie, P. & Penven, P. 2006. Current Large Marine Ecosystem (BCLME). *Africa,* 14:15-30.

Da Silva, N., Mailler, S. & Drobinski, P. 2020. Aerosol indirect effects on the temperature-precipitation scaling. *Atmospheric Chemistry and Physics,* 20(10):6207-6223.

Sinha, P., Jaeglé, L., Hobbs, P. V. & Liang, Q. 2004. Transport of biomass burning emissions from southern Africa. *Journal of Geophysical Research D: Atmospheres,* 109(20):1-15.

Skogen, M.D. 1999. A biophysical model applied to the Benguela upwelling system. *South African Journal of Marine Science,* (21):235-249.

Small, J.D., Chuang, P.Y., Feingold, G. & Jiang, H. 2009. Can aerosol decrease cloud lifetime? *Geophysical Research Letters,* 36(16):1-5.

Smith, S.J. & Andres, R. 2004. Historical sulfur dioxide emissions 1850-2000 : Methods and Results. *Methods*. (January). http://www.osti.gov/energycitations/product.biblio.jsp?osti_id=15020102.

Sporre, M.K., Glantz, P., Tunved, P., Swietlicki, E., Kulmala, M. & Lihavainen, H. 2012. A study of the indirect aerosol effect on subarctic marine liquid low-level clouds using MODIS cloud data and ground-based aerosol measurements. *Atmospheric Research,* 116:56-66.

Stanski, H.R., L.J. Wilson, and W.R.B. 1989. Survey of common verification methods in meteorology. *World Weather Watch Tech. Rept. No.8*. WMO/TD No.

Storelvmo, T., Kristjánsson, J.E., Myhre, G., Johnsrud, M. & Stordal, F. 2006. Combined

observational and modeling based study of the aerosol indirect effect. *Atmospheric Chemistry and Physics,* 6(11):3583-3601.

Susskind, J., Blaisdell, J.M. & Iredell, L. 2014. Improved methodology for surface and atmospheric soundings, error estimates, and quality control procedures: the atmospheric infrared sounder science team version-6 retrieval algorithm. *Journal of Applied Remote Sensing,* 8(1):084994.

Susskind, J., Schmidt, G.A., Lee, J.N. & Iredell, L. 2019. Recent global warming as confirmed by AIRS. *Environmental Research Letters,* 14(4).

Swap, R.J., Annegarn, H.J., Suttles, J.T., King, M.D., Platnick, S., … Scholes, R.J. 2003. Africa burning: A thematic analysis of the Southern African Regional Science Initiative (SAFARI 2000). *Journal of Geophysical Research: Atmospheres,* 108(13):1-15.

Tegen, I., Hollrig, P., Chin, M., Fung, I., Jacob, D. & Penner, J. 1997. Contribution of different aerosol species to the global aerosol extinction optical thickness: Estimates from model results. *Journal of Geophysical Research Atmospheres,* 102(20):23895-23915.

Tesfaye, M., Botai, J., Sivakumar, V. & Mengistu Tsidu, G. 2013. Evaluation of regional climatic model simulated aerosol optical properties over South Africa using ground-based and satellite observations. *ISRN Atmospheric Sciences,* 2013(March 2016):1-17.

Thatcher, M., McGregor, J., Dix, M. & Katzfey, J. 2015. A new approach for coupled regional climate modeling using more than 10, 000 cores. *IFIP Advances in Information and Communication Technology,* 448:599-607.

Tlhalerwa, K., Freiman, M.T. & Piketh, S.J. 2005. Aerosol deposition off the southern african west coast by berg winds. *South African Geographical Journal,* 87(2):152-161.

Tummon, F., Solmon, F., Liousse, C. & Tadross, M. 2010. Simulation of the direct and semidirect aerosol effects on the southern Africa regional climate during the biomass burning season. *Journal of Geophysical Research Atmospheres,*

115(19):1-20.

Twomey, S. 1977. The influence of pollution on the shortwave albedo of clouds. *Journal of Atmospheric Sciences,* 34(7):1149-1152.

Tyson, P.D and Preston-Whyte, R.A. 2000. *The weather and climate of Southern Africa*. Cape Town: Oxford University Press.

Tyson, P.D. & D'Abreton, P.C. 1998. Transport and recirculation of aerosols off Southern Africa: macroscale plume structure. *Atmospheric Environment,* 32(9):1511-1524.

Tyson, P.D. & Von Gogh, R.G. 1976. The use of a monostatic acoustic radar to assess the stability of the lower atmosphere over Johannesburg. *South African Geographical Journal,* 58(1):57-67.

Tyson, P.D., Garstang, M. & Swap, R. 1996. Large-scale recirculation of air over Southern Africa. *Journal of Applied Meteorology,* 35(12):2218-2236.

Vickery, K.J., Eckardt, F.D. & Bryant, R.G. 2013. A sub-basin scale dust plume source frequency inventory for southern Africa, 2005-2008. *Geophysical Research Letters,* 40(19):5274-5279.

Wagner, T., Beirle, S., Deutschmann, T. & Penning De Vries, M. 2010. A sensitivity analysis of ring effect to aerosol properties and comparison to satellite observations. *Atmospheric Measurement Techniques,* 3(6):1723-1751.

Wedepohl, P.M., Lutjeharms, J.R.E. & Meeuwis, J.M. 2000. Surface drift in the South-East Atlantic Ocean. *South African Journal of Marine Science,* 7615(22):71-79.

Wees, D., van der Werf, G.R., Randerson, J.T. Rogers, B.M., Chen, Y., Veraverbeke, S., Giglio, L., & Morton, D.C., 2022. Global biomass burning fuel consumption and emissions at 500 m spatial resolution based on the Global Fire Emissions Database (GFED), *Geoscientific Model Development*, 15(22): 8411-8437.

Wood, R. 2015. Stratus and Stratocumulus. *Encyclopedia of Atmospheric Sciences. 2nd ed*. 2:196-200. http://dx.doi.org/10.1016/B978-0-12-382225-3.00396-0.

Wood, T.S. & Baldwin, S. 1985. Fuelwood and Charcoal. (9):407-429. **JOURNAL?**

Yu, H., Remer, L.A., Kahn, R.A., Chin, M. & Zhang, Y. 2013. Satellite perspective of aerosol intercontinental transport: from qualitative tracking to quantitative characterization. *Atmospheric Research,* 124(November 2018):73-100.

Yuan, T., Li, Z., Zhang, R. & Fan, J. 2008. Increase of cloud droplet size with aerosol optical depth: An observation and modeling study. *Journal of Geophysical Research Atmospheres,* 113(4):1-16.

Zhang, M.H., Lin, W.Y., Klein, S.A., Bacmeister, J.T., Bony, S., … Zhang, J.H. 2005. Comparing clouds and their seasonal variations in 10 atmospheric general circulation models with satellite measurements. *Journal of Geophysical Research D: Atmospheres,* 110(15):1-18.

Zhang, T., Zang, L., Mao, F., Wan, Y. & Zhu, Y. 2020. Evaluation of Himawari-8/AHI, MERRA-2, and CAMS aerosol products over China. *Remote Sensing,* 12(10):1-16.

Zhao, A., Ryder, C.L. & Wilcox, L.J. 2022. How well do the CMIP6 models simulate dust aerosols? *Atmospheric Chemistry and Physics,* 22(3):2095-2119.

Zheng, X., Xi, B., Dong, X., Logan, T., Wang, Y. & Wu, P. 2020. Investigation of aerosol-cloud interactions under different absorptive aerosol regimes using Atmospheric Radiation Measurement (ARM) southern Great Plains (SGP) ground-based measurements. *Atmospheric Chemistry and Physics,* 20(6):3483-3501.

Zuidema, P., Redemann, J., Haywood, J., Wood, R., Piketh, S., … Formenti, P. 2016. Smoke and clouds above the southeast Atlantic: Upcoming field campaigns probe absorbing aerosol's impact on climate. *Bulletin of the American Meteorological Society,* 97(7):1131-1135.

Zuidema, P., Chang, P., Medeiros, B., Kirtman, B.P., Mechoso, R., … Xu, Z. 2016. Challenges and prospects for reducing coupled climate model sst biases in the eastern tropical atlantic and pacific oceans: The U.S. Clivar eastern tropical oceans synthesis working group. *Bulletin of the American Meteorological Society,* 97(12):2305-2327.